T.C.
GEBZE TECHNICAL UNIVERSITY
GRADUATE SCHOOL

SEISMIC PERFORMANCE OF WATER DISTRIBUTION NETWORKS: EVENT-BASED DAMAGE ANALYSIS IN KAHRAMANMARAŞ AND SCENARIO-BASED RISK ASSESSMENT FOR YALOVA

ŞEYHMUS CAN TUNÇ

A THESIS OF MASTER OF SCIENCE
DEPARTMENT OF CIVIL ENGINEERING

ADVISOR: PROF. DR. SELÇUK TOPRAK

DECEMBER 2025

T.C.
GEBZE TECHNICAL UNIVERSITY
GRADUATE SCHOOL

SEISMIC PERFORMANCE OF WATER DISTRIBUTION NETWORKS: EVENT-BASED DAMAGE ANALYSIS IN KAHRAMANMARAŞ AND SCENARIO-BASED RISK ASSESSMENT FOR YALOVA

ŞEYHMUS CAN TUNÇ

A THESIS OF MASTER OF SCIENCE
DEPARTMENT OF CIVIL ENGINEERING

ADVISOR: PROF. DR. SELÇUK TOPRAK

DECEMBER 2025

T.C.
GEBZE TEKNİK ÜNİVERSİTESİ
LİSANSÜSTÜ EĞİTİM ENSTİTÜSÜ

İÇME SUYU DAĞITIM ŞEBEKELERİNİN SİSMİK PERFORMANSI: KAHRAMANMARAŞ'TA DEPREM SONRASI HASAR DEĞERLENDİRMESİ VE YALOVA İÇİN SENARYO BAZLI RİSK ANALİZİ

ŞEYHMUS CAN TUNÇ

YÜKSEK LİSANS
İNŞAAT MÜHENDİSLİĞİ ANABİLİM DALI

DANIŞMAN: PROF. DR. SELÇUK TOPRAK

ARALIK 2025

MASTER of SCIENCE JURY APPROVAL FORM

A thesis submitted by Şeyhmus Can TUNÇ defended on 30/12/2025 before the jury formed with the 16/12/2025 date and 2025/70 numbered decision of the GTU Graduate Administration Board, has been accepted as a MASTER of SCIENCE thesis in the Department of Civil Engineering.

JURY

MEMBER
(THESIS ADVISOR) : Prof. Dr. Selçuk TOPRAK

MEMBER : Prof. Dr. Ferit ÇAKIR

MEMBER : Assist. Prof. Dr. Engin NACAROĞLU

APPROVAL

Gebze Technical University Graduate Administration Board
…..…/..…/……..… date and ……/…….. numbered decision.

SIGNATURE/SEAL

To my dear family, for their endless support, and the families who lost their loved ones in the 2023 Kahramanmaras Earthquakes...

ABSTRACT

Türkiye has experienced numerous destructive earthquakes throughout its history, and these events have caused significant damage to urban lifeline systems. This thesis investigates earthquake-induced damage to water distribution networks through two complementary and interlinked approaches: (i) an event-based assessment grounded in post-earthquake field evidence, and (ii) a scenario-based infrastructure risk assessment for a seismically vulnerable urban area. Within this scope, an integrated framework is developed that combines field observations, municipal damage records, geotechnical investigations and analyses, and empirical models to evaluate the seismic performance of water infrastructure systems.

In the first part of the study, detailed observations of the drinking water system in Kahramanmaraş Province are presented, including damage to distribution lines, transmission mains, reservoirs, and related facilities based on post-earthquake inspections conducted after the 2023 Kahramanmaraş earthquakes. Liquefaction susceptibility analyses were performed for the city center, and the results were consistent with field observations, indicating no surface manifestation of liquefaction. Accordingly, the observed damage was attributed primarily to transient ground deformation (TGD), and PGV-based repair-rate relationships were developed for PVC, AC, and PE pipelines. The derived relationships indicate higher damage levels than those reported in the literature, reflecting the deteriorated condition of the network prior to the earthquake. The Kahramanmaraş case study therefore establishes a data-driven baseline for damage–ground motion relationships under predominantly TGD-controlled conditions.

In the second part of the study, the same analytical workflow is transferred to Yalova as a future earthquake case study. Yalova was selected as a pilot region within the MARTEST–SATREPS project, and two alternative ground-motion scenarios were considered: a Mw 7.5 TBEC-based earthquake scenario and a Mw 7.0 stochastic scenario. Building upon the Kahramanmaraş baseline, the framework in Yalova is expanded to explicitly incorporate liquefaction-related permanent ground deformation (PGD) through the evaluation and spatial mapping of liquefaction vulnerability indices (LPI, LSI, and LSN), together with liquefaction-induced free-field settlements. These geotechnical outcomes are integrated with TGD- and PGD-induced repair-rate models to estimate expected pipeline damage, and a comparison of the two scenarios highlights differences in the relative contributions of transient and permanent ground deformations to overall infrastructure damage.

Overall, this thesis emphasizes the critical importance of resilient water infrastructure systems for ensuring service continuity following major earthquakes. The repair-rate relationships and the integrated, transferable workflow developed in this study provide a practical basis for earthquake-induced damage estimation and infrastructure risk assessment in seismically active regions.

Keywords: Kahramanmaraş, Earthquake, Water Infrastructure, Yalova, Liquefaction, Risk Assessment.

ÖZET

Türkiye, tarih boyunca birçok yıkıcı depreme maruz kalmış ve bu depremler kentsel altyapı sistemlerinde önemli hasarlara yol açmıştır. Bu çalışma, içme suyu dağıtım şebekelerinde deprem kaynaklı hasarları iki tamamlayıcı ve birbiriyle ilişkili yaklaşım çerçevesinde incelemektedir: (i) deprem sonrası saha bulgularına dayalı olay temelli değerlendirme ve (ii) sismik açıdan kırılgan kentsel bir alan için senaryo temelli altyapı risk değerlendirmesi. Bu kapsamda, su altyapı sistemlerinin sismik performansını değerlendirmek için saha gözlemleri, belediye hasar kayıtları, geoteknik araştırmalar ve analizler ile ampirik modelleri birleştiren entegre bir çerçeve geliştirilmiştir.

Çalışmanın ilk bölümünde, 2023 Kahramanmaraş depremleri sonrasında yapılan deprem sonrası incelemelere dayalı olarak, Kahramanmaraş ilindeki içme suyu sistemine ilişkin ayrıntılı gözlemler sunulmaktadır. Bu gözlemler arasında dağıtım hatları, iletim şebekeleri, rezervuarlar ve ilgili tesislerdeki hasarlar yer almaktadır. Şehir merkezi için sıvılaşma duyarlılık analizleri yapılmış ve sonuçlar saha gözlemleriyle tutarlı bulunmuş, yüzeyde sıvılaşma belirtilerine dair herhangi bir bulgu tespit edilmemiştir. Bu doğrultuda, gözlemlenen hasarların temel nedeni geçici zemin deformasyonu (TGD) olarak değerlendirilmiş ve PVC, AC ve PE boru hatları için PGV tabanlı onarım oranı ilişkileri geliştirilmiştir. Elde edilen ilişkiler, deprem öncesinde sistemin yıpranmış durumunu yansıtan, literatürde bildirilenlerden daha yüksek hasar seviyelerini göstermektedir. Kahramanmaraş vaka çalışması, bu nedenle, ağırlıklı olarak TGD'nin kontrolündeki koşullarda hasar-zemin hareketi ilişkileri için veriye dayalı bir temel oluşturmaktadır.

Çalışmanın ikinci bölümünde, aynı analitik süreç, geleceğe yönelik bir deprem vaka çalışması olarak Yalova'ya uygulanmıştır. Yalova, MARTEST–SATREPS projesi kapsamında pilot bölge olarak seçilmiş ve iki alternatif kuvvetli yer hareketi senaryosu dikkate alınmıştır: Mw 7,5 TBDY bazlı deprem senaryosu ve Mw 7,0 stokastik temelli senaryo. Kahramanmaraş'ta oluşturulan temel üzerine inşa edilen bu aşamada, çerçeve Yalova özelinde sıvılaşma kaynaklı kalıcı zemin deformasyonlarını (PGD) açık biçimde içerecek şekilde genişletilmiştir. Bu amaçla, sıvılaşma duyarlılığının değerlendirilmesi ve mekânsal haritalanması kapsamında LPI, LSI ve LSN indisleri ile sıvılaşma kaynaklı yüzey oturmaları hesaplanmıştır. Elde edilen geoteknik çıktılar, TGD ve PGD etkilerini temsil eden onarım oranı modelleriyle birleştirilerek beklenen boru hasarları tahmin edilmiş; iki senaryonun karşılaştırılmasıyla geçici ve kalıcı zemin deformasyonlarının toplam altyapı hasarına yönelik görece katkıları ortaya konmuştur.

Sonuç olarak, bu tez büyük depremler sonrası hizmet sürekliliğinin sağlanmasında dayanıklı su altyapı sistemlerinin kritik önemini vurgulamaktadır. Geliştirilen onarım oranı ilişkileri ile bütünleşik ve başka bölgelere aktarılabilir çalışma akışı, deprem kaynaklı hasar tahmini ve sismik risk değerlendirmesi için pratik bir temel sunmaktadır.

Anahtar Kelimeler: Kahramanmaraş, Deprem, Su Altyapısı, Yalova, Sıvılaşma, Risk Analizi.

ACKNOWLEDGEMENTS

I would like to give my special thanks to my supervisor, Prof. Dr. Selçuk TOPRAK, who has not only shared his extensive knowledge with me but also guided me with patience and wisdom throughout this journey. He supported my involvement in field investigations, which led me to dedicate myself to science after witnessing the destruction caused by the 2023 Kahramanmaraş Earthquakes in Hatay, Kahramanmaraş, Gaziantep, and Adıyaman. His advice, encouragement, understanding, and support gave me the motivation and willpower to succeed in this thesis.

I also want to sincerely thank my family and my loved ones, who have been there for me and have always been the motivation for me throughout this journey. Their endless patience and support through my education helped me to sustain my success.

Moreover, I would like to express my sincere gratitude to Assoc. Prof. Hadi KHANBABAZADEH for the valuable courses he taught during both my graduate and undergraduate studies, which significantly shaped my academic foundation. I am also deeply thankful to Assist. Prof. Dr. Engin NACAROĞLU for his continuous support, guidance, and the knowledge he has shared with me, as well as to Prof. Dr. Ferit ÇAKIR for his contributions as a jury member and for his insightful comments. In addition, I would like to thank Prof. Dr. Ayşegül ASKAN GÜNDOĞAN and her students for providing the ground motion parameters within the scope of the MARTEST-SATREPS project, which were utilized in the Yalova scenario-based assessments.

Finally, I would like to express my sincere gratitude to KASKI (Kahramanmaraş Water and Sewerage Administration) management and personnel, the Kahramanmaraş Metropolitan Municipality for providing the geotechnical data, and the employees of Yalova Municipality for their important support in conducting this study. Studies related to Yalova have been performed as part of the MARTEST-SATREPS project supported by JICA; therefore, I would like to thank the MARTEST-SATREPS Project team for their valuable contributions and collaboration.

TABLE OF CONTENTS

	Page
ABSTRACT	vi
ÖZET	vii
ACKNOWLEDGEMENTS	viii
TABLE OF CONTENTS	ix
LIST OF SYMBOLS AND ABBREVIATIONS	xi
LIST OF FIGURES	xii
LIST OF TABLES	xix
1. INTRODUCTION	1
2. RESEARCH BACKGROUND	5
2.1. Earthquake Effects on Buried Pipeline Systems	5
2.2. Liquefaction and Ground Failures	10
3. METHODOLOGY	15
3.1. Processing of Pipeline Damage Records	16
3.2. Quantitative Analysis of Pipeline Damages	21
3.3. Liquefaction Analysis Methodology	22
3.3.1. Liquefaction Susceptibility Evaluation Methods	26
3.3.2. Index-Based Assessment Methods	33
3.3.3. Liquefaction-Induced Settlement Estimation Methods	38
3.3.3.1. Tokimatsu and Seed [1984] Free-Field Settlement Procedure	38
3.3.3.2. Ishihara and Yoshimine [1992] Free-Field Settlement Procedure	39
3.3.3.3. Shamoto et al. [1998] Free-Field Settlement Procedure	42
3.3.3.4. Wu et al. [2003] Free-Field Settlement Procedure	45
3.3.3.5. Cetin et al. [2009] Free-Field Settlement Procedure	46
4. REGIONAL OVERVIEW OF KAHRAMANMARAŞ PROVINCE	48
4.1. Geography, Climate and Economic Structure	48
4.2. Geological Formation	49
4.3. Seismic Characteristics	49
4.4. Water Supply System	53
5. OBSERVED DAMAGES AFTER THE 2023 KAHRAMANMARAŞ EARTHQUAKES	57
5.1. Structural Damages	57
5.2. Water Infrastructure Systems	62
5.2.1. Treatment Plants	66
5.2.2. Transmission Lines	66
5.2.3. Water Tanks	67
5.2.4. Distribution Lines	68
5.2.5. Post-Earthquake Recovery Efforts	73
6. LIQUEFACTION SUSCEPTIBILITY MAPPING OF KAHRAMANMARAŞ PROVINCE	74
6.1. Comparison of Results Based on Different Susceptibility Methods	78
6.2. Comparison of Results Based on Different PGA Sources	79
6.3. Comparison of Results Based on Different Susceptibility Criteria	80

6.4. Comparison of LPI, LSI and LSN Results 80
7. WATER INFRASTRUCTURE DAMAGE ASSESSMENT OF KAHRAMANMARAŞ CITY CENTER 91
8. RISK ASSESSMENT FOR YALOVA 100
8.1. Regional Overview of Yalova Province 100
8.1.1. Geography, Climate, and Economic Structure 100
8.1.2. Geological Structure 101
8.1.3. Seismic Characteristics 102
9. LIQUEFACTION SUSCEPTIBILITY MAPPING OF YALOVA CITY CENTER 103
9.1. Scenario 1: TBEC 2018 Mw 7.5 Earthquake 107
9.2. Scenario 2: Prince Islands Mw 7.0 Earthquake 111
9.3. Comparison of the Results 115
10. ASSESSMENT OF LIQUEFACTION-INDUCED FREE-FIELD SETTLEMENTS IN YALOVA CITY CENTER 116
10.1. Scenario 1: TBEC 2018 Mw 7.5 Earthquake 116
10.1.1. Tokimatsu and Seed [1984] Procedure 116
10.1.2. Ishihara and Yoshimine [1992] Procedure 117
10.1.3. Shamoto et al. [1998] Procedure 120
10.1.4. Wu et al. [2003] Procedure 121
10.1.5. Cetin et al. [2009] Procedure 122
10.2. Scenario 2: Prince Islands Mw 7.0 Earthquake 123
10.2.1. Tokimatsu and Seed [1984] Procedure 123
10.2.2. Ishihara and Yoshimine [1992] Procedure 124
10.2.3. Shamoto et al. [1998] Procedure 126
10.2.4. Wu et al. [2003] Procedure 127
10.2.5. Cetin et al. [2009] Procedure 128
11. PIPELINE DAMAGE ASSESSMENT OF YALOVA CITY CENTER 130
11.1. Scenario 1: TBEC 2018 Mw 7.5 Earthquake 134
11.2. Scenario 2: Prince Islands Mw 7.0 Earthquake 140
12. CONCLUSIONS 149

REFERENCES 152
BIOGRAPHY 163
PUBLICATIONS AND PRESENTATIONS FROM THE THESIS 164

LIST OF SYMBOLS AND ABBREVIATIONS

a_{max}	:	Maximum Acceleration
C_B	:	Borehole Diameter Factor
C_E	:	Energy Ratio Factor
C_N	:	Overburden Pressure Factor
C_R	:	Rod Length Factor
C_S	:	Sampling Method Factor
D_R	:	Relative Density
ϵ_v	:	Volumetric Strain
g	:	Gravitational Acceleration
γ_{max}	:	Maximum Shear Strain
N_m	:	Number of Blows Required for 30 cm Penetration
$(N_1)_{60}$	:	Normalized SPT Blow Count
r_d	:	Stress Reduction Factor
σ_{vo}	:	Total Stress
σ'_{vo}	:	Effective Stress
V_s	:	Shear Wave Velocity
V_{s30}	:	Average Shear Wave Velocity for Upper 30-m Depth
w_c	:	Water Content
AC	:	Asbestos Cement
AFAD	:	Disaster and Emergency Management Agency
CI	:	Cast Iron
CPT	:	Cone Penetration Test
CRR	:	Cyclic Resistance Ratio
CSR	:	Cyclic Stress Ratio
FC	:	Fines Content
FS	:	Factor of Safety
GIS	:	Geographic Information System
GRP	:	Glass Reinforced Plastic
HDPE	:	High-Density Polyethylene
KASKI	:	Kahramanmaraş Water and Sewerage Administration
LiDAR	:	Light Detection and Ranging
LL	:	Liquid Limit
LPI	:	Liquefaction Potential Index
LSI	:	Liquefaction Severity Index
LSN	:	Liquefaction Severity Number
MASW	:	Multi-channel Analysis of Surface Waves
MSF	:	Magnitude Scaling Factor
PGA	:	Peak Ground Acceleration
PGD	:	Permanent Ground Deformation
PGV	:	Peak Ground Velocity
PI	:	Plasticity Index
PL	:	Plasticity Limit
PE	:	Polyethylene
PPRC	:	Polypropylene Random Copolymer
PVC	:	Polyvinyl Chloride
SPT	:	Standard Penetration Test
TGD	:	Transient Ground Deformation

LIST OF FIGURES

	Page
Figure 1.1: Map showing the provinces affected by the 2023 Kahramanmaraş earthquakes.	1
Figure 1.2: Map showing Yalova Province, its town boundaries, and their proximity to the fault lines.	3
Figure 2.1: Schematic illustration showing the primary geohazards that affect buried pipelines [Toprak et al., 2024a].	6
Figure 2.2: Conceptual illustration of the liquefaction mechanism in saturated soils before, during and after the shaking.	10
Figure 2.3: Liquefaction-induced ground deformations observed in İskenderun, Türkiye, following the 2023 Kahramanmaraş Earthquakes: (a) settlement due to liquefaction and (b) sand boils [Toprak et al., 2024a]; (c) lateral spreading [Toprak et al., 2025c].	11
Figure 3.1: Methodological framework adopted in this study.	15
Figure 3.2: Distribution of call durations, indicating the number of days between the initiation and closure of calls.	17
Figure 3.3: Flowchart summarizing the filtering processes applied to the call records.	18
Figure 3.4: Temporal distribution of daily filtered malfunction reports recorded through the 185 Emergency Call Center between August 2022 and December 2024.	19
Figure 3.5: Cumulative frequency of daily filtered malfunction reports.	20
Figure 3.6: Comparison of the number of daily call records after the earthquake with the pre-earthquake average.	20
Figure 3.7: Liquefaction assessment methodology followed in the analysis of Kahramanmaraş Province.	24
Figure 3.8: Liquefaction assessment methodology followed in the analysis of Yalova Province.	25
Figure 3.9: Relationship between cyclic stress ratio and corrected SPT blow count with volumetric strain curves [Tokimatsu and Seed, 1984].	38
Figure 3.10: Output of the interpolation algorithm showing test depths and distances to the nearest curves for the Tokimatsu and Seed [1984] method.	39
Figure 3.11: Relationship between the factor of safety for liquefaction and volumetric strain (ε_v), with relative density (D_R) and N_1 curves [Ishihara and Yoshimine, 1992].	40
Figure 3.12: Relationship between cyclic stress ratio and adjusted SPT blow count with volumetric strain curves [Shamoto et al., 1998].	43
Figure 3.13: Output of the interpolation algorithm showing test depths and distances to the nearest curves for the Shamoto et al. [1998] method: (a) Fines Content < 10%, (b) 10% ≤ Fines Content < 20%, (c) Fines Content ≥ 20%.	44
Figure 3.14: Reconsolidation volumetric strain curves based on $(N_1)_{60cs}$ and CSR [Wu et al., 2003].	45

Figure 3.15: Visual output of the interpolation process displaying depths of test points and their distances to Wu et al. [2003] reference curves. 45
Figure 4.1: Map of the geological structure of Kahramanmaraş city center. 49
Figure 4.2: Map of the seismicity of the earthquake-affected region. 50
Figure 4.3: The distribution of the earthquake events by magnitude. 51
Figure 4.4: Quarterly distribution of the earthquake events. 51
Figure 4.5: Map showing the water sources and transmission lines in the city center. 55
Figure 4.6: Material types of the pipeline network in Kahramanmaraş city center. 56
Figure 4.7: The distribution map of the pipeline network based on pipe types. 56
Figure 5.1: Google Earth satellite imagery of Azerbaijan Boulevard, showing the extent of structural damage: (a) before the earthquakes (10 April 2022) and (b) after the earthquakes (16 February 2023). 58
Figure 5.2: Examples of earthquake-induced damage observed during the field survey in the city center: (a) damaged and abandoned multi-story building, (b–d) collapsed buildings with heavily damaged adjacent structures and debris from the collapses. 58
Figure 5.3: Structural damage documented during the field investigation in the city center: (a) damaged building awaiting demolition, (b) severely damaged and non-functional structure, (c) structural element with visible damage, and (d) buckled structural system indicating serious deformation. 59
Figure 5.4: Post-earthquake reconstruction efforts supported by the Republic of Azerbaijan: (a) construction site of post-earthquake housing, and (b) newly constructed residential building. 60
Figure 5.5: Earthquake-induced ground deformations in Ekinözü Town (Courtesy of Ekinözü Municipality): (a) pavement cracks caused by ground displacement, (b) road damage due to soil stability issues, (c) surface cracking and displacement, and (d) ground uplift affecting tree alignment and soil surface. 61
Figure 5.6: Drone images showing building demolitions and debris removal operations in Elbistan Town (Courtesy of Elbistan Municipality). 62
Figure 5.7: Overview of damages in infrastructure systems [Toprak et al., 2024a]. 63
Figure 5.8: Post-earthquake activities carried out by KASKI (Courtesy of KASKI): (a) repair of a damaged 250 mm AC pipe, (b) capping operations, and (c) water supply efforts to container cities. 65
Figure 5.9: Removed pipes from the balancing reservoir at the Ayvalı Treatment Plant [Toprak et al., 2024d]. 66
Figure 5.10: Collapsed elevated tank in the Çiğdemtepe Neighborhood: (a) before the earthquake, (b) after the collapse (Courtesy of KASKI), and (c–d) the newly constructed tank (Google Maps). 67
Figure 5.11: Damaged tanks in Kadincik (a) and Osmandede (b) neighborhoods (Courtesy of KASKI). 68

Figure 5.12: Examples of earthquake-induced damage in CI pipes: (a) 63 mm diameter pipe with evident corrosion and leakage; (b) 150 mm diameter pipe showing leakage at a displaced lead-sealed joint (Courtesy of KASKI). 69
Figure 5.13: Damage and repair practices observed in AC pipes after the earthquakes: (a) 150 mm pipe leaking from a separated joint; (b) same pipe section repaired using a metal clamp; (c) completely fractured 100 mm pipe with high-pressure water leakage; (d) 100 mm pipe repaired with a clamp; (e) removed 100 mm AC pipe section showing complete fracture; (f) repaired condition of the same 100 mm pipe (Courtesy of KASKI). 70
Figure 5.14: Damage and repair operations observed in PE pipes after the earthquakes: (a) 100 mm pipe with puncture; (b) subsequent repair using a mechanical clamp; (c) 80 mm pipe with complete fracture and leakage; (d) subsequent repair using a mechanical clamp (Courtesy of KASKI). 71
Figure 5.15: Earthquake-induced damage and subsequent repair in PVC pipes: (a) 75 mm pipe with visible cracking; (b) subsequent repair of the pipe; (c) 100 mm pipe exhibiting cracks and active leakage; (d) subsequent repair using PVC fittings (Courtesy of KASKI). 72
Figure 6.1: Map showing the spatial distribution of SPT boreholes in the study area. 74
Figure 6.2: Map showing the spatial distribution of GWT in the study area. 75
Figure 6.3: Spatial distribution of blow counts: (a) at 1.5 meters, (b) at 3.0 meters, (c) at 4.5 meters, (d) at 6.0 meters, (e) at 7.5 meters, and (f) at 9.0 meters. 76
Figure 6.4: Spatial point distribution to determine PGA and PGV values from Toprak et al. [2025a]. 77
Figure 6.5: Visualization and spatial distribution map based on the PGA values from Toprak et al. [2025a]. 77
Figure 6.6: Visualization and spatial distribution map based on the PGV values from Toprak et al. [2025a]. 78
Figure 6.7: Comparison of PGA values obtained in accordance with TBEC 2018 with PGA values from Toprak et al. [2025a] at the borehole locations. 79
Figure 6.8: LPI map calculated using the Boulanger and Idriss [2014] method for factor of safety estimation, with input PGA based on TBEC 2018. 81
Figure 6.9: LSI map calculated using the Boulanger and Idriss [2014] method for factor of safety estimation, with input PGA based on TBEC 2018. 81
Figure 6.10: LSN map calculated using the Boulanger and Idriss [2014] method for factor of safety estimation, with input PGA based on TBEC 2018. 82
Figure 6.11: LPI map calculated using the Boulanger and Idriss [2014] method for factor of safety estimation, with input ground motion from Toprak et al. [2025a]. 82

Figure 6.12: LSI map calculated using the Boulanger and Idriss [2014] method for factor of safety estimation, with input ground motion from Toprak et al. [2025a]. 83
Figure 6.13: LSN map calculated using the Boulanger and Idriss [2014] method for factor of safety estimation, with input ground motion from Toprak et al. [2025a]. 83
Figure 6.14: LPI map calculated using the Youd et al. [2001] method for factor of safety estimation, with input PGA based on TBEC 2018. 84
Figure 6.15: LSI map calculated using the Youd et al. [2001] method for factor of safety estimation, with input PGA based on TBEC 2018. 84
Figure 6.16: LSN map calculated using the Youd et al. [2001] method for factor of safety estimation, with input PGA based on TBEC 2018. 85
Figure 6.17: LPI map calculated using the Youd et al. [2001] method for factor of safety estimation, with input ground motion from Toprak et al. [2025a]. 85
Figure 6.18: LSI map calculated using the Youd et al. [2001] method for factor of safety estimation, with input ground motion from Toprak et al. [2025a]. 86
Figure 6.19: LSN map calculated using the Youd et al. [2001] method for factor of safety estimation, with input ground motion from Toprak et al. [2025a]. 86
Figure 6.20: Comparison graph of calculated LPI values: (a) No Criteria, (b) Boulanger and Idriss [2006], (c) Bray and Sancio [2006], and (d) Seed et al. [2003]. 87
Figure 6.21: Comparison graph of calculated LSI values: (a) No Criteria, (b) Boulanger and Idriss [2006], (c) Bray and Sancio [2006], and (d) Seed et al. [2003]. 88
Figure 6.22: Comparison graph of calculated LSN values: (a) No Criteria, (b) Boulanger and Idriss [2006], (c) Bray and Sancio [2006], and (d) Seed et al. [2003]. 89
Figure 6.23: Critical layer conditions assessed with the boundary curves of Ishihara [1985]. 90
Figure 7.1: Spatial distribution of damage points on the pipeline network. 92
Figure 7.2: Relationship between PGV and repair rate for AC pipelines. 95
Figure 7.3: Relationship between PGV and repair rate for PVC pipelines. 96
Figure 7.4: Relationship between PGV and repair rate for PE pipelines. 97
Figure 7.5: Comparison of RR–PGV relationships for AC pipes between this study and the empirical models proposed in the literature. 98
Figure 7.6: Comparison of RR–PGV relationships for PVC pipes between this study and the empirical model proposed in the literature. 99
Figure 8.1: Map showing the geological structure of Yalova city center and its surroundings. 101
Figure 8.2: Map showing the seismicity of the Marmara Region. 102
Figure 9.1: Spatial distribution of all SPT, MASW, and CPT locations within the study area. 104
Figure 9.2: Spatial distribution of ground water table within the study area. 104
Figure 9.3: Spatial distribution of V_{s30} within the study area. 105

Figure 9.4. Spatial distribution of PGA values considered in Scenario 1 (TBEC 2018 Mw 7.5 earthquake). 107
Figure 9.5: LPI map calculated using the Youd et al. [2001] method for factor of safety estimation. 108
Figure 9.6: LSI map calculated using the Youd et al. [2001] method for factor of safety estimation. 108
Figure 9.7: LSN map calculated using the Youd et al. [2001] method for factor of safety estimation. 109
Figure 9.8: LPI map calculated using the Boulanger and Idriss [2014] method for factor of safety estimation. 109
Figure 9.9: LSI map calculated using the Boulanger and Idriss [2014] method for factor of safety estimation. 110
Figure 9.10: LSN map calculated using the Boulanger and Idriss [2014] method for factor of safety estimation. 110
Figure 9.11: Spatial distribution of PGA values considered in Scenario 2 (Prince Islands Mw 7.0 earthquake, MARTEST–SATREPS project). 111
Figure 9.12: LPI map calculated using the Youd et al. [2001] method for factor of safety estimation. 112
Figure 9.13: LSI map calculated using the Youd et al. [2001] method for factor of safety estimation. 112
Figure 9.14: LSN map calculated using the Youd et al. [2001] method for factor of safety estimation. 113
Figure 9.15: LPI map calculated using the Boulanger and Idriss [2014] method for factor of safety estimation. 113
Figure 9.16: LSI map calculated using the Boulanger and Idriss [2014] method for factor of safety estimation. 114
Figure 9.17: LSN map calculated using the Boulanger and Idriss [2014] method for factor of safety estimation. 114
Figure 10.1: Spatial distribution of liquefaction-induced free-field settlements in the Yalova shoreline and city center, estimated using the Tokimatsu and Seed [1984] procedure. 117
Figure 10.2: Spatial distribution of liquefaction-induced free-field settlements in the Yalova shoreline and city center, estimated using the Ishihara and Yoshimine [1992] and Zhang et al. [2004] procedure. 118
Figure 10.3: Spatial distribution of liquefaction-induced free-field settlements in the Yalova shoreline and city center, estimated using the Ishihara and Yoshimine [1992] and Yoshimine et al. [2006] procedure. 119
Figure 10.4: Spatial distribution of liquefaction-induced free-field settlements in the Yalova shoreline and city center, estimated using the Shamoto et al. [1998] procedure. 120
Figure 10.5: Spatial distribution of liquefaction-induced free-field settlements in the Yalova shoreline and city center, estimated using the Wu et al. [2003] procedure. 121
Figure 10.6: Spatial distribution of liquefaction-induced free-field settlements in the Yalova shoreline and city center, estimated using the Cetin et al. [2009] procedure. 122

Figure 10.7: Spatial distribution of liquefaction-induced free-field settlements in the Yalova shoreline and city center, estimated using the Tokimatsu and Seed [1984] procedure. 124
Figure 10.8: Spatial distribution of liquefaction-induced free-field settlements in the Yalova shoreline and city center, estimated using the Ishihara and Yoshimine [1992] and Zhang et al. [2004] procedure. 125
Figure 10.9: Spatial distribution of liquefaction-induced free-field settlements in the Yalova shoreline and city center, estimated using the Ishihara and Yoshimine [1992] and Yoshimine et al. [2006] procedure. 126
Figure 10.10: Spatial distribution of liquefaction-induced free-field settlements in the Yalova shoreline and city center, estimated using the Shamoto et al. [1998] procedure. 127
Figure 10.11: Spatial distribution of liquefaction-induced free-field settlements in the Yalova shoreline and city center, estimated using the Wu et al. [2003] procedure. 128
Figure 10.12: Spatial distribution of liquefaction-induced free-field settlements in the Yalova shoreline and city center, estimated using the Cetin et al. [2009] procedure. 129
Figure 11.1: Map of the water source, transmission pipelines, storage tanks, and pumping stations in Yalova. 130
Figure 11.2: Transmission pipeline material distribution and pipe length by diameter for the Yalova Province water supply system. 131
Figure 11.3: Pipeline material percentages within the water distribution network managed by Yalova Municipality. 131
Figure 11.4: Spatial distribution of the water distribution network with respect to pipe materials within the Yalova Municipality water system. 132
Figure 11.5: Distribution pipeline material percentages in the study area. 133
Figure 11.6: Spatial distribution of the water distribution network within liquefiable and non-liquefiable regions based on the LPI map. 134
Figure 11.7: Spatial distribution of the water distribution network within liquefiable and non-liquefiable regions based on the LSN map. 135
Figure 11.8: Distribution of pipeline materials and their corresponding lengths within liquefied and non-liquefied zones based on LPI in the study area. 135
Figure 11.9: Distribution of pipeline materials and their corresponding lengths within liquefied and non-liquefied zones based on LSN in the study area. 136
Figure 11.10: Spatial distribution of the water distribution network within liquefiable and non-liquefiable regions based on the LPI map. 141
Figure 11.11: Spatial distribution of the water distribution network within liquefiable and non-liquefiable regions based on the LSN map. 141
Figure 11.12: Distribution of pipeline materials and their corresponding lengths within liquefied and non-liquefied zones based on LPI in the study area. 142

Figure 11.13: Distribution of pipeline materials and their corresponding lengths within liquefied and non-liquefied zones based on LSN in the study area. 142

LIST OF TABLES

Page

Table 3.1: Number of filtered call records per month for the period from August 6, 2022, to August 15, 2023. 19

Table 3.2: $[\emptyset^{-1}(\beta_c)]^2$ values corresponding to selected confidence levels used in the screening criteria formulation. 22

Table 3.3: Correction factors for SPT-N values used in this study [Youd et al., 2001]. 28

Table 3.4: Liquefaction susceptibility criteria used in the study. 30

Table 3.5: Classification of liquefaction potential based on LPI value adopted in this study [Iwasaki et al., 1982]. 34

Table 3.6: Classification of liquefaction severity based on LSI value used in this study [Sonmez and Gokceoglu, 2005]. 35

Table 3.7: LSN ranges, category names, and observed land effects considered in this study [Tonkin and Taylor, 2013]. 37

Table 3.8: ΔN_f values determined based on fines content ranges. 42

Table 4.1: The PGA, PGV, and Peak Ground Displacement (PGD) values recorded by AFAD stations during the Mw 7.7 Pazarcık earthquake. 52

Table 4.2: The PGA, PGV, and PGD values measured by AFAD stations during the Mw 7.6 Elbistan earthquake. 52

Table 4.3: Names and storage volumes of water tanks located in the city center of Kahramanmaraş. 54

Table 4.4: Technical specifications of the pumping stations transferring water to upper zones in the Kahramanmaraş city center. 54

Table 5.1: District-based water delivery rates in Kahramanmaraş following the February 2023 earthquakes. 64

Table 7.1: Repair rates calculated for different pipeline material types to assess the overall system performance. 92

Table 7.2: Total lengths of pipelines within each PGV interval. 94

Table 7.3: Number of pipeline damages classified by PGV intervals. 94

Table 7.4: PGV classes and corresponding repair rates for AC pipelines. 95

Table 7.5: PGV classes and corresponding repair rates for PVC pipelines. 96

Table 7.6: PGV classes and corresponding repair rates for PE pipelines. 97

Table 9.1: V_{s30} reference values obtained from AFAD strong-motion stations used for the verification of the interpolated V_{s30} map. 106

Table 11.1: Total lengths of pipelines within each PGV interval in non-liquefiable regions identified based on the LPI assessment. 136

Table 11.2: Total lengths of pipelines within each PGV interval in non-liquefiable regions identified based on the LSN assessment. 137

Table 11.3: Total lengths of pipelines within each LPI interval in liquefiable regions. 137

Table 11.4: Total lengths of pipelines within each LSN interval in liquefiable regions. 137

Table 11.5: Total lengths of pipelines within S_{v1D} interval in liquefiable zones, calculated using the Ishihara and Yoshimine [1992] method. 138

Table 11.6: Summary of the predicted number of damages for Scenario 1 based on the available repair-rate relationships in the literature, considering liquefiable and non-liquefiable regions identified using the LPI map. 139
Table 11.7: Summary of the predicted number of damages for Scenario 1 based on the available repair-rate relationships in the literature, considering liquefiable and non-liquefiable regions identified using the LSN map. 140
Table 11.8: Total lengths of pipelines within each PGV interval in non-liquefiable regions identified based on the LPI assessment. 143
Table 11.9: Total lengths of pipelines within each PGV interval in non-liquefiable regions identified based on the LSN assessment. 143
Table 11.10: Total lengths of pipelines within each LPI interval in liquefiable regions. 144
Table 11.11: Total lengths of pipelines within each LSN interval in liquefiable regions. 144
Table 11.12: Total lengths of pipelines within S_{v1D} interval in liquefiable zones, calculated using the Ishihara and Yoshimine [1992] method. 145
Table 11.13: Summary of the predicted number of damages for Scenario 2 based on the available repair-rate relationships in the literature, considering liquefiable and non-liquefiable regions identified using the LPI map. 145
Table 11.14: Summary of the predicted number of damages for Scenario 2 based on the available repair-rate relationships in the literature, considering liquefiable and non-liquefiable regions identified using the LSN map. 146

1. INTRODUCTION

Türkiye is located in one of the most seismically active regions in the world and has experienced numerous destructive earthquakes throughout its history. Among these events, the earthquake sequence that occurred on February 6, 2023, represents one of the most devastating disasters in recent decades. The first earthquake, with a moment magnitude of Mw 7.7, occurred near the Pazarcık district of Kahramanmaraş at 04:17, followed by a second major event with a magnitude of Mw 7.6 near Elbistan at 13:24 on the same day **[Toprak et al., 2025a]**. This sequence affected 11 provinces, including Kahramanmaraş, Hatay, Gaziantep, Malatya, Adıyaman, Adana, Şanlıurfa, Kilis, Osmaniye, Diyarbakır, and Elazığ, impacting more than 14 million people (**Figure 1.1**). According to official records, over 50,000 lives were lost, nearly 100,000 people were injured, and hundreds of thousands of buildings were either severely or moderately damaged **[SBB, 2023]**.

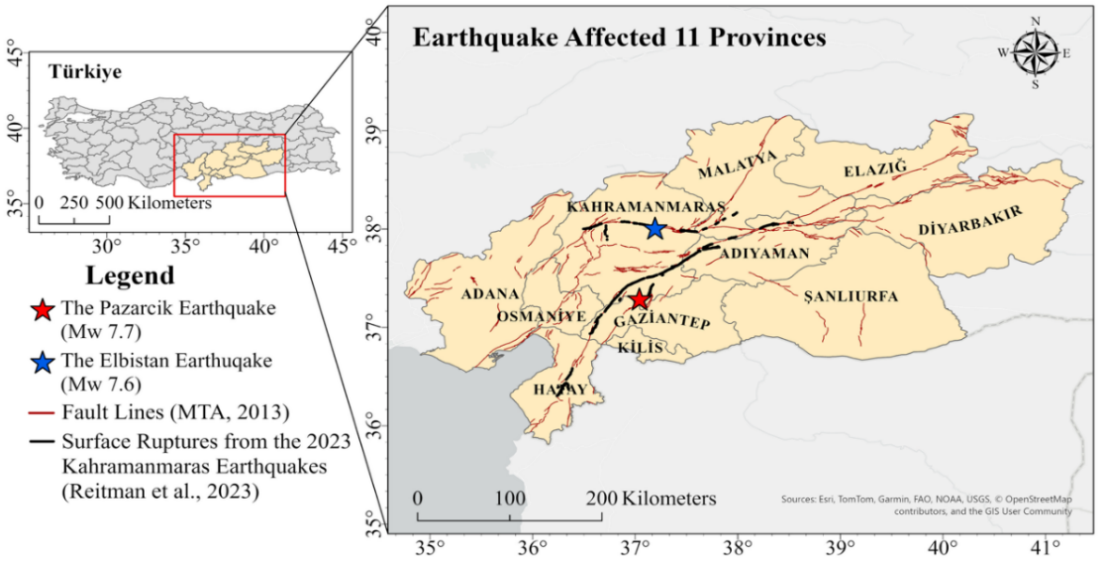


Figure 1.1: Map showing the provinces affected by the 2023 Kahramanmaraş earthquakes.

Beyond the widespread structural damage, the 2023 Kahramanmaraş earthquakes caused severe disruptions to the critical lifeline systems that support urban functionality and societal sustainability **[Toprak et al., 2024a]**. Water distribution networks, wastewater systems, transportation infrastructure, energy supply, and

communication networks were significantly affected by earthquake-induced ground shaking and geotechnical hazards **[Görüm et al., 2023; Unal et al., 2024; Toprak et al., 2025c]**. In particular, water infrastructure systems experienced extensive damage, including pipeline failures, malfunctioning pumping stations, damaged reservoirs, and deterioration of water quality due to increased turbidity and contamination **[Toprak et al., 2025d; 2026b]**. These failures led to prolonged service interruptions and demonstrated the vulnerability of buried pipeline systems under strong seismic loading **[Toprak et al. 2024b]**.

Earthquake-induced damage to buried pipelines is generally governed by two primary mechanisms: transient ground deformation (TGD) and permanent ground deformation (PGD) **[Toprak et al., 2015]**. TGD refers to temporary ground movements associated with seismic wave propagation, while PGD results from lasting ground displacements caused by phenomena such as liquefaction-induced settlement, lateral spreading, landslides, and surface faulting **[e.g., O'Rourke et al. 2014]**. Numerous studies have shown that the relative contribution of these mechanisms varies depending on local geotechnical conditions, ground motion characteristics, and the structural properties of the pipeline network. Understanding the dominant damage mechanisms is therefore essential for developing reliable damage prediction models and improving the seismic resilience of water infrastructure systems.

Although widespread liquefaction was documented in several regions affected by the 2023 Kahramanmaraş earthquakes—such as İskenderun and Gölbaşı—no surface manifestation of liquefaction was observed in the city center of Kahramanmaraş. Post-earthquake field investigations and geotechnical analyses consistently indicated that the observed damage to the water distribution network in the city center was predominantly governed by transient ground deformation rather than liquefaction-induced permanent ground deformation. Liquefaction susceptibility analyses were nevertheless conducted to validate field observations, to ensure methodological completeness, and to establish a consistent analytical framework that could be transferred to other regions with different geotechnical characteristics.

In this context, the Kahramanmaraş case provides a unique opportunity to perform an event-based assessment of water infrastructure damage under predominantly TGD-controlled conditions. The availability of detailed post-earthquake field observations and municipal damage records allows for the development of data-driven relationships

between seismic ground motion parameters and observed pipeline damage. These relationships form a validated baseline that can be tested and extended within a scenario-based risk assessment framework for other seismically vulnerable regions.

One such region is Yalova Province, which is located along the southern coast of the Marmara Sea and lies in close proximity to the Marmara seismic gap (**Figure 1.2**). Yalova experienced severe damage during the 17 August 1999 Kocaeli Earthquake (Mw 7.4), during which liquefaction-induced ground deformations, including settlements and lateral spreading were widely documented in coastal areas **[GEER, 1999; PEER, 2000a]**.

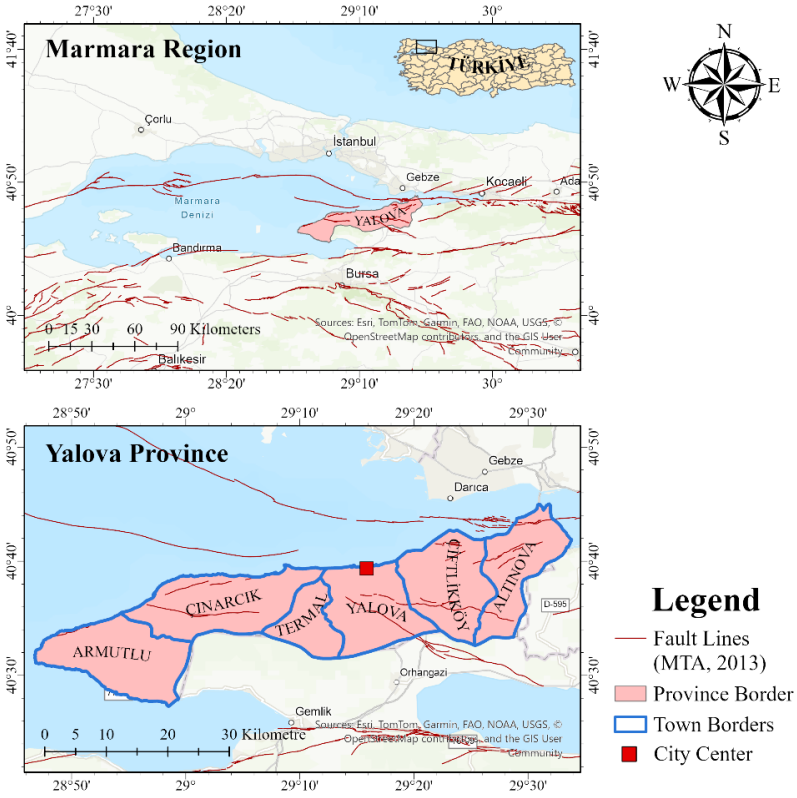


Figure 1.2: Map showing Yalova Province, its town boundaries, and their proximity to the fault lines.

Previous studies have consistently identified Yalova as a region with high liquefaction susceptibility under strong ground motions, particularly in areas characterized by shallow groundwater levels and young alluvial deposits **[Toprak et al., 2025e]**. Owing to its seismic history, geotechnical vulnerability, and data availability, Yalova was selected as a pilot region within the scope of the MARTEST-SATREPS project for scenario-based earthquake risk assessment.

Within this framework, this thesis integrates an event-based damage assessment conducted in Kahramanmaraş with a scenario-based infrastructure risk assessment for Yalova. The primary objectives of this study are to (i) conduct an event-based evaluation of earthquake-induced damage to the water distribution network in Kahramanmaraş using post-earthquake field observations and municipal damage records; (ii) develop peak ground velocity (PGV)-based repair-rate relationships for different pipeline materials under predominantly TGD-controlled conditions; and (iii) apply the derived and existing relationships within a scenario-based risk assessment framework for Yalova Province, explicitly incorporating liquefaction susceptibility and liquefaction-induced ground deformation effects.

The main contributions of this study include the assessment of earthquake-induced damage to the Kahramanmaraş water distribution system, the development of data-driven repair-rate relationships based on recent large-magnitude earthquake damage, and the development of an integrated and transferable workflow that combines seismic hazard characterization, geotechnical analysis, and infrastructure damage modeling. The proposed framework provides a practical basis for evaluating earthquake-induced damage and supporting risk-informed decision-making for urban water infrastructure systems in seismically active regions.

2. RESEARCH BACKGROUND

2.1. Earthquake Effects on Buried Pipeline Systems

Over the past decades, numerous major earthquakes worldwide have caused significant damage to buried pipeline systems and other lifeline networks. Comprehensive literature reviews on earthquake-induced pipeline damage mechanisms and performance assessments have also been presented by **Toprak [1998]**, **Nacaroğlu [2010]**, and **Ceylan [2020]**. For instance, **Toprak [1998]** reported that the 1994 Mw 6.7 Northridge Earthquake in the United States severely damaged the Los Angeles water distribution network, with over 1,000 failure locations and damage to three major transmission lines. **Davis et al. [2012]** examined the same event in detail, focusing on water delivery, fire protection, quantity, quality, and overall functionality. **Chung et al. [1996]** reported that after the 1995 Mw 6.9 Kobe Earthquake, approximately one million households lost access to water due to earthquake-induced damage, and most of the system was not restored until nearly three weeks later. **Erdik [2000]** investigated the damage to drinking water and sewerage systems following the 1999 Mw 7.4 Kocaeli Earthquake and assessed their economic implications. In the same year, **Shih and Chang [2006]** thoroughly investigated the damage to water infrastructure caused by the Mw 7.7 Chi-Chi Earthquake in Taiwan. **Scawthorn et al. [2006]** evaluated the performance of water, wastewater, and energy systems after the 2004 Mw 6.6 Niigata Ken Chuetsu Earthquake in Japan. **Maruyama et al. [2011]** analyzed the spatial distribution of damage to buried pipelines caused by the 2007 Mw 6.6 Niigata Chuetsu-Oki Earthquake in Japan. **Tang et al. [2011]** analyzed the impacts of the 2010 Mw 8.8 Biobío Earthquake in Chile, which severely affected multiple lifeline systems, including seaports, communication networks, electric power, transportation infrastructure, airports, water supply, and wastewater services. **O'Rourke et al. [2014]** documented widespread failures in water, wastewater, and gas distribution systems during the 2010 and 2011 Canterbury earthquake sequence in Christchurch, New Zealand, particularly in areas affected by liquefaction. **Wham et al. [2017]** investigated the damage sustained by water supply systems following the 2016 Kumamoto Earthquakes in Japan, highlighting service

disruptions, pipeline failures, and severe liquefaction effects. **Lemnitzer et al. [2021]** examined the performance of critical lifelines after the 2017 Mw 7.1 Central Mexico Earthquake, which left more than six million people without water and resulted in over 2,300 reported leaks and pipe breakages. Most recently, **Toprak et al. [2024a]** reported that the 2023 Kahramanmaraş earthquakes in Türkiye caused severe damage to pipeline systems in multiple provinces, including Hatay, Kahramanmaraş, Gaziantep, and Adıyaman.

These cases highlight the importance of identifying the mechanisms responsible for pipeline damage during earthquakes. Earthquake-induced damage to buried pipelines is generally classified into TGD and PGD in the literature. TGD refers to temporary ground movements generated by the propagation of the seismic waves, while PGD involves lasting ground displacements resulting from the geotechnical hazards such as liquefaction-induced settlement, lateral spreading, landslides, rockfalls, and surface faulting (**Figure 2.1**).

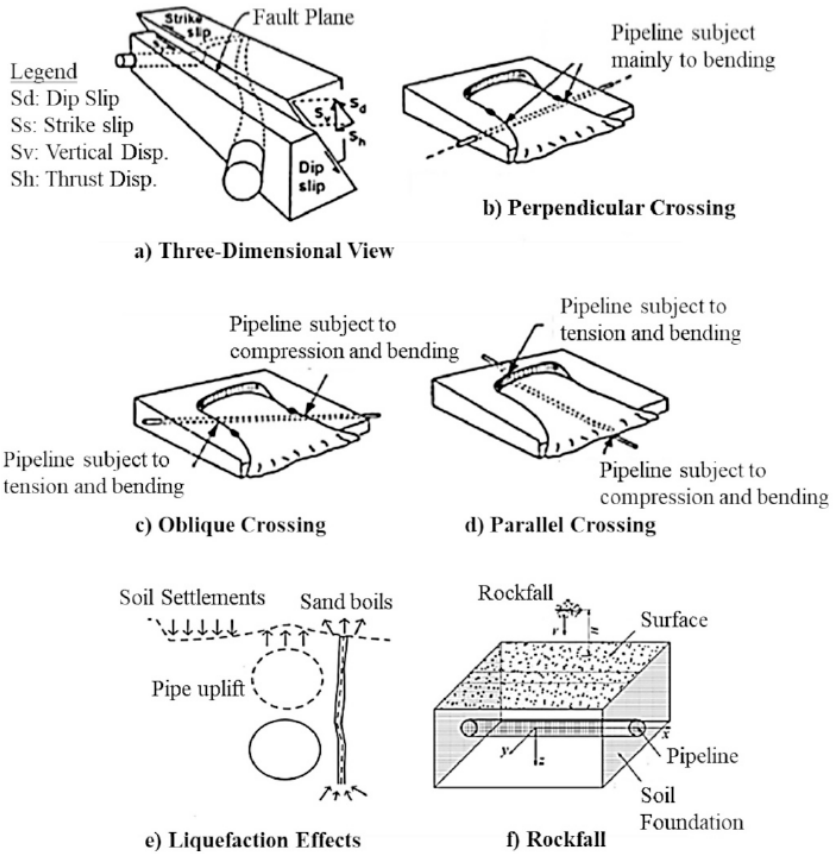


Figure 2.1: Schematic illustration showing the primary geohazards that affect buried pipelines **[Toprak et al., 2024a]**.

PGD-related damage to buried pipelines has been extensively documented in field investigations, laboratory experiments, and numerical analyses. In studies focusing on liquefaction-induced PGD, **Takada et al. [1987]** conducted shaking table model tests to examine the behavior of buried pipelines under fully and partially liquefied soil conditions, considering both fixed-end and free-end boundary constraints. The results showed that pipelines tended to uplift before the completion of liquefaction and settle afterwards due to post-liquefaction settlement. Bending strains were greater in partially liquefied soils compared to fully liquefied conditions, with higher values observed under fixed-end than free-end conditions. **O'Rourke et al. [2014]** investigated the Christchurch, New Zealand, earthquake sequence, where liquefaction-induced ground deformations caused extensive pipeline damage. Using Light Detection and Ranging (LiDAR) surveys, they mapped permanent ground displacements and quantified damage patterns, demonstrating a strong correlation between failures and the severity of these ground deformations. More recently, **Toprak et al. [2018; 2019]** further investigated pipeline damages in liquefied areas and developed new empirical correlations for cast iron (CI), polyvinyl chloride (PVC), and asbestos cement (AC) pipelines using multiple liquefaction-related parameters to assess vulnerability.

In contrast, research addressing PGD caused by fault rupture, such as the study conducted by **Ha et al. [2010]** investigated the effects of fault rupture on buried pipelines through case history observations from the 1999 Kocaeli Earthquake and centrifuge model tests. The results showed that pipelines subjected to compressive forces were highly susceptible to buckling, whereas tensile forces primarily caused deformation without localized failures. **Chaudhari et al. [2013]** used a finite element model to assess how variations in pipe diameter, wall thickness, burial depth, and fault angle affect the seismic response of steel pipelines. Their findings indicated that, in addition to material properties, geometric factors play a decisive role in governing the behavior of pipelines subjected to fault-induced displacements. **Vazouras et al. [2015]** examined the response of buried pipelines to strike-slip fault displacement, emphasizing the role of pipe–soil interaction in governing deformation mechanisms. By combining numerical simulations with closed-form solutions, they provided a detailed assessment of axial strain distributions, bending effects, and potential failure scenarios. More recently, **Toprak et al. [2025c]** observed damage to the Düzbağ

transmission line at the fault intersection caused by the 2023 Kahramanmaraş earthquakes. They reported that the pipeline experienced compressive forces due to left-lateral sliding movement, resulting in severe deformation in the buried pipelines. Furthermore, **Uckan et al. [2024]** performed numerical modelling to simulate the response of the damaged pipeline segment.

In the literature, there are also studies addressing the effects of landslide-induced transverse PGD on buried pipelines. **Ni et al. [2018]** developed a simplified two-dimensional numerical model, representing pipelines as beam-type structures and surrounding soil as Winkler springs, to evaluate the fragility of pipelines subjected to landslide-induced transverse PGD. Using a large set of randomly generated input parameters, they combined this model with a supervised machine learning technique to establish predictive relationships between input variables and maximum tensile strain demands. The study produced empirical fragility curves, demonstrating that pipeline vulnerability increases with greater PGD but can be mitigated by factors such as burial depth, soil stiffness, and pipe flexibility.

In addition to PGD, TGD can also affect the performance of buried pipeline systems by causing widespread damage through seismic wave propagation. In numerous studies, the extent of pipeline damage under TGD has been quantified using the repair rate (RR), defined as the number of repairs per kilometer of pipeline length and typically expressed in repairs/km. One of the earliest documented efforts to relate pipeline damage to seismic parameters was conducted by **Katayama et al. [1975]**, who developed empirical correlations for AC and CI pipelines based on peak ground acceleration (PGA) data from six different earthquake events. This was followed by **Barenberg [1988]**, who was among the first to correlate peak ground velocity (PGV) with pipeline damages for CI pipelines. **Eguchi [1991]** developed fragility curves associating Modified Mercalli Intensity (MMI) with repair rates for AC, CI, and PVC pipelines and observed the considerably greater vulnerability of AC pipes relative to the other materials. **Eidinger et al. [1995]** further improved these correlations by using data from seven major earthquakes to establish robust PGV-based repair rate predictions. **Toprak [1998]** examined the repair rates of water distribution systems and established correlations with various seismic parameters, including PGA, PGV, and MMI. Later, **Milashuk and Crane [2012]** examined pipeline damage after the 2010 Darfield and 2011 Christchurch earthquakes, concentrating on the areas affected

by TGD. They created new regression models that merged PGV intervals to increase accuracy in their study. Their regression models showed that repair rate estimates aligned with the 95% prediction band established by earlier regressions. More recently, **O'Rourke et al. [2014]** analyzed the 2010–2011 Canterbury earthquake sequence in Christchurch, New Zealand, and developed empirical RR–PGV relationships specifically for AC and CI pipelines. These correlations have subsequently provided a foundation for assessing buried pipeline vulnerability in seismic regions.

The damage relationships developed in past studies offer an effective framework for predicting the performance of urban infrastructure systems under potential seismic loading. For example, **Toprak et al. [2009]** conducted a detailed evaluation of the seismic performance of water infrastructure network in Denizli, Türkiye, by applying empirical models under various earthquake magnitude scenarios. Their study emphasized the relative effects of transient and permanent ground deformations on buried pipeline damage and demonstrated, through GIS-based analyses, how repair rates varied according to pipe material and shaking intensity. These predictive studies enable the identification of vulnerable components within the system, allowing decision-makers to enhance infrastructure preparedness and reduce seismic risk.

In summary, numerous studies in the literature have demonstrated that there is a clear link between earthquake-induced ground deformations and buried pipeline damage. Ground deformations, both temporary and permanent, play critical roles in determining the severity of pipeline failures. Understanding these mechanisms is crucial for improving pipeline resilience and establishing earthquake-resilient societies in seismic regions.

2.2. Liquefaction and Ground Failures

The term liquefaction was initially proposed by **Kubo and Mogami [1953]** and became one of the critical subjects of Geotechnical Earthquake Engineering. It is well-known that the liquefaction phenomenon occurs in saturated sandy soils during earthquakes and leads to loss of soil-bearing capacity. The sudden increase in pore water pressure in fully or partially saturated sandy soils can cause a decrease in effective stress. This process is illustrated in **Figure 2.2**.

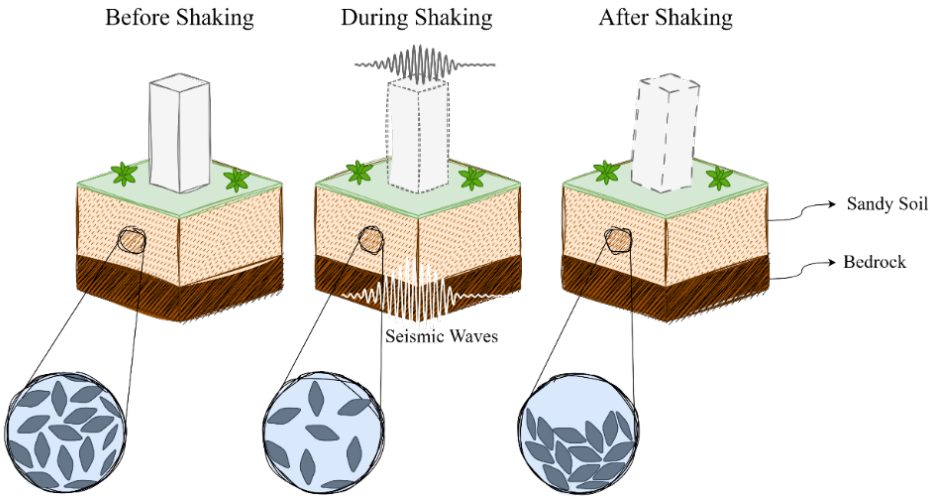


Figure 2.2: Conceptual illustration of the liquefaction mechanism in saturated soils before, during and after the shaking.

As a result of the liquefaction, free-field settlements—referring to the vertical subsidence of the ground surface (**Figure 2.3a**)—sand boils, which describe the emergence of sand and water to the ground surface due to excess pore water pressure (**Figure 2.3b**), and lateral spreading, characterized by the horizontal displacement of the ground (**Figure 2.3c**), may occur. These manifestations are frequently observed in areas with shallow groundwater and low relative density soils, particularly under seismic loading with high cyclic stress ratios. The extent and distribution of these effects largely depend on site-specific conditions such as soil stratigraphy, saturation level, and ground motion characteristics. These phenomena can severely compromise the stability of buildings and infrastructure by reducing the soil's bearing capacity. Structures may tilt, settle unevenly, or collapse entirely, while infrastructures may experience significant deformation, rupture, or loss of functionality due to ground displacement.



Figure 2.3: Liquefaction-induced ground deformations observed in İskenderun, Türkiye, following the 2023 Kahramanmaraş earthquakes: (a) settlement due to liquefaction and (b) sand boils **[Toprak et al., 2024a]**; (c) lateral spreading **[Toprak et al., 2025c]**.

Liquefaction manifestations have been widely reported following major earthquakes around the world. In the literature, numerous studies have focused on events such as the Mw 7.6 1964 Niigata Earthquake in Japan, the Mw 9.2 1964 Great Alaska Earthquake and the Mw 6.9 1989 Loma Prieta Earthquake in the United States, the Mw 7.4 1999 Kocaeli Earthquake in Türkiye, the Mw 7.1 2010 and Mw 6.2 2011 Christchurch Earthquakes in New Zealand, and the Mw 7.7 and Mw 7.6 2023 Kahramanmaraş earthquakes in Türkiye. For instance, **Ishihara and Koga [1981]** visited earthquake-affected zones such as Kawagishi-cho and South Bank and conducted site reconnaissance after the 1964 Niigata Earthquake. They observed sand boils, lateral spreading, liquefaction-induced settlements reaching 50 centimeters, as well as building tilting of approximately 80 degrees. **Youd [2014]** compiled site reconnaissances conducted in earthquake-affected regions such as Anchorage, and

Valdez after the 1964 Great Alaska Earthquake and summarized liquefaction, lateral spreading, settlement, and structural damage in detail. **Boulanger et al. [1995]** meticulously reported the earthquake effects, liquefaction-induced ground deformations, and field investigations as well as subsurface soil conditions in Moss Landing Area after the 1989 Loma Prieta Earthquake.

Moreover, the extent of the liquefaction manifestation along the Kocaeli Bay after the 1999 Kocaeli Earthquake was observed and well-documented by **GEER [1999]**. Their report included liquefaction-induced settlements in buildings in addition to the sites that exhibited sand ejecta and lateral spreading observed both on-site and in aerial imagery. Additionally, the studies conducted by **PEER [2000a; 2000b]** and **Cetin et al. [2004a]** showed surface cracks at the Yalova Port and confirmed the occurrence of liquefaction-induced lateral spreading in the coastal area of Yalova, with ground displacements observed up to approximately 0.3 meters. **Cubrinovski et al. [2012]** conducted comprehensive field visits in Christchurch, New Zealand after the 2010-2011 Christchurch Earthquakes. They made ground surveying measurements at 120 locations and reported lateral ground displacements of about two to three meters along the Avon and Kaipoi rivers. In addition, they observed severe failures in buildings' foundations, road bridges, and failures in the city's water and wastewater pipeline systems.

Ulusay et al. [2024] and **Cetin et al. [2025a]** visited earthquake-affected regions following the 2023 Kahramanmaraş earthquakes and observed widespread liquefaction manifestation resulting in sand ejecta, lateral spreading, and vertical settlements reaching up to two meters. Moreover, **Toprak et al. [2024a]** investigated Atatürk Boulevard area in İskenderun and observed that the wastewater treatment plant faced settlement due to liquefaction, along with the presence of sand boils in the area. Similarly, **Bassal et al. [2024]** also conducted a field study in İskenderun following the 2023 Kahramanmaraş earthquakes and observed extensive liquefaction-induced ground deformations such as widespread sediment ejecta, ground settlements reaching up to 700 mm, and seaward lateral spreading as well as post-earthquake flooding exacerbated by these ground movements. **Flora et al. [2024]** conducted a field survey in Adıyaman Gölbaşı to assess liquefaction effects following the earthquake and documented severe ground deformations, including extreme settlements and tilting of buildings due to liquefaction in alluvial deposits with a shallow groundwater table.

Using in-situ tests, they calculated the Liquefaction Potential Index (LPI) and found high susceptibility in several areas. In addition, **Taftsoglou et al. [2023]** identified liquefaction phenomena at 760 sites using a remote sensing approach, without the need to visit the site. Therefore, these observations demonstrate that liquefaction represents a significant seismic hazard and underscore the importance of liquefaction susceptibility assessments.

There are numerous studies focusing on the liquefaction susceptibility assessments in the literature. For instance, **Seed and Idriss [1971]** proposed a basic framework for liquefaction analyses by developing the stress-based method. Following that, **Seed et al. [1985]** updated the relationships with a wide-range of field data and improved the reliability of the method. Subsequently, **Youd et al. [2001]** updated the parameters at the NCEER workshop and prepared comprehensive recommendations for field applications. Moreover, **Cetin et al. [2004b]** developed stress-based analysis with a probabilistic approach and presented a novel method. Afterwards, **Idriss and Boulanger [2008]** and **Boulanger and Idriss [2014]** refined the method with updated earthquake data, laboratory tests, and proposed updated correction factors for SPT and CPT based analyses.

In addition to the simplified procedure research, there are liquefaction vulnerability indexes frequently used in the liquefaction assessment studies proposed by the researchers. For example, **Iwasaki et al. [1982]** originally proposed the Liquefaction Potential Index (LPI) and later **Toprak and Holzer [2003]** adapted it for CPT applications. Following that, **Sonmez and Gokceoglu [2005]** introduced the Liquefaction Severity Index (LSI) by integrating moderate and no liquefaction classes. Further, the Liquefaction Severity Number (LSN) was developed by **Tonkin and Taylor [2013]** by including volumetric strain in the calculations.

Moreover, the analyses of liquefaction-induced deformations (e.g. liquefaction-induced settlements, lateral spreading) are as significant as the determination of liquefaction susceptibility. There are several empirical methods developed to estimate liquefaction-induced settlements based on field and laboratory data in the literature. To estimate post-liquefaction free-field settlements, **Tokimatsu and Seed [1984]** proposed a widely used technique based on Standard Penetration Test (SPT) data. **Ishihara and Yoshimine [1992]** presented another method for estimating volumetric strains incorporating the relationship between shear strain, relative density, and factor

of safety. Following that, a new approach utilizing SPT-based shear strain evaluation with fines content corrections along with unified charts was presented by **Shamoto et al. [1998]**. Later, **Wu et al. [2003]** developed new semi-empirical procedures for estimating ground settlements and proposed various curves as a function of the Cyclic Shear Stress Ratio and SPT blow count. **Cetin et al. [2009]** analyzed 49 case histories from seven earthquakes in detail and suggested a probabilistic-based approach to estimate the settlement. Lastly, **Bray and Macedo [2017]** developed an approach to estimate liquefaction-induced building settlement by incorporating shear-induced settlement and ejecta-induced settlement in addition to the free-field settlement.

Building on these studies, determining the liquefaction susceptibility and assessing the potential degree of the resulting ground deformations are crucial steps. Such evaluations provide essential information for decision-makers under both current conditions and potential future earthquake scenarios and can lead to the application of appropriate soil improvement techniques. When integrated into broader urban planning and disaster risk management strategies, these measures reduce physical damage, minimize economic losses and social disruption, and contribute to the development of earthquake-resilient and sustainable cities.

3. METHODOLOGY

The following sections provide a detailed explanation of the methodology used for processing the pipeline damage records, conducting the quantitative analysis of pipeline damages, and the procedures applied in liquefaction assessments. Initially, the pipeline damage records for Kahramanmaraş Province were processed and verified, followed by liquefaction analyses and the analysis of damage relationships. Subsequently, liquefaction analyses were conducted for Yalova Province, and the relationship obtained from the Kahramanmaraş case along with the existing relationships in the literature was applied to assess potential infrastructure damage. The overall workflow is illustrated in **Figure 3.1**.

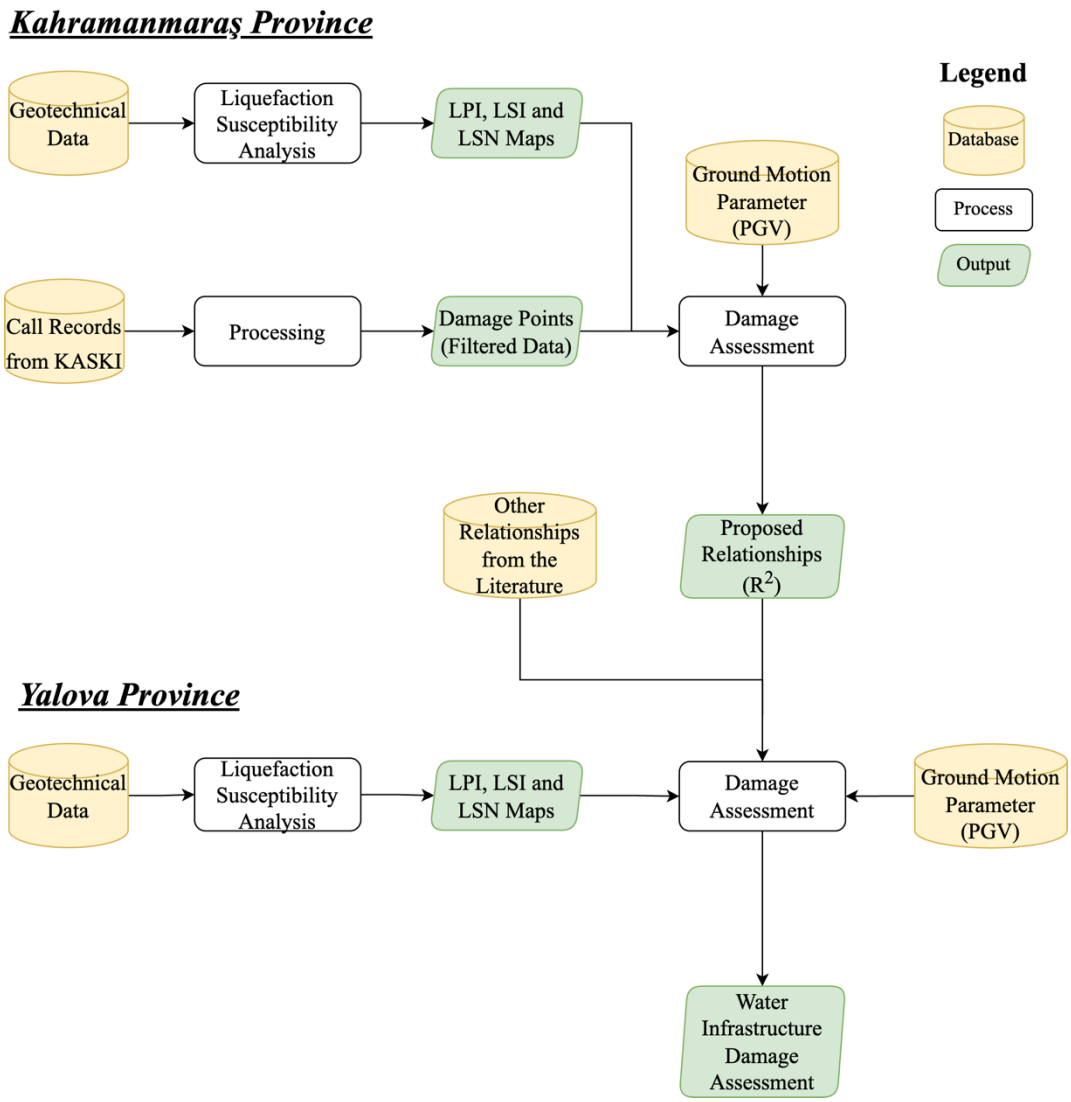


Figure 3.1: Methodological framework adopted in this study.

3.1. Processing of Pipeline Damage Records

Following the devastating earthquakes, issues related to drinking water were reported by citizens and officially recorded through the 185 Emergency Call Center. When a call report was received, the operator simultaneously transmitted the work order to the relevant branch manager and foreman via mobile communication channels and portable digital devices. The order was then assigned to the responsible team leaders, who conducted on-site inspections and initiated repairs according to the urgency of the case. After the repair was completed, the responsible team closed the record in the system. Each entry included information such as district, neighborhood, street or avenue name, building number, the date the call was received, and the date it was closed. While the calls were being registered in the system, operators classified each case as either related to the distribution network or to the subscriber's internal system. This classification was made without on-site verification, and following the earthquake, the urgency of response and the involvement of other water and sewerage administrations from different provinces further complicated the distinction between distribution network failures and subscriber-related issues.

To address the limitations of the available call records, meetings were held with KASKI officials to evaluate alternative data sources that could provide more reliable information on repair activities. As a result, detailed repair reports for November and December 2023 were obtained from the subcontractor responsible for the works. These reports contained verified, field-based information, including the repair date, material type, diameter of the repaired pipe, address, and photographs taken before and after the intervention. The photographic evidence was examined alongside the technical details, and in consultation with KASKI officials, a classification framework was established. In central neighborhoods, pipes with diameters of 50 mm and below were classified as subscriber-related, while in rural areas the threshold was set at 32 mm. Applying this criterion in combination with the photographic records enabled the distinction between subscriber and network-related damages. Accordingly, 49% of the repairs pertained to the distribution network, whereas 51% were linked to subscriber systems. This statistic, together with the consultations held with KASKI officials, provided guidance for comparing the number of damage call records obtained after the filtering process.

Subsequently, to eliminate the possibility of a recorded call referring to the same damage more than once, a statistical analysis of the start and the end dates of the calls was performed. The difference between start and end dates was calculated, and the average resolution time for damage call records was found to be 10 days. The bar graph in **Figure 3.2** illustrates the distribution of these resolution times, showing how long it took for the calls to be resolved. Therefore, in cases where a second issue was reported on the same street within ten days, it was not considered a separate damage; only cases reported after ten days were included in the analysis.

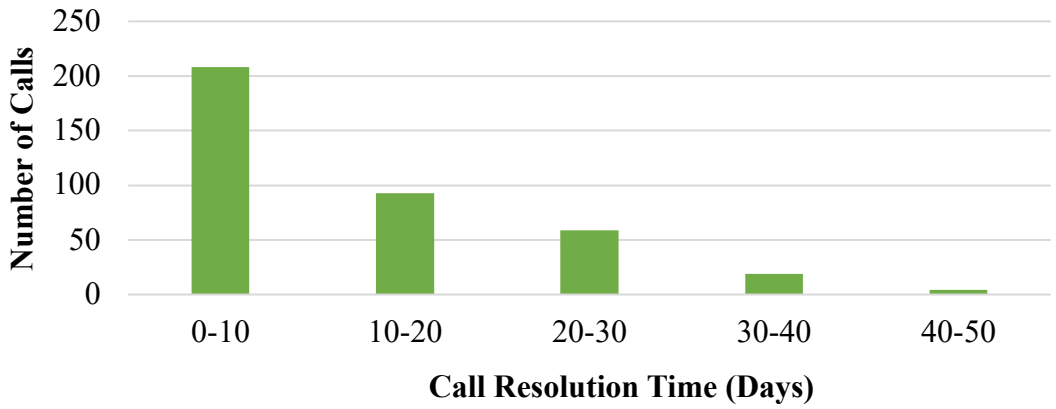


Figure 3.2: Distribution of call durations, indicating the number of days between the initiation and closure of calls.

After following the filtering processes above, an additional filtering step was conducted to exclude subscriber-related issues. If a reported issue was the only call received from a particular street, it was considered likely to be subscriber-related and was therefore removed from the dataset. The flowchart in **Figure 3.3** summarizes the filtering processes applied to the initial dataset.

Initially, the dataset comprised 11,345 damage call records from February 6 to August 15, 2023. This range was chosen because the initial frequency analysis of repair data showed that the damage from the 2023 earthquakes data corresponded primarily to this period. Following the filtering procedures, the dataset was further reduced to 5,496 records. This final number corresponds to approximately 48.44% of the initial 11,345 calls, closely matching the 49% network damage rate determined from the subcontractor's data. This consistency indicates that the filtering process successfully refined the call records into a dataset accurately representing actual network-related damage.

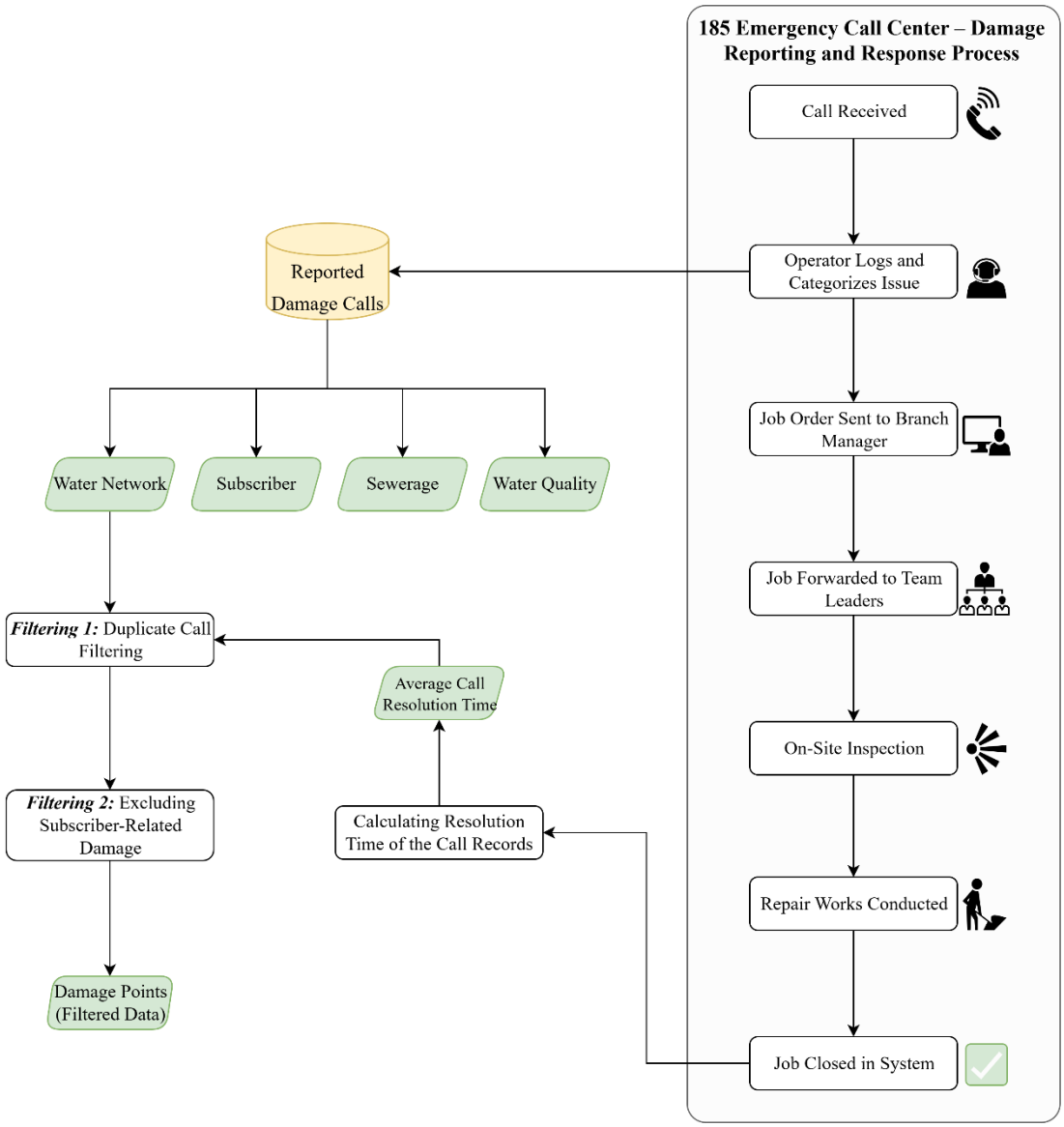


Figure 3.3: Flowchart summarizing the filtering processes applied to the call records.

The filtered number of call records on a monthly basis, covering the initial-frequency period used in the analysis from August 6, 2022, to August 15, 2023, is presented in **Table 3.1**. Additionally, to observe how the call records evolved over time, data covering the period from August 1, 2022, to December 30, 2024, were compiled. Furthermore, the temporal distribution of the recorded filtered calls is detailed in **Figure 3.4**. As illustrated in **Table 3.1** and **Figure 3.4**, the impact of the earthquake on the increase in call records is clearly observable. While the number of calls in January 2023 is 251, this figure surged to a record high of 830 in February due to the earthquake. Additionally, the approximately 400% increase in damage reports mentioned by KASKI is also reflected in this dataset.

Table 3.1: Number of filtered call records per month for the period from August 6, 2022, to August 15, 2023.

Year	Months	Call Records
2022	August	387
	September	317
	October	320
	November	228
	December	223
2023	January	251
	February	830
	March	880
	April	847
	May	887
	June	761
	July	894
	August	421

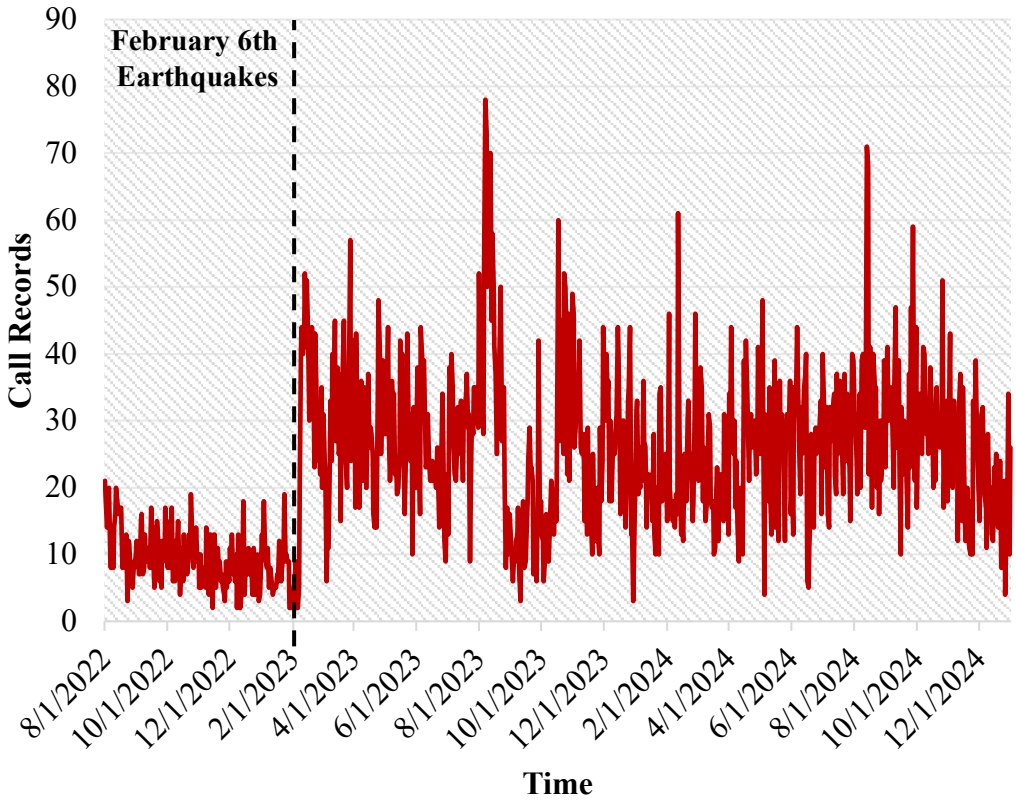


Figure 3.4: Temporal distribution of daily filtered malfunction reports recorded through the 185 Emergency Call Center between August 2022 and December 2024.

Furthermore, the cumulative frequency of reported damages was calculated and presented in **Figure 3.5**, where the initial frequency and the post-earthquake steady-state levels are clearly marked. The initial phase was taken as the reference period for damage assessments, and subsequent analyses were conducted accordingly. A noticeable shift between these phases occurred on August 15, 2023, indicating a relatively significant breakpoint in the trend. **Figure 3.6** compares the daily number of call reports following the earthquakes with the pre-earthquake average, revealing that post-event reports remained significantly elevated for an extended period and dropped after August 15, 2023.

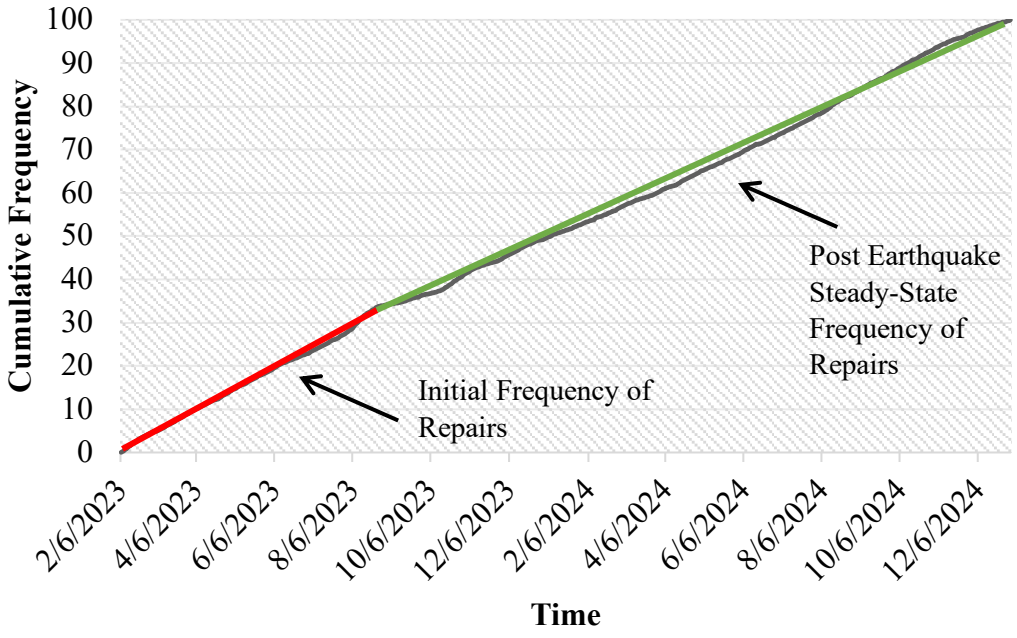


Figure 3.5: Cumulative frequency of daily filtered malfunction reports.

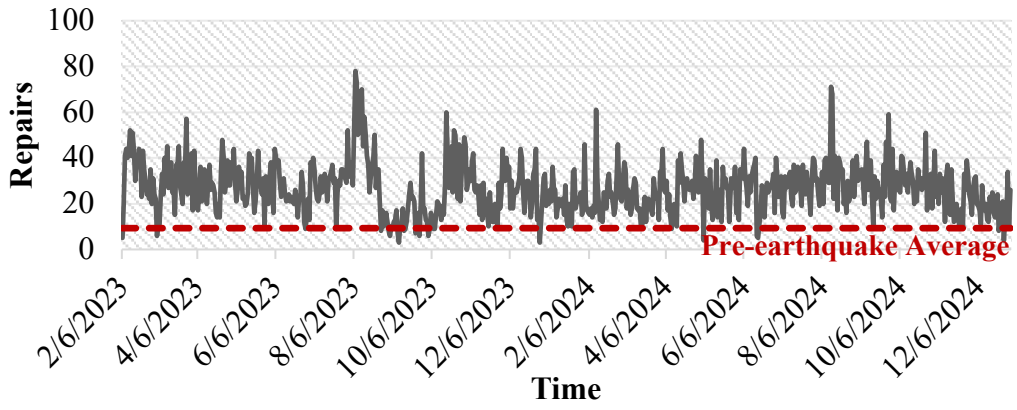


Figure 3.6: Comparison of the number of daily call records after the earthquake with the pre-earthquake average.

3.2. Quantitative Analysis of Pipeline Damages

In this thesis, the quantitative analysis of pipeline damage was performed using the Repair Rate (RR) approach, a widely adopted method in the literature. The repair rate was calculated using **Equation 3.1**.

$$RR = \frac{\text{Number of Repairs}}{\text{Pipeline Length (km)}} \tag{3.1}$$

In addition to repair rate calculations, screening criteria proposed by **O'Rourke et al. [2014]** were used. In this context, based on **Equation 3.2**, the minimum sampling lengths required to obtain statistically meaningful results were determined, assuming that pipeline damage follows a Poisson distribution and that a normal approximation is valid under the central limit theorem.

$$x \geq \frac{[\emptyset^{-1}(\beta_c)]^2}{\alpha^2(RR)} \tag{3.2}$$

In **Equation 3.2**, α represents the acceptable margin of error, β_c denotes the confidence level parameter (with corresponding values provided in **Table 3.2**), and x refers to the minimum sampling length necessary for reliable estimation. In this study, a confidence level of 90% and a margin of error (α) of 0.5 were generally adopted.

In the subsequent stages of the study, TGD-related damages were evaluated with respect to the spatial distribution of PGV and the types of pipe materials present in the Kahramanmaraş water network. The analysis focused on how ground motion intensity and material characteristics influenced the extent of the observed damage. Detailed results and interpretations of this assessment are provided meticulously in Section 7. For Yalova Province, these relationships were utilized to conduct a risk assessment by integrating the TGD patterns derived from this study with empirical PGD-damage correlations reported in the literature. In this context, liquefaction susceptibility analyses were performed for the potential earthquake scenarios, and LPI, LSI, and LSN were calculated to enable the application of these PGD relationships. The results of this assessment are presented in Section 12 in detail.

Table 3.2: $[\emptyset^{-1}(\beta_c)]^2$ values corresponding to selected confidence levels used in the screening criteria formulation.

Confidence Level (β_c)	$[\emptyset^{-1}(\beta_c)]^2$
90%	2.7060
85%	2.0700
80%	1.6430
70%	1.0740
60%	0.6660
50%	0.4549

3.3. Liquefaction Analysis Methodology

Within the scope of the liquefaction assessments of the thesis study, a comprehensive Python algorithm was developed, and liquefaction susceptibility analyses were performed for Kahramanmaraş and Yalova Province according to **Youd et al. [2001]** and **Boulanger and Idriss [2014]** methods. For Kahramanmaraş Province, both the PGA values obtained from the Türkiye Earthquake Hazard Map (TDTH), which is based on the probabilistic seismic hazard methodology defined in the Turkish Building Earthquake Code **[TBEC, 2018]**, and the values proposed by **Toprak et al. [2025a]** were considered. On the other hand, for Yalova Province, PGA values were derived both from TDTH in accordance with the TBEC 2018 approach and from earthquake scenarios developed within the scope of the SATREPS-MARTEST project. In addition, the availability of CPT tests in Yalova Province enabled the CPT-based liquefaction susceptibility analysis to be performed. The LPI, LSI, and LSN were calculated, and spatial distribution maps of the results were prepared for both provinces.

Furthermore, since Yalova province is more susceptible to liquefaction and ground deformation, liquefaction-induced free-field settlements proposed by **Tokimatsu and Seed [1984]**, **Ishihara and Yoshimine [1992]**, **Shamoto et al. [1998]**, **Wu et al. [2003]** and **Cetin et al. [2009]** were applied.

The developed algorithm performs the analyses in accordance with the methodology given below.

1) The algorithm assigns soil properties to SPT depths by considering the layers where laboratory tests (soil type, unit weight, fines content, water content, liquid limit, plastic limit, etc.) were performed.
2) If no ground water level is detected in the boreholes, the algorithm does not perform the analysis.
3) If there is no unit weight value in the layer, the algorithm assigns a value by following the procedure given below.
    a. The algorithm initially checks whether the adjacent layers (above and below it) are the same type of ground.
    b. If the adjacent layers are the same type, it takes the average of the unit weight. However, if only one adjacent layer is the same, it takes the value of that layer.
    c. If there are no adjacent layers of the same type, it assumes $18\,\frac{kN}{m^3}$ when performing the analysis.
4) The designed algorithm can apply the criteria of **Seed et al. [2003]**, **Bray and Sancio [2006]** and **Boulanger and Idriss [2006]**. However, if water content, plasticity limit or liquid limit in the layer is not present, it performs the analysis without applying criteria.
5) The dz value, which is an important factor used in LPI, LSI and settlement calculations, is determined according to various conditions in the algorithm.
    a. The depth range (dz) is the upper depth subtracted from the lower depth. However, if the SPT depth is above the groundwater level, the dz value is considered as zero.
    b. If there are successive SPT depths in the same layer, the lower depth is calculated as the average of the current SPT depth and the next SPT depth.
    c. In the first SPT depth of a layer, the upper depth is the uppermost boundary of the layer. If the SPT depth is below the water level and is the first test of the layer, the upper depth is the water level depth. In the last test of the layer, the lower depth is the lower boundary of the layer.
    d. If the SPT depth is exactly at the boundary between the two layers, the test belongs to the lower layer.

e. If there are no tests in a layer, no dz calculation is performed for that layer.

6) After the analyses are completed, it generates graphs and creates results as an Excel file.

The methodology adopted for the Kahramanmaraş Province is given in **Figure 3.7**, while the methodology followed for the Yalova Province is given in **Figure 3.8**.

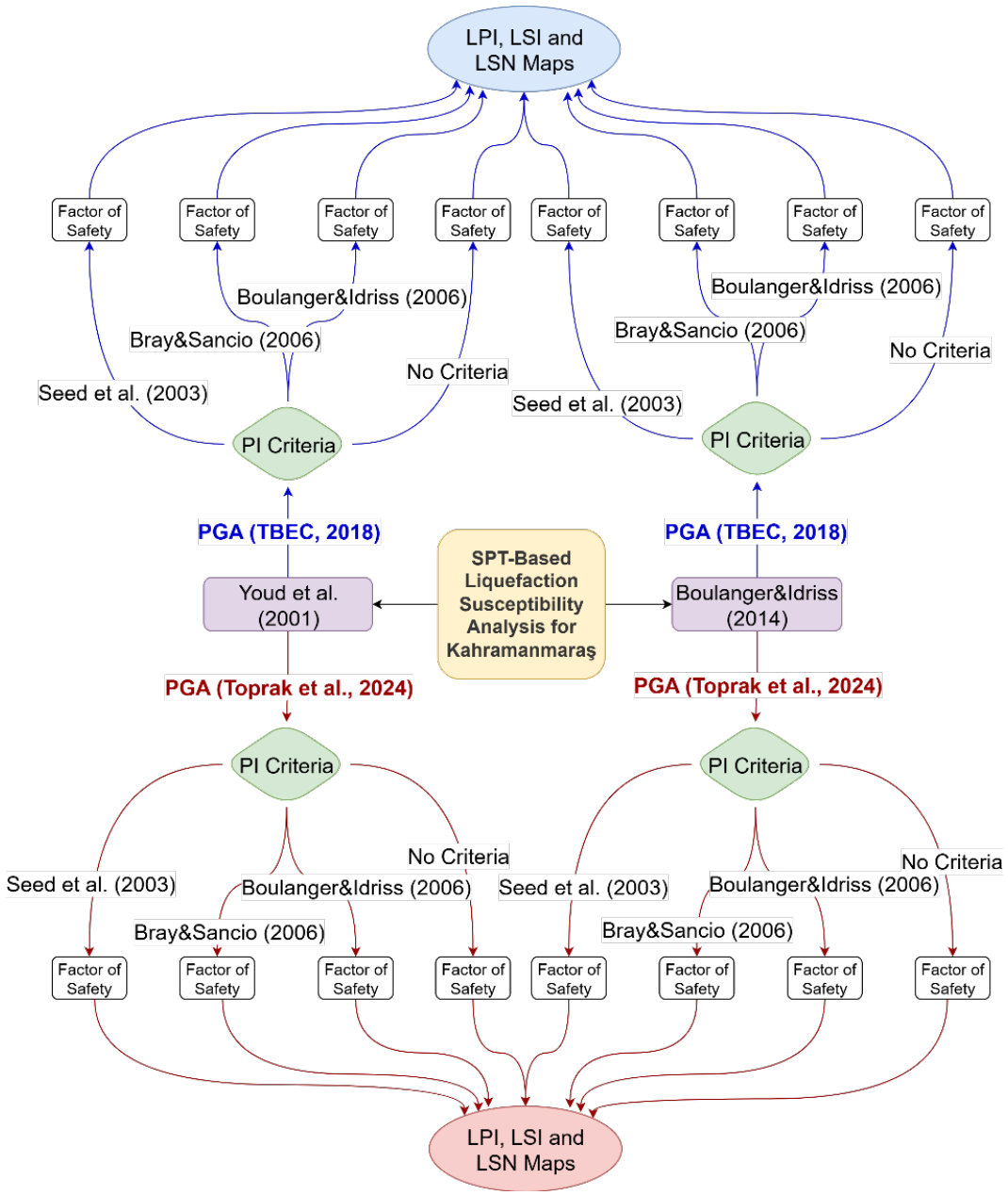


Figure 3.7: Liquefaction assessment methodology followed in the analysis of Kahramanmaraş Province.

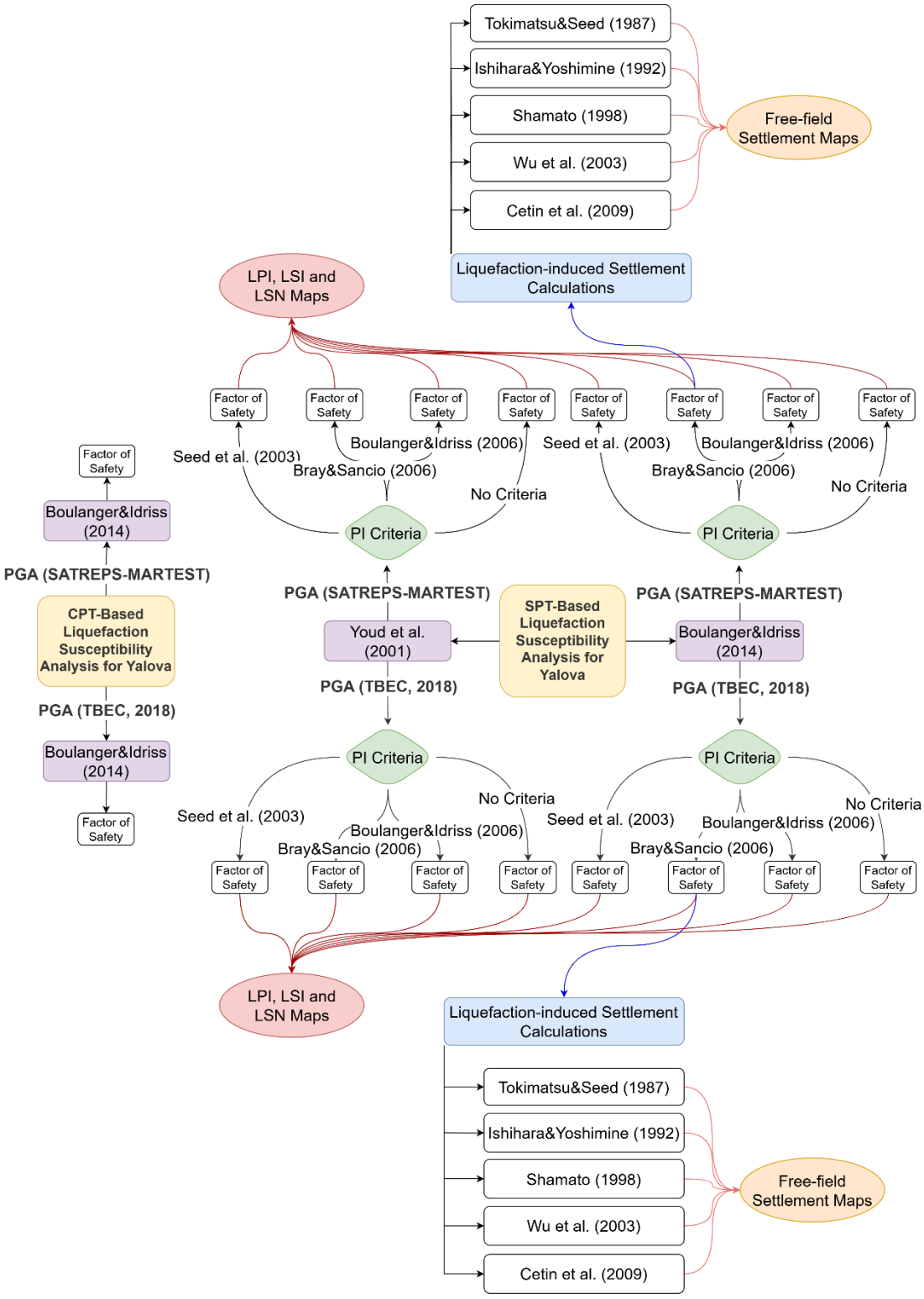


Figure 3.8: Liquefaction assessment methodology followed in the analysis of Yalova Province.

3.3.1. Liquefaction Susceptibility Evaluation Methods

In this study, liquefaction susceptibility was evaluated using two widely used methods: **Youd et al. [2001]** and **Boulanger and Idriss [2014]**. These simplified procedures evaluate liquefaction potential through a comparison between the cyclic stress ratio (CSR) and the cyclic resistance ratio (CRR) of the soil **(Equation 3.3)**.

$$FS = \frac{CRR}{CSR} \tag{3.3}$$

The equation used to calculate the CSR is the same in both methods and was originally proposed by **Seed and Idriss [1971] (Equation 3.4)**.

$$CSR = 0.65\left(\frac{a_{max}}{g}\right)\left(\frac{\sigma_{vo}}{\sigma'_{vo}}\right)r_d \tag{3.4}$$

a_{max} is the maximum ground acceleration recorded during an earthquake, and its unit is g (gravitational acceleration). σ_{vo} and σ'_{vo} are the total soil stress and effective soil stress in $\frac{kN}{m^2}$, respectively. r_d is the stress reduction factor and it is a function of the depth. This factor is calculated with different approaches. While the equation proposed by **Liao and Whitman [1986] (Equation 3.5)** was used in **Youd et al. [2001]** analysis, the equations developed by **Idriss [1999] (Equations 3.6-3.8)** were employed in the analysis by **Boulanger and Idriss [2014]**.

$$r_d = \begin{cases} 1.0 - 0.00765z, & z \leq 9.15\ m \\ 1.174 - 0.0267z, & 9.15\ m < z \leq 23\ m \end{cases} \tag{3.5}$$

$$r_d = exp[\alpha(z) + \beta(z) \cdot M] \tag{3.6}$$

$$\alpha(z) = -1.012 - 1.126sin\left(\frac{z}{11.73} + 5.133\right) \tag{3.7}$$

$$\beta(z) = 0.106 + 0.118sin\left(\frac{z}{11.28} + 5.142\right) \tag{3.8}$$

While M is the moment magnitude of the earthquake, Z is the depth below the ground surface in meters in the equations. Since **Equation 3.5** is valid up to a depth of 23 meters, the analyses based on **Youd et al. [2001]** were limited to this depth.

The two methods used in liquefaction analysis consist of different CRR formulations. The analysis proposed by **Youd et al. [2001]** is based on the formulation in **Equation 3.9**, which is valid only in the $(N_1)_{60} < 30$ range. Therefore, the CRR value is considered as 1.0 in the analysis, and the soil is assumed not to liquefy when the $(N_1)_{60}$ value exceeds this threshold.

$$CRR = \frac{1}{34 - (N_1)_{60}} + \frac{(N_1)_{60}}{135} + \frac{50}{[10 \cdot (N_1)_{60} + 45]^2} - \frac{1}{200} \tag{3.9}$$

In **Equation 3.9**, the value $(N_1)_{60}$ represents the normalized SPT blow count and were calculated by using **Equation 3.10**.

$$(N_1)_{60} = N_m C_N C_E C_B C_R C_S \tag{3.10}$$

In the equation above, N_m is the SPT blow count, and C_N, C_E, C_B, C_R, and C_S are the overburden correction factor, hammer energy ratio correction, borehole correction factor, rod length correction factor, and correction for sampling method, respectively. These factors were selected by using **Table 3.3**. However, while **Youd et al. [2001]** uses **Equation 3.11** in the C_N calculation, **Boulanger and Idriss [2014]** applies **Equation 3.12**.

$$C_N = \left(\frac{P_a}{\sigma'_{vo}}\right)^{0.5} \leq 1.7 \tag{3.11}$$

$$C_N = \left(\frac{P_a}{\sigma'_{vo}}\right)^{0.784 - 0.0768\sqrt{(N_1)_{60}}} \leq 1.7 \tag{3.12}$$

P_a is the atmospheric pressure and considered as 100 kPa in the analysis.

Table 3.3: Correction factors for SPT-N values used in this study **[Youd et al., 2001]**.

Factor	Equipment Variable	Term	Correction
Energy Ratio	Donut Hammer	C_E	0.5 to 1.0
	Safety Hammer		0.7 to 1.2
	Automatic-trip Donut-type Hammer		0.8 to 1.3
Borehole Diameter	65 mm to 115 mm	C_B	1.00
	150 mm		1.05
	200 mm		1.15
Rod Length	<3 m	C_R	0.75
	3 m to 4 m		0.80
	4 m to 6 m		0.85
	6 m to 10 m		0.95
	10 m to 30 m		1.00
Sampling Method	Standard Sampler	C_S	1.0
	Sampler without Liners		1.1 to 1.3

Following that, $(N_1)_{60cs}$ which is the correction of $(N_1)_{60}$ to an equivalent clean sand value were calculated as a function of the fines content (FC) in **Equation 3.13** for the **Youd et al. [2001]** method, and **Equation 3.14** for the **Boulanger and Idriss [2014]** method. In the developed algorithm, if the FC value is not available, the alpha value is considered as 0 and the beta value is assumed as 1.

$$(N_1)_{60cs} = \alpha + \beta \cdot (N_1)_{60} \tag{3.13a}$$

$$\alpha = 0 \text{ and } \beta = 1 \text{ for } FC\ (\%) \leq 5\% \tag{3.13b}$$

$$\alpha = exp\left[1.76 - \left(\frac{190}{FC^2}\right)\right] \text{ and } \beta = \left[0.99 + \left(\frac{FC^{1.5}}{1000}\right)\right] \text{ for } 5 < FC\ (\%)\ < 35\% \tag{3.13c}$$

$$\alpha = 5 \text{ and } \beta = 1.2 \text{ for } FC\ (\%) \geq 35\% \tag{3.13d}$$

$$(N_1)_{60cs} = (N_1)_{60} + \Delta(N_1)_{60} \tag{3.14a}$$

$$\Delta(N_1)_{60} = exp\left(1.63 + \frac{9.7}{FC + 0.01} - \left(\frac{15.7}{FC + 0.01}\right)^2\right) \tag{3.14b}$$

Further, the CRR value for the procedure of **Boulanger and Idriss [2014]** was calculated using **Equation 3.15**. It should be noted that $CRR_{7.5}$ value is valid when the σ'_{v0} is 1 atm.

$$CRR_{7.5} = exp\left[\frac{(N_1)_{60cs}}{14.1} + \left(\frac{(N_1)_{60cs}}{126}\right)^2 - \left(\frac{(N_1)_{60cs}}{23.6}\right)^3 + \left(\frac{(N_1)_{60cs}}{25.4}\right)^4 - 2.8\right] \tag{3.15}$$

In order to adjust CRR for the other σ'_{v0} values, the K_σ and C_σ parameters given in **Equation 3.17** and **Equation 3.18** were computed and substituted into **Equation 3.16**.

$$CRR_{7.5} = CRR_{7.5,\sigma'_{v0}=1\ atm} K_\sigma \tag{3.16}$$

$$K_\sigma = 1 - C_\sigma ln\left(\frac{\sigma'_{v0}}{P_a}\right) \leq 1.1 \tag{3.17}$$

$$C_\sigma = \frac{1}{18.9 - 2.55\sqrt{(N_1)_{60cs}}} \leq 0.3 \tag{3.18}$$

Subsequently, Magnitude Scaling Factor (MSF) calculation was performed in order to use different earthquake magnitudes. While **Equation 3.19** was used in **Youd et al. [2001]** analysis, **Equation 3.20** and **Equation 3.21** were used in **Boulanger and Idriss [2014]**.

$$MSF = \frac{10^{2.24}}{M_w^{2.56}} \tag{3.19}$$

$$MSF = 1 + (MSF_{max} - 1)\left(8.64exp\left(\frac{-M_w}{4}\right) - 1.325\right) \tag{3.20}$$

$$MSF_{max} = 1.09 + \left(\frac{(N_1)_{60cs}}{31.5}\right)^2 \leq 2.2 \tag{3.21}$$

Lastly, the factor of safety (FS) for each SPT depth was calculated using **Equation 3.22**.

$$FS = \frac{CRR_{7.5}}{CSR} \cdot MSF \tag{3.22}$$

Following that, the liquefaction susceptibility criteria for silts and clays proposed by **Seed et al. [2003]**, **Bray and Sancio [2006]**, and **Boulanger and Idriss [2006]** were performed in the analyses and these criterions were presented in **Table 3.4**.

In the algorithm, it is initially checked whether the soil properties fulfil the moderately susceptible criterion. If this criterion is met, the relevant layer is considered to be non-liquefiable, and the factor of safety value is assigned as 2.0. However, if any of the parameters such as PI, LL or W_c are not present in the datasheet, the criterion cannot be applied; in this case, the soil is considered liquefiable, and liquefaction analysis is performed, and factor of safety is calculated.

Table 3.4: Liquefaction susceptibility criteria used in the study.

Studies	Susceptible	Moderately Susceptible	Non-liquefiable
Seed et al. [2003]	$PI < 12\%$ $LL < 37\%$ $\frac{w_c}{LL} > 0.80$	$12\% < PI < 20\%$ $37\% < LL < 47\%$ $\frac{w_c}{LL} \geq 0.85$	
Bray and Sancio [2006]	$PI < 12\%$ $\frac{w_c}{LL} > 0.85$	$12\% \leq PI < 18\%$ $\frac{w_c}{LL} > 0.80$	
Boulanger and Idriss [2006]	$PI < 3\%$	$3\% \leq PI \leq 6\%$	$PI \geq 7\%$

Moreover, liquefaction susceptibility analysis was conducted based on CPT data according to the procedure proposed by **Boulanger and Idriss [2014]**, where CPT tests were available. Firstly, the corrected cone resistance (q_t) was calculated using **Equation 3.23**.

$$q_t = q_c + (1 - a)(u_2 - u_0) \tag{3.23}$$

Here, q_c is the measured cone tip resistance, u_2 is the pore-water pressure acting on the cone, u_0 is the hydrostatic pore-water pressure, and a is the cone's net area ratio.

Following that, the friction (F) and the normalized tip ratio (Q) were calculated using **Equation 3.24** and **Equation 3.25**, respectively.

$$F = \frac{f_s}{q_t - \sigma_{vo}} \times 100 \tag{3.24}$$

$$Q = \left(\frac{q_c - \sigma_{vo}}{P_a}\right)\left(\frac{P_a}{\sigma'_{vo}}\right)^n \tag{3.25}$$

Here, n is the stress-exponent parameter and calculated using **Equation 3.26**.

$$n = 0.381 I_c + 0.05\left(\frac{\sigma'_{vo}}{P_a}\right) - 0.15 \leq 1.0 \tag{3.26}$$

Where I_c is the soil behavior type index and calculated using **Equation 3.27**.

$$I_c = \left[\left(3.47 - log(Q)\right)^2 + \left(1.22 + log(F)\right)^2\right]^{0.5} \tag{3.27}$$

In next, the normalized cone resistance was computed using **Equation 3.28**.

$$q_{c1N} = \left(\frac{q_c}{P_a}\right) C_N \tag{3.28}$$

Here, C_N is the overburden correction factor and was calculated using **Equation 3.29**.

$$C_N = \left(\frac{\mathrm{P_a}}{\sigma'_{vo}}\right)^{1.338 - 0.249((q_{c1N})_{cs})^{0.264}} \leq 1.7 \tag{3.29}$$

In the equation above, $(q_{c1N})_{cs}$ is limited to values between 21 and 254. Furthermore, the clean-sand equivalent cone resistance $((q_{c1N})_{cs})$ was calculated using **Equation 3.30**.

$$(q_{c1N})_{cs} = q_{c1N} + \Delta q_{c1N} \tag{3.30}$$

Here, Δq_{c1N} is the equivalent clean sand adjustment for CPT and was computed using **Equation 3.31**.

$$\Delta q_{c1N} = \left(11.9 + \frac{q_{c1N}}{14.6}\right) exp\left(1.63 - \frac{9.7}{FC + 2} - \left(\frac{15.7}{FC + 2}\right)^2\right) \tag{3.31}$$

Where FC corresponds to the fines content and was determined using **Equation 3.32**.

$$\mathrm{I_c} = \frac{(\mathrm{FC} + 137)}{80} - \mathrm{C_{FC}} \tag{3.32}$$

Subsequently, the CRR for the moment magnitude 7.5 earthquake was calculated using **Equation 3.33**. It should be noted that resulting $CRR_{7.5}$ value is valid for an effective overburden stress of 1 atm.

$$\begin{aligned}\mathrm{CRR}_{\mathrm{M=7.5},\sigma'_{v0}=1\mathrm{atm}} &= \exp\left(\frac{(q_{c1N})_{cs}}{113} + \left(\frac{(q_{c1N})_{cs}}{1000}\right)^2 - \left(\frac{(q_{c1N})_{cs}}{140}\right)^3 \right. \\ &\left. + \left(\frac{(q_{c1N})_{cs}}{137}\right)^4 - 2.80\right)\end{aligned} \tag{3.33}$$

In order to adjust CRR for the other σ'_{v0} values, the K_σ and C_σ parameters given in **Equation 3.17** and **Equation 3.34** were computed and substituted into **Equation 3.16**.

$$C_\sigma = \frac{1}{37.3 - 8.27((q_{c1N})_{cs})^{0.264}} \leq 0.3 \tag{3.34}$$

Subsequently, MSF calculation was performed in order to use different earthquake magnitudes using **Equation 3.20** and **Equation 3.35**.

$$MSF_{max} = 1.09 + \left(\frac{(q_{c1N})_{cs}}{180}\right)^2 \leq 2.2 \tag{3.35}$$

Furthermore, the shear stress reduction coefficient was computed using **Equations 3.6-3.8** and then substituted into the CSR calculation, which was performed using **Equation 3.4.**

Lastly, the factor of safety for each CPT depth was calculated using **Equation 3.22**.

3.3.2. Index-Based Assessment Methods

Index-based liquefaction assessments quantify the overall potential for liquefaction manifestation at a borehole location and provide a single representative value. These methods are widely used to illustrate the spatial distribution of liquefaction susceptibility. In addition, they classify the results into categories, offering further insight into the potential severity of liquefaction.

Within the scope of the thesis, the LPI proposed by **Iwasaki et al. [1982]** was estimated by using **Equation 3.36** and results were discussed in detail.

$$LPI = \int_0^{20\,m} F(z)W(z)dz \tag{3.36}$$

Subsequently, the F(z) and W(z) values were computed according to the formulations provided in **Equation 3.37** and **Equation 3.38**.

$$F(z) = 1 - FS \text{ for } FS < 1.0 \tag{3.37a}$$

$$F(z) = 0 \text{ for } FS \geq 1.0 \tag{3.37b}$$

$$W(z) = 10 - 0.5z \text{ for } z < 20\,m \tag{3.38a}$$

$$W(z) = 0 \text{ for } z > 20\,m \tag{3.38b}$$

As indicated in the above equation, LPI was calculated for depths up to 20 m, considering only cases where FS was less than 1.0. Subsequently, the results were classified according to the intervals in **Table 3.5** and used in the map labelling.

In addition to the original formulation proposed by **Iwasaki et al. [1982]**, the practical interpretation of LPI as an indicator of ground failure and surface was supported by **Toprak and Holzer [2003]**. Their CPT-based evaluations showed that LPI values of 5 and 15 correspond to approximately 58% and 93% likelihood of observable field

deformation, respectively. Furthermore, LPI has been applied extensively in hazard mapping studies as well as correlations with building and pipeline damages **[Holzer et al., 2002; Holzer et al., 2003; Jinguuji and Toprak, 2017; Toprak et al., 2019]**, supporting its role as a practical indicator for evaluating building and pipeline vulnerability under liquefaction.

Table 3.5: Classification of liquefaction potential based on LPI value adopted in this study **[Iwasaki et al., 1982]**.

***LPI* Intervals**	**Category**
$\boldsymbol{LPI = 0}$	Very Low
$\boldsymbol{0 < LPI \leq 5}$	Low
$\boldsymbol{5 < LPI \leq 15}$	High
$\boldsymbol{LPI > 15}$	Very High

The LSI, on the other hand, was calculated using **Equation 3.39** for each borehole, and the values were categorized according to **Table 3.6**.

$$LSI = \int_0^{20\,m} P_L(z)W(z)dz \tag{3.39}$$

$P_L(z)$ refers to the probability of liquefaction at a given depth and is the function of FS.

For cases where FS is less than or equal to 1.411, the probability of liquefaction was evaluated using **Equation 3.40**; otherwise, it was taken as zero.

$$P_L = \frac{1}{1+\left(\frac{FS}{0.96}\right)^{4.5}} \text{ for } FS \leq 1.411 \tag{3.40a}$$

$$P_L = 0 \text{ for } FS > 1.411 \tag{3.40b}$$

Moreover, the term $W(z)$ was calculated using **Equation 3.38**, in a manner consistent with the formulation applied in the LPI calculation.

Table 3.6: Classification of liquefaction severity based on LSI value used in this study **[Sonmez and Gokceoglu, 2005]**.

***LSI* Intervals**	**Category**
$\boldsymbol{LSI = 0}$	Non-liquefied
$\boldsymbol{0 < LSI < 15}$	Very Low
$\boldsymbol{15 \leq LSI < 35}$	Low
$\boldsymbol{35 \leq LSI < 65}$	Moderate
$\boldsymbol{65 \leq LSI < 85}$	High
$\boldsymbol{85 \leq LSI < 100}$	Very High

Further, to assess the severity of potential liquefaction-induced deformations within the soil profile, the LSN method of **Tonkin and Taylor [2013]** was applied. The calculations were performed along the soil profile to a depth of 20 m, in accordance with **Equation 3.41**.

$$LSN = 1000 \int_0^{20\,m} \frac{\varepsilon_v}{z} dz \tag{3.41}$$

In the equation above, the volumetric strain (ε_v) was calculated based on the empirical correlations proposed by **Zhang et al. [2002]**. In these calculations, FS was used directly, while the SPT blow counts were converted into $(q_{c1N})_{cs}$ values for evaluation.

The parameter ε_v is explicitly defined as a function of both FS and $(q_{c1N})_{cs}$, and its value is determined through the combination of these two parameters, as expressed in **Equation 3.42**.

If $FS \leq 0.5$,	$\varepsilon_v = 102(q_{c1N})_{cs}^{-0.82}$	For $33 \leq (q_{c1N})_{cs} \leq 200$	(3.42a)
If $FS = 0.6$,	$\varepsilon_v = 102(q_{c1N})_{cs}^{-0.82}$	For $33 \leq (q_{c1N})_{cs} \leq 147$	(3.42b)
If $FS = 0.6$,	$\varepsilon_v = 2411(q_{c1N})_{cs}^{-1.45}$	For $147 \leq (q_{c1N})_{cs} \leq 200$	(3.42c)
If $FS = 0.7$,	$\varepsilon_v = 102(q_{c1N})_{cs}^{-0.82}$	For $33 \leq (q_{c1N})_{cs} \leq 110$	(3.42d)
If $FS = 0.7$,	$\varepsilon_v = 1701(q_{c1N})_{cs}^{-1.42}$	For $110 \leq (q_{c1N})_{cs} \leq 200$	(3.42e)
If $FS = 0.8$,	$\varepsilon_v = 102(q_{c1N})_{cs}^{-0.82}$	For $33 \leq (q_{c1N})_{cs} \leq 80$	(3.42f)
If $FS = 0.8$,	$\varepsilon_v = 1690(q_{c1N})_{cs}^{-1.46}$	For $80 \leq (q_{c1N})_{cs} \leq 200$	(3.42g)
If $FS = 0.9$,	$\varepsilon_v = 102(q_{c1N})_{cs}^{-0.82}$	For $33 \leq (q_{c1N})_{cs} \leq 60$	(3.42h)
If $FS = 0.9$,	$\varepsilon_v = 1430(q_{c1N})_{cs}^{-1.48}$	For $60 \leq (q_{c1N})_{cs} \leq 200$	(3.42i)
If $FS = 1.0$,	$\varepsilon_v = 64(q_{c1N})_{cs}^{-0.93}$	For $33 \leq (q_{c1N})_{cs} \leq 200$	(3.42j)
If $FS = 1.1$,	$\varepsilon_v = 11(q_{c1N})_{cs}^{-0.65}$	For $33 \leq (q_{c1N})_{cs} \leq 200$	(3.42k)
If $FS = 1.2$,	$\varepsilon_v = 9.7(q_{c1N})_{cs}^{-0.69}$	For $33 \leq (q_{c1N})_{cs} \leq 200$	(3.42l)
If $FS = 1.3$,	$\varepsilon_v = 7.6(q_{c1N})_{cs}^{-0.71}$	For $33 \leq (q_{c1N})_{cs} \leq 200$	(3.42m)
If $FS = 2.0$,	$\varepsilon_v = 0.0$	For $33 \leq (q_{c1N})_{cs} \leq 20$	(3.42n)

Following that, the calculated LSN values were categorized according to **Table 3.7** for use in mapping. This classification was adapted from **Tonkin and Taylor [2013]**, which systematically outlined observed land effects corresponding to various LSN ranges based on extensive field observations following the 2010–2011 Christchurch Earthquakes.

LSN is not only a significant indicator for observed land effects but also a practical measure for assessing the condition of buried infrastructure in liquefaction-affected areas. For instance, **Toprak et al. [2019]** reported that areas with higher LSN values corresponded to higher repair rates in water distribution lines, indicating a direct relationship between LSN and infrastructure damage.

Table 3.7: LSN ranges, category names, and observed land effects considered in this study **[Tonkin and Taylor, 2013]**.

LSN Range	Category Name (Used in the Mapping)	Predominant Performance
$\mathbf{0 < LSN < 10}$	Very Low	Little to no expression of liquefaction, minor effects.
$\mathbf{10 < LSN < 20}$	Low	Minor expression of liquefaction, some sand boils.
$\mathbf{20 < LSN < 30}$	Moderate	Moderate expression of liquefaction, with sand boils and some structural damage.
$\mathbf{30 < LSN < 40}$	High	Moderate to severe expression of liquefaction, settlement can cause structural damage.
$\mathbf{40 < LSN < 50}$	Very High	Major expression of liquefaction, undulations and damage to ground surface, severe total and differential settlement of structures.
$\mathbf{LSN > 50}$	Severe	Severe damage, extensive evidence of liquefaction at surface, severe total and differential settlements affecting structures, damage to services

3.3.3. Liquefaction-Induced Settlement Estimation Methods

3.3.3.1. Tokimatsu and Seed [1984] Free-Field Settlement Procedure

Tokimatsu and Seed [1984] studied liquefaction-induced settlements and related the degree of volumetric strain to the corrected SPT blow number. The graph in **Figure 3.9** shows field data from different regions such as Niigata, Arahama, and Hachinohe. These results represent one of the earliest and most fundamental approaches for predicting liquefaction-induced settlements.

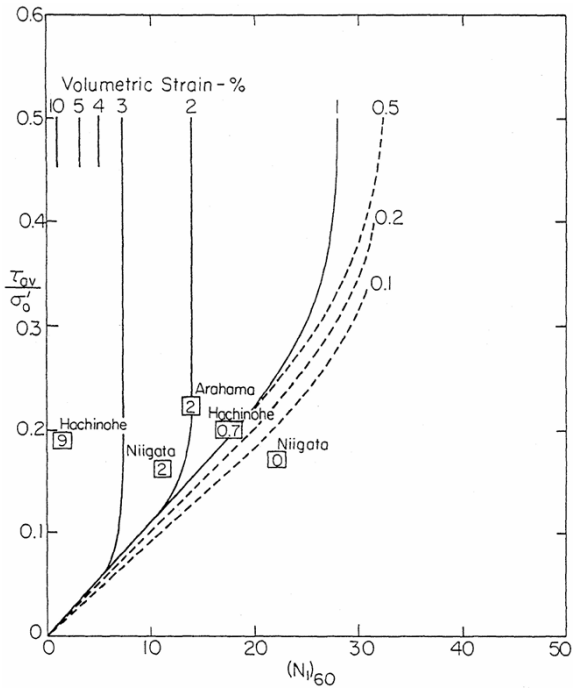


Figure 3.9: Relationship between cyclic stress ratio and corrected SPT blow count with volumetric strain curves **[Tokimatsu and Seed, 1984]**.

The volumetric strain curves given in **Figure 3.9** were first digitized, and the plots were generated using the Python algorithm. The $(N_1)_{60}$ and CSR values obtained from each borehole were then plotted on the same graph. Subsequently, the two closest curves to each point were identified. If FS was less than or equal to 1.0, volumetric strain was calculated; otherwise, it was taken as zero. Using linear interpolation, volumetric strain values were calculated based on the inverse of the distance to these curves and were then used in the settlement calculation. **Figure 3.10** presents the output of the described algorithm, where the values above the points indicate the test depth, and the dashed lines represent the perpendicular distances from each point to

the nearest two curves. In addition, if the test point remained below the lowest curve, the volumetric strain value corresponding to the lowest curve was assigned to the point without performing interpolation.

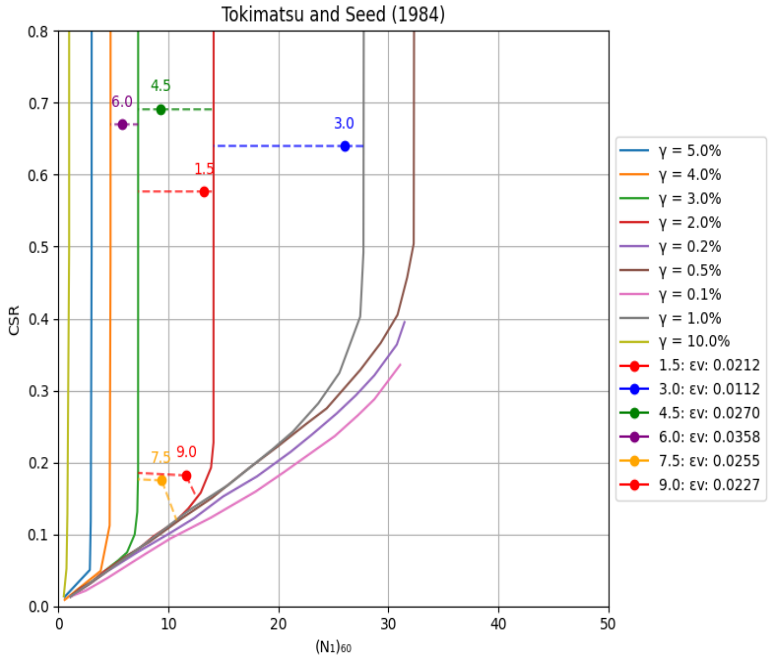


Figure 3.10: Output of the interpolation algorithm showing test depths and distances to the nearest curves for the **Tokimatsu and Seed [1984]** method.

Finally, the calculated volumetric strain values were used to determine the total liquefaction-induced free-field settlement in accordance with **Equation 3.43**.

$$S = \int_0^{z_{max}} \varepsilon_v \cdot dz \tag{3.43}$$

Here, ε_v and dz represent the volumetric strain and the layer thickess, respectively.

3.3.3.2. Ishihara and Yoshimine [1992] Free-Field Settlement Procedure

Ishihara and Yoshimine [1992] investigated the behavior of sandy soils in laboratory tests to predict post-liquefaction settlements. For this purpose, horizontal shear loads were applied to sand samples of varying densities using a simple shear apparatus. The resulting data were presented in the chart shown in **Figure 3.11**, which incorporates FS itself rather than cyclic shear stress.

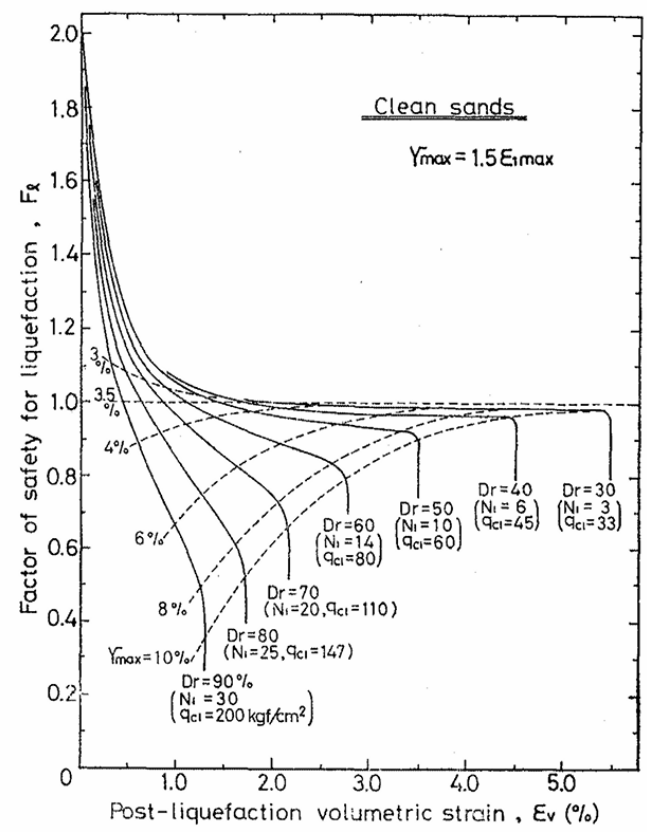


Figure 3.11: Relationship between the factor of safety for liquefaction and volumetric strain (ε_v), with relative density (D_R) and N_1 curves **[Ishihara and Yoshimine, 1992]**.

Volumetric strain values were calculated using **Figure 3.11**, which was digitized and mathematically expressed by **Yoshimine et al. [2006]** as given in **Equation 3.44**.

$$\varepsilon_v = 1.5 \cdot exp(-2.5D_R) \cdot min(0.08, \gamma_{max}) \tag{3.44}$$

Here, D_R denotes the relative density, calculated using **Equation 3.45** provided by **Idriss and Boulanger [2003]**, and γ_{max} represents the maximum shear strain, determined using **Equation 3.46**-**Equation 3.48**.

$$D_R = \sqrt{\frac{(N_1)_{60cs}}{46}} \tag{3.45}$$

It should be noted that D_R value is valid when $(N_1)_{60cs}$ is less than 46.

Subsequently, γ_{max} was calculated using the formulation originally developed by **Yoshimine et al. [2006]**, with a limiting value (γ_{lim}) incorporated as proposed by **Idriss and Boulanger [2008] (Equation 3.48)**.

$$\gamma_{lim} = 1.859(1.1 - D_R)^3 \geq 0 \tag{3.46}$$

$$F_\alpha = 0.032 + 4.7\, D_R - 6.0\, (D_R)^2 \tag{3.47}$$

$$\gamma_{max} = 0 \text{ for } FS > 2 \tag{3.48a}$$

$$\gamma_{max} = min\left(\gamma_{lim}, 0.035(2 - FS)\left(\frac{1-F_\alpha}{FS-F_\alpha}\right)\right) \text{ for } 2 > FS > F_\alpha \tag{3.48b}$$

$$\gamma_{max} = \gamma_{lim} \text{ for } FS \leq F_\alpha \tag{3.48c}$$

Moreover, the term γ_{max} was also estimated using **Equation 3.49** proposed by **Zhang et al. [2004]** in order to evaluate its influence on the settlement value. In this method, linear interpolation was applied between the given D_R values, and in cases where D_R was lower than 40%, a minimum value of 40% was assumed for the calculations.

$$\text{If } D_R = 90\%, \gamma_{max} = \begin{cases} 3.26(FS)^{-1.80}, & 0.7 \leq FS \leq 2.0 \\ 6.2, & FS \leq 0.7 \end{cases} \tag{3.49a}$$

$$\text{If } D_R = 80\%, \gamma_{max} = \begin{cases} 3.22(FS)^{-2.08}, & 0.56 \leq FS \leq 2.0 \\ 10, & FS \leq 0.56 \end{cases} \tag{3.49b}$$

$$\text{If } D_R = 70\%, \gamma_{max} = \begin{cases} 3.20(FS)^{-2.89}, & 0.59 \leq FS \leq 2.0 \\ 14.5, & FS \leq 0.59 \end{cases} \tag{3.49c}$$

$$\text{If } D_R = 60\%, \gamma_{max} = \begin{cases} 3.58(FS)^{-4.42}, & 0.66 \leq FS \leq 2.0 \\ 22.7, & FS \leq 0.66 \end{cases} \tag{3.49d}$$

$$\text{If } D_R = 50\%, \gamma_{max} = \begin{cases} 4.22(FS)^{-6.39}, & 0.72 \leq FS \leq 2.0 \\ 34.1, & FS \leq 0.72 \end{cases} \tag{3.49e}$$

$$\text{If } D_R = 40\%, \gamma_{max} = \begin{cases} 3.31(FS)^{-7.97}, & 1.0 \leq FS \leq 2.0 \\ 250(1 - FS), & 0.81 \leq FS \leq 1.0 \\ 51.2, & FS \leq 0.81 \end{cases} \tag{3.49f}$$

Lastly, the total liquefaction-induced free-field settlement was estimated in accordance with **Equation 3.43**.

3.3.3.3. Shamoto et al. [1998] Free-Field Settlement Procedure

Shamoto et al. [1998] developed a method for assessing both vertical and horizontal deformations in liquefied soils following the 1995 Hyogoken–Nambu Earthquake and presented three graphs in **Figure 3.12** based on varying fines content values.

In order to utilize the empirical charts, the SPT blow count must be corrected using several factors. One of these is the overburden stress correction, applied to eliminate the influence of effective vertical stress in the soil. The corrected value, denoted as N_1, was calculated using **Equation 3.50**.

$$N_1 = C_N \cdot N = \left(\frac{1.7}{\sigma'_v + 0.7}\right) \cdot N \tag{3.50}$$

Here, σ'_v is in kgf/cm² and represents the effective vertical stress in the soil profile.

Following that, N_1 was further adjusted by a correction factor based on the fines content using **Equation 3.51**.

$$N_a = N_1 + \Delta N_f \tag{3.51}$$

Here, ΔN_f was calculated following the procedures given in **Table 3.8**.

Table 3.8: ΔN_f values determined based on fines content ranges.

Fines Content (FC) (%)	ΔN_f
0 – 5	0
5 – 10	Linear Interpolation
10 and more	$\Delta N_f = 0.1 \cdot FC + 4$

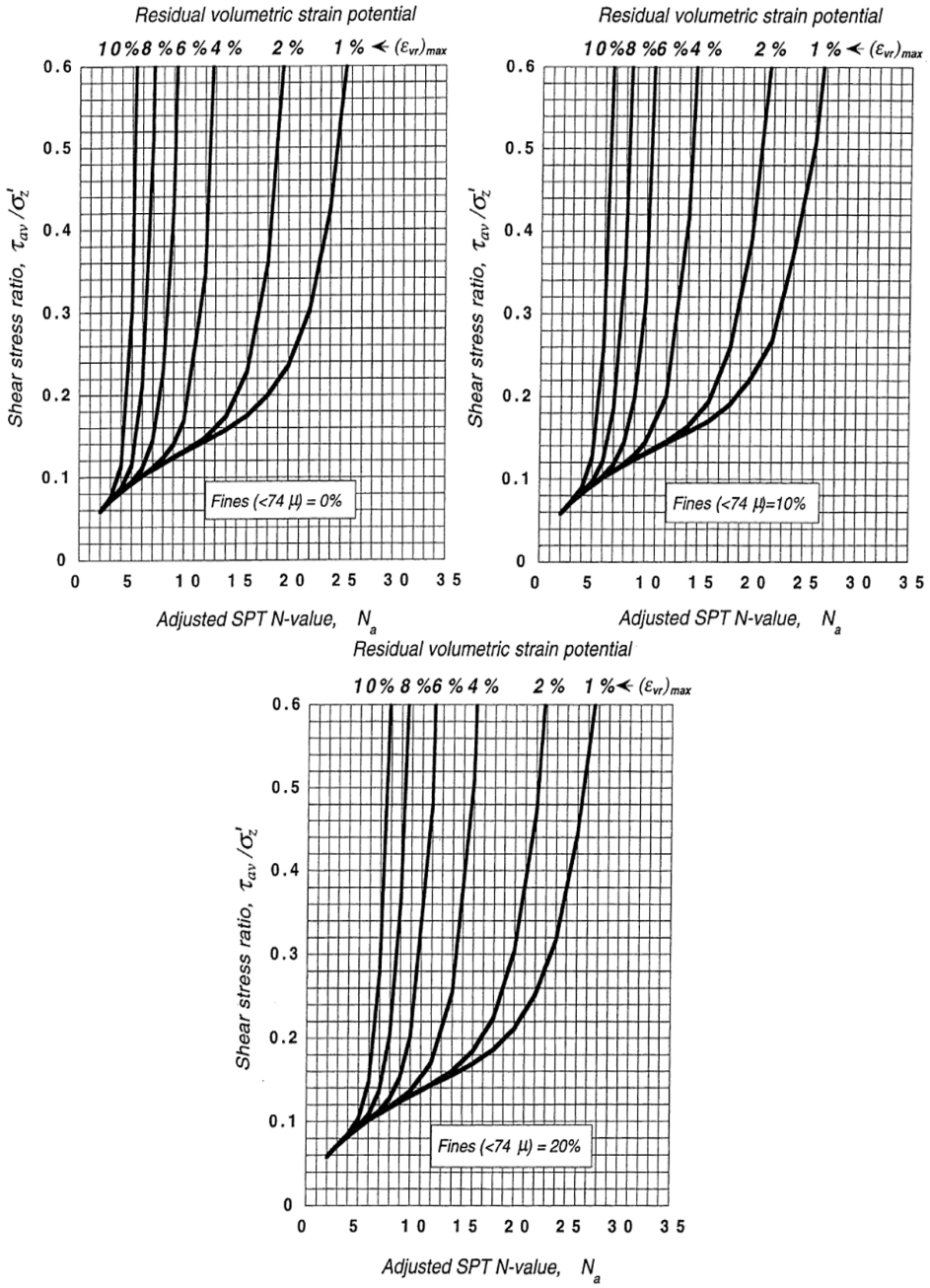


Figure 3.12: Relationship between cyclic stress ratio and adjusted SPT blow count with volumetric strain curves **[Shamoto et al., 1998]**.

Subsequently, each graph was digitised and plotted in Python. The algorithm first determined which graph to use based on the FC value of the SPT test and then performed linear interpolation between the two curves closest to the test point. **Figure 3.13** presents the algorithm output, with sample test points shown for illustrative purposes.

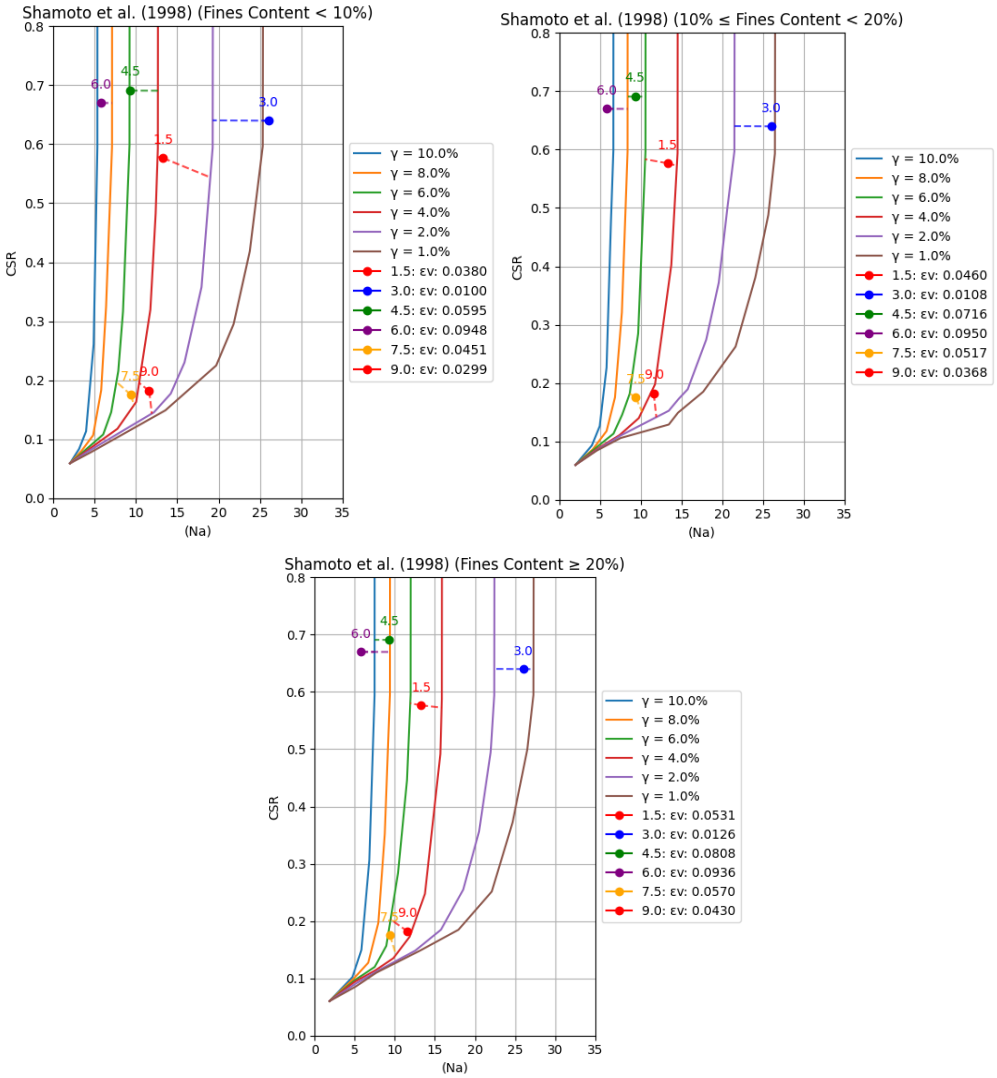


Figure 3.13: Output of the interpolation algorithm showing test depths and distances to the nearest curves for the **Shamoto et al. [1998]** method: (a) Fines Content < 10%, (b) 10% ≤ Fines Content < 20%, (c) Fines Content ≥ 20%.

Accordingly, the post-liquefaction vertical settlement (D_S) was calculated by multiplying the volumetric strain values by the corresponding layer thicknesses, summing the results over depth, and multiplying the total by the correction factor C_S.

$$D_S = C_S \cdot \int_0^H (\varepsilon_{vr})_{max}(z)dz \tag{3.52}$$

Here, C_S value was taken as 0.84 based on the regression analysis in the cited study.

3.3.3.4. Wu et al. [2003] Free-Field Settlement Procedure

As part of this thesis, another free-field liquefaction-induced settlement estimation method proposed by **Wu et al. [2003]** was utilized. For this purpose, the original chart presented in **Figure 3.14** was digitized, and the resulting interpolation-based strain curves are shown in **Figure 3.15**, illustrating the relationships among CSR, $(N_1)_{60cs}$, and reconsolidation volumetric strain.

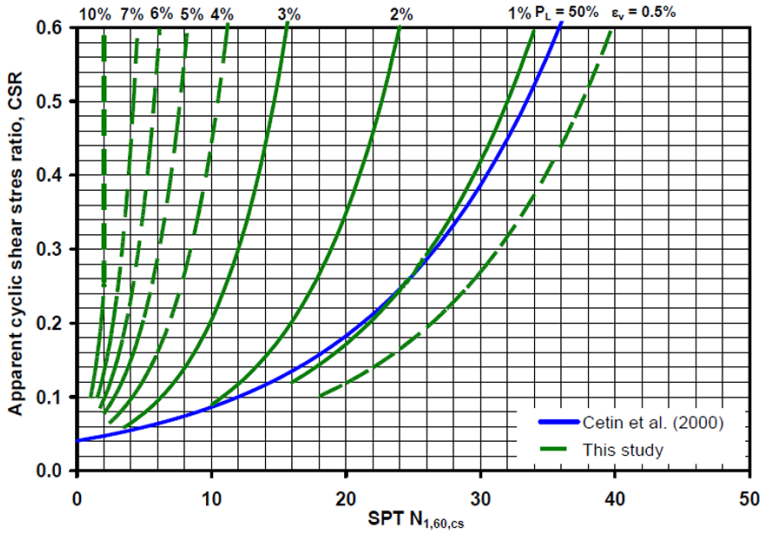


Figure 3.14: Reconsolidation volumetric strain curves based on $(N_1)_{60cs}$ and CSR **[Wu et al., 2003]**.

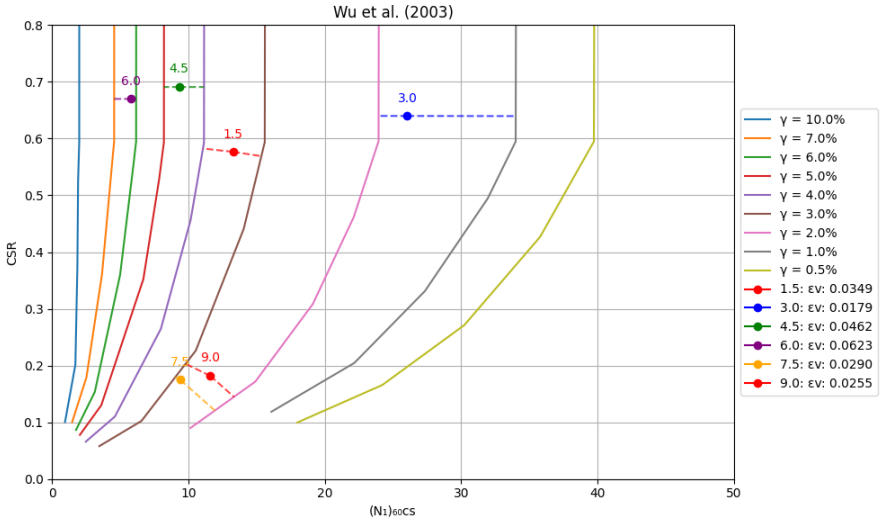


Figure 3.15: Visual output of the interpolation process displaying depths of test points and their distances to **Wu et al. [2003]** reference curves.

In the final step, liquefaction-induced free-field settlement was computed based on **Equation 3.43**.

3.3.3.5. Cetin et al. [2009] Free-Field Settlement Procedure

Cetin et al. [2009] developed a semi-empirical, probabilistic model to estimate liquefaction-induced settlements in saturated cohesionless soils after earthquakes. The method was calibrated using 49 high-quality field data sets from earthquakes of varying magnitudes. In the analysis, the relationship given in **Equation 3.53** was used to convert the field CSR to its laboratory equivalent under 1 atm confining pressure and 20 loading cycles.

$$CSR_{SS,20,1D,1atm} = \frac{CSR_{field}}{K_{md}K_{M_w}K_{\sigma}} \tag{3.53}$$

Due to the multidirectional nature of the loading, the K_{md} coefficient, which is a function of relative density, was calculated using **Equation 3.54**.

$$K_{md} = 0.361\, ln(D_R) - 0.579 \tag{3.54}$$

Moreover, the K_{M_W} correction factor, which accounts for the effect of earthquake duration on volumetric strain, was calculated using **Equation 3.55**. Since longer earthquakes generate more loading cycles and result in greater volumetric deformation, this coefficient is defined as a function of moment magnitude.

$$K_{M_W} = \frac{87.1}{{M_W}^{2.217}} \tag{3.55}$$

Following that, the effect of the vertical effective stress on CSR was corrected using the method proposed by **Youd et al. [2001]**, as expressed in **Equation 3.56**.

$$K_{\sigma} = (\frac{\sigma'_{vo}}{P_a})^{f-1} \tag{3.56}$$

The term f in **Equation 3.56** was calculated using **Equation 3.57**.

$$f = 1 - 0.005D_R \tag{3.57}$$

Following that, the volumetric strain was computed based on the formulation provided in **Equation 3.58**. However, it should be noted that this equation is applicable only for $(N_1)_{60cs}$ values between 5 and 40, and CSR values between 0.05 and 0.60.

$$\begin{aligned} &ln(\varepsilon_v) \\ &= ln\left[1.879\, ln\left(\frac{780.416\, ln\left(CSR_{SS,20,1D,1atm}\right) - (N_1)_{60cs} + 2{,}442.465}{636.613\,(N_1)_{60cs} + 306.732}\right)\right. \\ &\left. + 5.583\right] \pm 0.689 \end{aligned} \tag{3.58}$$

Since the layers near the surface contributed more to liquefaction-induced settlement, the study suggested a weight factor up to a critical depth of 18 m. This weight factor was calculated using **Equation 3.59**.

$$DF_i = 1 - \frac{d_i}{z_{cr} = 18m} \tag{3.59}$$

Subsequently, the equivalent volumetric strain was calculated using **Equation 3.60**.

$$\varepsilon_{v,eqv.} = \frac{\sum \varepsilon_{v,i} t_i DF_i}{\sum t_i DF_i} \tag{3.60}$$

Ultimately, the calculated equivalent volumetric strain was multiplied by the overall layer thickness, as expressed in **Equation 3.61**.

$$s_{estimated} = \varepsilon_{v,eqv.} \sum t_i \tag{3.61}$$

In summary, the free-field settlement methods applied in this thesis are presented in detail together with their formulas and calculation procedures. The results were generated using the developed algorithm and compared comprehensively.

4. REGIONAL OVERVIEW OF KAHRAMANMARAŞ PROVINCE

4.1. Geography, Climate, and Economic Structure

Kahramanmaraş is a metropolitan city located in the southeastern part of Türkiye, with a population of 1,134,105 as of the end of 2024 **[Turkish Statistical Institute, 2025]**. The city consists of eleven towns: Onikişubat, Dulkadiroğlu, Elbistan, Afşin, Türkoğlu, Pazarcık, Göksun, Andırın, Çağlayancerit, Nurhak and Ekinözü. The city center constitutes the towns of Dulkadiroğlu and Onikişubat. Covering a total area of 14,518 km², the province shares borders with Malatya and Adıyaman to the east, Kayseri and Adana to the west, Gaziantep and Osmaniye to the south, and Sivas to the north.

In terms of climate, Kahramanmaraş is situated at the junction of three distinct geographical regions. In the lowland areas, the Mediterranean climate prevails, while moderately continental climate characteristics appear toward the north as elevation increases. The city's average annual temperature ranges between 5°C and 28°C, and the annual precipitation varies from 0.5 to 127 kg/cm². Winters are mild and rainy, whereas summers are hot and dry. Approximately 42% of the province's land is covered by forests and shrublands, 27% by cultivated areas, and 24% by meadows and pastures **[Kahramanmaraş Metropolitan Municipality, 2025]**.

Regarding its economy, Kahramanmaraş has a structure supported by the industrial, agricultural, and service sectors. The industrial sector plays a significant role, with strong activity particularly in textiles, metal kitchenware, paper, and food production **[Eastern Mediterranean Development Agency, 2025]**. The city is a leading producer of metal kitchenware, with approximately 60% of Türkiye's total production produced in the city. Moreover, it accounts for 30% of national yarn and 10% of woven fabric production, underscoring its status as one of Türkiye's leading provinces in the textile industry **[Commodity Exchange of Kahramanmaraş, 2017]**.

4.2. Geological Formation

From a geological perspective, clastic and carbonate units, along with neritic limestone, are observed in the elevated parts of the city center, while alluvial fan deposits, undivided quaternary units, and similar deposits are generally found in low-lying areas. A significant portion of urban development is located on these alluvial and colluvial units. Furthermore, the presence of numerous fault lines across the central area indicates significant seismic hazard potential.

In addition, **Yeleser [2006]** reported that the Kahramanmaraş plain, which formed under the influence of the East Anatolian Fault (EAF), consists largely of quaternary sediments such as alluvium and slope debris. These units are prevalent particularly in the southwestern parts of the city, at elevations ranging from 450 to 500 meters. The stratigraphic sequence also includes older formations like the Koruk and Eloğlu Formations, as well as various ophiolitic and carbonate complexes, further emphasizing the geological complexity of the region. The geological structure of the city center is presented in detail in **Figure 4.1**.

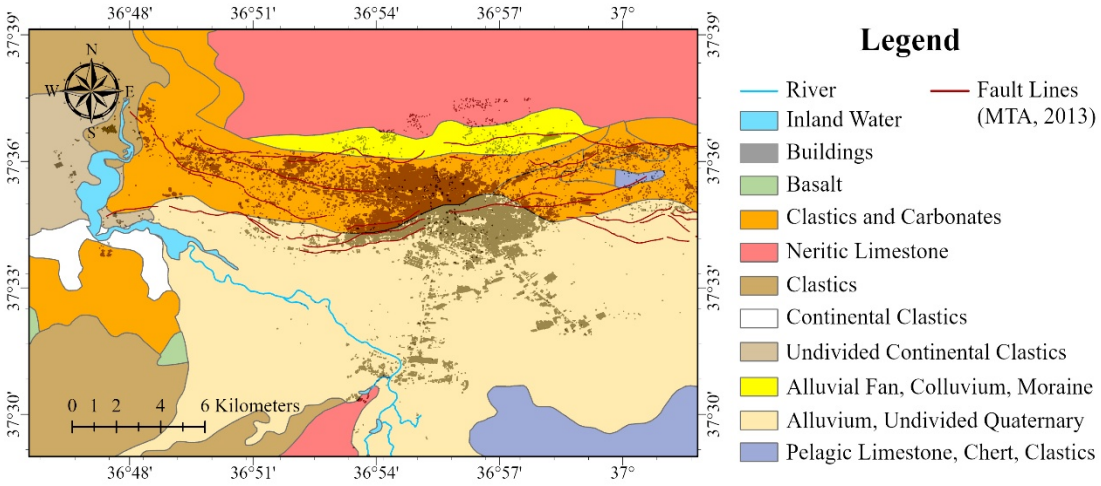


Figure 4.1: Map of the geological structure of Kahramanmaraş city center.

4.3. Seismic Characteristics

Kahramanmaraş Province is located within a zone of high seismic activity governed by the dynamics of the East Anatolian Fault Zone. This active, strike-slip fault system extends across eastern Türkiye, from Bingöl–Karlıova in the northeast to Türkoğlu–

Samandağ in the southwest. Tectonic deformation along the EAF is primarily compressional in nature and forms part of a broader interaction with the Dead Sea Fault System, reflecting the relative northeastward motion of the Arabian plate **[Arpat and Şaroğlu, 1972]**. The fault's southwestern portion can be further delineated into the Karasu and Misis segments, both historically associated with significant seismic events, such as the 1822 Hatay and 1874 Hazar Lake earthquakes **[Ambraseys, 1989; Demirtas, 1998]**.

Recently, this seismically active region was struck by two highly destructive earthquakes. The first event, with a magnitude of 7.7, occurred approximately 40 km from the city center in Pazarcık, while the second event, with a magnitude of 7.6, struck about 54 km away in Elbistan. The spatial distribution of the mainshocks, aftershocks, and associated surface ruptures is illustrated in **Figure 4.2**.

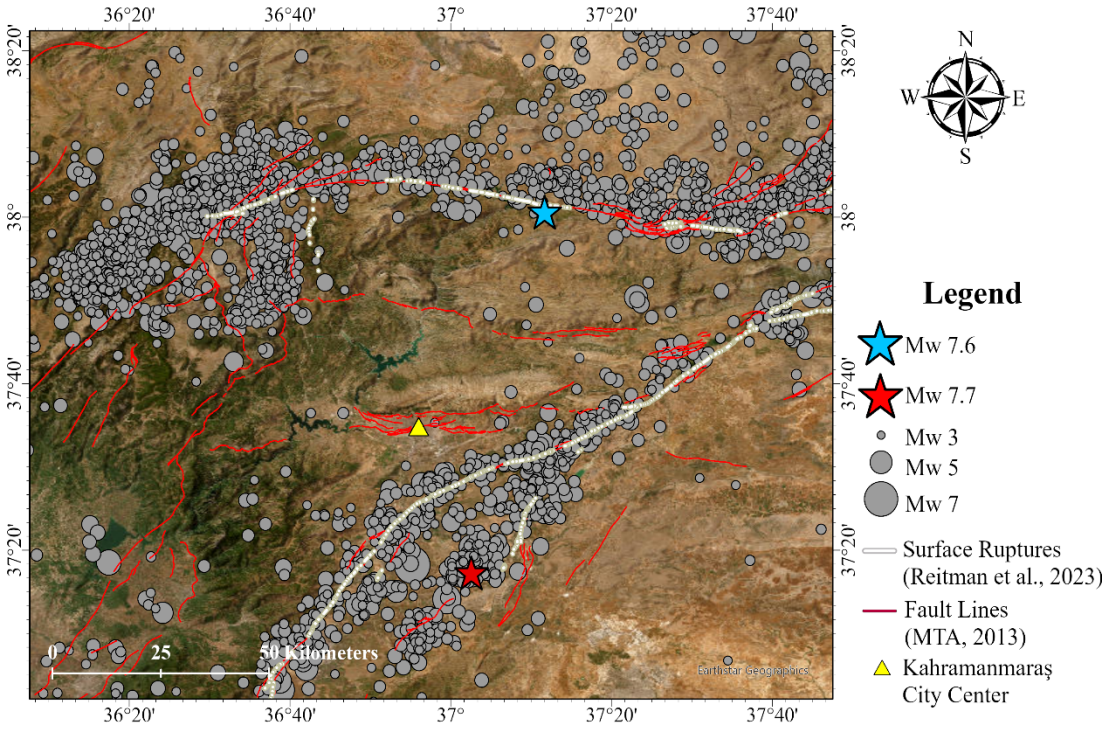


Figure 4.2: Map of the seismicity of the earthquake-affected region.

Figure 4.2 shows that aftershocks are predominantly concentrated along the fault zones where surface ruptures were observed and are distributed over a wide area, indicating extensive rupture propagation following both mainshocks.

Furthermore, between February 6, 2023, and June 6, 2025, the region experienced over 3,800 earthquakes with magnitudes greater than 3.0, all occurring within a 200 km radius of the city center. While the magnitude distribution of these events is presented in **Figure 4.3**, the number of earthquakes is presented in **Figure 4.4**.

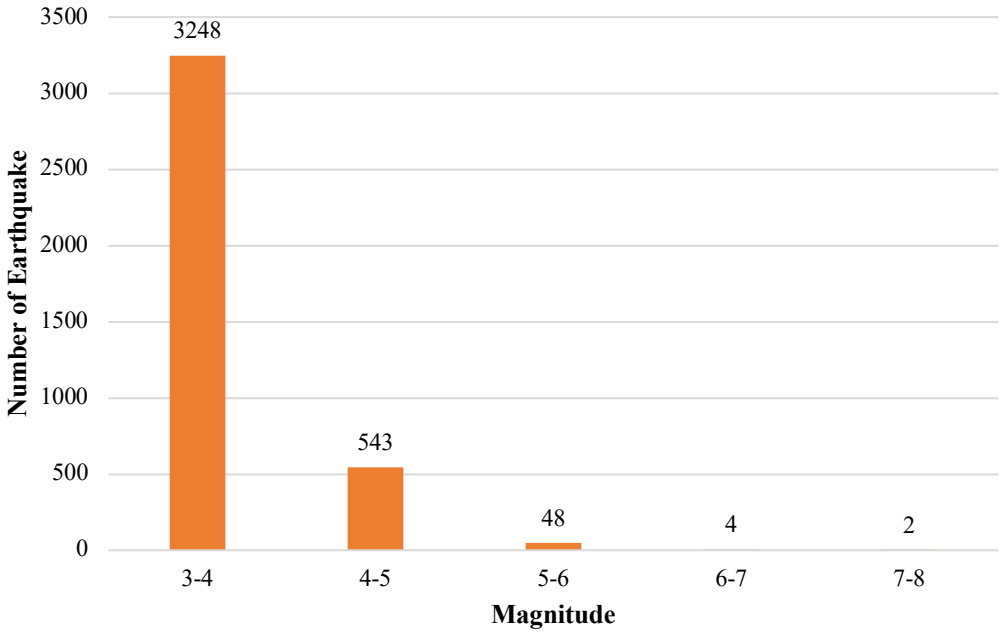


Figure 4.3: The distribution of the earthquake events by magnitude.

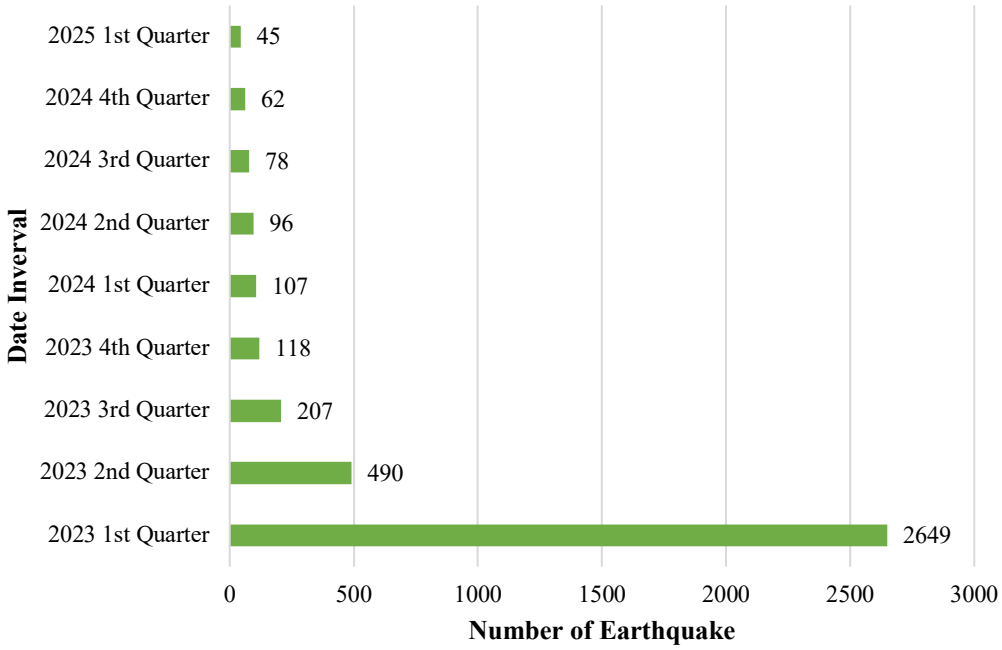


Figure 4.4: Quarterly distribution of the earthquake events.

Ground motion recordings from strong-motion stations provide further insight into the shaking characteristics of these events. Among the stations listed, the maximum PGA and PGV during the Mw 7.7 earthquake were recorded at station TK4625, with values of 466.33 cm/s² and 75.65 cm/s, respectively (**Table 4.1**). According to USGS data, PGV values ranged between 20 and 50 cm/s, while PGA values varied between approximately 196.13 and 490 cm/s² during this mainshock.

During the Mw 7.6 earthquake, the highest PGA and PGV values were observed at station TK4617, measured at 82.69 cm/s² and 27.36 cm/s, respectively (**Table 4.2**). USGS data indicate that during this second event, PGV values were around 20 cm/s, and PGA values ranged approximately between 50 and 98 cm/s².

Table 4.1: The PGA, PGV, and Peak Ground Displacement (PGD) values recorded by AFAD stations during the Mw 7.7 Pazarcık earthquake.

Station Code	Vs30 (m/s)	PGA (cm/sn2) (N-S)	PGA (cm/sn2) (E-W)	PGA (cm/sn2) (U-D)	PGV (cm/sn) (N-S)	PGV (cm/sn) (E-W)	PGV (cm/sn) (U-D)	PGD (cm) (N-S)	PGD (cm) (E-W)	PGD (cm) (U-D)
TK4617	574	145.33	115.16	110.59	28.47	26.10	19.95	29.79	41.34	19.64
TK4618	715	125.66	159.42	134.42	23.44	26.35	19.12	22.58	46.91	20.24
TK4619	545	302.03	194.74	175.51	30.42	30.03	19.11	32.18	48.91	19.22
TK4620	484	300.40	320.93	185.34	31.82	37.35	15.35	23.61	57.38	18.57
TK4621	714	363.80	295.56	253.92	31.94	45.14	20.87	32.03	59.93	16.42
TK4624	280	357.25	310.89	157.48	59.04	49.72	35.66	37.71	18.95	18.87
TK4625	345	447.00	466.33	344.07	75.65	49.84	28.94	46.29	19.87	20.32
TK4626	317	108.81	223.09	112.27	17.94	28.06	5.92	19.44	20.95	5.01

Table 4.2: The PGA, PGV, and PGD values measured by AFAD stations during the Mw 7.6 Elbistan earthquake.

Station Code	Vs30 (m/s)	PGA (cm/sn2) (N-S)	PGA (cm/sn2) (E-W)	PGA (cm/sn2) (U-D)	PGV (cm/sn) (N-S)	PGV (cm/sn) (E-W)	PGV (cm/sn) (U-D)	PGD (cm) (N-S)	PGD (cm) (E-W)	PGD (cm) (U-D)
TK4617	574	55.97	82.69	54.79	22.62	27.36	13.67	21.65	36.91	9.20
TK4620	484	66.82	81.33	57.03	21.48	23.44	13.36	20.09	38.21	10.57
TK4624	280	65.00	79.75	38.61	18.52	17.89	8.72	17.39	32.76	9.26
TK4625	345	73.46	50.68	38.15	13.90	15.38	8.80	23.67	30.83	6.94

4.4. Water Supply System

Kahramanmaraş Water and Sewerage Administration (KASKI) serves 1,134,105 people in 11 towns, employing 946 staff and operating an extensive water supply infrastructure that includes transmission lines, treatment facilities, storage tanks, and distribution networks **[KASKI, 2024]**. The city center, consisting of the Dulkadiroğlu and Onikişubat towns, accounts for 55.32% of the 430,854 water subscribers. This service network is supplied from four different sources: Ayvalı Dam (1,000 L/s) to the east, Karasu (1,500 L/s) to the west, Pınarbaşı (500 L/s) to the north, and southern wells (Asfalt, Adana, and Sanayi) (645 L/s) to the south, to meet the drinking water demand of Kahramanmaraş city center. The locations of these sources and transmission lines conveying water to the city center are presented in **Figure 4.5**.

Water from Ayvalı Dam is conveyed to the Ayvalı Drinking Water Treatment Plant, completed in 2010 with a daily capacity of 90,000 m³, via a 10 km steel pipeline with a diameter of 1,400 mm **[Toprak et al. 2024c]**. The treated water is distributed to the city through the Ayvalı Transmission Line, consisting of steel pipes with a diameter of 1,500 mm and a total length of 27.2 km. The Karasu Transmission Line extends 64.6 km, of which 59.1 km consists of steel pipes and 5.5 km of glass-reinforced plastic (GRP) pipes, conveying water from the Karasu spring to the city center. Water from the Pınarbaşı spring is transported through 0.85 km of asbestos cement (AC) pipes and is supplied to the network by both gravity and pumping lines. The supply from the southern wells is entirely conveyed via pumping lines through 7.8 km of steel pipes and is chlorinated before being supplied to the distribution network **[BELGEP, 2022]**.

The city center is also served by 35 water tanks (**Table 4.3**), most of which are underground reinforced concrete structures with storage capacities ranging from 200 m³ to 10,000 m³. Five pumping stations (**Table 4.4**) operate to transfer water from lower elevations to the upper zones of the city, with flow rates ranging from 20 L/s to 111 L/s.

Table 4.3: Names and storage volumes of water tanks located in the city center of Kahramanmaraş.

No	Tank Name	Volume (m^3)	No	Tank Name	Volume (m^3)
1	Kavlakli	5,000	**19**	DM12	2,500
2	Ungut	1,000	**20**	DM19	-
3	DM23	5,000	**21**	TDM1	-
4	DM4	2,000	**22**	DM15	-
5	DM7	4,000	**23**	Tekke	-
6	DM3	3,000	**24**	TDM4	2,000
7	DM5	4,000	**25**	Tekerek	250
8	DM8	6,000	**26**	DM21 (ATV)	2,500
9	DM11	10,000	**27**	1000 m³ Tank	1,000
10	DM13	10,000	**28**	DM6	2,500
11	DM18	6,000	**29**	TDM3	-
12	DM16	10,000	**30**	200 m³ Tank	200
13	DM20	1,500	**31**	200 m³ Tank	200
14	DM22	2,000	**32**	300 m³ Tank	300
15	DM14	2,500	**33**	Dereli	-
16	DM1 (5/1)	2,500	**34**	Bulutoglu-Kurtul-Koseli	-
17	DM2 (5/2)	1,500	**35**	TDM2	500
18	DM10	5,000			

Table 4.4: Technical specifications of the pumping stations transferring water to upper zones in the Kahramanmaraş city center.

No	Station Name	Flow Rate (L/s)	Pump Power (kW)	Pumping Water Level (m)
1	TM23	60	75	80
2	TM5-1	35	55	90
	TM5-2	20	22	60
3	TM11-1	45	78	110
	TM11-2	111	90	58
4	TM7	60	110	120
5	TY1	37	45	69

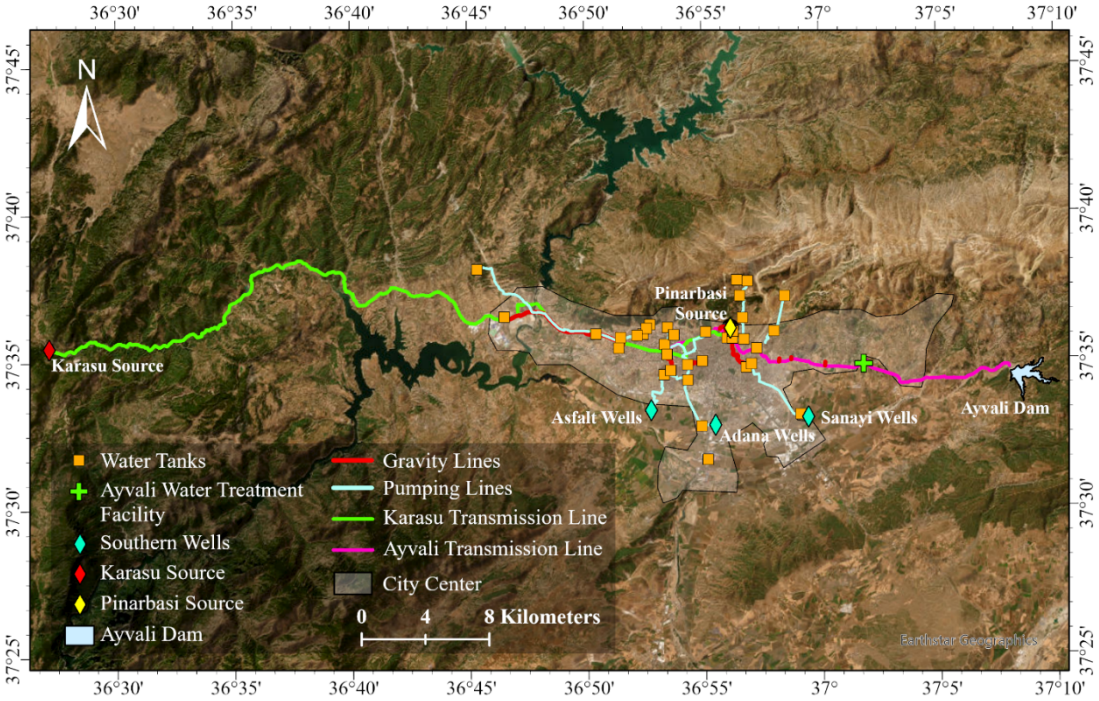


Figure 4.5: Map showing the water sources and transmission lines in the city center.

The percentages of pipe types in the distribution system in the Kahramanmaraş city center is given in detail in **Figure 4.6**. The water service has an infrastructure consisting of various pipe materials, including polyethylene (PE), polyvinyl chloride (PVC), asbestos cement (AC), cast iron (CI), concrete, steel, and polypropylene random copolymer (PPRC).

In the pre-earthquake system, the majority of the city's water distribution network (79%) consisted of PE pipes, which were widely distributed throughout the city center. AC and PVC pipes each accounted for 7% of the network, while CI pipes constituted 5% and steel pipes formed 2%. Concrete, PPRC, and other types of pipes each accounted for less than 1%. AC and CI pipes were generally located in relatively older settlement areas.

Prior to the spatial analysis, it was identified that some sections of the distribution lines were missing from the Geographic Information System (GIS) database. The updated layout of the network, including the segments added to address these gaps, is shown in **Figure 4.7**. The missing lines were digitized from printed layout maps obtained from KASKI, georeferenced, and integrated into the GIS environment to provide a more complete representation of the system.

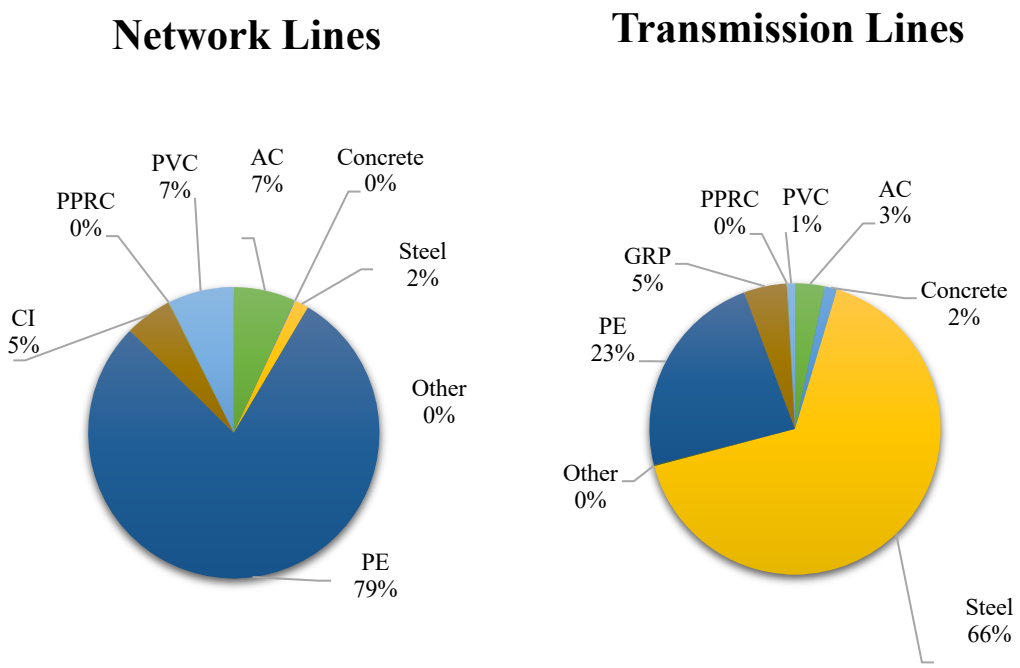


Figure 4.6: Material types of the pipeline network in Kahramanmaraş city center.

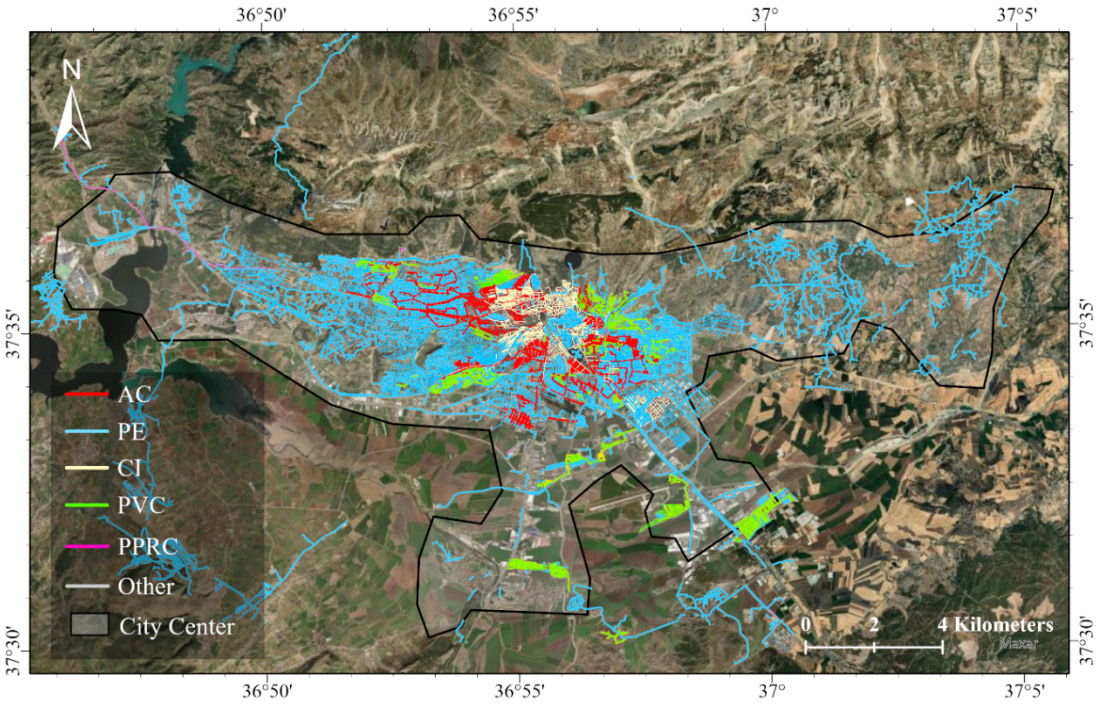


Figure 4.7: The distribution map of the pipeline network based on pipe types.

5. OBSERVED DAMAGES AFTER THE 2023 KAHRAMANMARAŞ EARTHQUAKES

5.1. Structural Damages

The 2023 Kahramanmaraş earthquakes caused extensive damage throughout Kahramanmaraş Province and its towns. Across the province, which has a total of 481,362 residential buildings, more than 99,000 were reported as heavily damaged or collapsed, 17,000 as moderately damaged, and 161,000 as lightly damaged **[SBB, 2023].** The spatial distribution and intensity of these structural damages were also significant for utility and field crews, as the concentration of collapsed buildings and debris in certain neighborhoods affected their accessibility to water distribution lines and the progression of repair efforts **[Toprak et al. 2026a]**. In heavily impacted areas, blocked streets and damaged roads restricted field access, delayed the identification of network issues, and limited the ability to operate maintenance equipment. Therefore, the documentation of structural damage is included here to clarify the physical conditions under which network issues were identified and addressed by the response teams.

Damage was more severe in Dulkadiroğlu Town, where lower elevations and older settlements are concentrated. In contrast, Onikişubat Town—characterized by higher elevations and newer developments extending toward the northwest—experienced comparatively less severe effects based on field observations. The most heavily impacted area was Azerbaycan Neighborhood (formerly Hayrullah), located in Dulkadiroğlu Town. The satellite imagery in **Figure 5.1** shows this area before and after the earthquake, clearly illustrating the extent of destruction. Structural damage and building collapses observed during field visits in the city center are presented in **Figure 5.2** and **Figure 5.3**.

a) b)

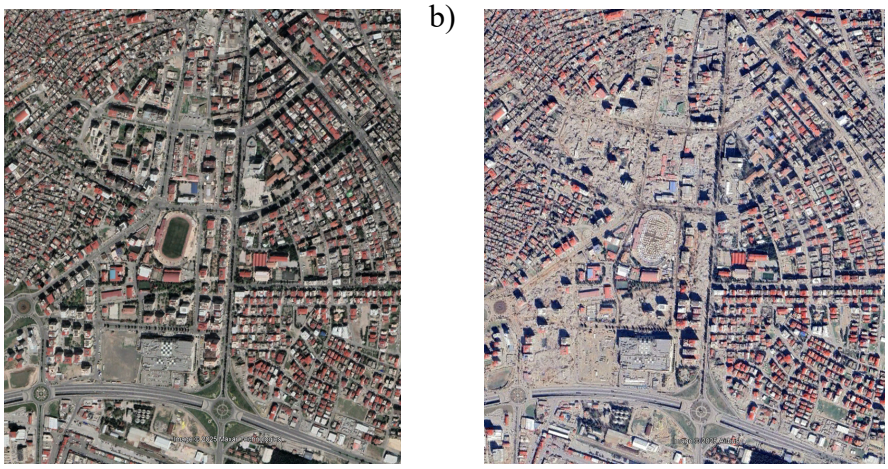


Figure 5.1: Google Earth satellite imagery of Azerbaijan Boulevard, showing the extent of structural damage: (a) before the earthquakes (10 April 2022) and (b) after the earthquakes (16 February 2023).

a) b)

c) d)

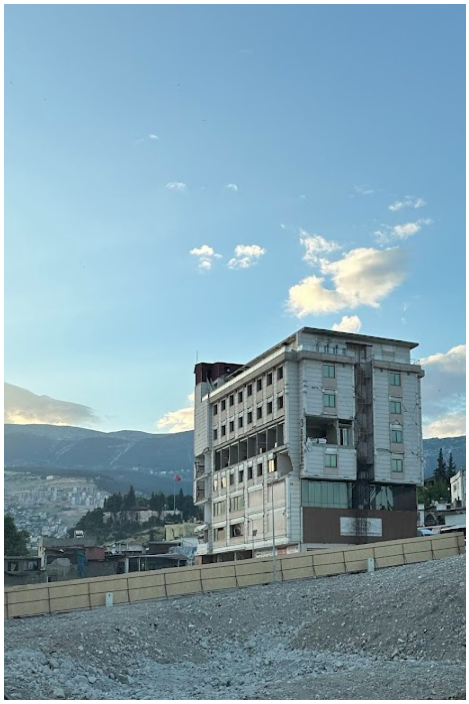


Figure 5.2: Examples of earthquake-induced damage observed during the field survey in the city center: (a) damaged and abandoned multi-story building, (b–d) collapsed buildings with heavily damaged adjacent structures and debris from the collapses.

a)



b)



c)



d)

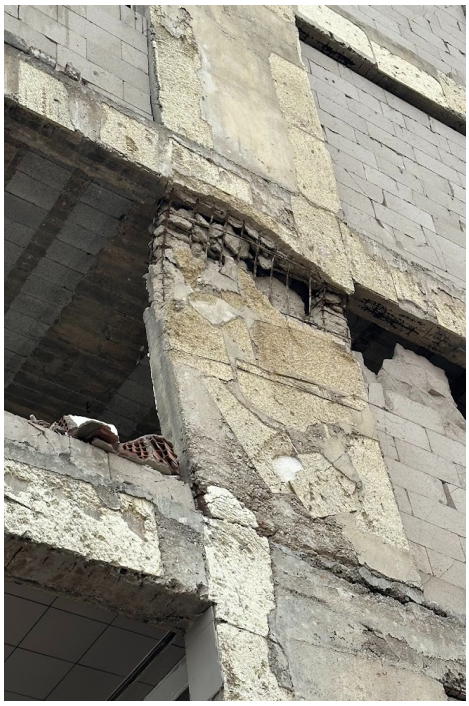


Figure 5.3: Structural damage documented during the field investigation in the city center: (a) damaged building awaiting demolition, (b) severely damaged and non-functional structure, (c) structural element with visible damage, and (d) buckled structural system indicating serious deformation.

In Azerbaijan Neighborhood, where the destruction was most severe, post-earthquake housing is being constructed with support from the Government of Azerbaijan. The newly built residential structures are predominantly low- to mid-rise buildings, generally ranging from three to six stories. Field observations confirmed that construction activities are actively ongoing. These observations are presented in **Figure 5.4**.

a) b)



Figure 5.4: Post-earthquake reconstruction efforts supported by the Republic of Azerbaijan: (a) construction site of post-earthquake housing, and (b) newly constructed residential building.

In addition to the destruction in the city center, towns such as Ekinözü, Elbistan, and Türkoğlu also sustained severe damage from the earthquake. Ekinözü is located approximately 94 km from the epicenter of the first earthquake and about 5.5 km from the second. In the town center, fault ruptures, ground uplifts, and slope stability issues were observed, as presented in **Figure 5.5**. Elbistan is situated approximately 22 km from the second epicenter and 109 km from the first. Buildings in the town suffered extensive damage, and the overall building stock exhibited significant structural deficiencies. These observations are presented in **Figure 5.6**.

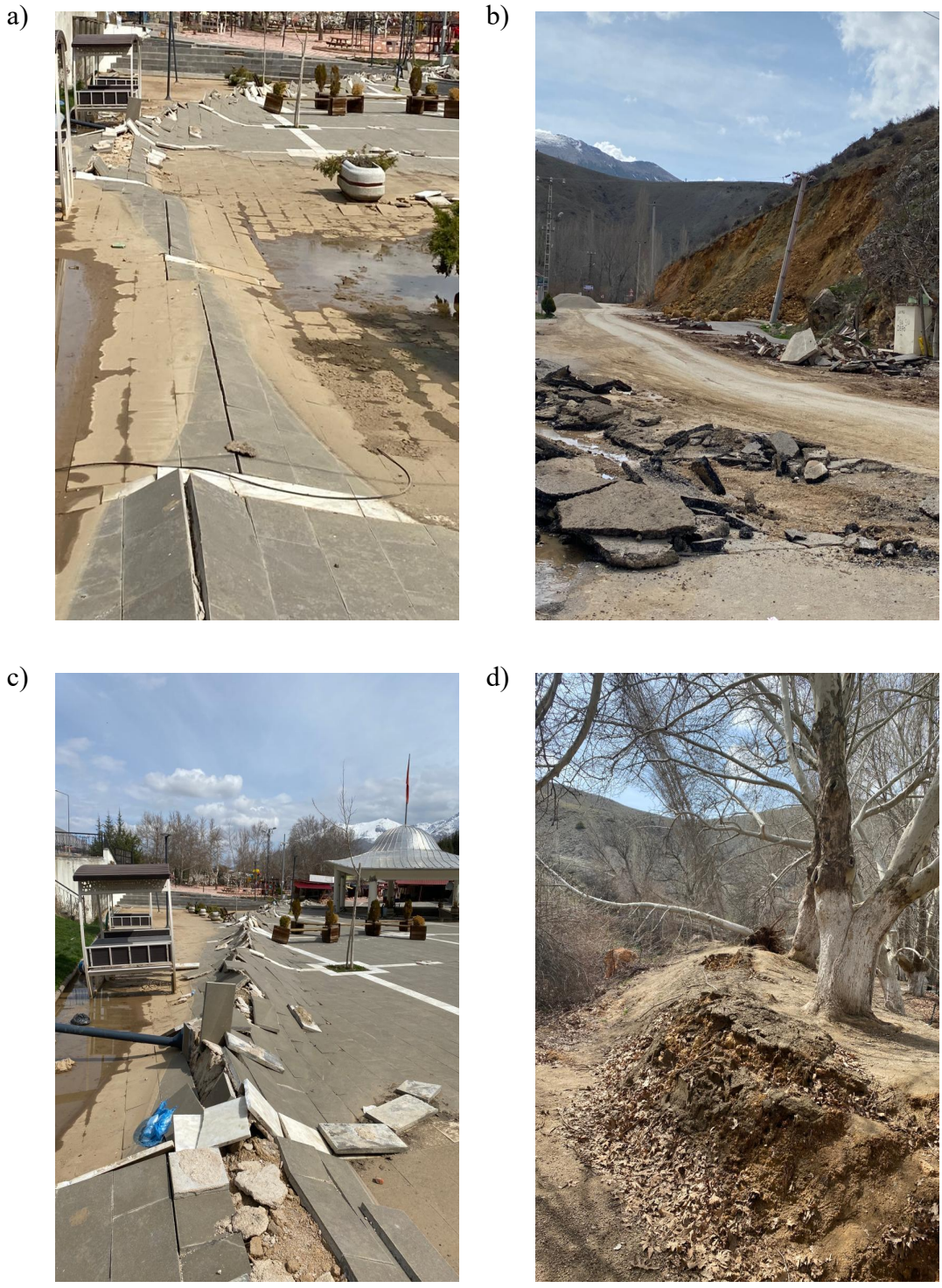


Figure 5.5: Earthquake-induced ground deformations in Ekinözü Town (Courtesy of Ekinözü Municipality): (a) pavement cracks caused by ground displacement, (b) road damage due to soil stability issues, (c) surface cracking and displacement, and (d) ground uplift affecting tree alignment and soil surface.



Figure 5.6: Drone images showing building demolitions and debris removal operations in Elbistan Town (Courtesy of Elbistan Municipality).

5.2. Water Infrastructure Systems

The earthquakes of February 6, 2023, caused extensive damage to water infrastructure systems in multiple provinces, underscoring their susceptibility to seismic hazards **[Toprak et al., 2025b]**. Numerous post-earthquake investigations have examined the impacts on these systems. **Toprak et al. [2024a]** carried out a comprehensive assessment of geologic and geotechnical conditions—such as liquefaction, surface faulting, landslides, and turbidity effects—on selected water infrastructure in

Kahramanmaraş, Gaziantep, Hatay, and Adıyaman (**Figure 5.7**). **Uckan et al. [2024]** evaluated major damage points in both water and hydrocarbon transmission lines and proposed measures to improve infrastructure resilience against future events. **Unal et al. [2024]** analyzed the vulnerability of natural gas pipelines, whereas **Wang et al. [2024]** developed a seismic fragility framework for buried pipelines using ground motion data. **Cetin et al. [2025b]** examined the performance of the Reyhanlı Dam, a key water supply for Hatay, identifying cracks, displacements, and ground deformations. Beyond structural impacts, the earthquakes also affected water quality. **Toprak et al. [2026b]** investigated post-earthquake increases in turbidity along the Göksu Stream using satellite imagery and examined the effects of landslides, rainfall, and seismicity. **Şimşek et al. [2024]** reported changes in water sources through on-site inspections and in-situ measurements. **Inan et al. [2024]** compared pre- and post-earthquake spring water samples to determine changes in mineral composition. **Toprak et al. [2024d]** compiled field observations on water systems in the affected region into a database, while **Toprak et al. [2025c]** investigated water supply interruptions, quality fluctuations, and pipeline failures during the recovery phase, providing targeted evaluations and recommendations for specific system components.

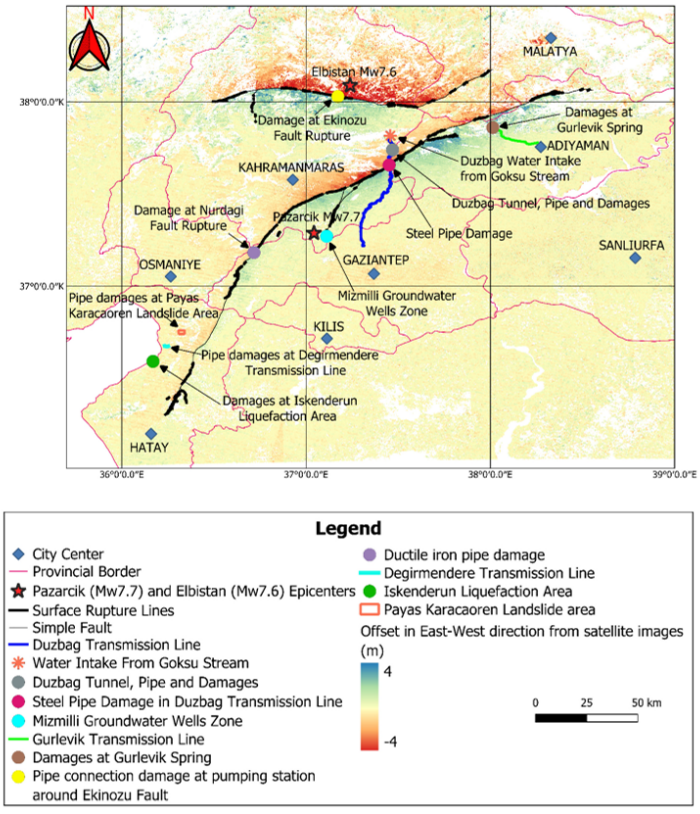


Figure 5.7: Overview of damages in infrastructure systems **[Toprak et al., 2024a]**.

Kahramanmaraş Province was among the provinces that sustained the most severe infrastructure damage during the 2023 earthquakes. While significant problems were observed in the city center's distribution network, no major issues were reported on the transmission lines. The water loss rate, which was around 55% before the earthquake, rose to nearly 75% afterward, and the number of daily failures increased by 400% **[KASKI, 2024]**. In an attempt to reduce losses, KASKI lowered the pressure in the network; however, this led to a reduction or complete cut in water flow to upper floors of buildings lacking booster pumps. Consequently, detecting and repairing damaged pipes has become the only viable solution to control the water loss. Within one month after the earthquakes, the water supply was restored to approximately 90% of the city, and repair efforts have continued **[KASKI, 2024]**. The proportions of water service delivered to each district following the earthquake are presented in **Table 5.1**. These impacts necessitated a rapid and coordinated post-earthquake response.

Table 5.1: District-based water delivery rates in Kahramanmaraş following the February 2023 earthquakes.

	February 12, 2023	**February 14, 2023**	**February 15, 2023**	**February 16, 2023**
City Center	%80-%95	90%	90%	90%
Andırın	90%	95%	95%	100%
Elbistan	70%	85%	90%	90%
Ekinözü	95%	90%	95%	95%
Afşin	90%	90%	95%	100%
Çaglayancerit	95%	100%	100%	100%
Pazarcık	80%	75%	75%	80%
Türkoğlu	100%	100%	100%	100%
Nurhak	60%	70%	70%	80%
Göksun	NA	100%	100%	100%

During the earthquake response, KASKI carried out various operations. While the repair of damaged pipelines was ongoing (**Figure 5.8a**), the capping of water lines from collapsed buildings was also being conducted simultaneously (**Figure 5.8b**). Additionally, efforts were made to supply water to the container cities established by

AFAD to provide shelter for earthquake victims (**Figure 5.8c**). Furthermore, immediately after the earthquake, water and sewerage administrations from other provinces—KASKI (Kayseri), BASKI (Balıkesir), BUSKI (Bursa), and SASKI (Sakarya)—assisted Kahramanmaraş Water and Sewerage Administration in addressing the damages and contributed to the restoration efforts. This situation highlights the importance of effective communication between institutions during disasters and the necessity of having an emergency response plan in place beforehand.

a) b) c)

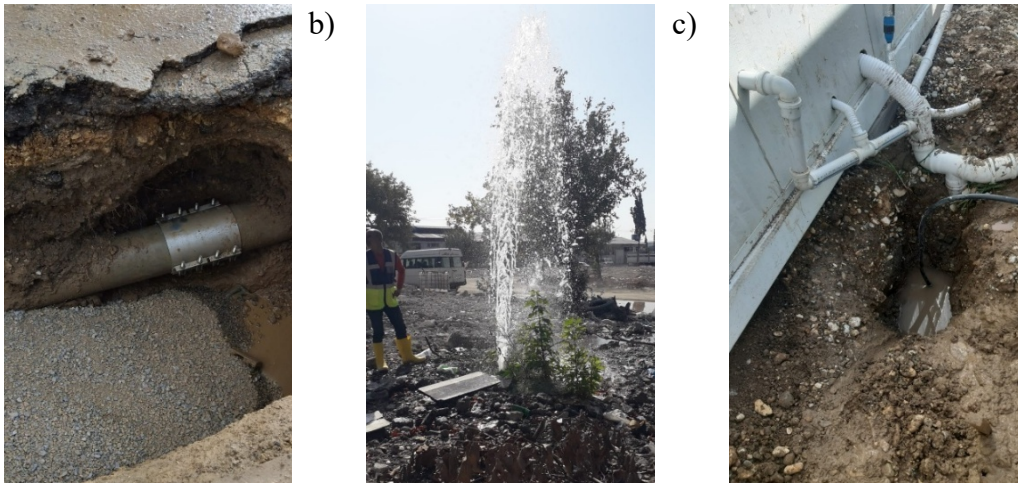


Figure 5.8: Post-earthquake activities carried out by KASKI (Courtesy of KASKI): (a) repair of a damaged 250 mm AC pipe, (b) capping operations, and (c) water supply efforts to container cities.

In addition to the damage sustained in the city center, several towns also experienced varying degrees of impact on their water infrastructure systems. In Afşin, the entire 202-kilometer drinking water distribution network had been renewed with polyethylene pipes before the earthquake. As a result, the town experienced only minor damage, limited to a few localized areas. Some malfunctions were reported due to direct well pumping into the system, but overall, the network performed well. Similarly, in Göksun, where the system had also been upgraded with polyethylene pipes prior to the event, the infrastructure showed strong performance with no major issues. In Pazarcık, the renewal of the water infrastructure was still ongoing at the time of the earthquake, which led to significant disruptions during and after the event. Elbistan had undergone substantial renewal efforts as well; although some old pipes remained in the network, no serious failures were reported. In Ekinözü, the distribution system had also been replaced with polyethylene pipes, which contributed to the absence of major problems following the earthquake.

5.2.1. Treatment Plants

Improving treatment facilities—one of the key components of infrastructure systems—against earthquakes and ensuring their continued operation after such events is essential to maintain access to clean water supplies for communities. The Ayvalı Drinking Water Treatment Plant, which treats water from the Ayvalı Dam, played a vital role in maintaining an uninterrupted water supply to the city center during the earthquake. A damage assessment was conducted at the Ayvalı Dam, but no damage was identified by KASKI. However, the treatment plant sustained damage, yet it continued to operate. Three 125 mm diameter PVC pressure pipes located in the balancing reservoir were damaged (**Figure 5.9**), and plans were made to replace them with similar PVC pipes having a pressure capacity of 10 bars **[Toprak et al., 2025c]**.



Figure 5.9: Removed pipes from the balancing reservoir at the Ayvalı Treatment Plant **[Toprak et al., 2024d]**.

5.2.2. Transmission Lines

No damage was reported in the transmission lines supplying water to the Kahramanmaraş city center.

5.2.3. Water Tanks

In the aftermath of the earthquake, communication was maintained with KASKI officials to exchange information. Based on the information shared during meetings with the administration, three water tanks—including one elevated tank—in Pazarcık sustained damage. These tanks were relatively old, estimated to be between 30 and 40 years old.

The elevated tank with a capacity of 30 tons, located in the Çiğdemtepe neighborhood totally collapsed. A reinforced concrete tank with a booster (hydrophore) system was constructed to replace at the same location. The conditions of the tank before the earthquake, after the collapse, and the newly constructed replacement are presented in **Figure 5.10**. According to the ground motion estimates reported by **Toprak et al. [2025a]**, this site was subjected to a PGA of 0.44 g and a PGV of 90.98 cm/s.



Figure 5.10: Collapsed elevated tank in the Çiğdemtepe Neighborhood: (a) before the earthquake, (b) after the collapse (Courtesy of KASKI), and (c–d) the newly constructed tank (Google Maps).

In addition, the 50-ton capacity reinforced concrete tank located in Kadıncık neighborhood was also damaged (**Figure 5.11a**), where cracks were observed in the load-bearing elements and spalling occurred on the ceiling. A 50-ton underground reinforced concrete tank was constructed at the same site. Moreover, in Osmandede neighborhood, a 50-ton reinforced concrete tank collapsed due to the earthquake (**Figure 5.11b**), and it was replaced by a 100-ton underground reinforced concrete tank. Based on the ground motion data provided by **Toprak et al. [2025a]**, the PGA and PGV in Kadıncık were estimated to be 0.51 g and 116.47 cm/s, respectively, while in Osmandede these values were 0.27 g and 66.69 cm/s.

a) b)



Figure 5.11: Damaged tanks in Kadıncık (a) and Osmandede (b) neighborhoods (Courtesy of KASKI).

5.2.4. Distribution Lines

The most significant damage in Kahramanmaraş was observed in the distribution network, primarily due to the presence of old and deteriorated pipelines. Failures were particularly concentrated in Dulkadiroğlu Town, where both the residential areas and the underlying infrastructure are relatively aged. Information obtained from KASKI officials, together with subcontractor repair records, indicated that pipes in the water network showed brittle behavior, leading to widespread failures and considerable operational difficulties.

In CI pipelines, lead-sealed joints placed at 4–5 m intervals were displaced by seismic-induced ground movements, causing joint separations and subsequent leakages. Beyond joint failures, longitudinal fractures were also identified along the pipe walls. The extent of the damage was further amplified by corrosion and insufficient maintenance, as shown in **Figure 5.12**.

a) b)

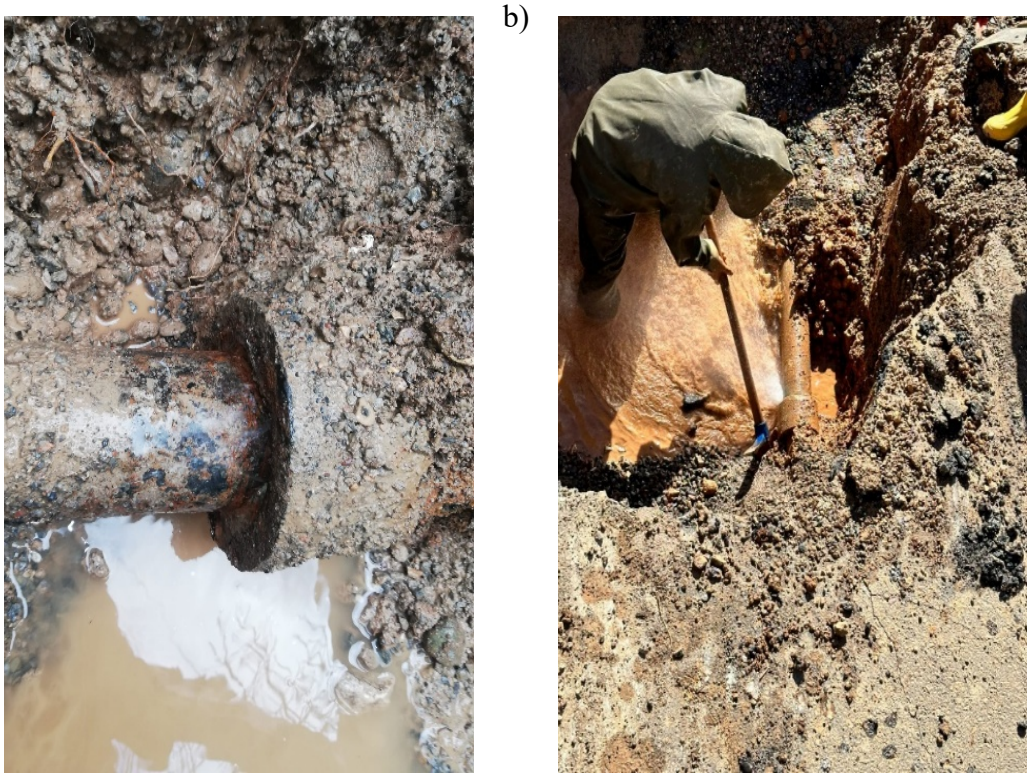


Figure 5.12: Examples of earthquake-induced damage in CI pipes: (a) 63 mm diameter pipe with evident corrosion and leakage; (b) 150 mm diameter pipe showing leakage at a displaced lead-sealed joint (Courtesy of KASKI).

Similarly, AC pipes displayed damage patterns comparable to those of CI pipes. Their limited resistance to axial forces frequently resulted in joint separations and longitudinal cracking. These observations were further confirmed in the field, as shown in **Figure 5.13**, which presents typical failure mechanisms in AC pipes, including joint displacements, circumferential fractures, and emergency repairs with metal clamps.



Figure 5.13: Damage and repair practices observed in AC pipes after the earthquakes: (a) 150 mm pipe leaking from a separated joint; (b) same pipe section repaired using a metal clamp; (c) completely fractured 100 mm pipe with high-pressure water leakage; (d) 100 mm pipe repaired with a clamp; (e) removed 100 mm AC pipe section showing complete fracture; (f) repaired condition of the same 100 mm pipe (Courtesy of KASKI).

Although PE pipes are generally regarded as earthquake-resistant, field observations in Kahramanmaraş indicated that their performance did not fully meet expectations. Several cases of fractures and leakages were recorded in the distribution network. As presented in **Figure 5.14**, 80 mm and 100 mm PE pipes exhibited cracks and local punctures, which required repair with mechanical clamps. This unexpected performance may be related to the material properties or the production quality of the pipes used in the system.



Figure 5.14: Damage and repair operations observed in PE pipes after the earthquakes: (a) 100 mm pipe with puncture; (b) subsequent repair using a mechanical clamp; (c) 80 mm pipe with complete fracture and leakage; (d) subsequent repair using a mechanical clamp (Courtesy of KASKI).

PVC pipes, similar to other pipe materials, were also affected by the earthquake, exhibiting water leakage as well as cracks along the pipe bodies (**Figure 5.15**). In many cases, the damaged segments were replaced with new pipes. These pipelines are joined at intervals of approximately 5–6 m using bell-and-spigot joints. Horizontal and vertical ground deformations during the earthquake caused loosening at these joints, which in turn resulted in separations and leakage.



Figure 5.15: Earthquake-induced damage and subsequent repair in PVC pipes: (a) 75 mm pipe with visible cracking; (b) subsequent repair of the pipe; (c) 100 mm pipe exhibiting cracks and active leakage; (d) subsequent repair using PVC fittings (Courtesy of KASKI).

Overall, the observations indicated that the existing distribution system was highly vulnerable to seismic effects. Consequently, KASKI has planned to renew the entire network with an earthquake-resistant infrastructure, as described in the following section.

5.2.5. Post-Earthquake Recovery Efforts

Following the destructive earthquakes, two major projects financed by the World Bank were initiated: FRIT II and TERRP (Türkiye Earthquake Recovery and Reconstruction Project). Although the FRIT II agreement was signed in 2021, the start of the project was delayed due to the earthquakes. However, the project has since commenced, and tendering procedures were conducted in 2024. Similarly, the TERRP project also went through its procurement process in 2024.

Within the scope of FRIT II, two projects are underway in the city center, whereas TERRP comprises six further projects. In total, eight infrastructure rehabilitation projects are being executed in the urban area. The sewer and stormwater networks primarily use concrete pipes, whereas polyethylene-based ductile pipes are employed in the potable water systems.

In the city center of Kahramanmaraş, following construction works will be carried out.

1) A total of 671 km of potable water pipeline—predominantly consisting of PE pipes—will be constructed.
2) 589 km of sewer lines will be built using concrete pipes.
3) 68 km of stormwater drainage lines will also be constructed with concrete pipes.
4) Additionally, 20 new underground reinforced concrete reservoirs will be built, and 4 existing reservoirs will be rehabilitated.

In the towns of the Kahramanmaraş Province, the planned works are as follows:

1) Pazarcık: Within the scope of TERRP, 120 km of sewer pipelines and 18 km of stormwater drainage lines will be constructed using concrete pipes. The potable water network in the town had already been renewed previously with polyethylene pipes.
2) Elbistan: As part of FRIT II and TERRP, 227 km of potable water pipelines (PE), 241 km of sewer pipelines (including 23 km of steel-reinforced corrugated pipes), and 41 km of stormwater drainage (concrete pipes) will be constructed.

6. LIQUEFACTION SUSCEPTIBILITY MAPPING OF KAHRAMANMARAŞ PROVINCE

In the literature, there are several studies focusing on the liquefaction susceptibility of Kahramanmaraş city center. For instance, **Cabalar et al. [2019]** evaluated liquefaction potential using 238 SPT boreholes and reported that boreholes with low SPT blow counts in the southern part of the city center are prone to liquefaction. However, no study specifically addressed the liquefaction susceptibility of the city center under the seismic conditions of the 2023 earthquakes, such as a moment magnitude of 7.7 and strong ground motions.

As part of the liquefaction susceptibility analysis conducted in this thesis, microzonation data from a study carried out by the Kahramanmaraş Metropolitan Municipality in 2011 were utilized. Within the scope of that microzonation study, the city center was divided into two regions, East and West. In the eastern section, 119 SPT boreholes were drilled, with a cumulative depth of 1,806.15 m, while in the western section, 168 SPT boreholes were drilled, reaching a total depth of 2,379.3 m. The SPT tests were performed at 1.5 m intervals down to 15.45 m, and the collected soil samples were subjected to laboratory testing. The spatial distribution of all boreholes in the city center is shown in **Figure 6.1**.

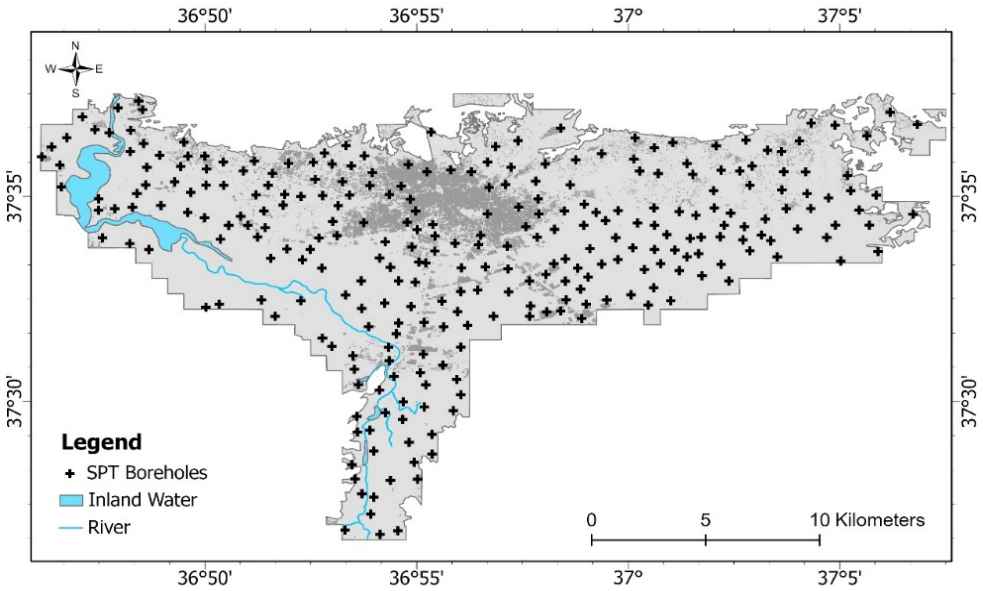


Figure 6.1: Map showing the spatial distribution of SPT boreholes in the study area.

The groundwater table, a critical parameter in liquefaction evaluations, was identified in 102 of the 287 boreholes drilled within the study area. Encountered depths ranged from 0.5 m to 12 m. The GWT data were interpolated using the Inverse Distance Weighting (IDW) method to generate a raster surface, which is shown in **Figure 6.2**. In the southern part of the city center, groundwater is not only encountered more frequently but is also generally found at shallower depths. This condition increases the geotechnical significance of the area, especially in terms of seismic hazard evaluations.

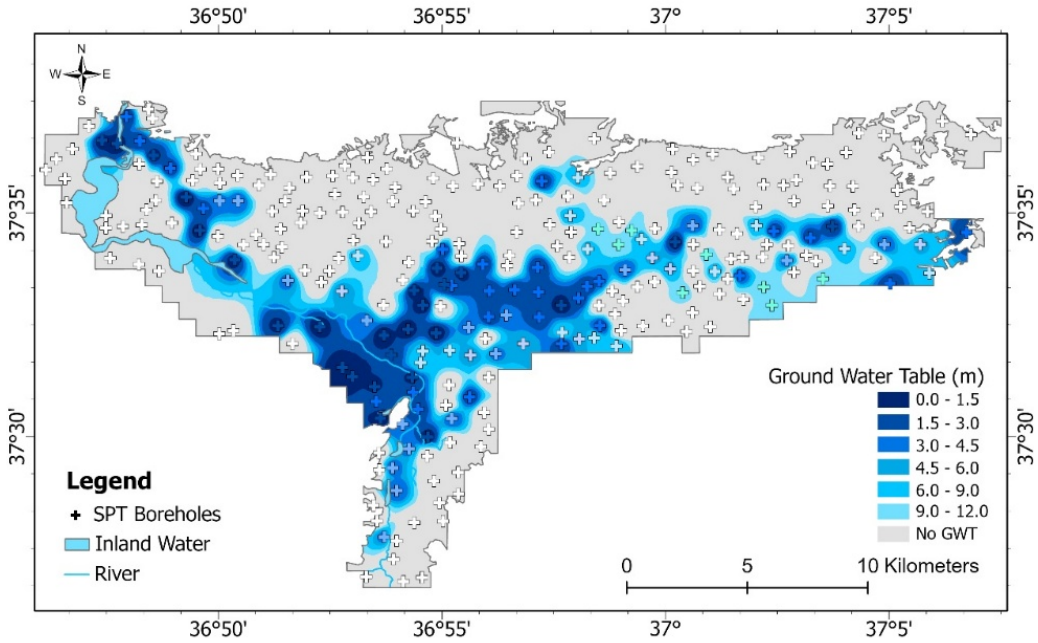


Figure 6.2: Map showing the spatial distribution of GWT in the study area.

When the SPT blow counts are examined, it is observed that these numbers generally increase with depth. For example, while the average value at 1.5 m depth ranges between 10 and 20 across the city center, it varies from 30 to more than 50 at a depth of 9 m. This trend indicates that soil becomes denser and more compacted with increasing depth, whereas shallow layers remain relatively weak. To illustrate this pattern, the SPT blow counts at selected depths were interpolated into raster surfaces using the IDW method and are presented in **Figure 6.3**.

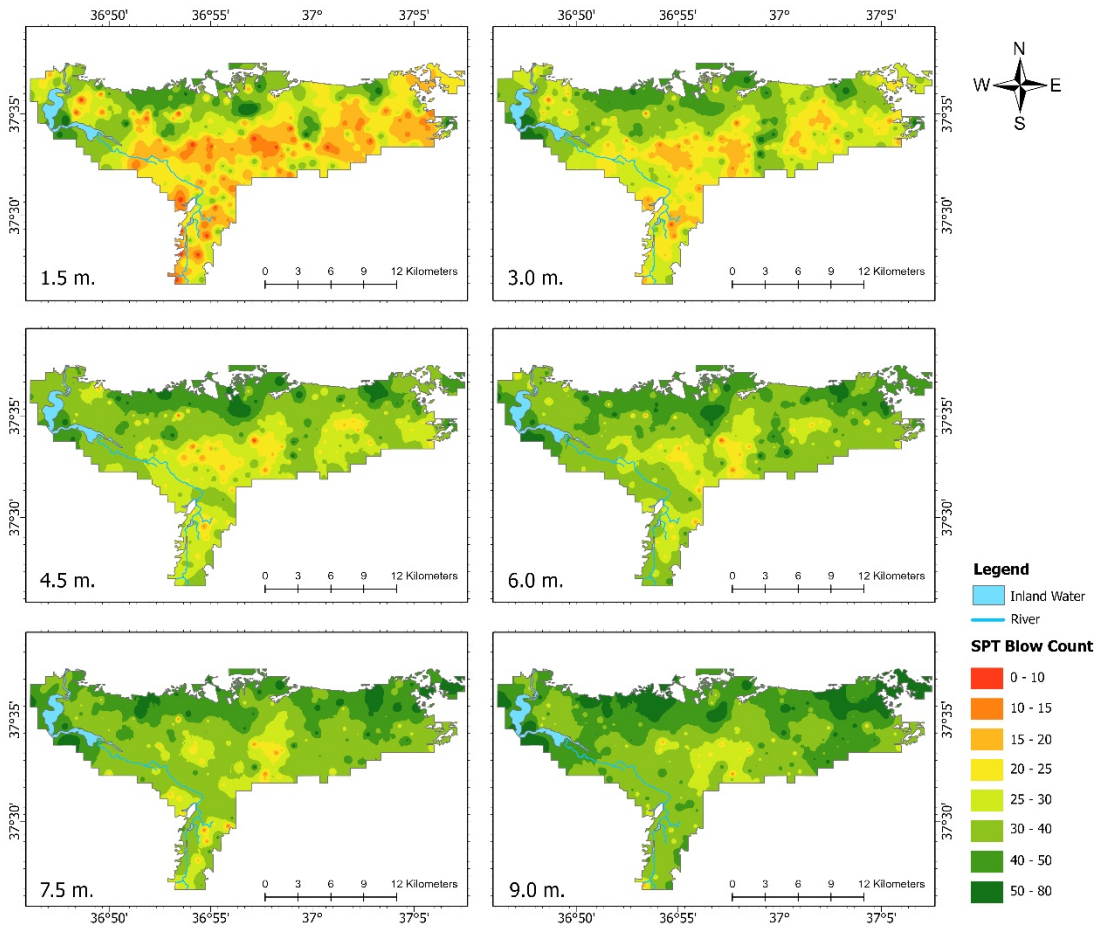


Figure 6.3: Spatial distribution of blow counts: (a) at 1.5 meters, (b) at 3.0 meters, (c) at 4.5 meters, (d) at 6.0 meters, (e) at 7.5 meters, and (f) at 9.0 meters.

Furthermore, the liquefaction susceptibility assessment for the Kahramanmaraş city center was carried out using two methods: **Youd et al. [2001]** and **Boulanger and Idriss [2014]**. A moment magnitude of Mw 7.7, corresponding to the Pazarcık earthquake, was adopted for the analysis. Additionally, as illustrated in **Figure 3.7** and described in detail in the Methodology section, acceleration values based on TBEC 2018 and **Toprak et al. [2025a]** were used. The PGA and PGV spatial point distributions shown in **Figure 6.4** were interpolated into raster datasets using the kriging tool in ArcGIS (**Figure 6.5** and **Figure 6.6**). The results of this study, together with detailed comparisons, are presented in the subsequent subsections.

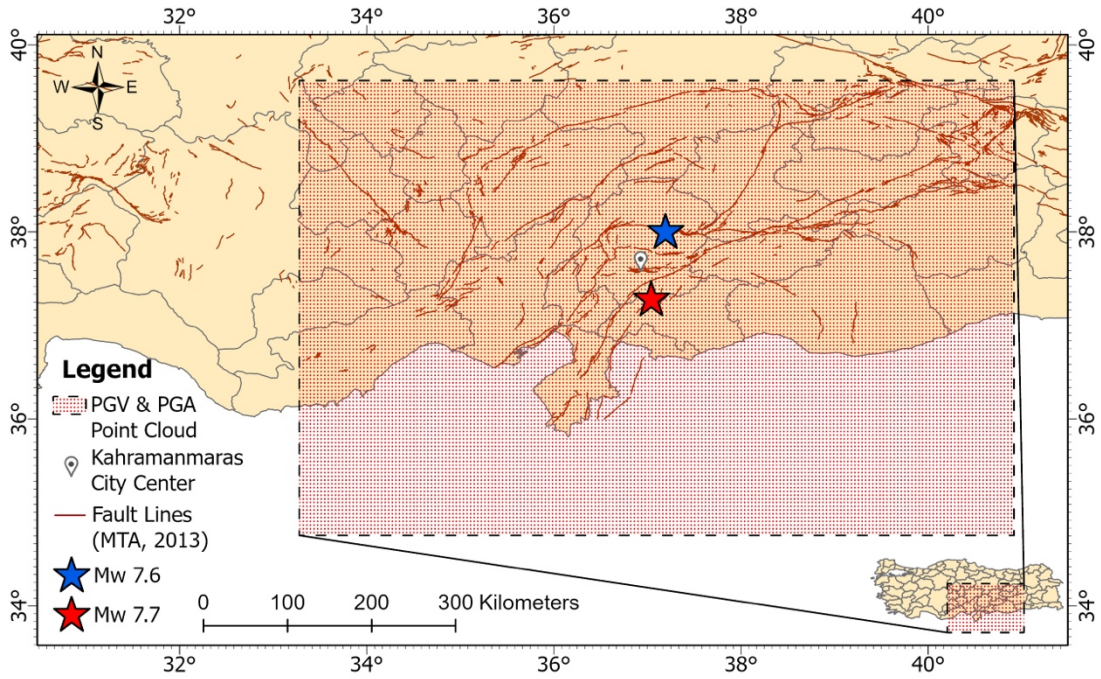


Figure 6.4: Spatial point distribution to determine PGA and PGV values from **Toprak et al. [2025a]**.

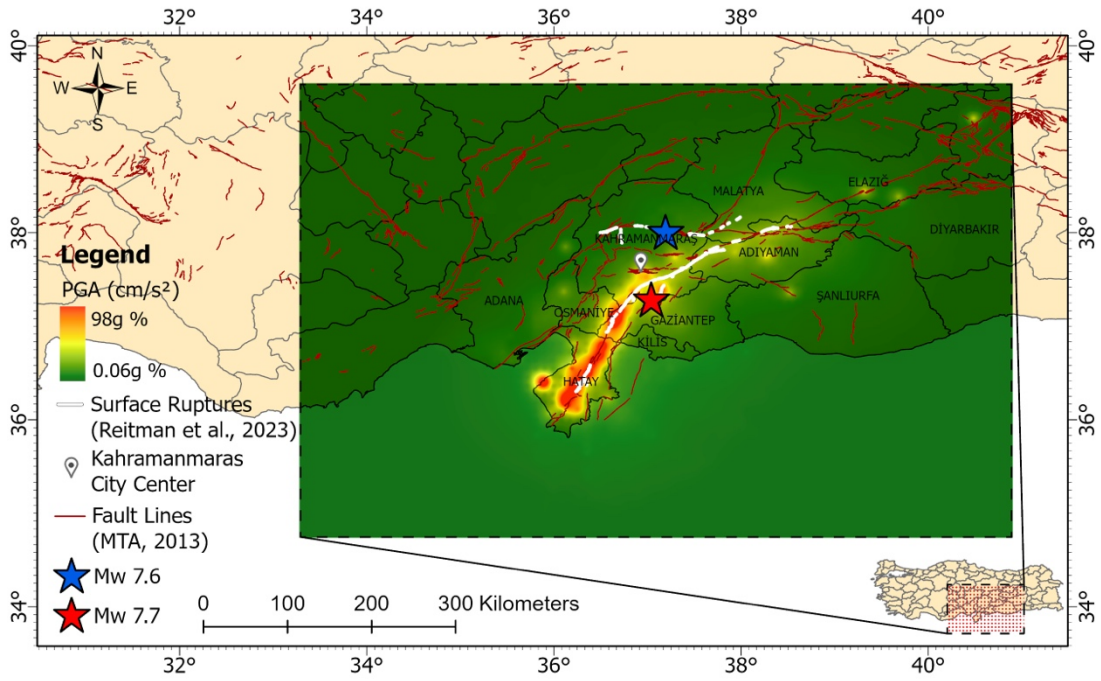


Figure 6.5: Visualization and spatial distribution map based on the PGA values from **Toprak et al. [2025a]**.

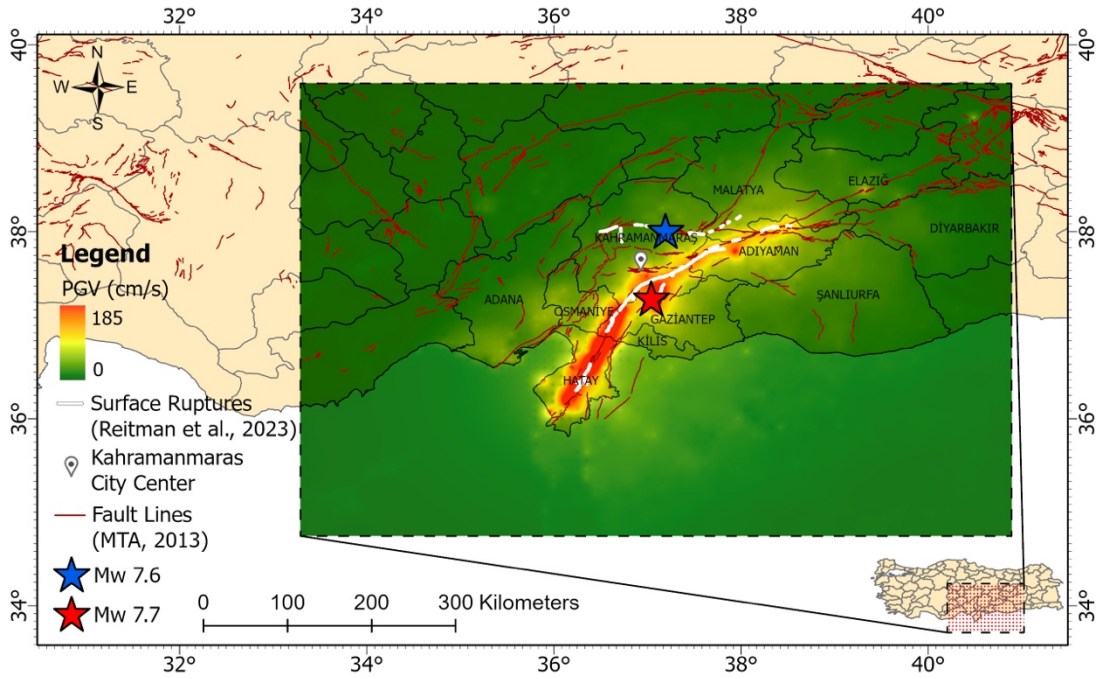


Figure 6.6: Visualization and spatial distribution map based on the PGV values from **Toprak et al. [2025a]**.

6.1. Comparison of Results Based on Different Susceptibility Methods

When the two methods are compared, the **Boulanger and Idriss [2014]** approach generally yielded lower factor of safety values in the SPT soundings conducted in the city center. As a result, the LPI, LSI and LSN maps generated using the FS values obtained from the **Boulanger and Idriss [2014]** method exhibit higher LPI, LSI and LSN values compared to those produced with the FS values from the **Youd et al. [2001]** method.

For instance, **Figure 6.8** and **Figure 6.11** present the LPI maps derived from the FS values calculated using the **Boulanger and Idriss [2014]** method, whereas **Figure 6.9** and **Figure 6.12** display the corresponding LSI maps. On the other hand, **Figure 6.14** and **Figure 6.17** show the LPI maps generated using the FS values from the **Youd et al. [2001]** method, while **Figure 6.15** and **Figure 6.18** illustrate the associated LSI maps. As an example, when **Figure 6.8** and **Figure 6.14** are compared, it can be observed that the areas classified as moderate and high are more extensive in **Figure 6.8**. This trend is also evident in the comparisons with the other figures.

6.2. Comparison of Results Based on Different PGA Sources

A comparison of the two PGA sources reveals that the acceleration values derived from the TDTH, which is based on the seismic hazard assessment defined in TBEC 2018, are generally higher than those reported by **Toprak et al. [2025a]** for the city center. These elevated acceleration levels resulted in greater cyclic stress ratios and consequently lower FS values. As a result, the LPI, LSI and LSN maps developed using the TDTH-based FS values indicate more severe liquefaction potential across the city center compared to those generated using the FS values derived from **Toprak et al. [2025a]**.

Specifically, **Figure 6.8** and **Figure 6.14** display the LPI maps generated using FS values computed from TDTH acceleration data, while **Figure 6.9** and **Figure 6.15** illustrate the corresponding LSI maps. In contrast, **Figure 6.11** and **Figure 6.17** represent the LPI maps obtained from **Toprak et al. [2025a]**, and **Figure 6.12** and **Figure 6.18** show the associated LSI results. For example, when **Figure 6.8** and **Figure 6.11** are examined, a broader extent of zones classified as moderate to high liquefaction potential is evident in **Figure 6.8**. This situation is consistently observed across the other figures as well. Furthermore, the variation in the PGA values from both sources is presented in **Figure 6.7**.

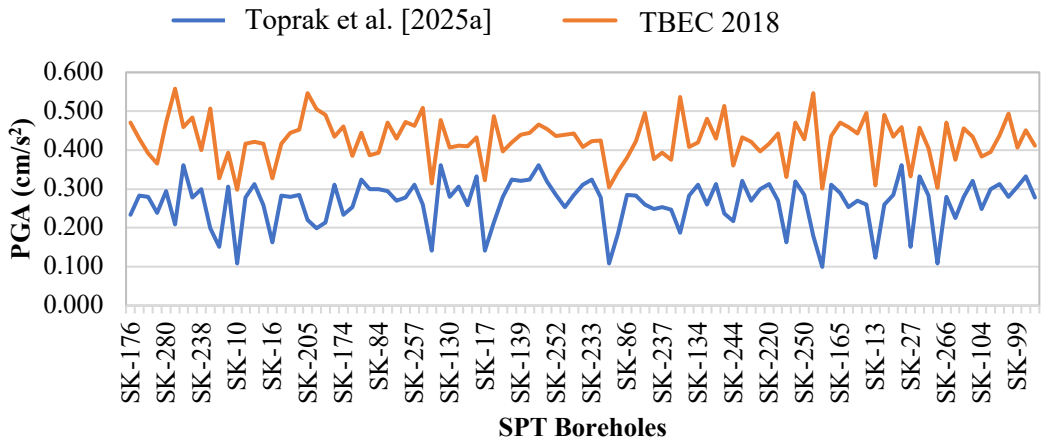


Figure 6.7: Comparison of PGA values obtained in accordance with TBEC 2018 with PGA values from **Toprak et al. [2025a]** at the borehole locations.

6.3. Comparison of Results Based on Different Susceptibility Criteria

As part of the thesis study, the liquefaction susceptibility analysis was enhanced by applying different criteria presented in **Table 3.4**. Separate LPI, LSI and LSN maps were generated and presented for four different cases: Without Criteria, **Seed et al. [2003]**, **Bray and Sancio [2006]**, and **Boulanger and Idriss [2006]**. The "Without Criteria" case, where no filtering was applied, represents a broader extent of liquefiable areas. In particular, the maps generated without applying any plasticity or grain size criteria shows a significantly wider distribution of high LPI, LSI and LSN values, indicating a possible overestimation of risk in regions with fine-grained soils. This is followed by the application of the **Bray and Sancio [2006]** criterion. Finally, **Seed et al. [2003]** and **Boulanger and Idriss [2006]** produced similar results. This similarity is likely to be due to the absence of LL, PL, PI, or water content data in some boreholes, which results in no filtering being applied in those locations.

6.4. Comparison of LPI, LSI and LSN Results

When the LPI and LSI results are compared, it is observed that LSI provides a more refined color classification due to having a greater number of defined susceptibility classes. In some areas, zones categorized as “Low” in the LPI maps were classified as “Very Low” in the LSI maps. Similarly, locations labeled as “Moderate” in LPI were identified as “Low” in LSI. However, the overall spatial distribution and concentration of susceptible zones remained consistent across both mapping approaches.

On the other hand, when LSN maps are compared with LPI and LSI, they are generally consistent with the regions identified as having liquefaction risk. However, since the LSN maps are classified into "No Risk", "Very Low", "Low", "Moderate", "High", "Very High", and "Severe", they provide a more detailed representation, especially in transitional zones. In general, the LSN maps indicate "No Risk" in the city center, while in localized areas the classification ranges from "Low" to "Severe".

A detailed comparison of the LPI, LSI and LSN results based on the combination of applied criteria, PGA source, and selected method is presented in **Figure 6.20**, **Figure 6.21** and **Figure 6.22**, respectively.

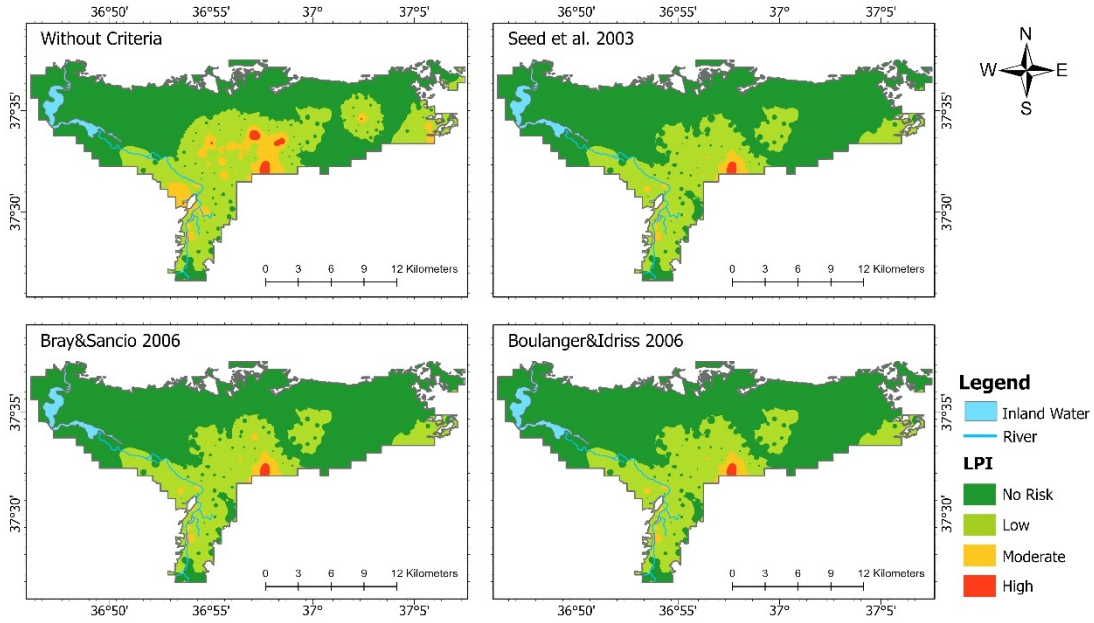


Figure 6.8: LPI map calculated using the **Boulanger and Idriss [2014]** method for factor of safety estimation, with input PGA based on TBEC 2018.

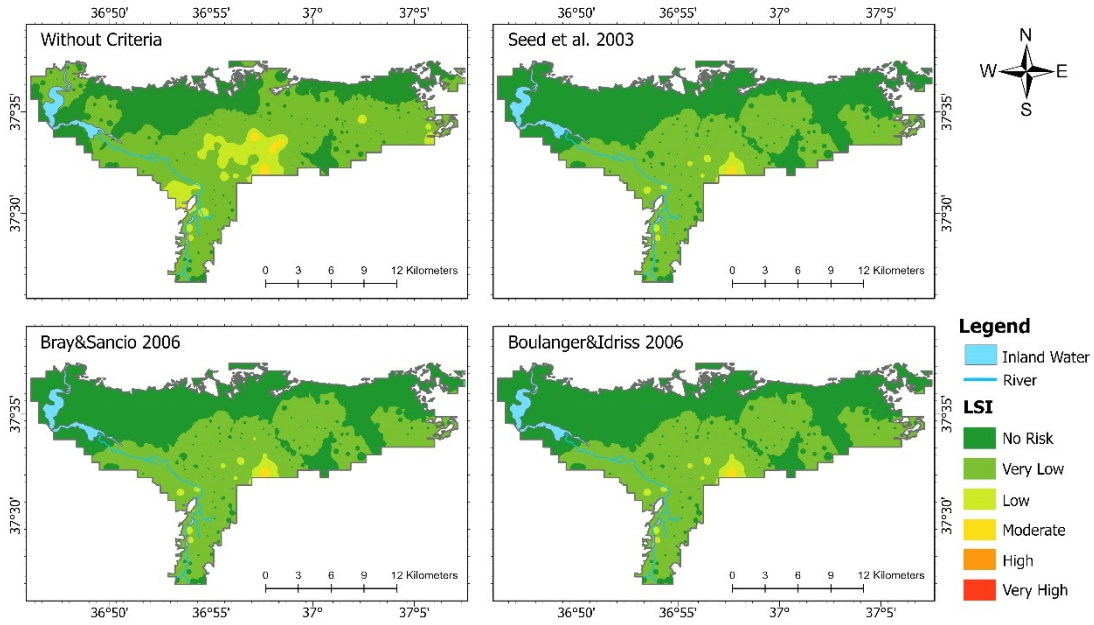


Figure 6.9: LSI map calculated using the **Boulanger and Idriss [2014]** method for factor of safety estimation, with input PGA based on TBEC 2018.

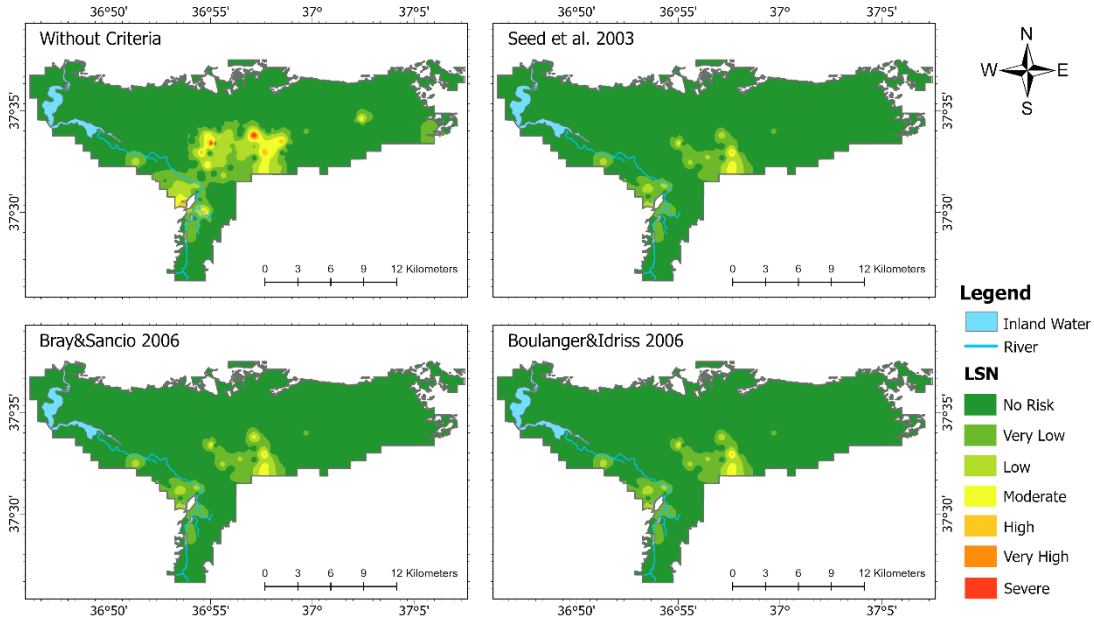


Figure 6.10: LSN map calculated using the **Boulanger and Idriss [2014]** method for factor of safety estimation, with input PGA based on TBEC 2018.

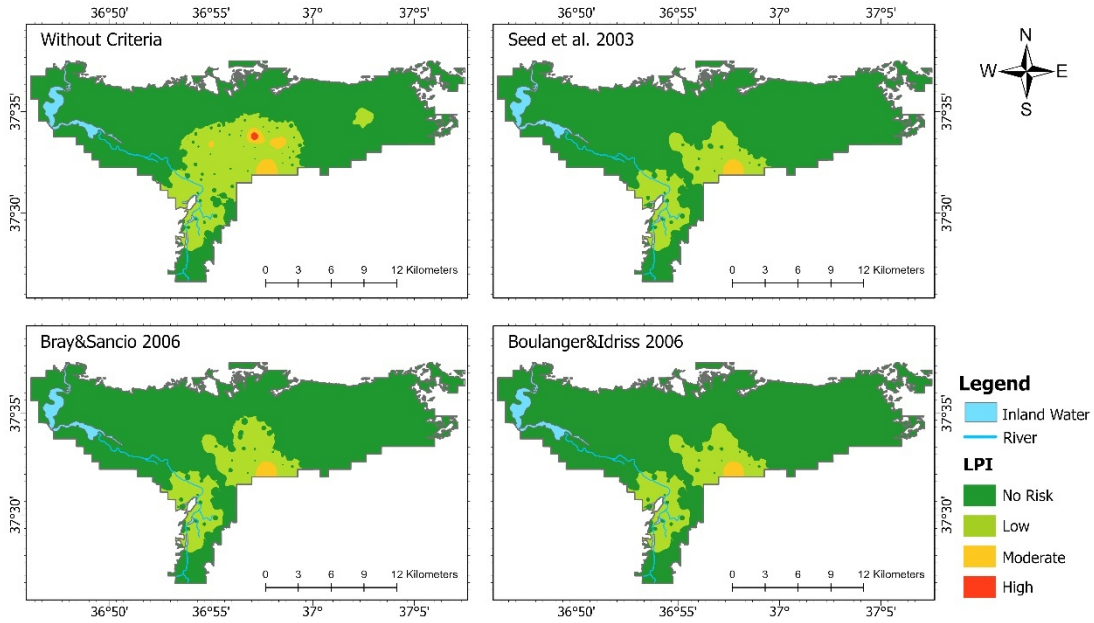


Figure 6.11: LPI map calculated using the **Boulanger and Idriss [2014]** method for factor of safety estimation, with input ground motion from **Toprak et al. [2025a]**.

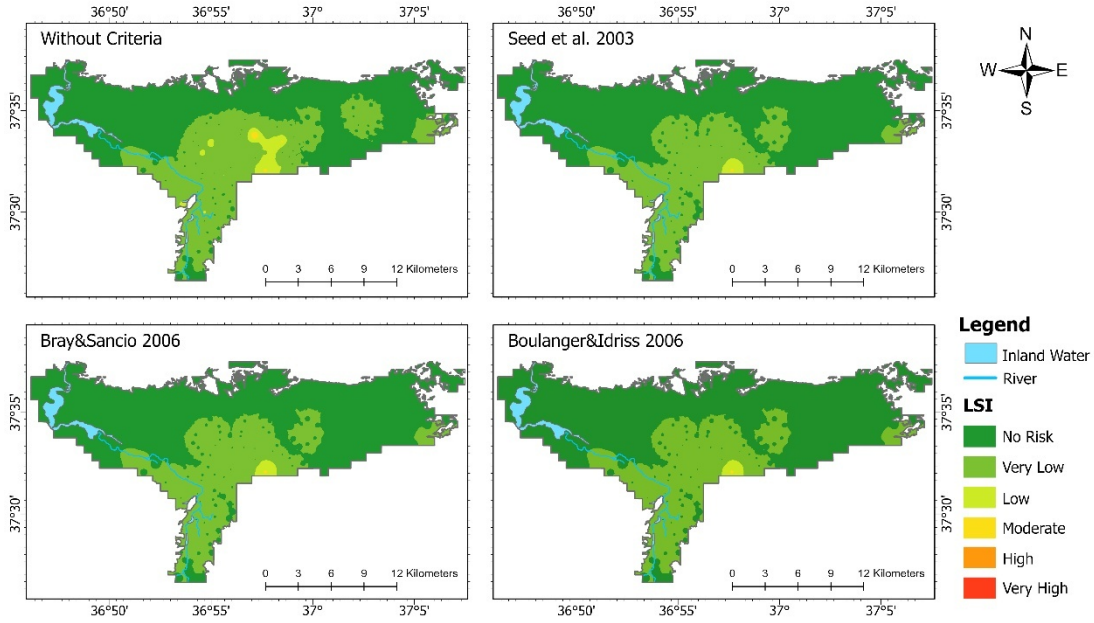


Figure 6.12: LSI map calculated using the **Boulanger and Idriss [2014]** method for factor of safety estimation, with input ground motion from **Toprak et al. [2025a]**.

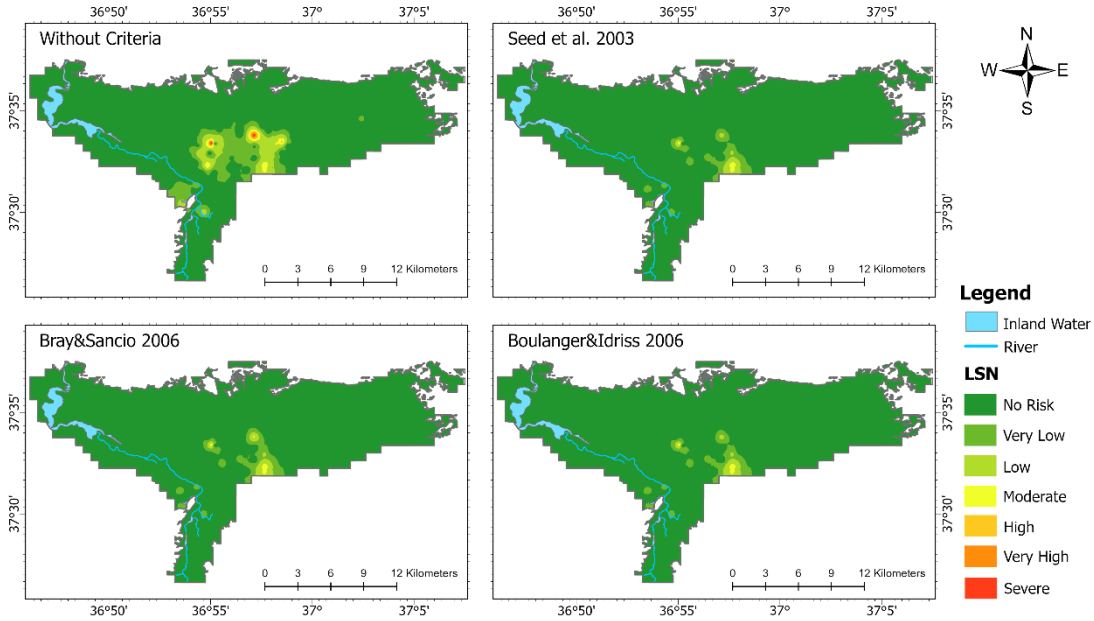


Figure 6.13: LSN map calculated using the **Boulanger and Idriss [2014]** method for factor of safety estimation, with input ground motion from **Toprak et al. [2025a]**.

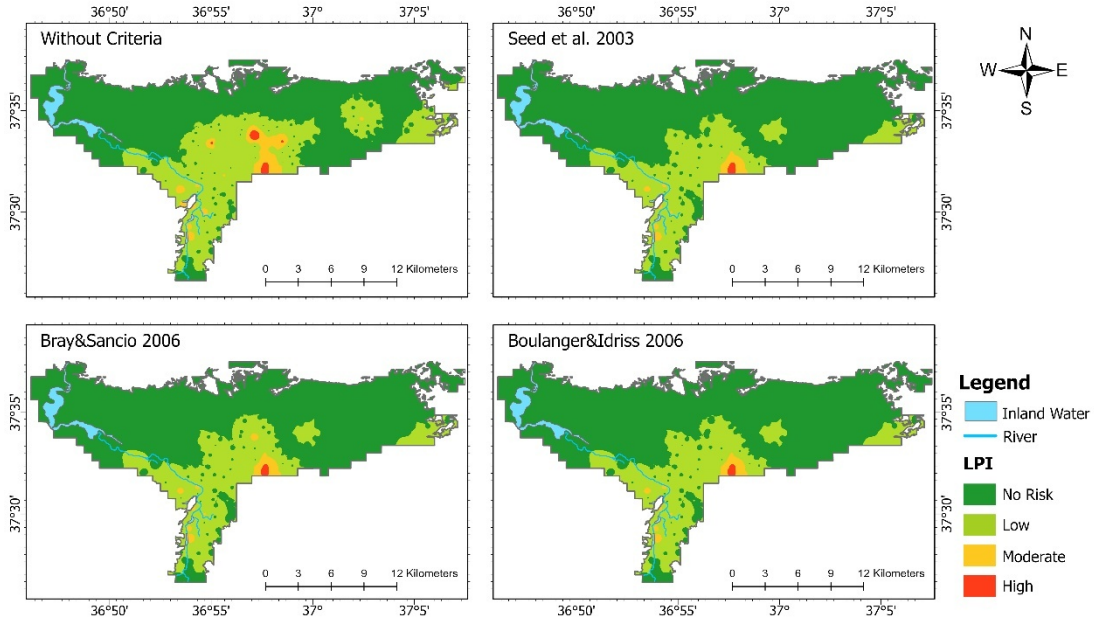


Figure 6.14: LPI map calculated using the **Youd et al. [2001]** method for factor of safety estimation, with input PGA based on TBEC 2018.

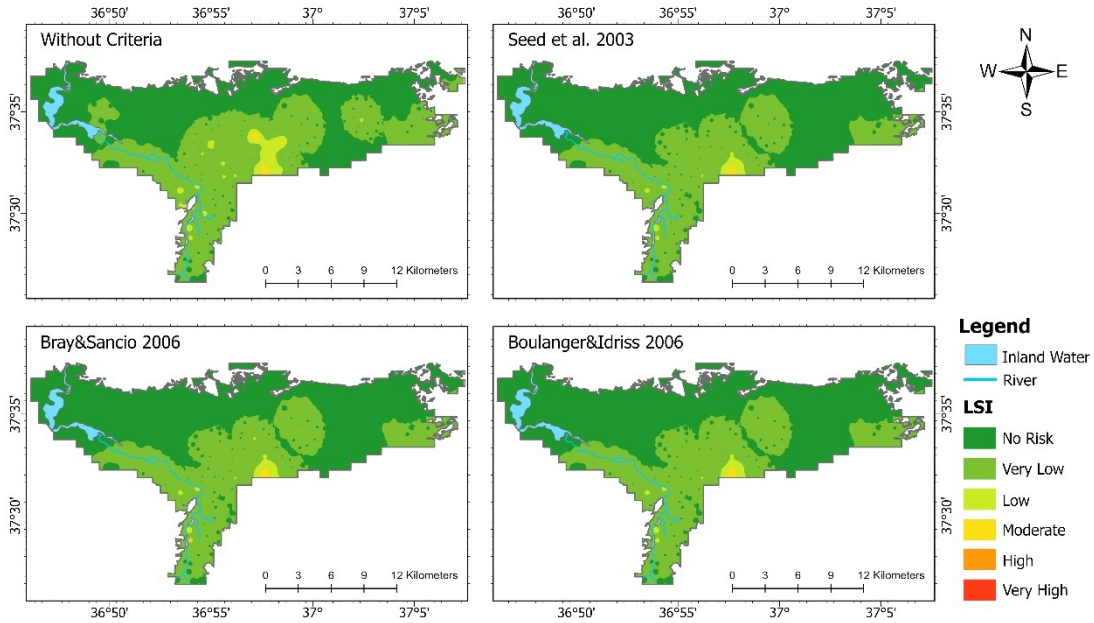


Figure 6.15: LSI map calculated using the **Youd et al. [2001]** method for factor of safety estimation, with input PGA based on TBEC 2018.

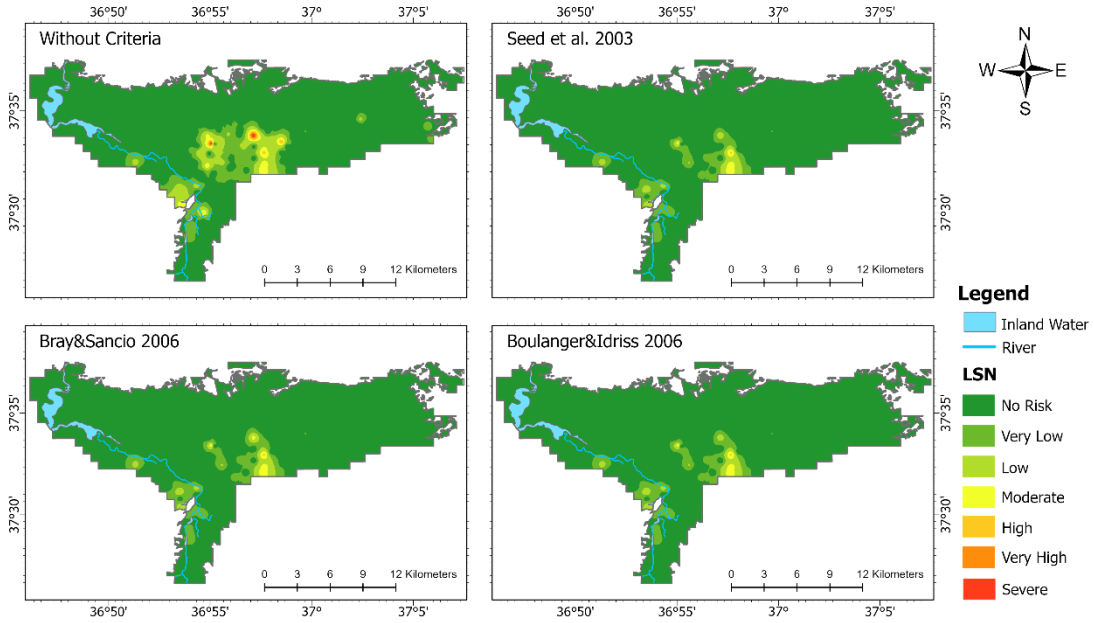


Figure 6.16: LSN map calculated using the **Youd et al. [2001]** method for factor of safety estimation, with input PGA based on TBEC 2018.

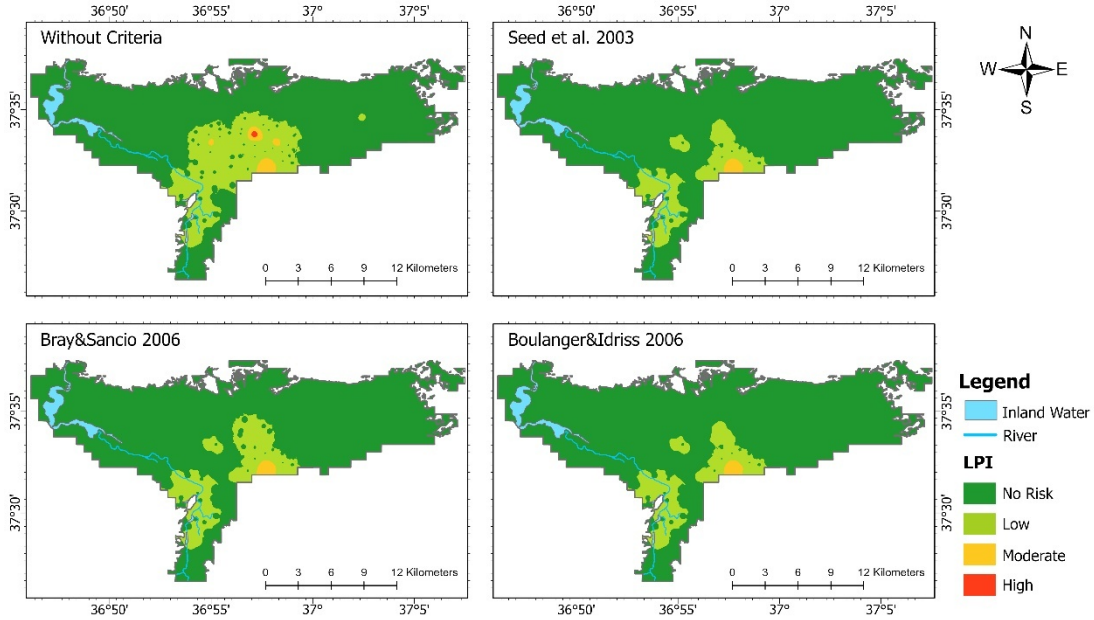


Figure 6.17: LPI map calculated using the **Youd et al. [2001]** method for factor of safety estimation, with input ground motion from **Toprak et al. [2025a]**.

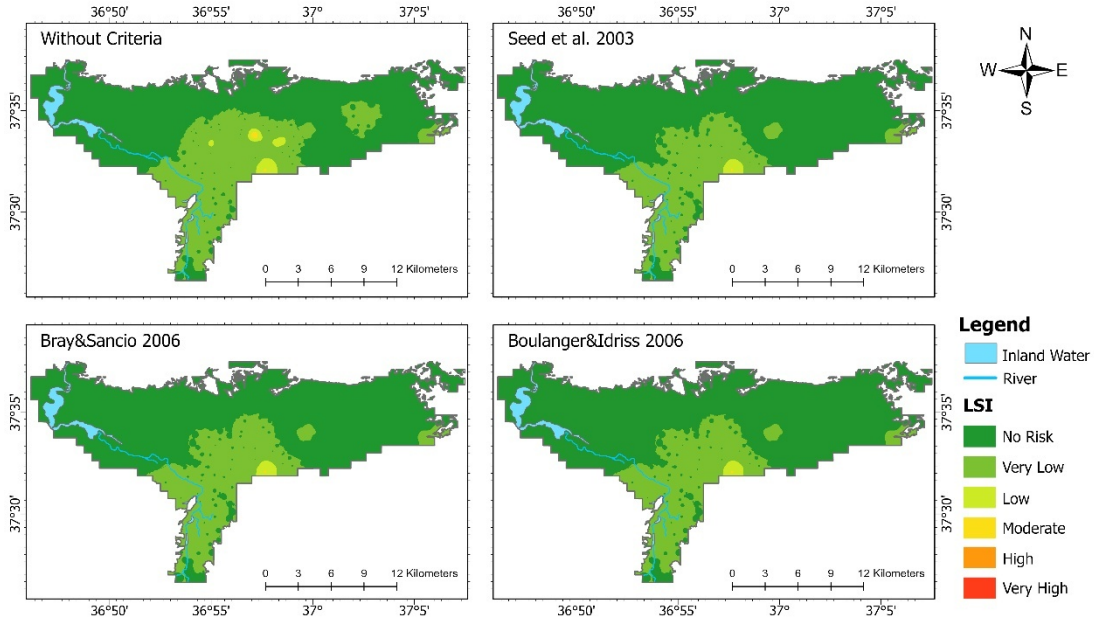


Figure 6.18: LSI map calculated using the **Youd et al. [2001]** method for factor of safety estimation, with input ground motion from **Toprak et al. [2025a]**.

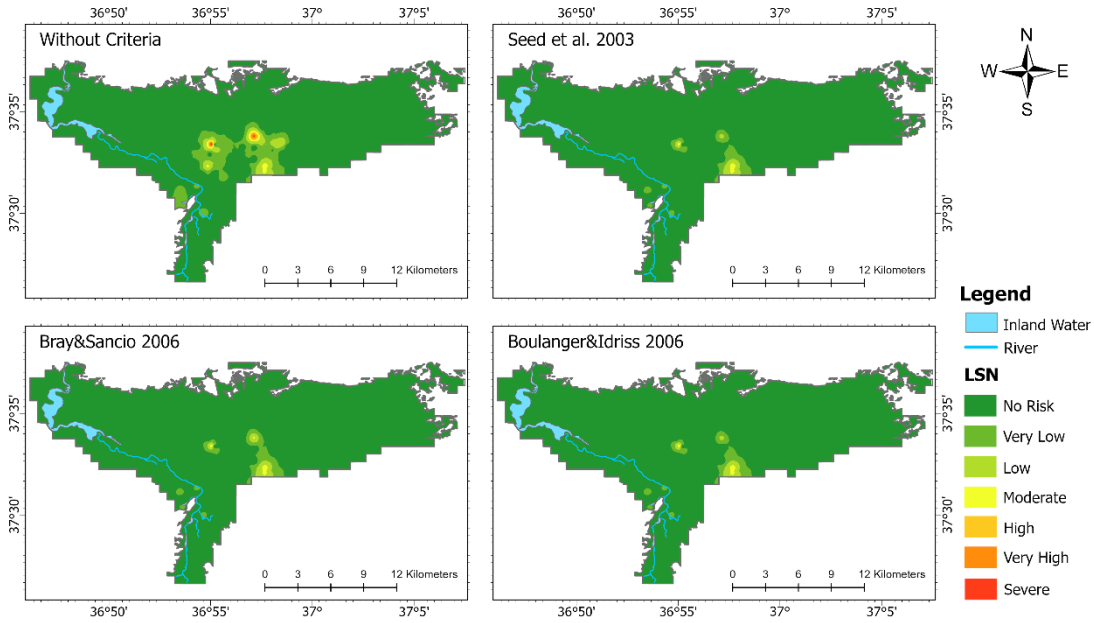


Figure 6.19: LSN map calculated using the **Youd et al. [2001]** method for factor of safety estimation, with input ground motion from **Toprak et al. [2025a]**.

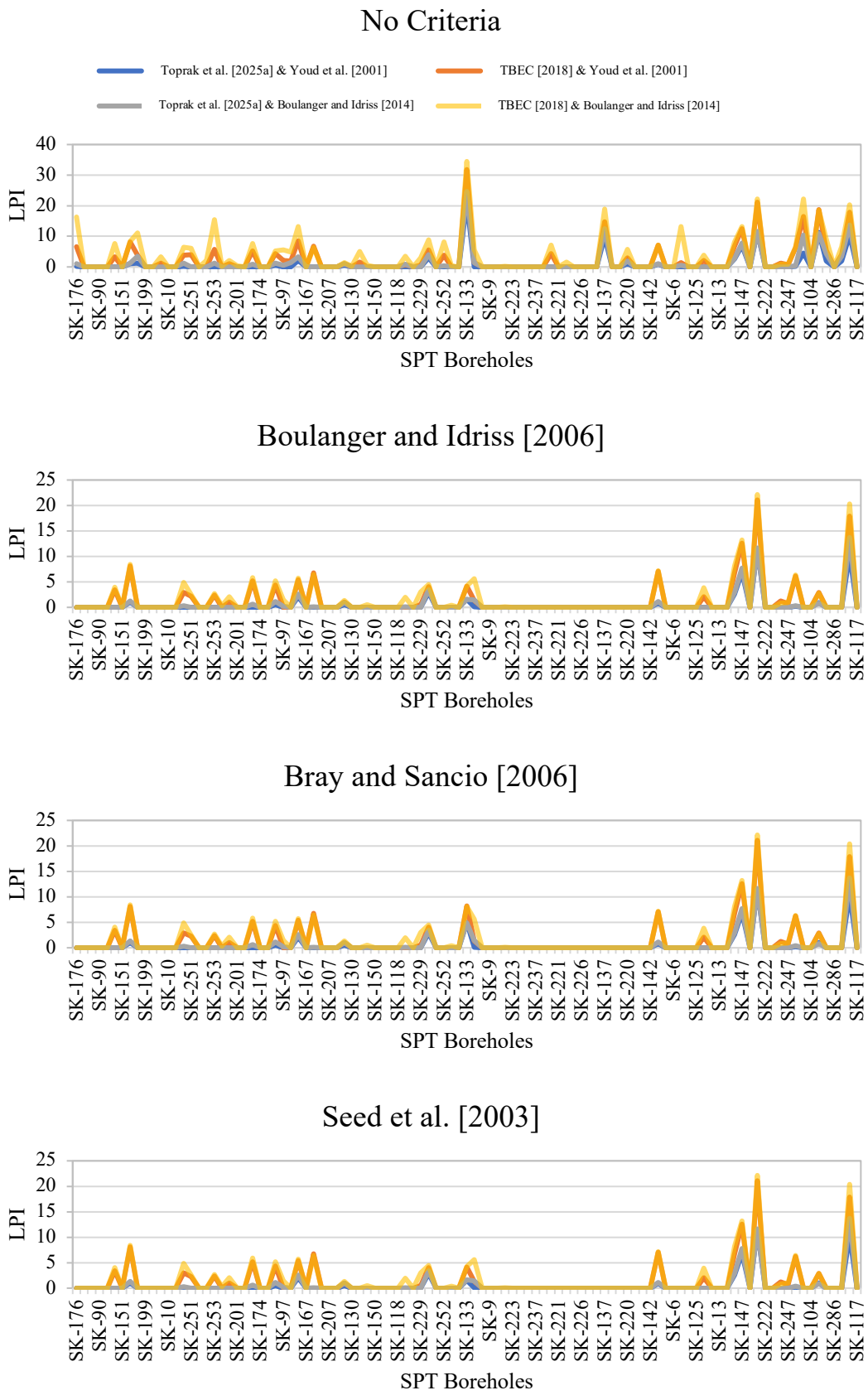


Figure 6.20: Comparison graph of calculated LPI values: (a) No Criteria, (b) **Boulanger and Idriss [2006]**, (c) **Bray and Sancio [2006]**, and (d) **Seed et al. [2003]**.

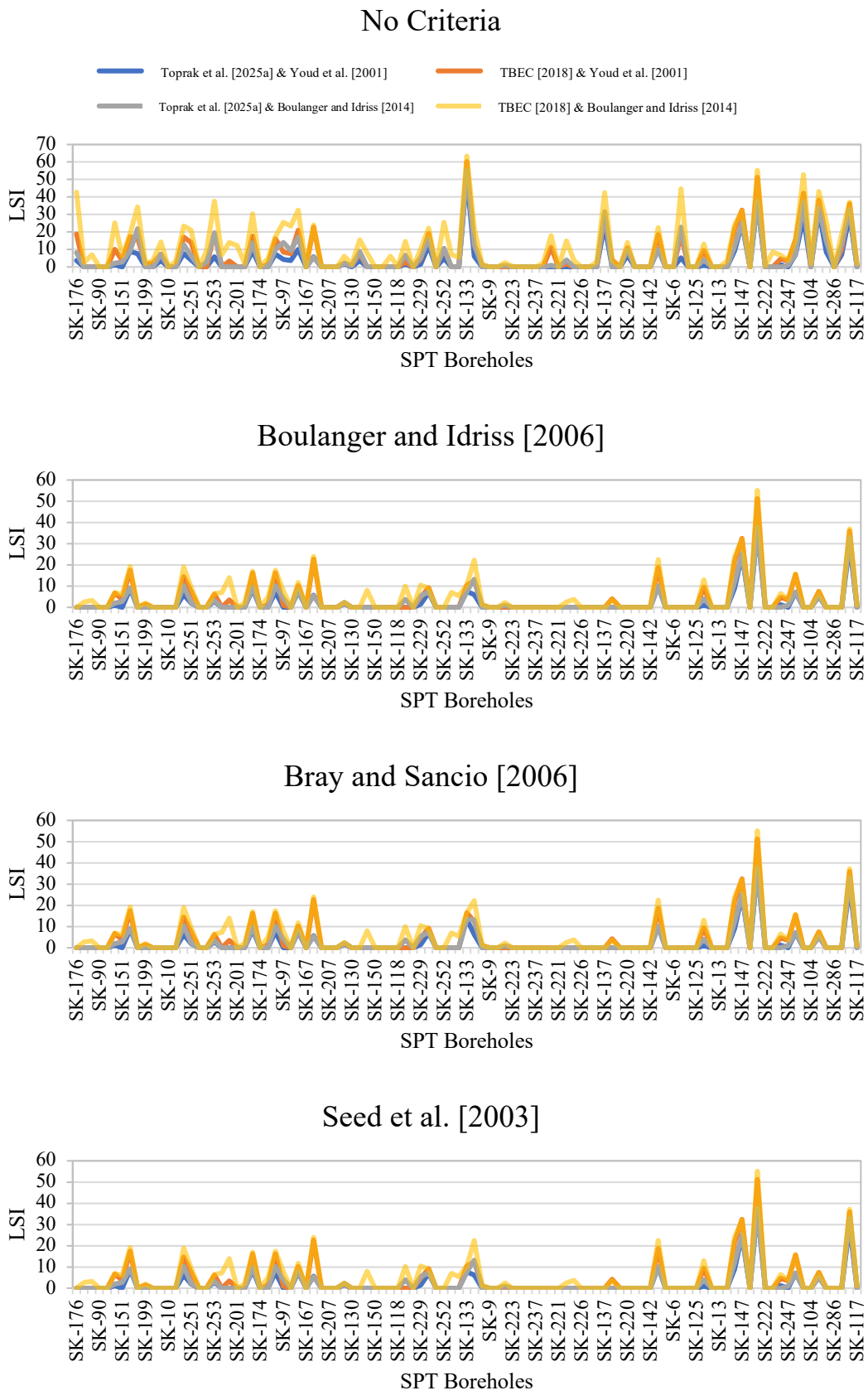


Figure 6.21: Comparison graph of calculated LSI values: (a) No Criteria, (b) **Boulanger and Idriss [2006]**, (c) **Bray and Sancio [2006]**, and (d) **Seed et al. [2003]**.

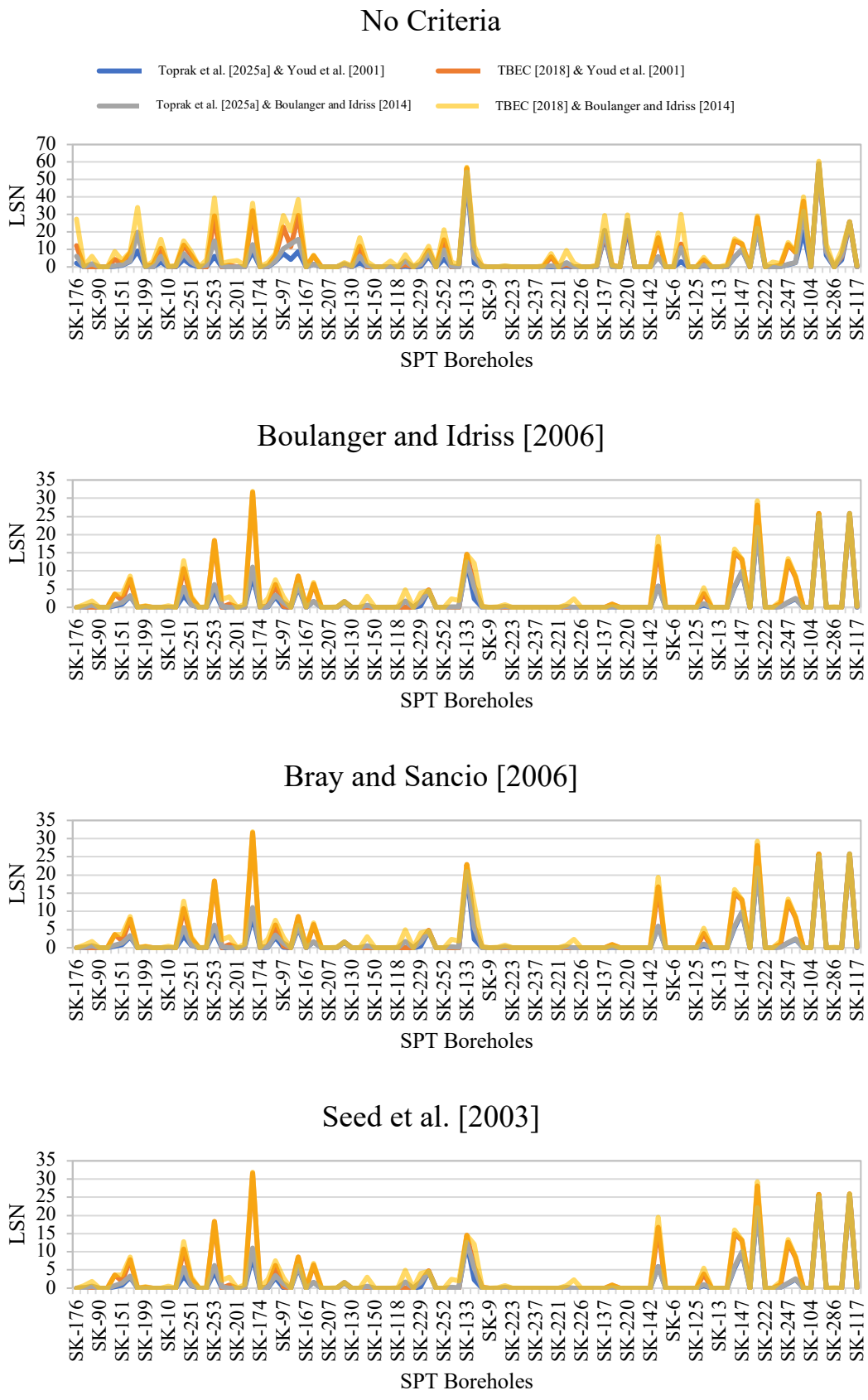


Figure 6.22: Comparison graph of calculated LSN values: (a) No Criteria, (b) **Boulanger and Idriss [2006]**, (c) **Bray and Sancio [2006]**, and (d) **Seed et al. [2003]**.

Although LPI, LSI, and LSN maps indicate liquefaction susceptibility in relatively localized areas, discussions with KASKI and municipality authorities, as well as field visits, confirmed that no liquefaction manifestation were observed in the city center. Therefore, the boundary curves proposed by **Ishihara [1985]** were applied to verify the absence of liquefaction manifestations, and the critical layers within the localized areas were plotted (**Figure 6.23**). The figure shows that the critical layers are relatively deep and remain below the boundary curves. Nevertheless, only one point fall within the zone where surface manifestation would be expected. For this location, post-earthquake satellite imagery was examined, and no indications of liquefaction manifestation were found.

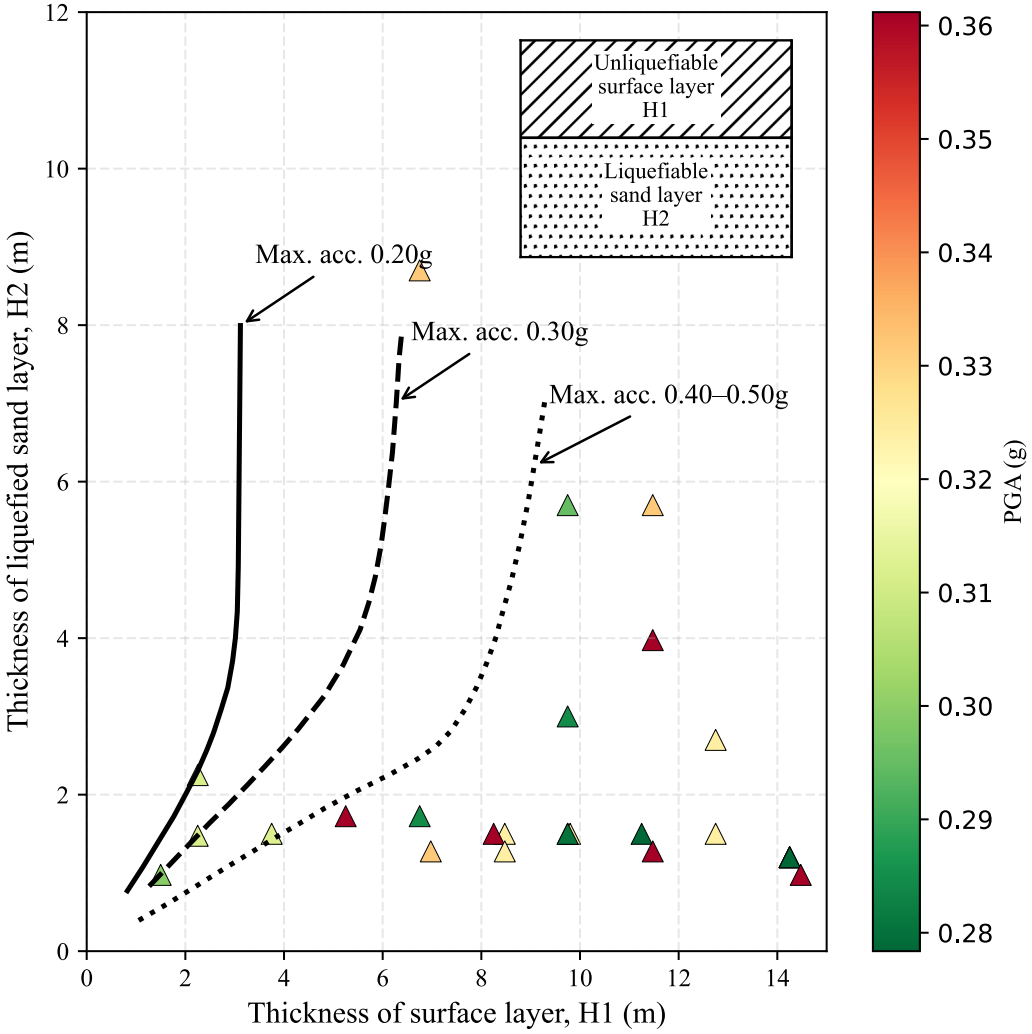


Figure 6.23: Critical layer conditions assessed with the boundary curves of **Ishihara [1985]**.

7. WATER INFRASTRUCTURE DAMAGE ASSESSMENT OF KAHRAMANMARAŞ CITY CENTER

Since no evidence of permanent ground deformation was observed in the city center and as discussed in the previous section, the area was not found to be susceptible to liquefaction. Therefore, pipeline damages were attributed to transient ground deformations. In this context, ground motion parameters for the 2023 Kahramanmaraş earthquakes, as reported by **Toprak et al. [2025a]**, were employed.

Following the filtering process applied to the damage call records as explained in Chapter 3.1, unique ID numbers were assigned to each call record. These ID numbers made it easier to track which damage information was being processed and to manage the entry of location data. For each call, the address details were manually searched using Google Maps and Yandex Maps, and their locations were marked as pins along the corresponding streets in Google Earth. The resulting dataset was then exported as a KMZ file and imported into ArcGIS Pro for further spatial analysis and mapping. To perform the analyses, the nearest coordinates of the damage points on the pipeline network and their shortest distance to the pipelines were first calculated using the Near tool. The resulting layer was exported as an Excel file, and a distance threshold of 10 meters was applied to ensure that damage points were not incorrectly associated with unrelated pipelines. This threshold was set because a small number of pipelines could not be digitized in areas where scanned infrastructure maps were unavailable. As a result, the total number of records decreased from 5,496 to 5,187. Subsequently, the coordinates of the damage points were transferred onto the pipeline network within the GIS system, ensuring that all damage points were precisely located on the pipelines for subsequent spatial analysis. Finally, the Spatial Join tool was used to transfer the pipeline attribute data, such as pipe material type, to the damage points. In addition, the PGV values from the PGV raster (**Figure 6.6**) were extracted and assigned to the damage points to enable analyses considering seismic ground motion intensity. This step enabled the identification of which types of pipelines were associated with the reported damages and the assessment of damage distribution with respect to PGV

levels. **Figure 7.1** shows the locations of damage points on the pipeline network after processing.

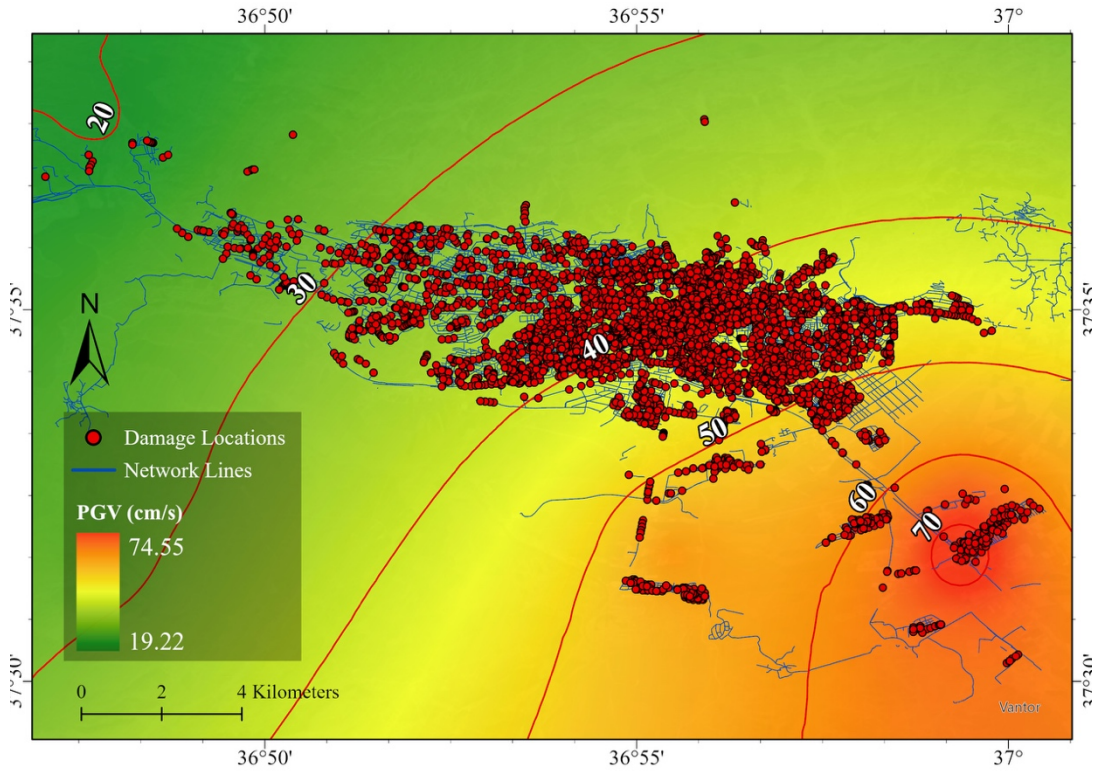


Figure 7.1: Spatial distribution of damage points on the pipeline network.

Furthermore, the distribution of damages across different pipeline materials was identified. The analysis revealed that 53% of the reported damages occurred in PE pipelines, followed by CI (21%), AC (14%), and PVC (12%). To assess the overall system performance, the repair rates for each material type were calculated and are presented in **Table 7.1**.

Table 7.1: Repair rates calculated for different pipeline material types to assess the overall system performance.

Pipe Material Type	Number of Damages	Pipeline Length (km)	Repair Rate (repairs/km)
AC	711	208.38	3.41
PE	2,752	1,816.68	1.51
CI	1,092	158.87	6.87
PVC	632	221.74	2.85
Total	5,187	2,405.67	2.16

Although PE pipelines had the highest number of damage cases, they exhibited the lowest repair rate (1.51) due to the extensive total length of PE pipelines in the network. In contrast, CI pipelines showed a significantly higher repair rate (6.87), indicating their greater susceptibility to damage despite representing a smaller portion of the network. AC pipelines had a repair rate of 3.41, while PVC pipelines exhibited a slightly lower rate of 2.85, both of which reflect moderate levels of vulnerability compared to PE and CI pipelines. Lastly, the system's repair rate was calculated as 2.16, providing a general measure of the network's performance.

The relationship between pipeline damages and the ground motion parameter PGV was examined further in detail. The PGV raster was first processed using the Int tool to convert floating-point values into integer classes. This step allowed the classification of PGV data and prepared it for conversion to polygon features. The integer raster was then converted into polygon features using the Raster to Polygon tool. Subsequently, PGV values were assigned to the pipeline system with the Intersect tool, allowing each pipeline segment to be associated with its corresponding PGV class. In the attribute table, a new field was created, and the length of each pipeline segment was calculated using the Calculate Geometry tool. Based on these values, the total lengths of pipelines within 5 cm/s PGV intervals were determined (**Table 7.2**). In addition, damage points were also classified according to these PGV ranges to analyze the distribution of damages with respect to ground motion intensity (**Table 7.3**).

Table 7.2: Total lengths of pipelines within each PGV interval.

PGV (cm/s)	AC	PE	CI	PVC	Total
20-25		156.90		25.72	182.61
25-30		197.51		43.57	241.08
30-35	23.27	327.87		12.00	363.13
35-40	62.87	316.38	78.49	33.86	491.61
40-45	88.21	257.10	57.29	34.40	436.99
45-50	34.03	224.39	10.08	12.06	280.56
50-55		85.01	13.02	14.54	112.57
55-60		58.87		21.70	80.57
60-65		104.35		8.33	112.68
65-70		56.76		6.97	63.74
70-75		28.47		8.59	37.06
75-80		3.07			3.07
Total	208.38	1,816.68	158.87	221.74	2,405.67

Table 7.3: Number of pipeline damages classified by PGV intervals.

PGV (cm/s)	AC	PE	CI	PVC	Total
20-25		20			20
25-30		98			98
30-35	45	386		16	447
35-40	211	734	468	120	1,533
40-45	303	698	513	134	1,648
45-50	152	641	46	52	891
50-55		107	65	69	241
55-60		24		102	126
60-65		21		45	66
65-70		14		44	58
70-75		9		50	59
Total	711	2,752	1,092	632	5,187

Repair rates for AC pipelines were evaluated across PGV classes to investigate the influence of ground motion intensity on damage occurrence. Damage was identified exclusively within the 30–50 cm/s PGV interval, as no AC pipelines existed in lower or higher PGV ranges. Within this range, repair rates increased notably, starting at 1.93 in the 30–35 cm/s class and rising to 3.36 and 4.47 in the 35–40 cm/s and 45–50 cm/s intervals, respectively (**Table 7.4**). The regression analysis showed a strong linear relationship between PGV and repair rates for AC pipelines (R^2 = 0.9071), as illustrated in **Figure 7.2**.

Table 7.4: PGV classes and corresponding repair rates for AC pipelines.

PGV (cm/s)	Number of Damages	Pipeline Length (km)	Repair Rate (repairs/km)
30-35	45	23.27	1.93
35-40	211	62.87	3.36
40-45	303	88.21	3.44
45-50	152	34.03	4.47

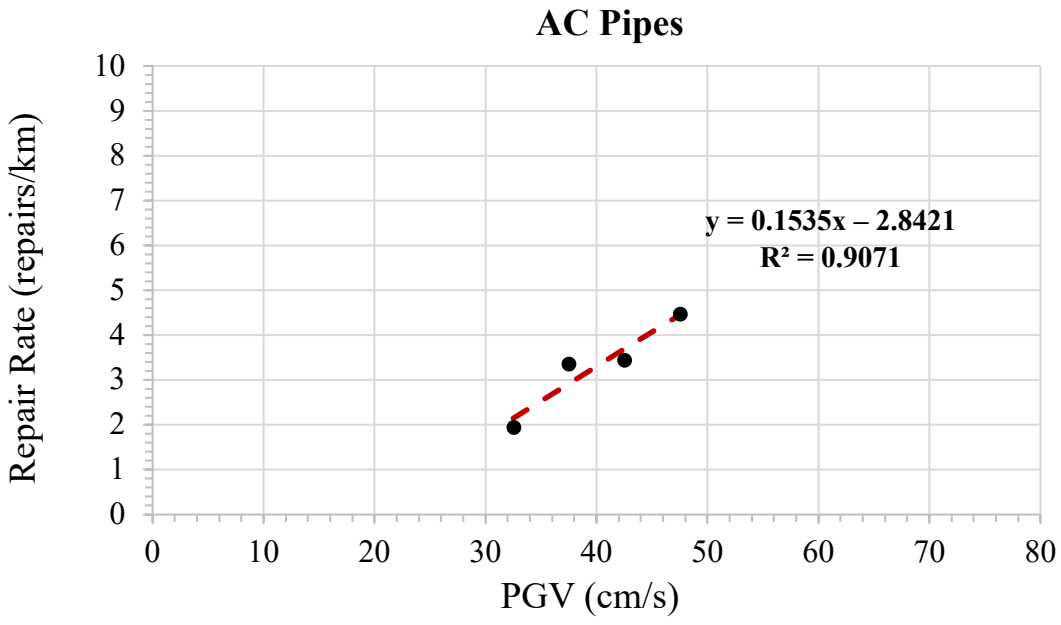


Figure 7.2: Relationship between PGV and repair rate for AC pipelines.

The analysis of PVC pipelines revealed that damage cases were distributed across a broad PGV range, with repair rates increasing progressively with ground motion intensity. Repair rates were not observed below 30 cm/s due to the absence of observed

damages in PVC pipelines in this range. The rates began at 1.33 repairs/km in the 30–45 cm/s interval and peaked at 6.31 repairs/km in the 65–70 cm/s interval (**Table 7.5**). The regression analysis supported this trend, showing a strong positive linear relationship between PGV and repair rates with a coefficient of determination of R^2 = 0.8491 (**Figure 7.3**).

Table 7.5: PGV classes and corresponding repair rates for PVC pipelines.

PGV (cm/s)	Number of Damages	Pipeline Length (km)	Repair Rate (repairs/km)
30-35	16	12.00	1.33
35-40	120	33.86	3.54
40-45	134	34.40	3.90
45-50	52	12.06	4.31
50-55	69	14.54	4.74
55-60	102	21.70	4.70
60-65	45	8.33	5.40
65-70	44	6.97	6.31
70-75	50	8.59	5.82

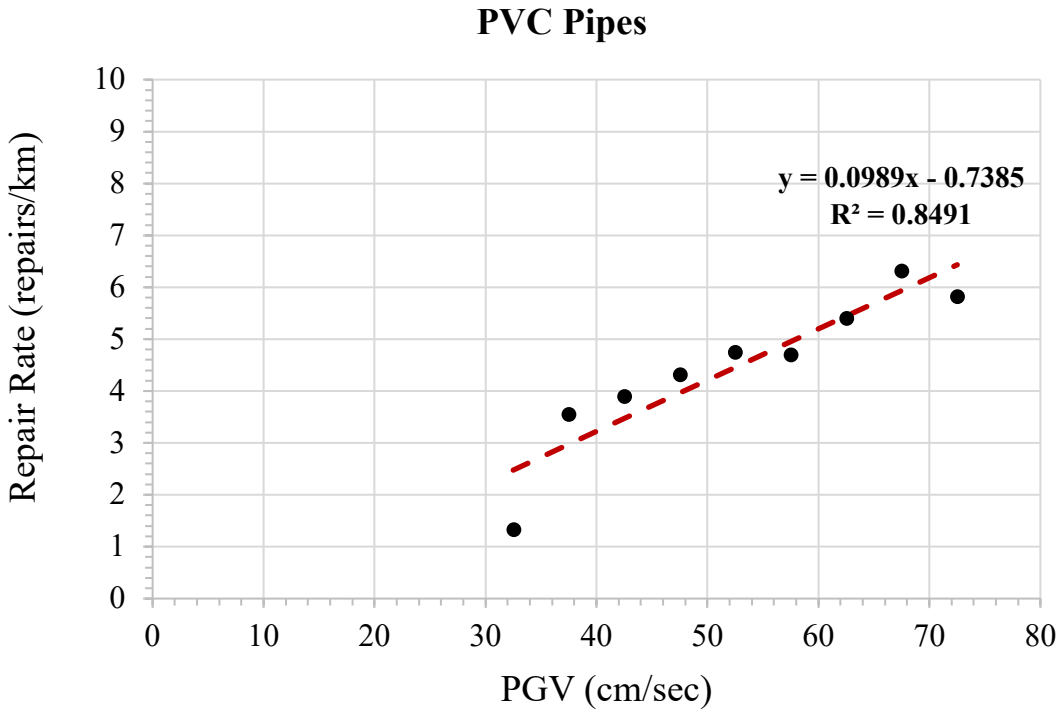


Figure 7.3: Relationship between PGV and repair rate for PVC pipelines.

In PE pipelines, repair rates were relatively low at lower PGV levels but showed a consistent increase as ground motion intensity rose. The repair rate began at 0.13 repairs/km in the 20–25 cm/s interval and reached its peak of 2.71 repairs/km in the 40–45 cm/s interval, before showing a slight decline to 2.42 repairs/km in the 45–55 cm/s range (**Table 7.6**). The regression analysis demonstrated a positive linear relationship between PGV and repair rates for PE pipelines, supported by a coefficient of determination of $R^2 = 0.8385$ (**Figure 7.4**).

Table 7.6: PGV classes and corresponding repair rates for PE pipelines.

PGV (cm/s)	Number of Damages	Pipeline Length (km)	Repair Rate (repairs/km)
20-25	20	156.90	0.13
25-30	98	197.51	0.50
30-35	386	327.87	1.18
35-40	734	316.38	2.32
40-45	698	257.10	2.71
45-55	748	309.40	2.42

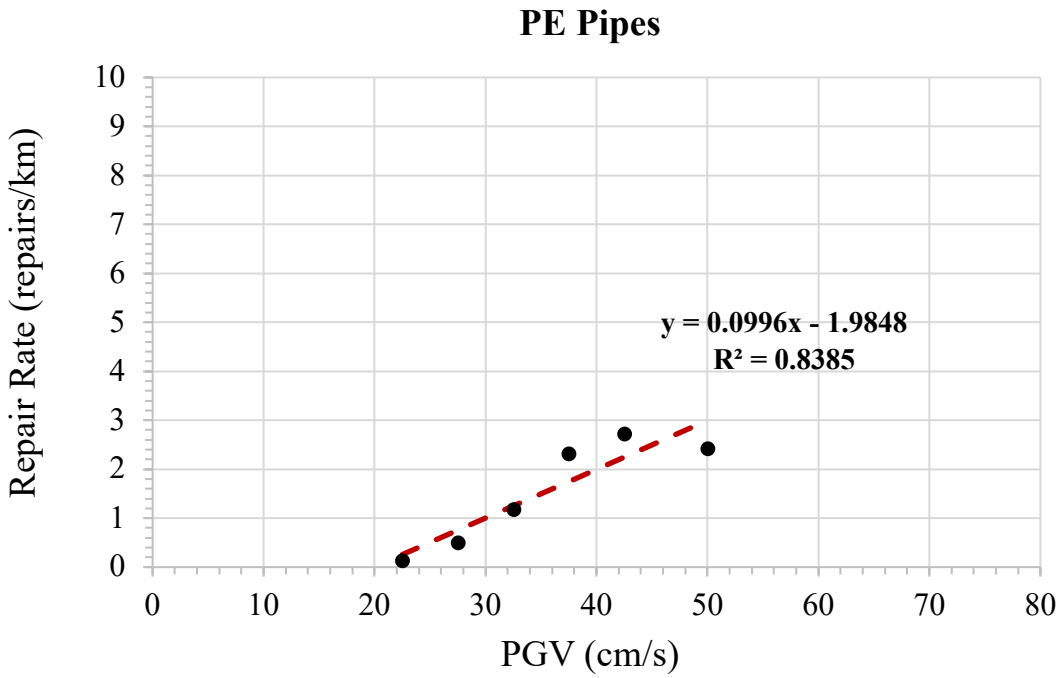


Figure 7.4: Relationship between PGV and repair rate for PE pipelines.

Further comparison for AC pipelines was made using the empirical equations proposed by **O'Rourke et al. [2014]**, which were developed from post-earthquake observations in Christchurch, New Zealand. It should be noted that the relationships proposed by **O'Rourke et al. [2014]** are based on the geometric mean of horizontal PGV components. In addition, the results were compared with the **ALA [2001]** and **HAZUS** correlations for brittle pipe systems (**Figure 7.5**). **HAZUS** adopts the damage correlation developed by **O'Rourke and Ayala [1993]** as part of its default analysis; accordingly, this correlation is referred to herein as the **HAZUS** relationship.

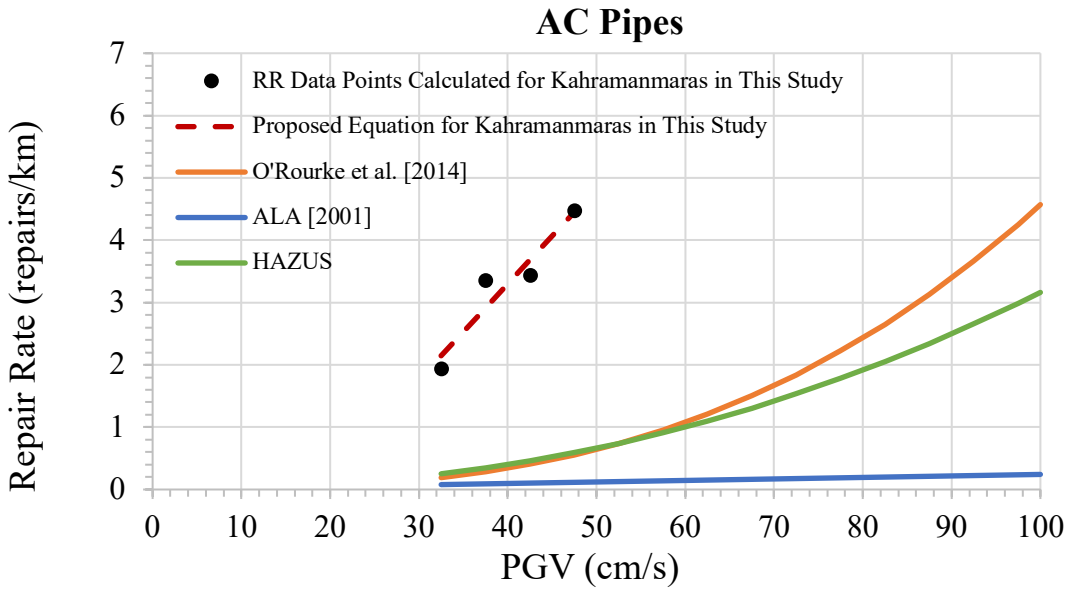


Figure 7.5: Comparison of RR–PGV relationships for AC pipes between this study and the empirical models proposed in the literature.

As shown in **Figure 7.5**, the RR values obtained for Kahramanmaraş are clearly higher than those proposed for Christchurch, despite the fact that PGV levels in Christchurch were generally higher. This suggests that the elevated RR values in Kahramanmaraş are not solely due to ground motion intensity but are also strongly influenced by the condition of the local water infrastructure. In Kahramanmaraş, a large portion of the AC pipes were installed in the 1960s and have not been fully renewed since then. Before the earthquake, the system already showed signs of deterioration, with water losses reaching around 55%. After the earthquake, this figure increased to approximately 75%, reflecting a major decline in system performance. Due to the extent of the damage and the aging state of the infrastructure, the entire system is currently undergoing full-scale reconstruction. In comparison, Christchurch had a

much lower pre-earthquake water loss rate of about 22%, based on reported total losses of 11.7 million m³ (including both non-revenue water and real system water losses) out of a total supply of 54.2 million m³ **[NZWW, 2010]**. These differences in infrastructure conditions likely explain why the RR values observed in this study are higher than those reported for Christchurch.

Further comparison for PVC pipelines was carried out using the **HAZUS** and **ALA [2001]** correlations, as well as the empirical relationship proposed by **Shih and Chang [2006]**. These models, which represent widely used formulations for assessing the performance of pipeline systems, provided an additional basis for evaluating the consistency of the predicted repair rates for PVC within the study area (**Figure 7.6**).

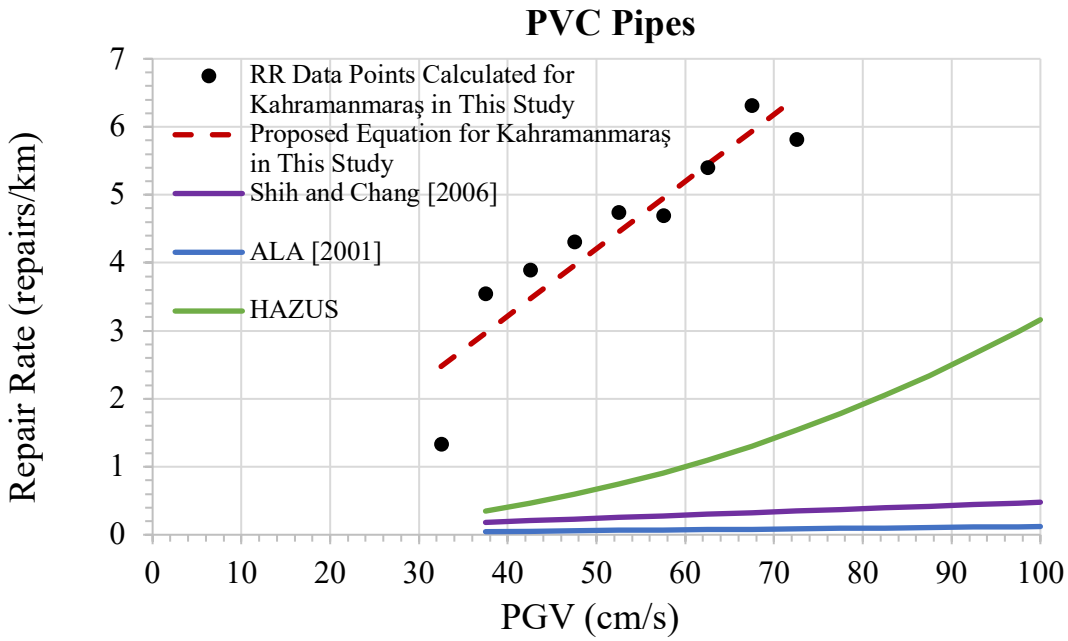


Figure 7.6: Comparison of RR–PGV relationships for PVC pipes between this study and the empirical model proposed in the literature.

As observed for the AC pipelines, **Figure 7.6** shows that the relationship obtained for Kahramanmaraş yields substantially higher repair rates for the PVC network compared with the other correlations. This difference is explained by the pre-earthquake condition of the system, as the PVC pipelines in the Kahramanmaraş city center were part of an aging and deteriorated network already experiencing significant operational issues. For instance, the average daily damage report prior to the earthquake was 9.3, whereas the typical U.S. average ranges between 0 and 1, and the corresponding value in Christchurch before the earthquakes was approximately 0–0.5.

8. RISK ASSESSMENT FOR YALOVA

In the following section, the relationships and findings derived from the 2023 Kahramanmaraş earthquakes—such as pipeline damage assessments—are utilized to make predictions for Yalova city center. Given Yalova's location in a seismically active region and the high probability of future earthquakes, the lessons learned from Kahramanmaraş Province provide a valuable framework for assessing potential risks.

8.1. Regional Overview of Yalova Province

8.1.1. Geography, Climate, and Economic Structure

Yalova is one of the important provinces in terms of trade and tourism in the Marmara Region of Türkiye. While covering an area of approximately 847 km^2, it borders the Sea of Marmara to the north, Kocaeli to the east, and Bursa to the south. The province consists of six towns: Armutlu, Çınarcık, Termal, Yalova (the city center), Çiftlikköy and Altınova. As of 2024, the population of Yalova is approximately 307,882 **[Turkish Statistical Institute, 2025]**.

Yalova has a transitional climate between the Mediterranean and Black Sea regions, with occasional continental influences. Summers are typically hot and dry, while winters are mild and rainy. The annual average temperature is around 14.6°C, with average temperatures of 6.5°C in the coldest month and 23.7°C in the warmest month. The city's natural landscape is dominated by maquis and forests, with forests sole covering approximately 55% of the province's land area **[Yalova Municipality, 2025]**. As for Yalova's industry and economy, they are primarily based on agriculture, industry, and services. In agriculture, although the cultivated area is relatively limited, greenhouse cultivation and ornamental plant production provide substantial economic value. In the industrial sector, transportation equipment manufacturing accounts for approximately 62.4% of total industrial employment. It is followed by metal products (6.8%), electricity and steam generation (5.6%), chemicals (4.3%), food products (4.0%), and paper products (3.6%). The service sector is supported by wholesale and retail trade, social services, and tourism **[Yalova Chamber of Commerce and Industry of, 2021]**.

8.1.2. Geological Structure

Yalova Province is located in a geologically diverse area. The city center is predominantly situated on alluvial, undivided quaternary deposits and terrestrial clastics (**Figure 8.1**). The alluvial units are widespread along stream channels, river deltas, and coastal plains within the province, typically characterized by low slope values ranging from 0% to 10%. In contrast, areas dominated by the Kılıç Formation, which is primarily located in the southern parts of Yalova Province, particularly between the villages of Çiftlikköy, Kazımiye, and Kılıç, exhibit more variable slopes ranging from 0%–10% to as steep as 10%–60%. This formation predominantly consists of laminated, thin bedded, moderately consolidated stiff clay, siltstone, marl, lenticular sandstone and mudstone beds **[Yalova Municipality, 2016]**.

Apart from the low-lying plains along the eastern coastline, Yalova largely features a mountainous topography. The southern section of the province is dominated by the Samanlı Mountains, which are structurally connected to the Kocaeli Range extending from Izmit to Sapanca. This mountain belt constitutes the principal highland system of the region. The highest elevation within the Samanlı Mountains in Yalova is Beşpınar Hill, reaching 926 meters above sea level. Additionally, the town of Armutlu is situated on the western foothills of Mount Taz, which rises to an elevation of 867 meters **[Yalova Municipality, 2025]**.

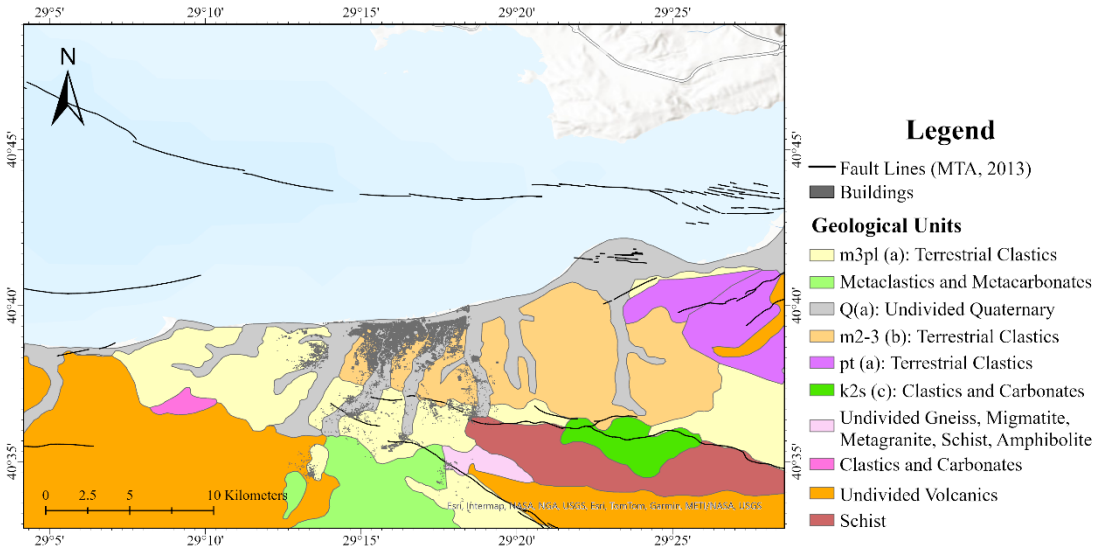


Figure 8.1: Map showing the geological structure of Yalova city center and its surroundings.

8.1.3. Seismic Characteristics

Yalova Province is positioned near the North Anatolian Fault Zone (NAF), one of Türkiye's most active seismic zones. Particularly, the earthquakes of August 17 and November 12, 1999, caused significant losses of life and property in Yalova. During these events, widespread structural damage was observed, including the collapse of residential buildings, and public facilities, as well as severe disruptions to lifeline systems such as water supply and electricity. According to official records, 2,504 people lost their lives in Yalova, while 8,585 residential and 764 commercial buildings sustained moderate damage, and 9,570 residential and 565 commercial buildings were severely damaged **[Governor of Yalova, 2019]**. This fault zone is approximately 1200 km long and characterized as a right-lateral strike-slip fault with a slip rate of about 1.0-2.0 cm per year **[Şengör et al., 2005]**. The segment located in the central part of the Sea of Marmara, which last ruptured in 1766, is expected by experts to generate an earthquake with a magnitude ranging between 7.1 and 7.4, accumulating approximately 4 meters of slip deficit **[Lange et al., 2019]**.

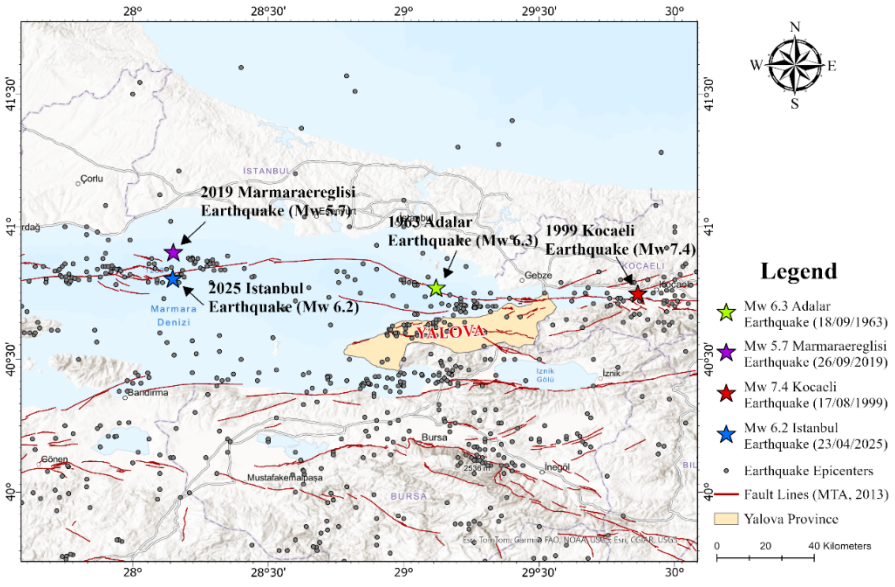


Figure 8.2: Map showing the seismicity of the Marmara Region.

Figure 8.2 visualizes more than 2,000 earthquakes with a magnitude greater than 3.5 that occurred within a 200 km radius in the region between January 1, 1900, and June 15, 2025, along with historically significant past earthquakes. The figure clearly indicates that the region is highly seismically active. Therefore, conducting earthquake hazard analyses for the city holds significant importance.

9. LIQUEFACTION SUSCEPTIBILITY MAPPING OF YALOVA CITY CENTER

Several studies have assessed the liquefaction susceptibility of Yalova using various geotechnical datasets under different seismic scenarios. For instance, **Yilmaz and Yavuzer [2005]** evaluated liquefaction potential based on data from 118 boreholes and produced liquefaction hazard maps indicating moderate to high susceptibility for a magnitude 7.4 earthquake scenario. Similarly, **Ozcep and Zarif [2009]** examined variations in the factor of safety against liquefaction using over 200 boreholes for various earthquake scenarios. Their results highlighted that coastal zones have become particularly vulnerable under ground motions exceeding 0.3g and magnitudes of 7.5. Similarly, **Capadag [2017]** also investigated the spatial distribution of liquefaction potential in Yalova under different seismic scenarios. The study concluded that while only some layers exhibited high susceptibility under a magnitude 6.5 event, most layers were vulnerable under a 7.0 event, and nearly all were highly susceptible under a magnitude 7.5 scenario. Recently, **Toprak et al. [2025e]** conducted susceptibility assessments by using liquefaction vulnerability indices such as LPI, LSI, and LSN based on SPTs in Yalova city center.

A comprehensive geotechnical investigation was carried out in Yalova city center by Yalova Municipality to investigate the local soil characteristics in detail. Within the scope of these geotechnical studies, a total of 273 boreholes were drilled using hydraulic D-500 type drilling rigs between April 3, 2014, and September 20, 2014, reaching depths ranging from 20.00 to 54.00 meters, and resulting in a cumulative drilling depth of 6,353.93 meters. Standard penetration tests were conducted at 3,793 different depth intervals within these boreholes. Additionally, Multichannel Analysis of Surface Waves (MASW) tests were performed at 80 distinct locations in the region. Based on these investigations, detailed liquefaction analyses utilizing SPT data were conducted in this thesis.

Furthermore, four Cone Penetration Test (CPT) profiles from the Yalova Harbor area, retrieved from the **PEER [2000b]**, were incorporated into the study to perform CPT-based liquefaction analyses. The spatial distribution of the geotechnical and geophysical tests used throughout the thesis is provided in **Figure 9.1**.

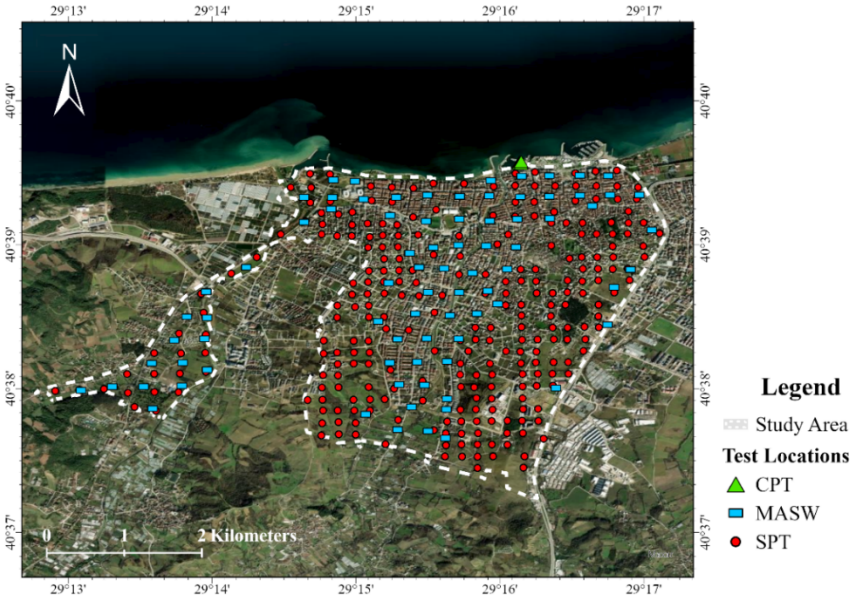


Figure 9.1: Spatial distribution of all SPT, MASW, and CPT locations within the study area.

The city center has varied groundwater conditions. For instance, in regions close to the coastline and the western parts of the study area, groundwater levels vary between 0.0 m and 5.0 m, whereas no groundwater table has been encountered in relatively higher elevations. Additionally, shallow groundwater levels were observed around Safran Creek, which flows through the center of the city and the study area. The spatial distribution of groundwater levels is visualized using the IDW method and presented in **Figure 9.2**.

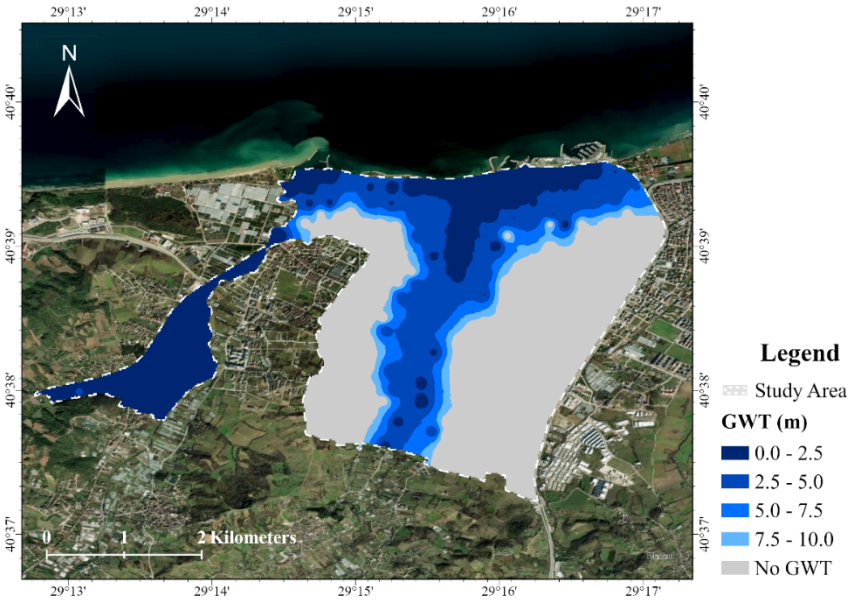


Figure 9.2: Spatial distribution of ground water table within the study area.

When examining the shear-wave velocities in the upper 30 meters (V_{s30}) across the study area, significant variations related to local soil conditions were observed. In regions with weaker soils, V_{s30} values were around 137 m/s, while in areas characterized by relatively stronger soils, velocities reached up to approximately 270 m/s. Generally, V_{s30} values ranged between 165 m/s and 195 m/s in the central portion of the study area, approximately 137 m/s in the western regions, and increased to between 210 m/s and 270 m/s towards the eastern side. The V_{s30} values were derived using MASW data and interpolated using the kriging method, with their spatial distribution provided in **Figure 9.3**.

Furthermore, the calculated V_{s30} values were used to classify the soils according to the local site classes defined in the Turkish Building Earthquake Code **[TBEC, 2018]**. Based on this classification, the study area consists of the ZD and ZE local site classes, indicating that the region has soil conditions associated with a higher potential for liquefaction and therefore poses significant seismic risk.

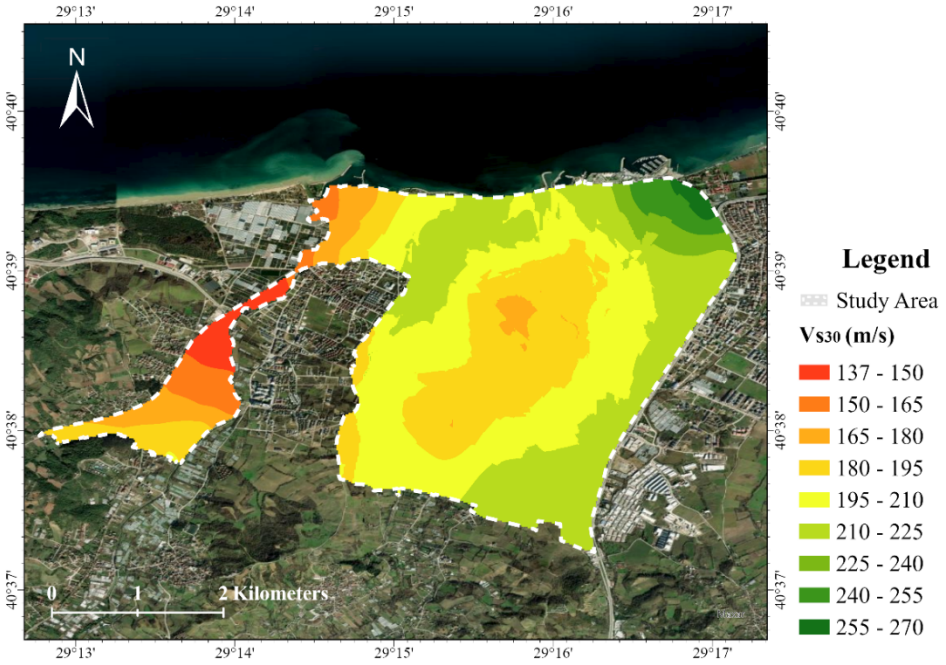


Figure 9.3: Spatial distribution of V_{s30} within the study area.

Additionally, the accuracy of the generated V_{s30} map was verified using reference V_{s30} values obtained from AFAD strong-motion stations located within the study area (**Table 9.1**). The comparison confirmed a strong correlation between the measured and interpolated values, supporting the validity of the developed V_{s30} distribution.

Table 9.1: V_{s30} reference values obtained from AFAD strong-motion stations used for the verification of the interpolated V_{s30} map.

Network	Code	Latitude	Longitude	Elevation (m)	V_{s30} (m/s)
TK	7705	40.6587	29.27955	3	261
TK	7703	40.65056	29.27896	58	280
TK	7708	40.65756	29.24725	2	195

Index-based liquefaction analyses were performed using data from 273 SPT boreholes distributed across the study area, and LPI, LSI, and LSN maps were generated to illustrate the spatial distribution of liquefaction potential. The results reveal that liquefaction risk is particularly high in locations with a shallow groundwater table, especially along the coastline, in the western part of the study area, and around Safran Creek. For these evaluations, two earthquake scenarios were considered: Scenario 1: TBEC 2018 Mw 7.5 Earthquake and Scenario 2: Prince Islands Mw 7.0 Earthquake. The detailed results for both scenarios are presented in the following subsections.

9.1. Scenario 1: TBEC 2018 Mw 7.5 Earthquake

In this scenario, a moment magnitude of Mw 7.5 was adopted, while the ground motion parameters were taken from TBEC 2018, corresponding to the design level associated with a 475-year return period. Liquefaction susceptibility was evaluated using the resulting PGA distribution (**Figure 9.4**), and LPI, LSI, and LSN maps were generated to highlight the spatial variation of liquefaction potential under this regional seismic source (**Figure 9.5**–**Figure 9.10**).

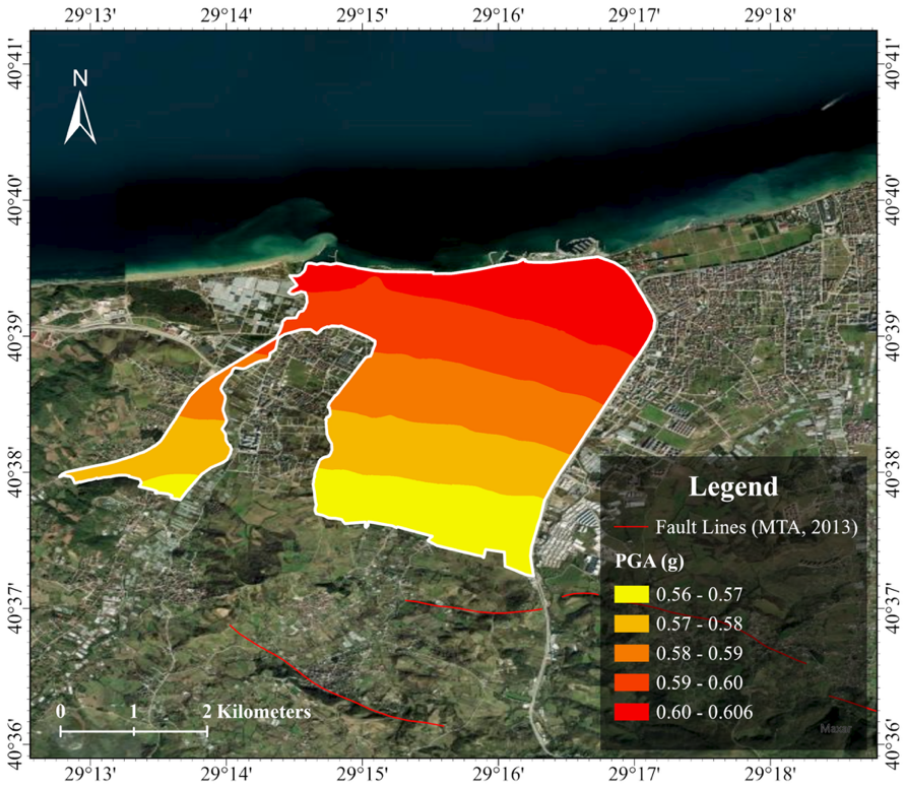


Figure 9.4: Spatial distribution of PGA values considered in Scenario 1 (TBEC 2018 Mw 7.5 earthquake).

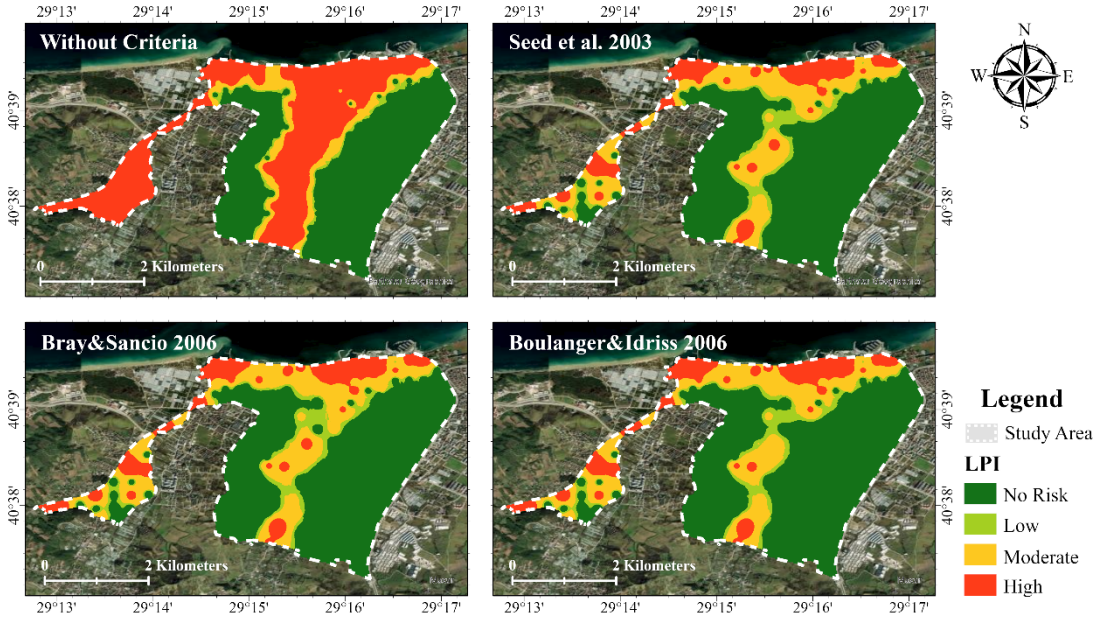


Figure 9.5: LPI map calculated using the **Youd et al. [2001]** method for factor of safety estimation.

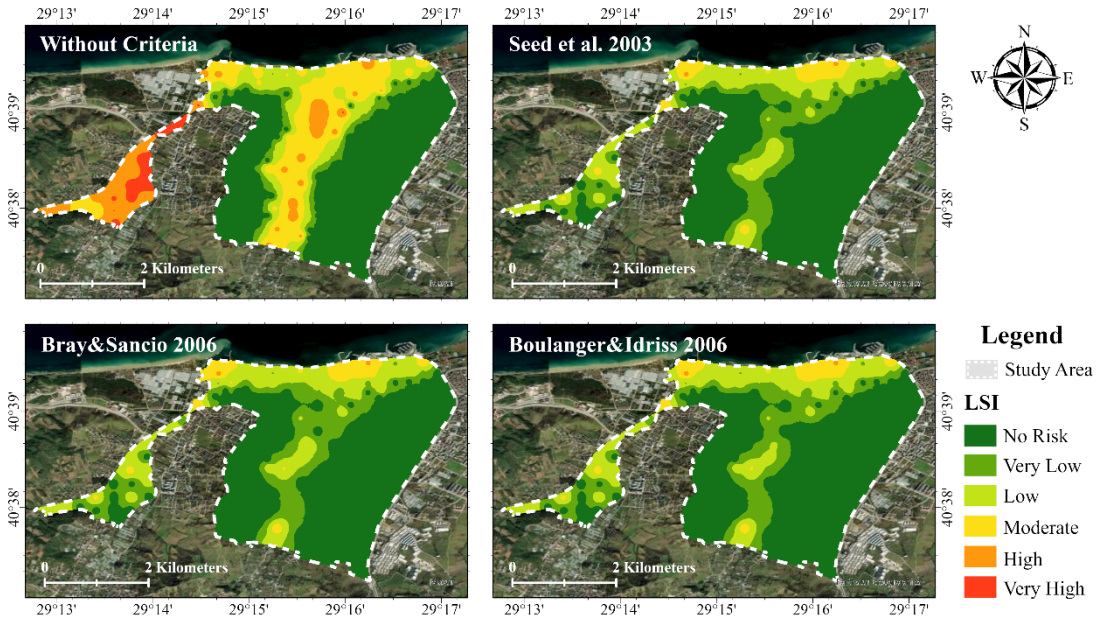


Figure 9.6: LSI map calculated using the **Youd et al. [2001]** method for factor of safety estimation.

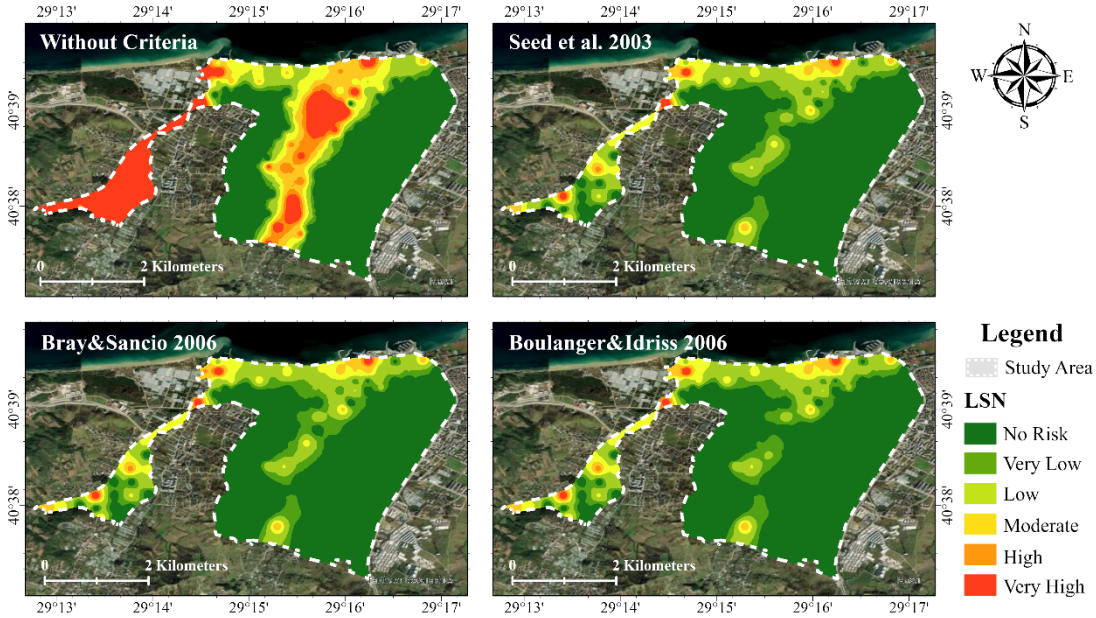


Figure 9.7: LSN map calculated using the **Youd et al. [2001]** method for factor of safety estimation.

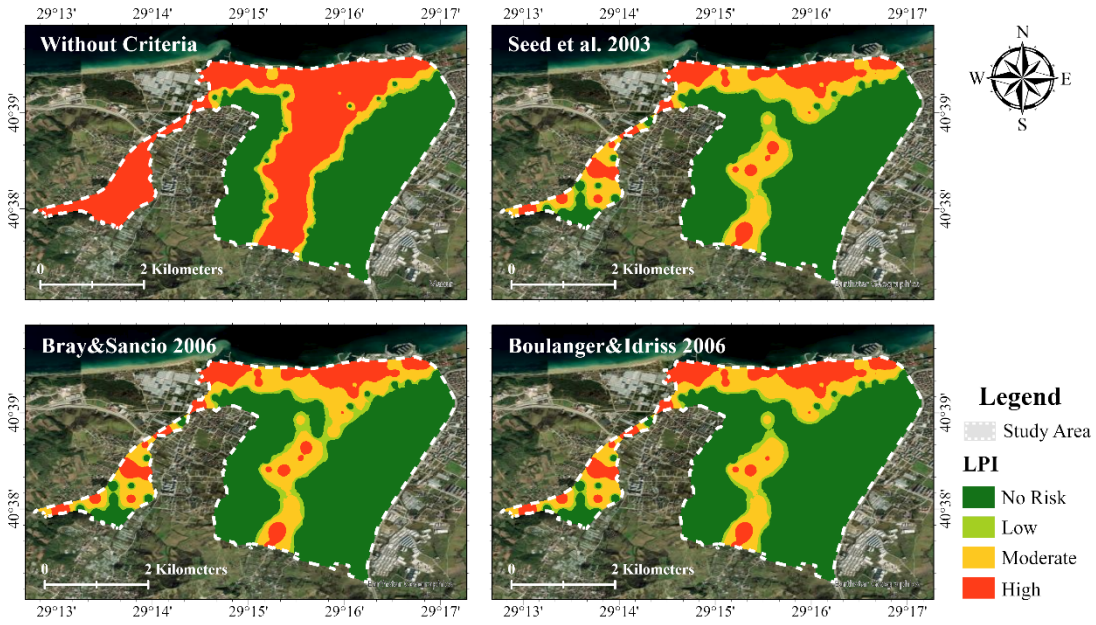


Figure 9.8: LPI map calculated using the **Boulanger and Idriss [2014]** method for factor of safety estimation.

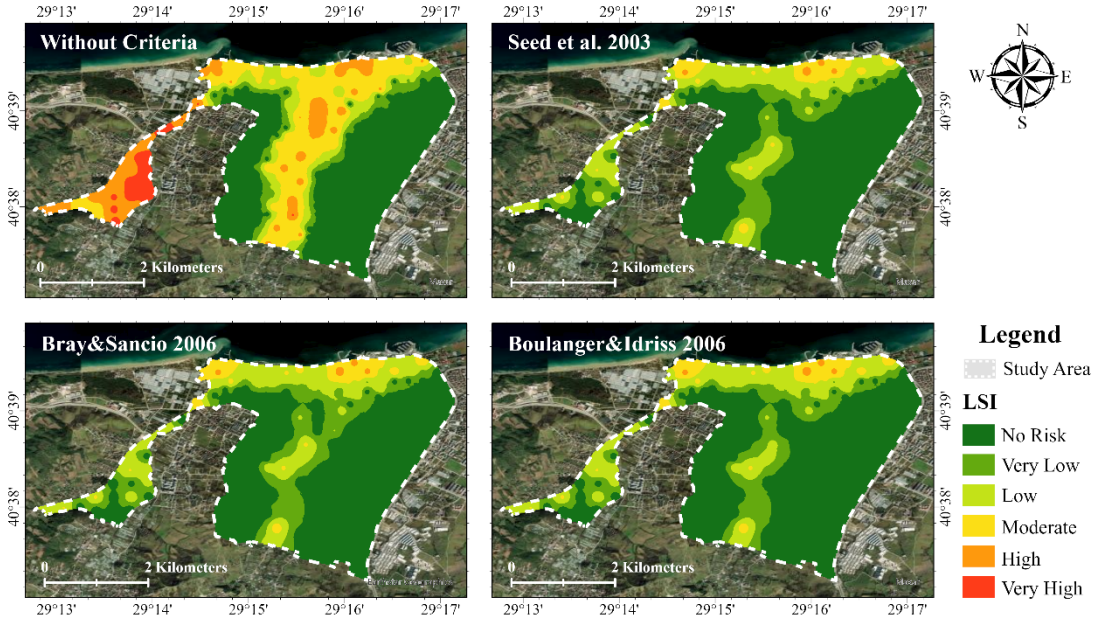


Figure 9.9: LSI map calculated using the **Boulanger and Idriss [2014]** method for factor of safety estimation.

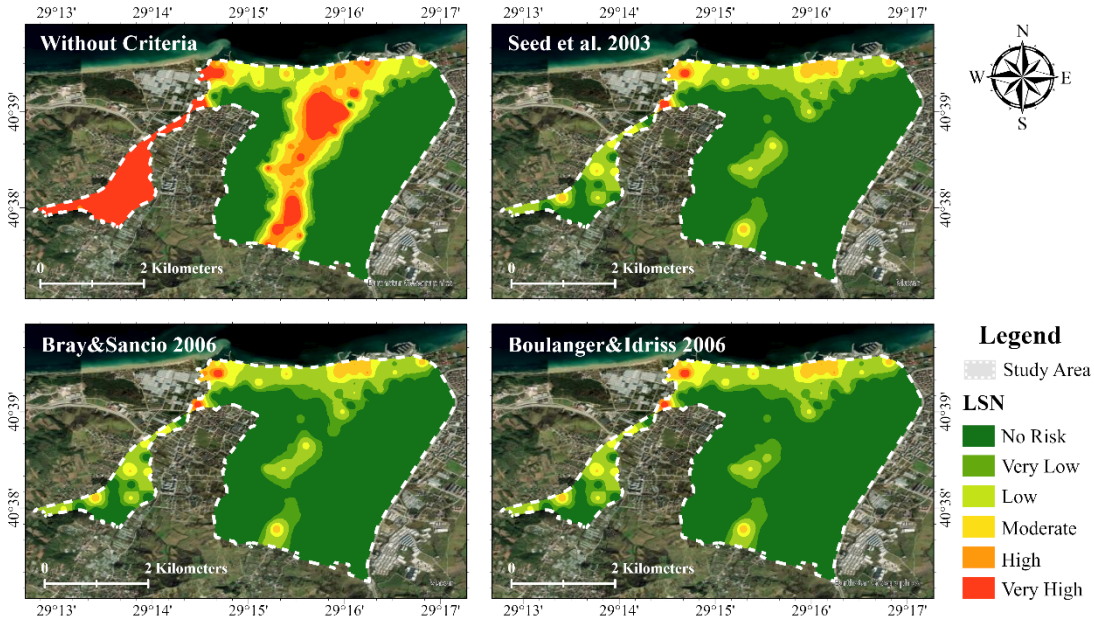


Figure 9.10: LSN map calculated using the **Boulanger and Idriss [2014]** method for factor of safety estimation.

9.2. Scenario 2: Prince Islands Mw 7.0 Earthquake

In this scenario, a moment magnitude of Mw 7.0 was considered, with ground motion parameters derived from the MARTEST–SATREPS project. As an output of this project, which was conducted on Yalova as the pilot area, the analyzed fault was modeled as a planar source with a strike of 110°, a dip angle of 90°, and a rupture length of 45.8 km. Liquefaction susceptibility was assessed using the corresponding PGA distribution (**Figure 9.11**), and LPI, LSI, and LSN maps were generated to highlight the spatial variation of liquefaction potential under this regional seismic source (**Figure 9.12**–**Figure 9.17**).

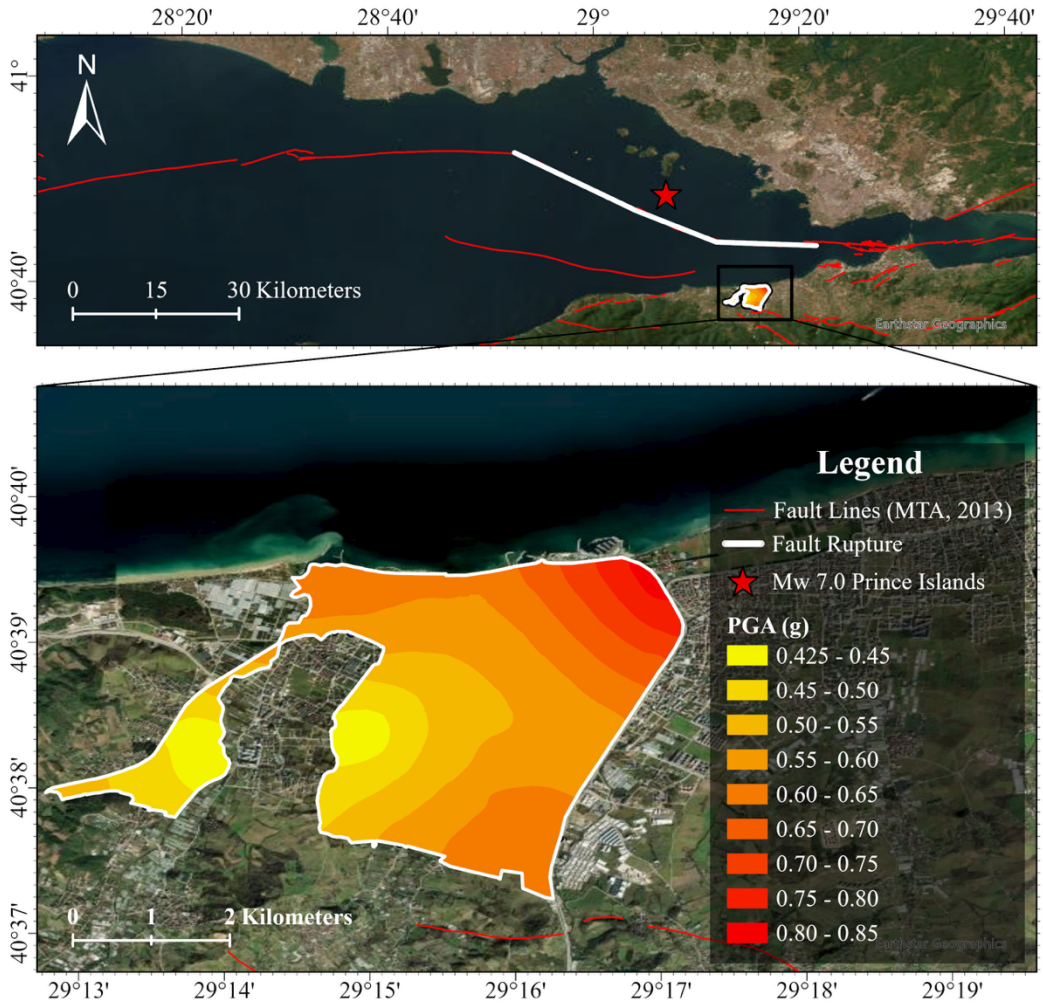


Figure 9.11: Spatial distribution of PGA values considered in Scenario 2 (Prince Islands Mw 7.0 earthquake, MARTEST–SATREPS project).

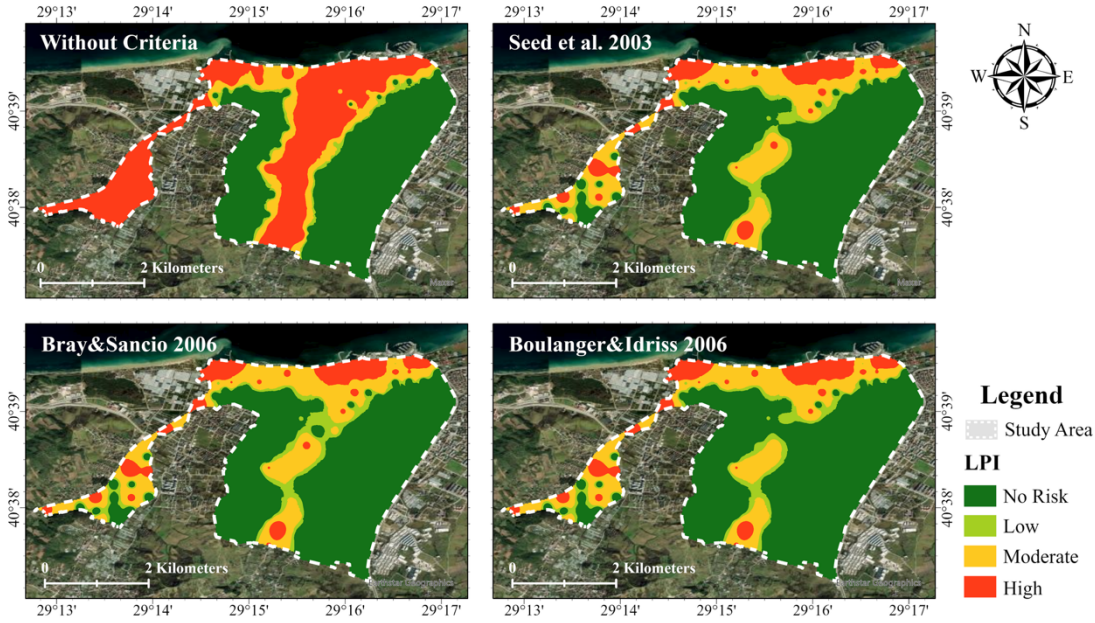


Figure 9.12: LPI map calculated using the **Youd et al. [2001]** method for factor of safety estimation.

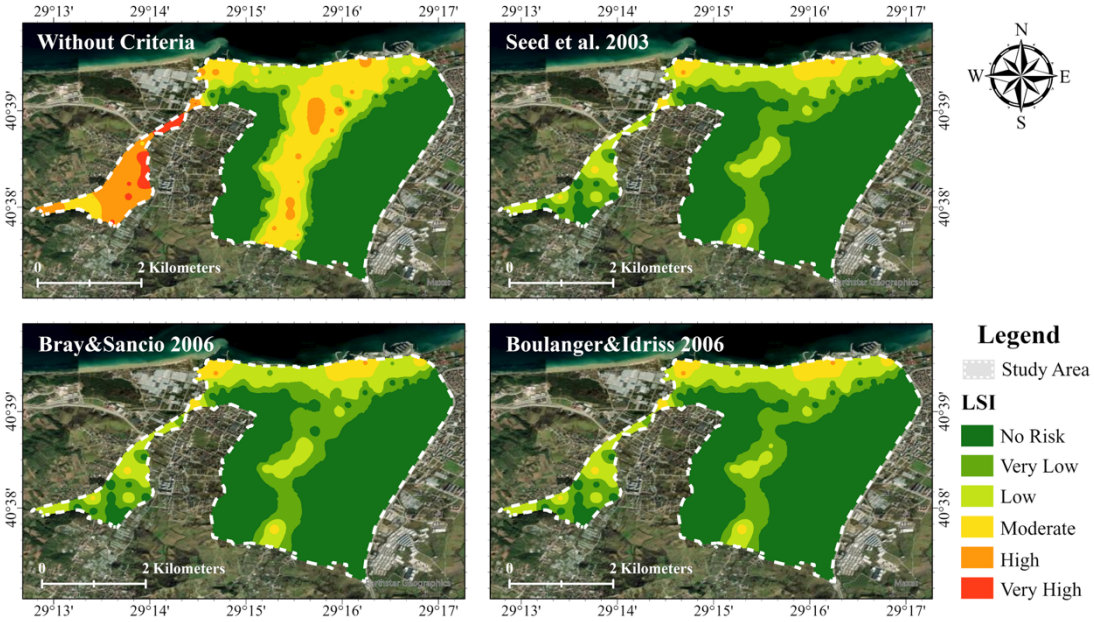


Figure 9.13: LSI map calculated using the **Youd et al. [2001]** method for factor of safety estimation.

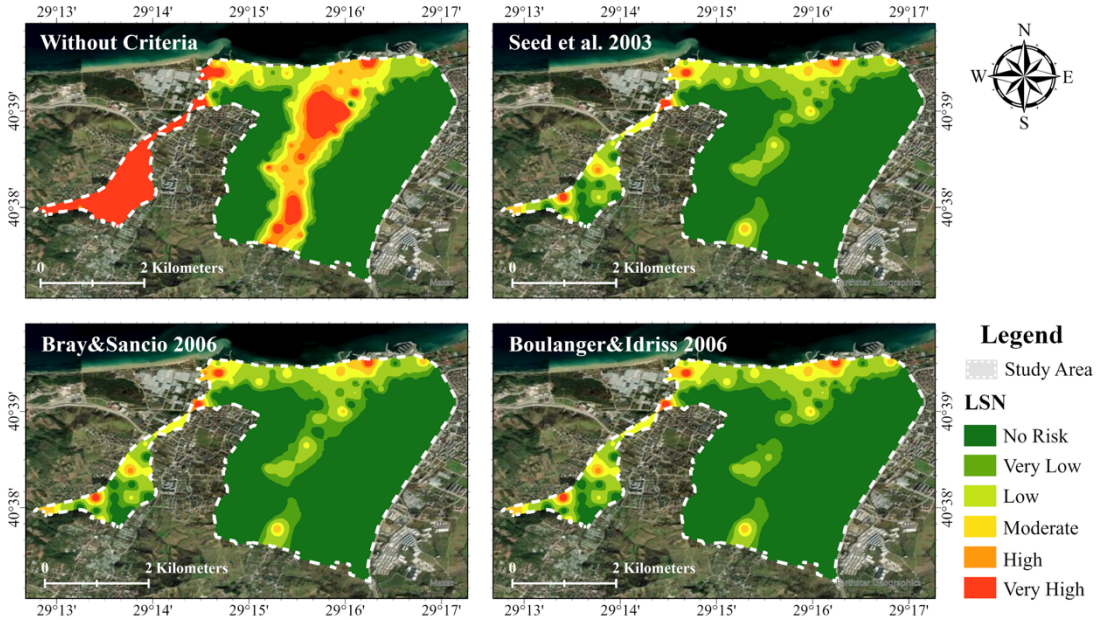


Figure 9.14: LSN map calculated using the **Youd et al. [2001]** method for factor of safety estimation.

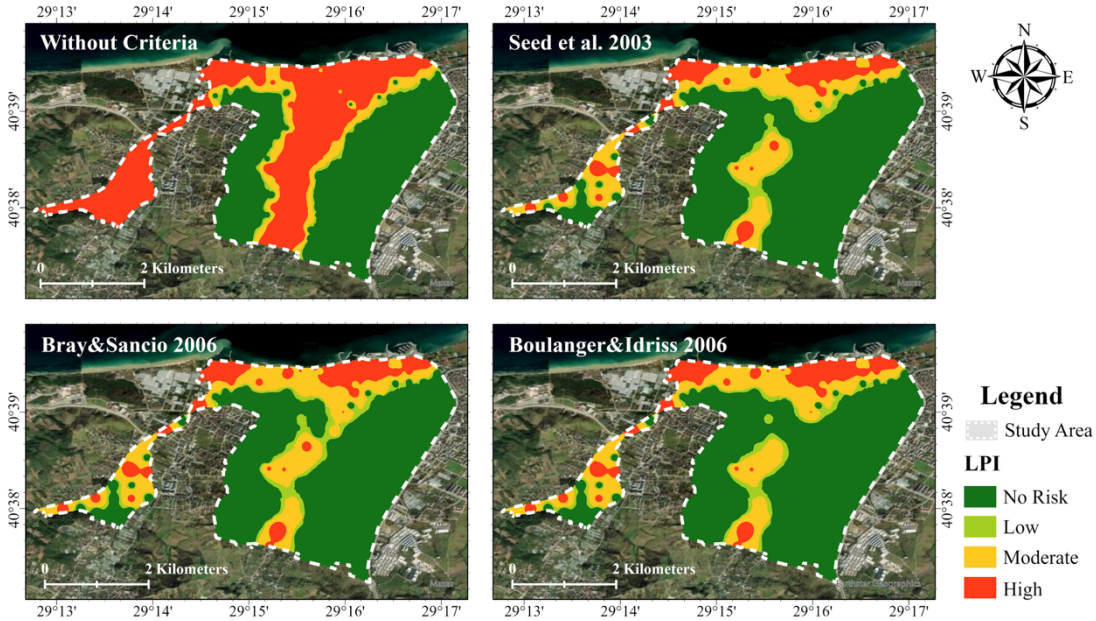


Figure 9.15: LPI map calculated using the **Boulanger and Idriss [2014]** method for factor of safety estimation.

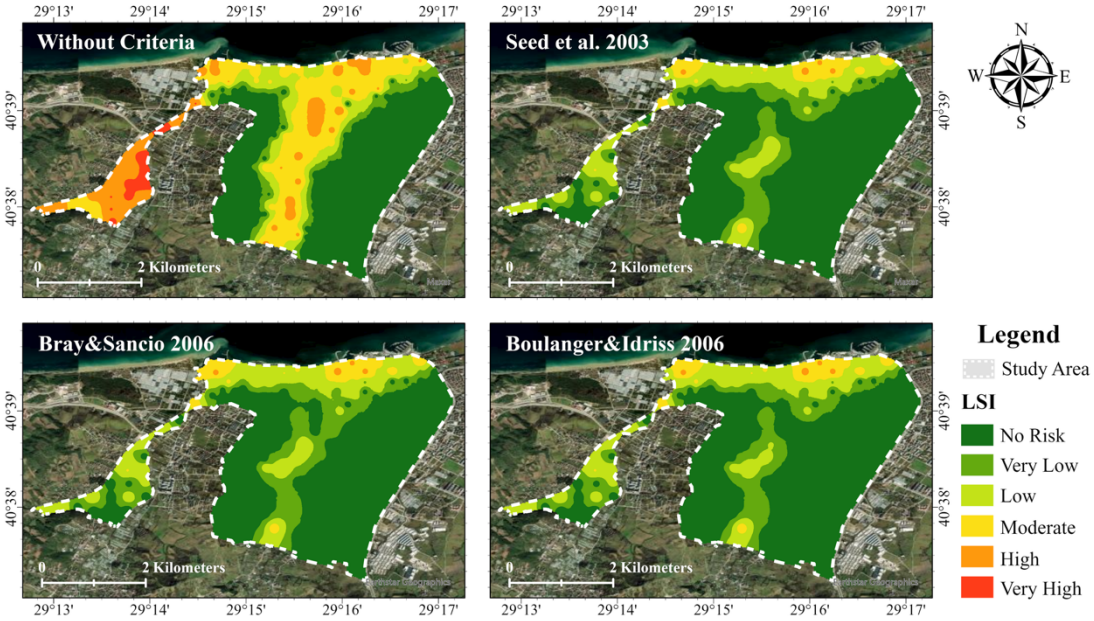


Figure 9.16: LSI map calculated using the **Boulanger and Idriss [2014]** method for factor of safety estimation.

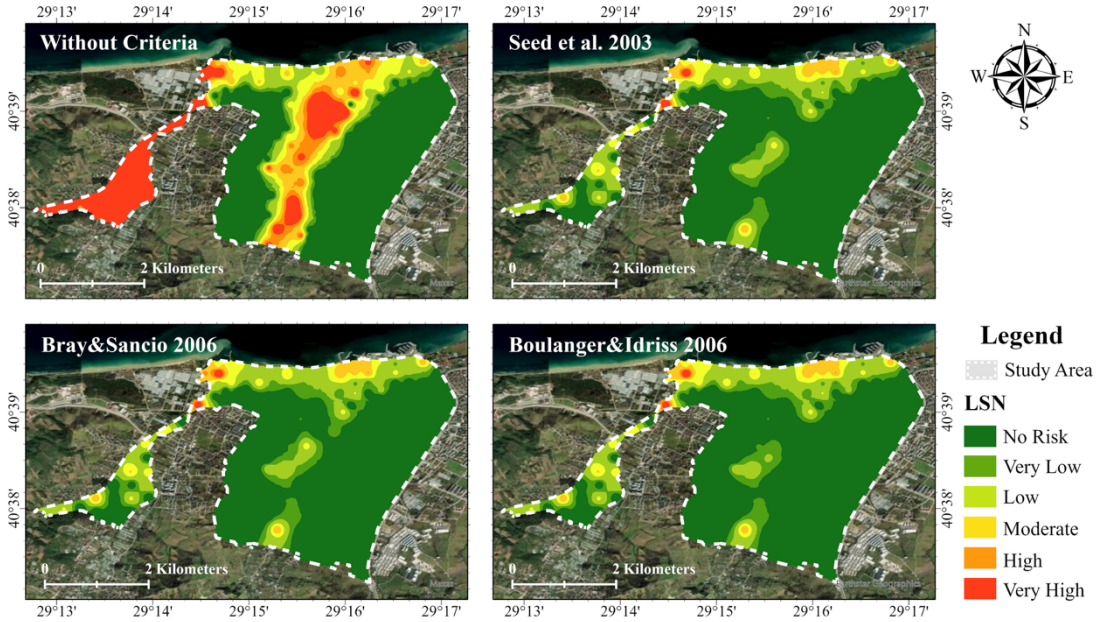


Figure 9.17: LSN map calculated using the **Boulanger and Idriss [2014]** method for factor of safety estimation.

9.3. Comparison of the Results

When the results of the two scenarios are compared, it is observed that similar regions exhibit a tendency toward liquefaction. Although the ground accelerations of the second scenario are higher than the first scenario, the smaller earthquake magnitude in the second scenario resulted in comparable outcomes.

Moreover, it should also be noted that the calculations performed using the method proposed by **Boulanger and Idriss [2014]** yielded slightly more susceptible results. This difference arises from the factor of safety values obtained by this method being marginally lower than those calculated according to **Youd et al. [2001]**.

In addition, when the applied criteria are compared, the without criteria case exhibits a fully susceptible distribution, whereas the other criteria yield similar results. Since the without criteria condition does not account for soil plasticity, this finding clearly demonstrates the importance of considering plasticity condition of soil in the liquefaction analyses.

Furthermore, when the LPI, LSI, and LSN maps are compared, the LPI maps exhibit a higher susceptibility distribution, whereas the LSI and LSN maps, owing to their larger number of classification groups, provide a more detailed representation of the spatial variability.

In conclusion, these comparisons show that although the overall spatial patterns of liquefaction susceptibility are consistent, the selected methods and criteria influence the severity levels and the detail of the results.

10. ASSESSMENT OF LIQUEFACTION-INDUCED SETTLEMENTS IN YALOVA CITY CENTER

The liquefaction-induced free-field settlements were evaluated to support the estimation of ground deformation effects on the water distribution network in Yalova city center. These settlements represent surface deformations under free-field conditions and provide a basis for evaluating potential infrastructure damage associated with liquefaction-induced ground movements. To obtain a robust assessment, multiple empirical approaches were applied in the settlement analyses.

Similar to the liquefaction susceptibility analysis, two earthquake scenarios were considered for the settlement assessments: Scenario 1, an Mw 7.5 earthquake with input PGA values derived from the TBEC 2018 seismic hazard assessment, and Scenario 2, an Mw 7.0 Prince Islands earthquake developed within the MARTEST–SATREPS framework. In these calculations, the liquefaction susceptibility method proposed by **Boulanger and Idriss [2014]** was employed, and the liquefaction susceptibility criteria suggested by **Bray and Sancio [2006]** for fine-grained soils were adopted. The results of free-field settlement analyses for both scenarios are presented and discussed in the following sections of this chapter.

10.1. Scenario 1: TBEC 2018 Mw 7.5 Earthquake

10.1.1. Tokimatsu and Seed [1984] Procedure

According to the free-field settlement values calculated using the **Tokimatsu and Seed [1984]** method, the highest settlement was observed at borehole A-SK-19, located on the Yalova Shore, with a value of 0.43 meters. Settlements of this magnitude may cause buildings to tilt, topple, or sink. Within the study area, no liquefaction-induced settlement was observed across 7.68 km², which corresponds to approximately 66.2% of the total area. A settlement between 0.00–0.05 meters was identified in 1.01 km² (8.74%), while 1.36 km² (11.72%) experienced settlements in the range of 0.05–0.10 meters. Additionally, 0.59 km² (5.08%) of the area showed settlements between 0.10–0.15 meters, 0.52 km² (4.51%) between 0.15–0.20 meters,

and 0.21 km² (1.79%) between 0.20–0.25 meters. The remaining 0.23 km² (1.95%) exhibited higher settlements ranging from 0.25 to 0.43 meters.

The spatial distribution of the estimated free-field settlements for both the Yalova Shore and the city center is illustrated in **Figure 10.1**, providing a clear visualization of the most affected areas within the study region.

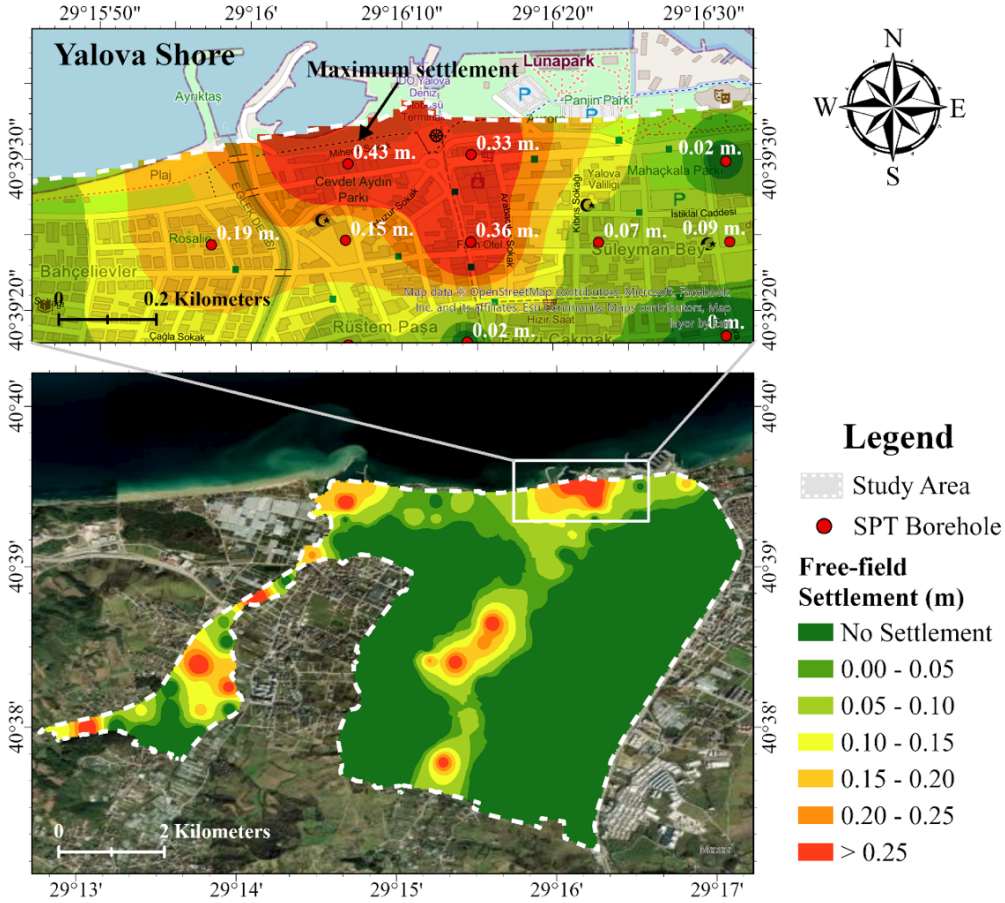


Figure 10.1: Spatial distribution of liquefaction-induced free-field settlements in the Yalova shoreline and city center, estimated using the **Tokimatsu and Seed [1984]** procedure.

10.1.2. Ishihara and Yoshimine [1992] Procedure

Further, results of the free-field settlement calculated using the methods proposed by **Ishihara and Yoshimine [1992]** and **Zhang et al. [2004]** indicate that the highest settlement occurred at the same borehole, A-SK-19, with a value of 0.56 meters. Compared to the values obtained from the **Tokimatsu and Seed [1984]** method, this approach generally yielded higher settlement estimates across the study area.

Specifically, while 62.4% of the area (7.25 km²) remained unaffected, settlements in the range of 0.00–0.05 meters occurred in 0.80 km² (6.89%). The range of 0.05–0.10 meters covered the largest affected portion with 1.57 km² (13.55%). Other ranges included 0.10–0.15 meters in 0.81 km² (6.98%), 0.15–0.20 meters in 0.52 km² (4.49%), and 0.20–0.25 meters in 0.29 km² (2.54%). The most severe settlements, ranging from 0.25 to 0.56 meters, were calculated across 0.37 km² (3.15%) of the study area.

The spatial distribution of free-field settlements calculated using **Ishihara and Yoshimine [1992]** and **Zhang et al. [2004]** in both Yalova Shore and city center is well presented in **Figure 10.2**.

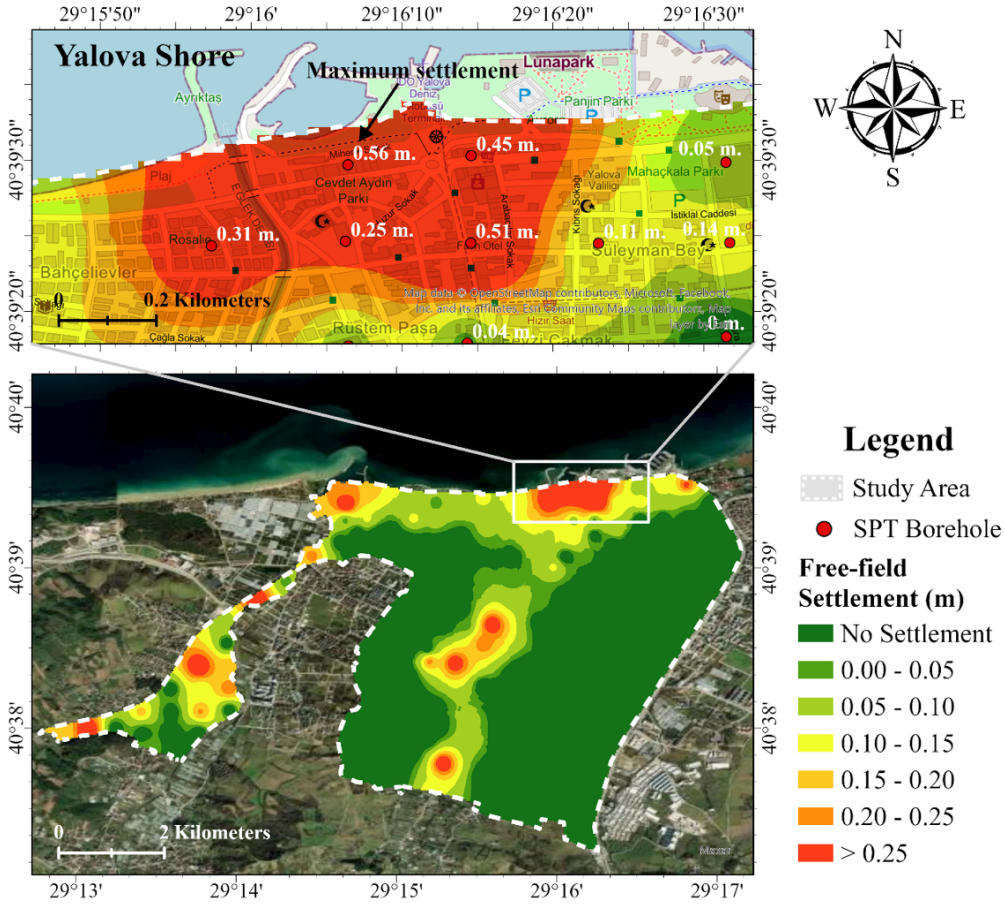


Figure 10.2: Spatial distribution of liquefaction-induced free-field settlements in the Yalova shoreline and city center, estimated using the **Ishihara and Yoshimine [1992]** and **Zhang et al. [2004]** procedure.

Moreover, the free-field settlements were estimated based on the method proposed by **Ishihara and Yoshimine [1992]** and maximum shear stresses established by **Yoshimine et al. [2006]**, in order to evaluate the influence of varying maximum shear stress assumptions on the settlement results. The maximum settlement was once again

observed at borehole A-SK-19, this time with a value of 0.55 meters. Compared to the free-field settlements estimated using the maximum shear stresses proposed by **Zhang et al. [2004]**, the results yielded slightly lower values.

The analyses results indicate that in a large portion of the area, covering approximately 7.36 km² (63.45%), no settlement occurs. The next most common class is 0.051–0.10 m, covering 1.59 km² (13.73%), followed by the 0.00–0.05 m range with 0.89 km² (7.65%). The 0.101–0.15 m and 0.151–0.20 m intervals account for 0.69 km² (5.94%) and 0.52 km² (4.46%), respectively. Areas with settlements between 0.201–0.25 m and 0.25–0.55 m are more limited, covering 0.25 km² (2.16%) and 0.30 km² (2.61%), respectively.

Figure 10.3 clearly illustrates the spatial variation of free-field settlements across both the Yalova shoreline and city center, as computed using the methods of **Ishihara and Yoshimine [1992]** and **Yoshimine et al. [2006]**.

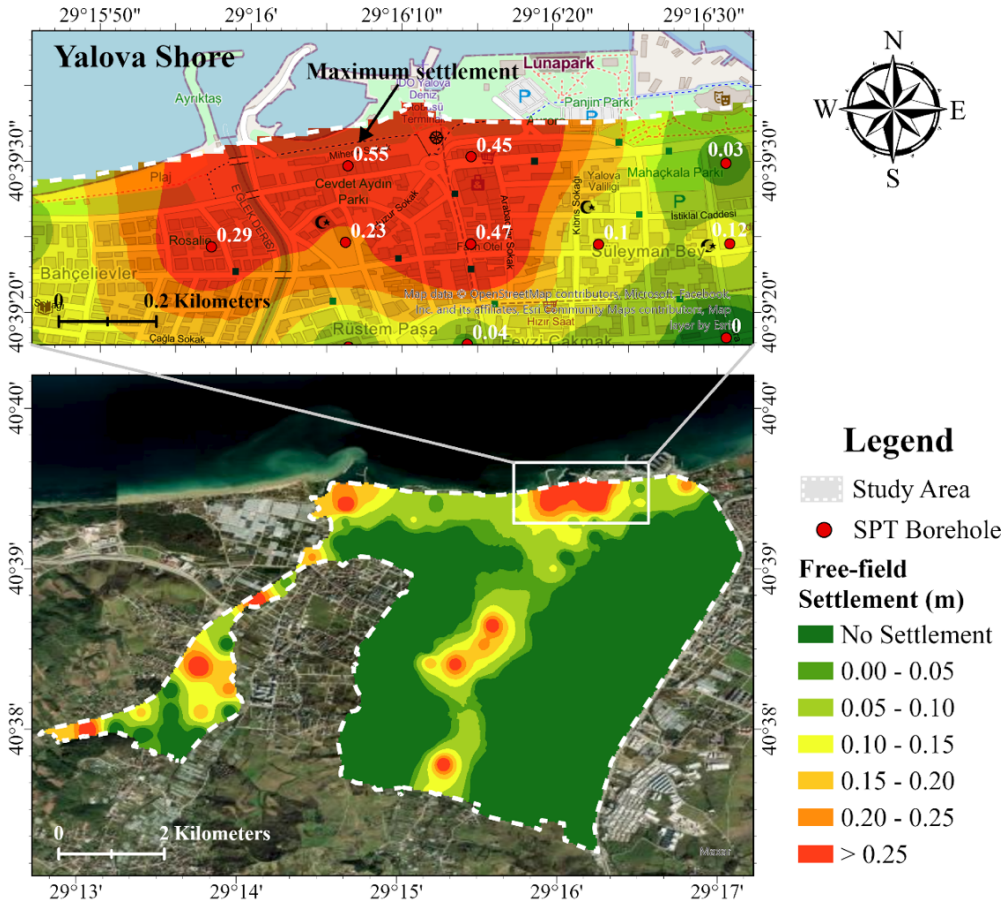


Figure 10.3: Spatial distribution of liquefaction-induced free-field settlements in the Yalova shoreline and city center, estimated using the **Ishihara and Yoshimine [1992]** and **Yoshimine et al. [2006]** procedure.

10.1.3. Shamoto et al. [1998] Procedure

Following that, free-field settlements were calculated using the method proposed by **Shamoto et al. [1998]**, and their spatial distribution is well-illustrated in **Figure 10.4**. As observed in the other methods, the maximum settlement was again calculated at borehole A-SK-19, with a value of 0.45 meters. Compared to the settlements estimated using the other methods, slightly lower values were generally observed throughout the study area.

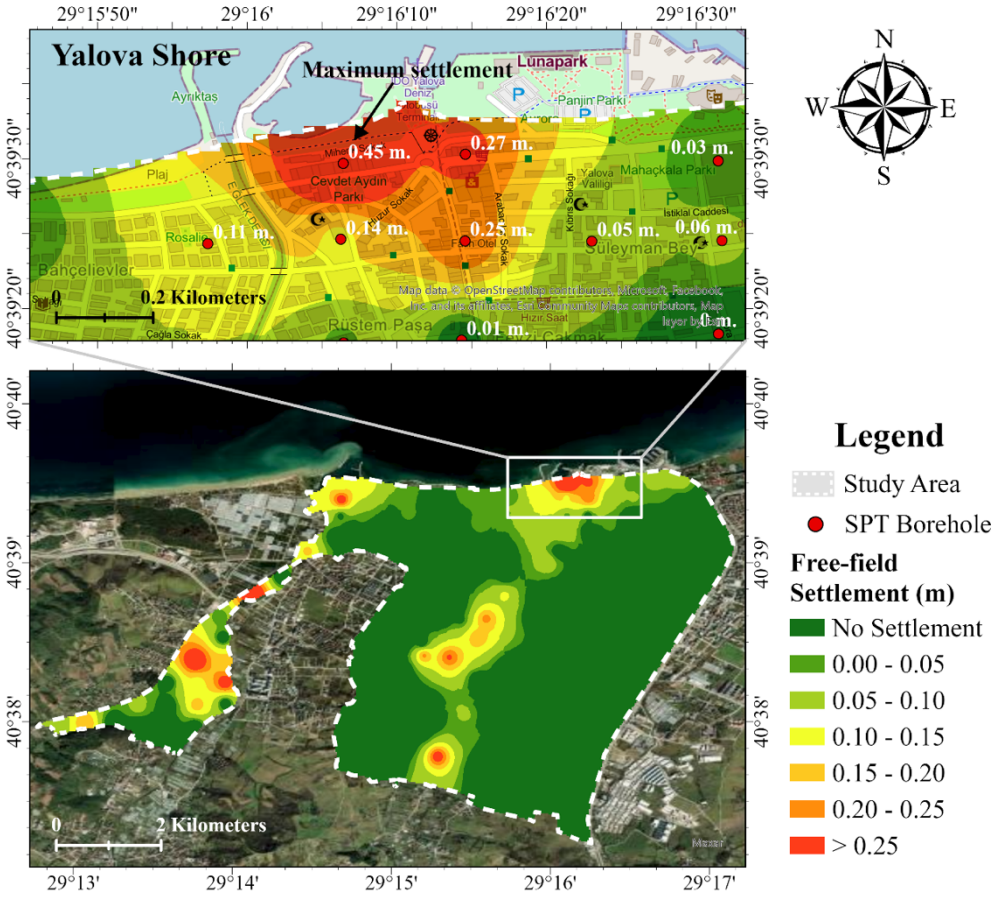


Figure 10.4: Spatial distribution of liquefaction-induced free-field settlements in the Yalova shoreline and city center, estimated using the **Shamoto et al. [1998]** procedure.

In this analysis, a large portion of the study area—approximately 8.13 km² (70.04%)—corresponds to regions where no actual settlement occurs. The 0.051–0.10 m and 0.00–0.05 m ranges cover 1.16 km² (9.99%) and 1.04 km² (8.97%) of the area, respectively. The 0.101–0.15 m class accounts for 0.66 km² (5.67%), while the 0.151–0.20 m range occupies 0.33 km² (2.84%). Higher settlement intervals of 0.201–0.25 m and 0.251–0.45 m are limited to smaller areas, with 0.15 km² (1.31%) and 0.14 km² (1.18%).

10.1.4. Wu et al. [2003] Procedure

Subsequently, the free-field settlements were estimated throughout the city center based on the method proposed by **Wu et al. [2003]** and the spatial distribution is clearly presented in **Figure 10.5**. The results indicate higher and more severe settlement values compared to those obtained from the other adopted methodologies. For example, while the maximum settlement at borehole A-SK-19 was previously estimated as 0.43, 0.56, 0.55, 0.45 and 0.34 meters using the other methods, it was calculated as 0.61 meters in this analysis.

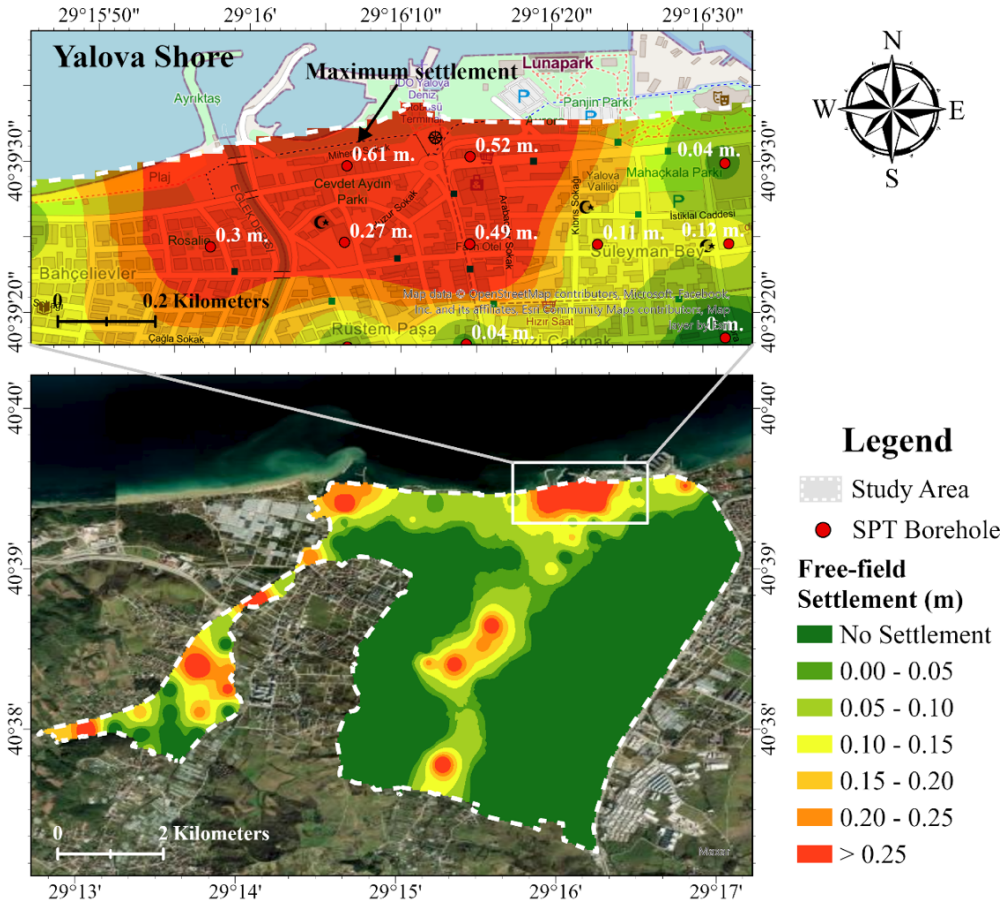


Figure 10.5: Spatial distribution of liquefaction-induced free-field settlements in the Yalova shoreline and city center, estimated using the **Wu et al. [2003]** procedure.

In terms of spatial distribution, a large portion of the study area—approximately 7.25 km² (62.45%)—falls into the category where no actual settlement occurs. The 0.051–0.10 m range covers 1.57 km² (13.56%), followed by the 0.00–0.05 m and 0.101–0.15 m intervals with 0.81 km² (7.01%) and 0.74 km² (6.36%), respectively.

The 0.151–0.20 m class occupies 0.48 km² (4.15%), while areas experiencing settlements in the range of 0.201–0.25 m and 0.251–0.65 m are more limited, covering 0.36 km² (3.07%) and 0.40 km² (3.40%), respectively.

10.1.5. Cetin et al. [2009] Procedure

Lastly, the methodology proposed by **Cetin et al. [2009]** to estimate the free-field settlements was adopted in the study and the spatial distribution is illustrated in **Figure 10.6**.

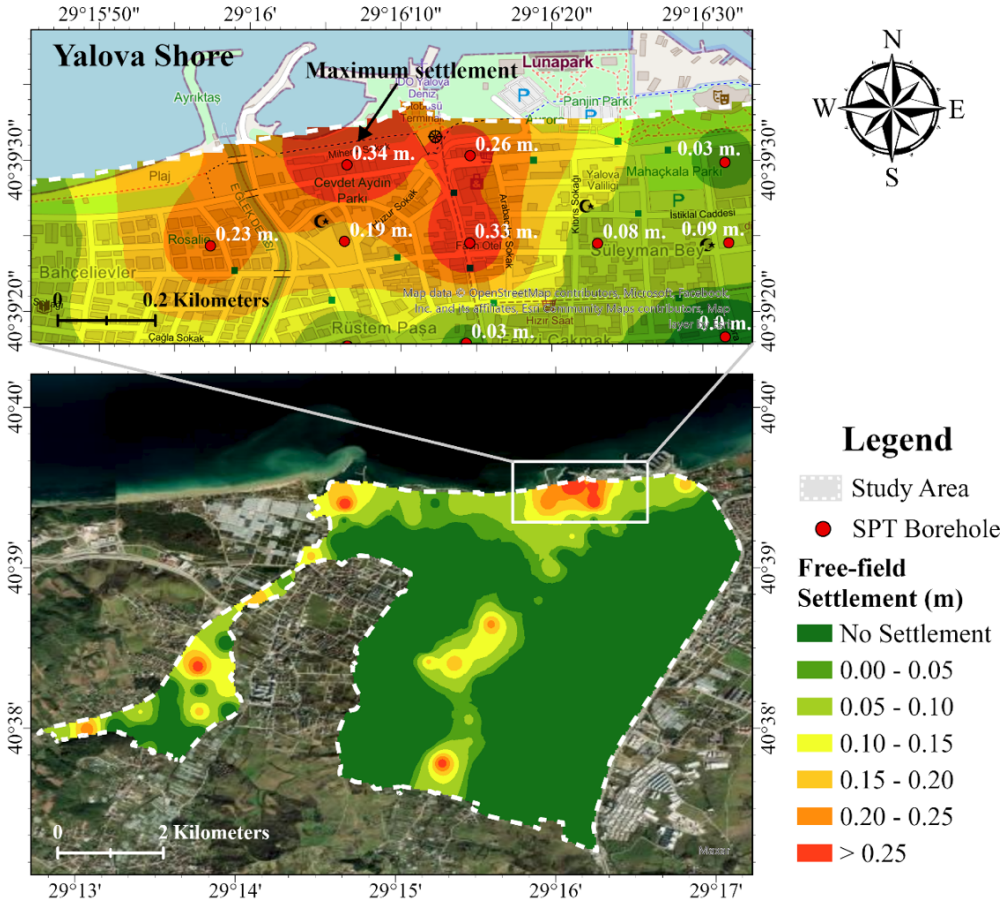


Figure 10.6: Spatial distribution of liquefaction-induced free-field settlements in the Yalova shoreline and city center, estimated using the **Cetin et al. [2009]** procedure.

Compared to the other methods applied, this procedure generally yielded lower settlement values. For example, at borehole A-SK-19, where the highest settlements were observed, the results from other methods ranged between 0.43 and 0.61 meters. In contrast, the **Cetin et al. [2009]** method estimated a settlement of 0.34 meters.

The analysis results indicate that a substantial portion of the area remained unaffected by liquefaction-induced settlement. Specifically, 69.04% of the region (8.02 km²) showed negligible settlement. Low levels of settlement between 0.00–0.05 meters were found in 0.93 km² (8.05%), and 1.52 km² (13.09%) was affected by settlements in the 0.05–0.10 meter range. Settlements between 0.10–0.15 meters were observed in 0.64 km² (5.49%), while smaller portions of the area experienced slightly higher settlements: 0.29 km² (2.49%) between 0.15–0.20 meters, 0.14 km² (1.19%) between 0.20–0.25 meters, and 0.08 km² (0.65%) in the 0.25–0.35-meter range.

10.2. Scenario 2: Prince Islands Mw 7.0 Earthquake

10.2.1. Tokimatsu and Seed [1984] Procedure

When the free-field settlements calculated using the **Tokimatsu and Seed [1984]** method are examined, the maximum value in the second scenario was obtained at borehole A-SK-19 on the Yalova Shore, reaching 0.43 meters. This outcome, consistent with the first scenario, further emphasizes the high susceptibility of this site to liquefaction-induced settlement. The spatial distribution of the calculated settlements for the second scenario is presented in **Figure 10.7**.

The comparison of the two scenarios demonstrates a consistent spatial distribution of liquefaction-induced settlements. In the second scenario, 66.4% of the study area is unaffected, closely matching the 66.2% obtained in the first scenario. The 0.05–0.10 m settlement range covers 11.8% of the area in the second scenario, again in close agreement with the 11.7% reported in the first. Similarly, 8.6% of the area is associated with 0.03–0.05 m settlements, compared to 8.7% in the first scenario, while 5.2% and 4.5% fall within the 0.10–0.15 m and 0.15–0.20 m ranges, respectively, values that are nearly identical to those of the first scenario. Minor variations are observed in the highest settlement classes, where the second scenario yields 1.8% of the area for both the 0.20–0.25 m and 0.25–0.45 m intervals.

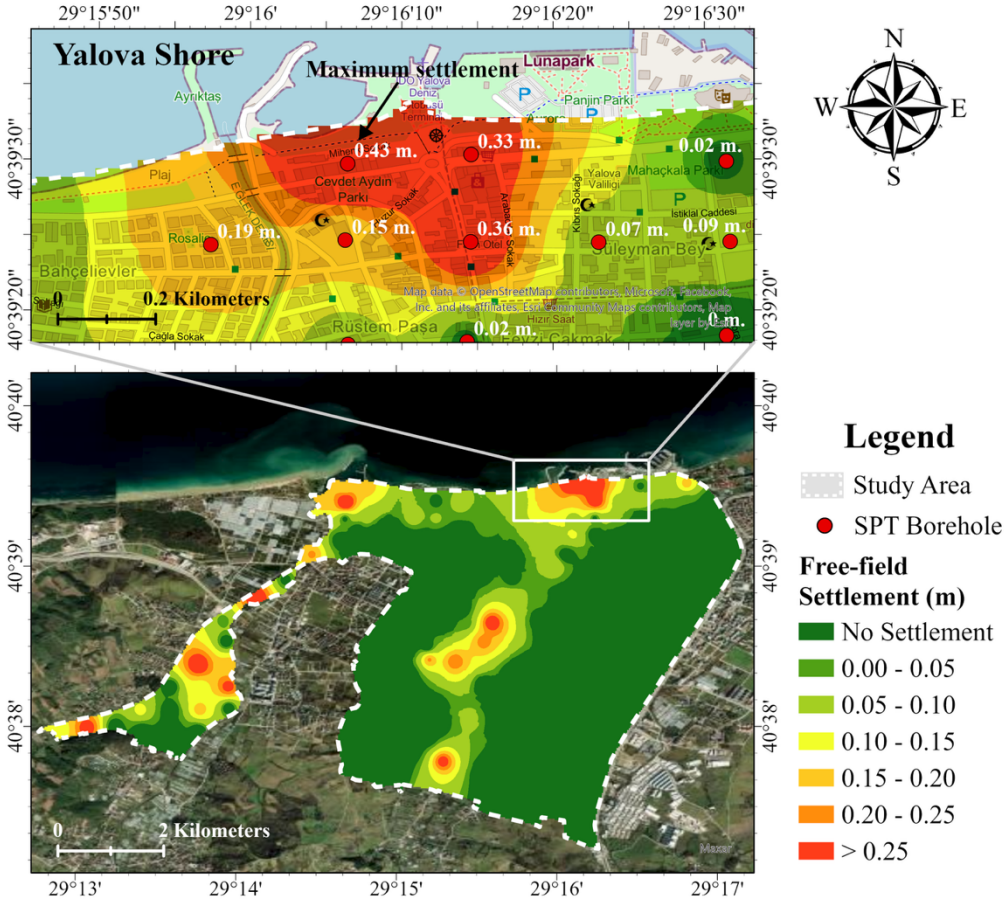


Figure 10.7: Spatial distribution of liquefaction-induced free-field settlements in the Yalova shoreline and city center, estimated using the **Tokimatsu and Seed [1984]** procedure.

10.2.2. Ishihara and Yoshimine [1992] Procedure

According to the free-field settlement analysis carried out with the **Ishihara and Yoshimine [1992]** and **Zhang et al. [2004]** method, the second scenario yielded its maximum value at borehole A-SK-19 on the Yalova Shore, where a settlement of 0.56 meters was calculated. This situation is consistent with the first scenario. The spatial distribution of settlements estimated for the second scenario is illustrated in **Figure 10.8**.

In the second scenario, 62.9% of the study area (7.30 km²) remained unaffected, which is very close to the 62.4% obtained in the first scenario. Settlements in the range of 0.00–0.05 meters covered 0.81 km² (7.02%), nearly identical to the 0.80 km² (6.89%) calculated in the first scenario. The 0.05–0.10 meter range again represented the largest affected portion, with 1.54 km² (13.30%) in the second scenario compared to 1.57 km² (13.55%) in the first. Similarly, the 0.10–0.15 meter interval accounted for 0.79 km²

(6.83%) in the second scenario, slightly lower than the 0.81 km² (6.98%) of the first. The 0.15–0.20 and 0.20–0.25 meter ranges produced nearly the same areal proportions in both scenarios (4.5% and 2.6%). Minor variation was observed in the most severe class, where settlements between 0.25 and 0.45 meters covered 0.33 km² (2.85%) in the second scenario, compared with 0.37 km² (3.15%) in the first.

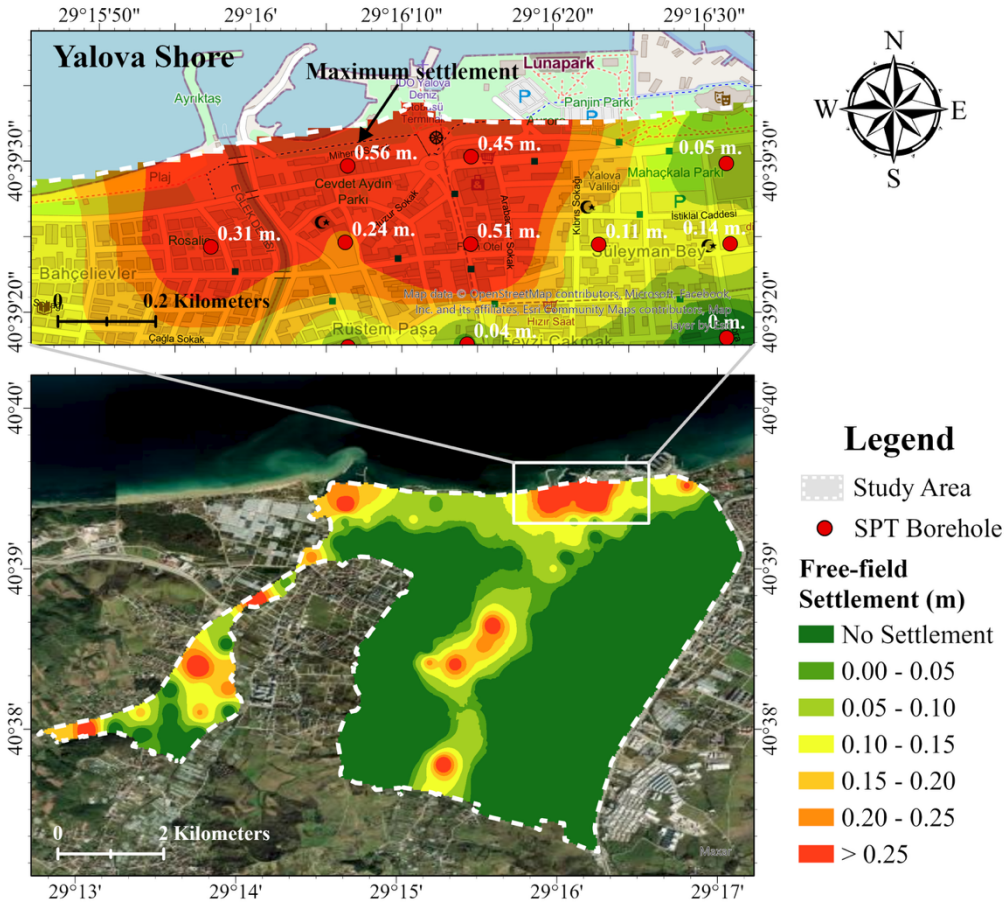


Figure 10.8: Spatial distribution of liquefaction-induced free-field settlements in the Yalova shoreline and city center, estimated using the **Ishihara and Yoshimine [1984]** and **Zhang et al. [2004]** procedure.

Furthermore, when the methods of **Ishihara and Yoshimine [1992]** and **Yoshimine et al. [2006]** are examined, a similar situation to the first scenario is observed. In the second scenario, 63.8% of the study area (7.39 km²) remained unaffected, which is nearly identical to the 63.5% obtained in the first scenario. The 0.05–0.10 m range again represented the largest affected portion, covering 1.59 km² (13.73%), exactly the same proportion as in the first scenario. The 0.00–0.05 m settlements accounted for 0.88 km² (7.60%), also very close to the 0.89 km² (7.65%) previously calculated. Similarly, the 0.10–0.15 m and 0.15–0.20 m ranges were associated with 0.69 km²

(5.97%) and 0.51 km² (4.39%) of the area, respectively, values consistent with those of the first scenario. The highest settlement classes showed only slight differences, with 0.25 km² (2.15%) in the 0.20–0.25 m interval and 0.28 km² (2.39%) in the 0.25–0.45 m interval. The spatial distribution of settlements estimated for the second scenario is illustrated in **Figure 10.9**.

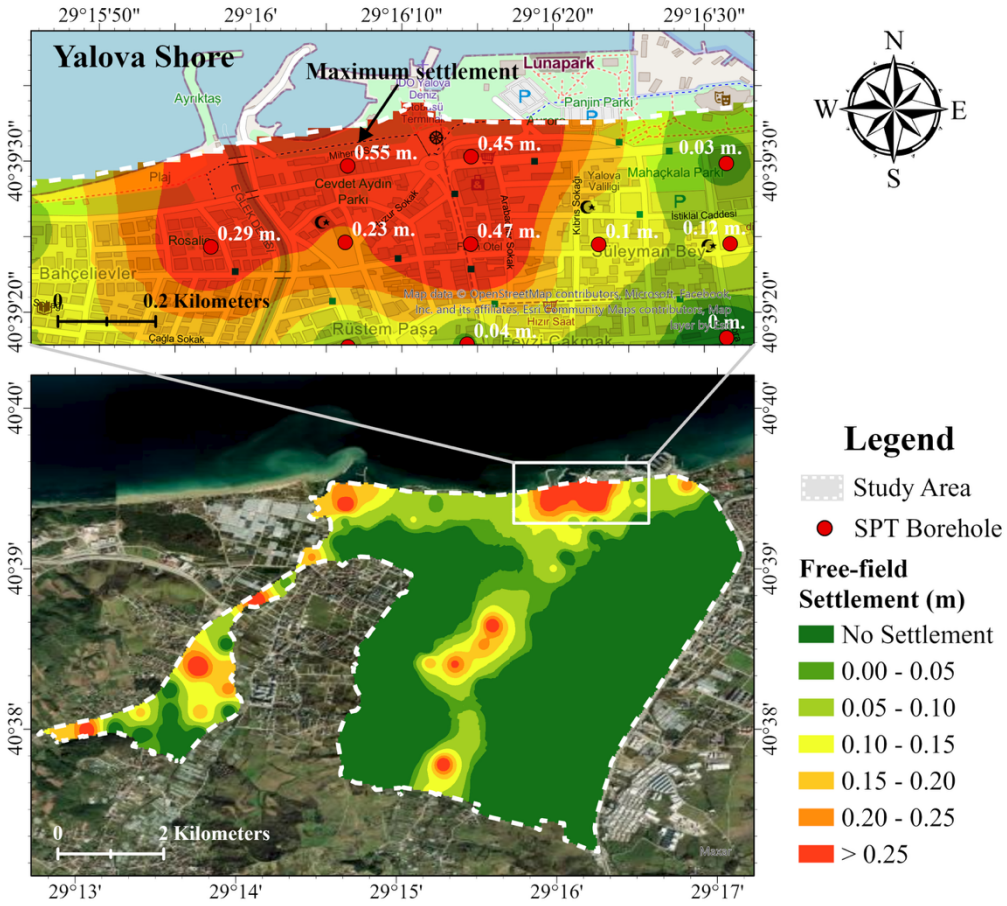


Figure 10.9: Spatial distribution of liquefaction-induced free-field settlements in the Yalova shoreline and city center, estimated using the **Ishihara and Yoshimine [1992]** and **Yoshimine et al. [2006]** procedure.

10.2.3. Shamoto et al. [1998] Procedure

The settlements calculated using the method of **Shamoto et al. [1998]**, similar to the other settlement results, produced outcomes consistent with the first scenario. In the second scenario, 70.4% of the study area (8.17 km²) remained unaffected, a value nearly identical to the 70.0% obtained in the first scenario. The 0.05–0.10 m and 0.00–0.05 m ranges covered 1.17 km² (10.08%) and 1.04 km² (8.96%), respectively, both closely matching the proportions of the first scenario. The 0.10–0.15 m interval

accounted for 0.67 km² (5.80%), while the 0.15–0.20 m range slightly decreased to 0.30 km² (2.58%). Higher settlement classes were limited to small areas, with 0.13 km² (1.12%) in the 0.20–0.25 m range and 0.13 km² (1.09%) in the 0.25–0.45 m range, again consistent with the first scenario. The spatial distribution of settlements for the second scenario is shown in **Figure 10.10**.

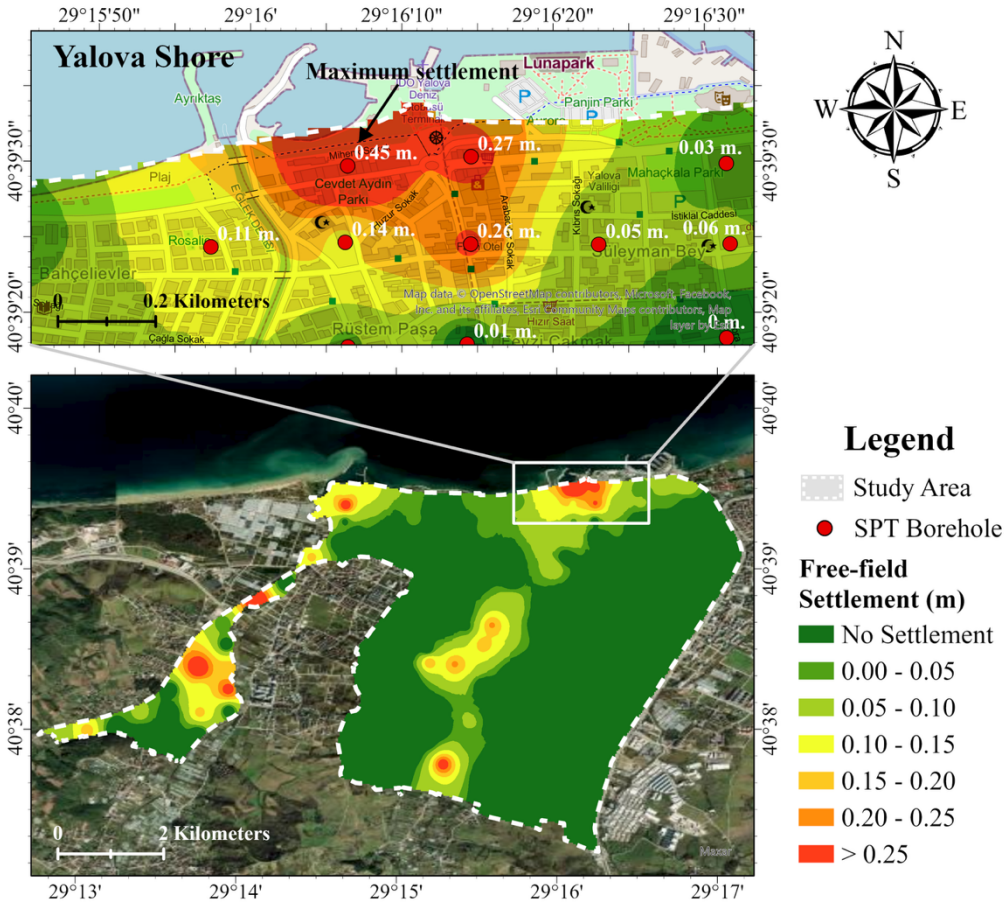


Figure 10.10: Spatial distribution of liquefaction-induced free-field settlements in the Yalova shoreline and city center, estimated using the **Shamoto et al. [1998]** procedure.

10.2.4. Wu et al. [2003] Procedure

The settlements calculated using the method of **Wu et al. [2003]** produced results consistent with those of the first scenario. In the second scenario, 62.9% of the study area (7.27 km²) was classified as unaffected, closely matching the 62.5% obtained in the first scenario. The 0.05–0.10 m interval again represented the largest affected portion, covering 1.59 km² (13.73%), which is nearly identical to the 1.57 km² (13.56%) in the first scenario. The 0.00–0.05 m and 0.10–0.15 m classes accounted for

0.81 km² (7.04%) and 0.78 km² (6.74%), respectively, values comparable to those of the first scenario. Similarly, the 0.15–0.20 m range covered 0.49 km² (4.28%), while the higher settlement classes of 0.20–0.25 m and 0.25–0.45 m were limited to 0.31 km² (2.67%) and 0.30 km² (2.63%), respectively. The spatial distribution of settlements for the second scenario is shown in **Figure 10.11**.

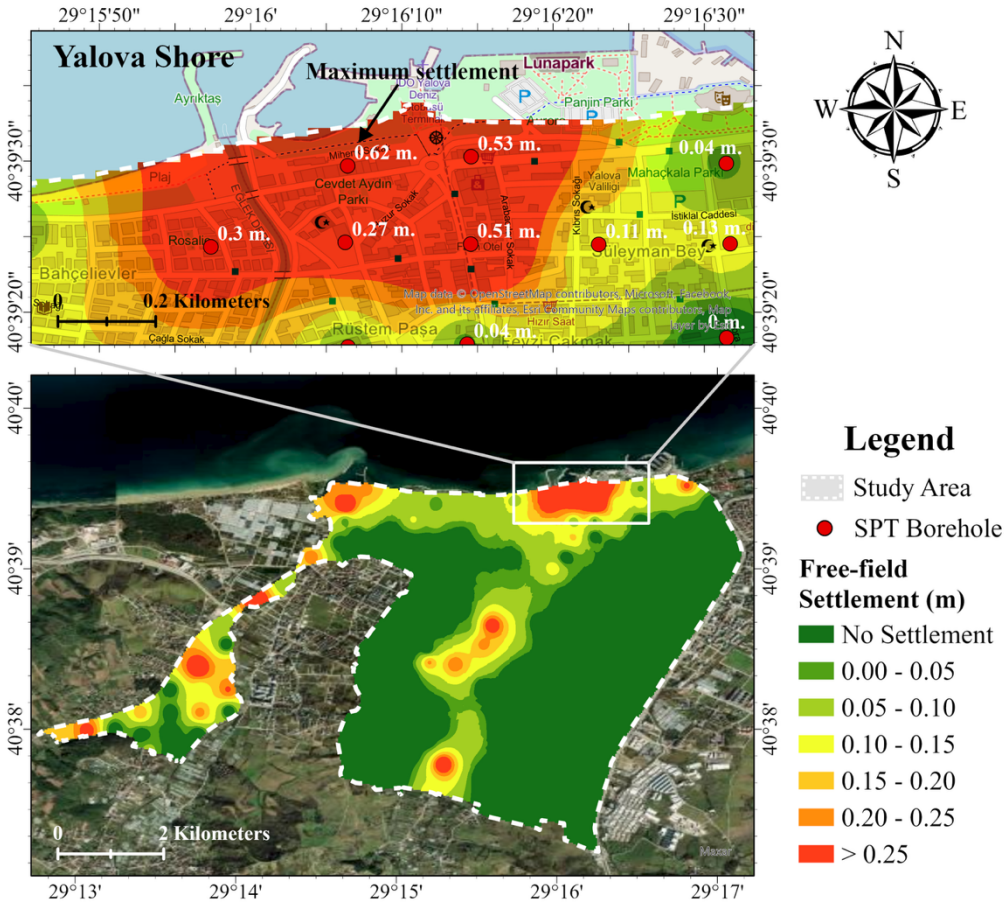


Figure 10.11: Spatial distribution of liquefaction-induced free-field settlements in the Yalova shoreline and city center, estimated using the **Wu et al. [2003]** procedure.

10.2.5. Cetin et al. [2009] Procedure

Similarly, the settlements calculated using the method of **Cetin et al. [2009]** show results in close agreement with the first scenario. In the second scenario, 69.3% of the study area (8.04 km²) remained unaffected, almost identical to the 69.0% obtained in the first scenario. Low levels of settlement in the 0.00–0.05 m range covered 0.92 km² (7.96%), while the 0.05–0.10 m class accounted for 1.54 km² (13.28%), values consistent with the calculated in the first scenario. The 0.10–0.15 m interval was

associated with 0.61 km² (5.27%), slightly lower than the 0.64 km² (5.49%) in the first scenario. Higher settlement classes were more limited, with 0.27 km² (2.31%) in the 0.15–0.20 m range, 0.13 km² (1.12%) in the 0.20–0.25 m range, and 0.09 km² (0.78%) in the 0.25–0.45 m interval. The spatial distribution of settlements for the second scenario is illustrated in **Figure 10.12**.

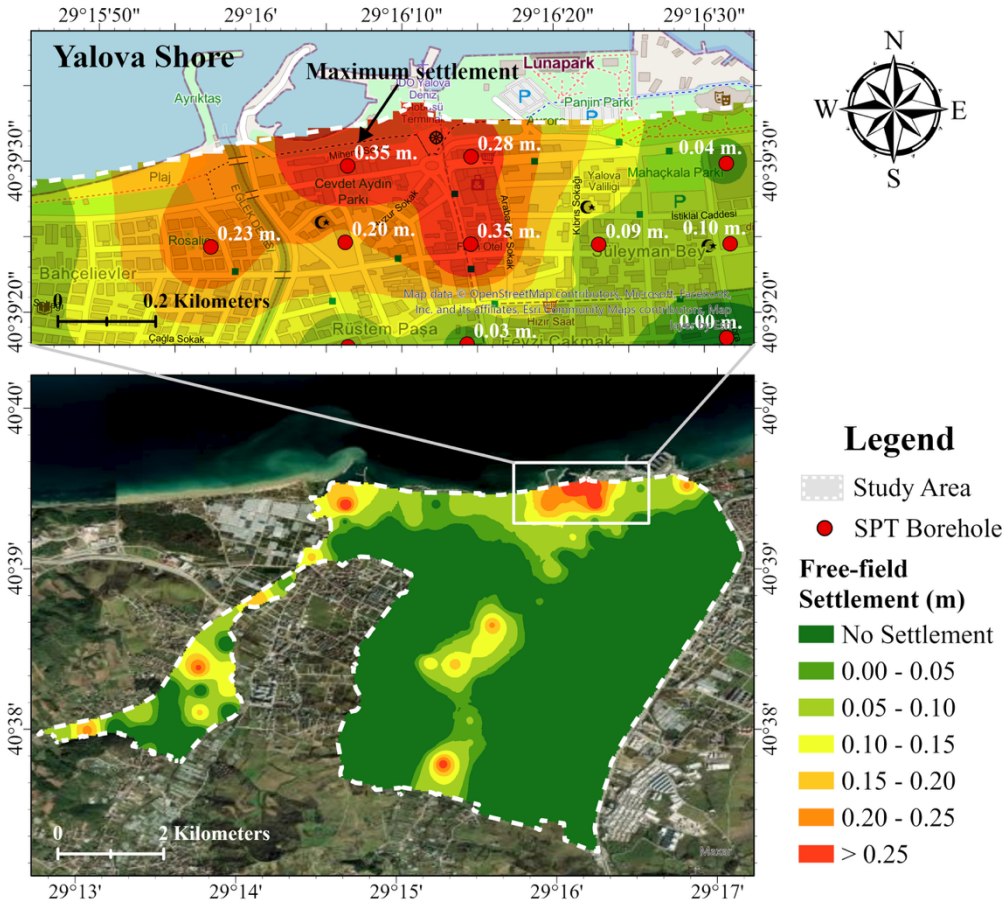


Figure 10.12: Spatial distribution of liquefaction-induced free-field settlements in the Yalova shoreline and city center, estimated using the **Cetin et al. [2009]** procedure.

11. PIPELINE DAMAGE ASSESSMENT OF YALOVA CITY CENTER

Yalova Municipality provides continuous water service to its 157,499 residents in the city center. The city's drinking water is supplied primarily from the Gökçe Dam. The Gökçe Dam, located on the Gökçedere in Termal, Yalova, is a rock-fill structure constructed between 1980 and 1989, with a reservoir capacity of 26 hm³ and a surface area of 1 km² **[DSI, 2025]**. The water released from the Gökçe Dam is conveyed to the treatment plant and subsequently distributed to the city through steel pipelines ranging from 600 to 1,400 mm in diameter and High-density Polyethylene (HDPE) pipelines ranging from 280 to 500 mm (**Figure 11.1**). The transmission system has a total length of approximately 62.94 km, of which 43.16 km (69%) consists of steel pipelines and 19.78 km (31%) consist of HDPE pipelines (**Figure 11.2**). The system also includes 16 water storage tanks with capacities between 50 and 5,000 tons and six pumping stations that support distribution across the service area. These storages consist of buried reinforced concrete and modular structures, with the oldest reservoir constructed in 1984-1985.

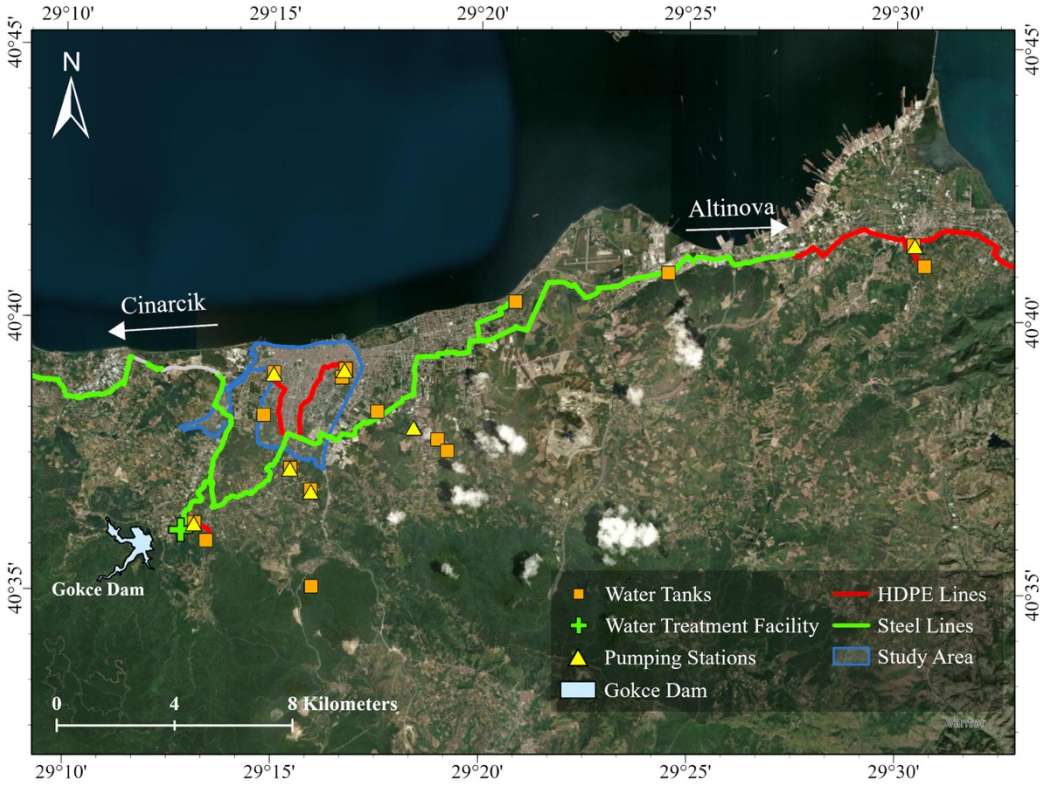


Figure 11.1: Map of the water source, transmission pipelines, storage tanks, and pumping stations in Yalova.

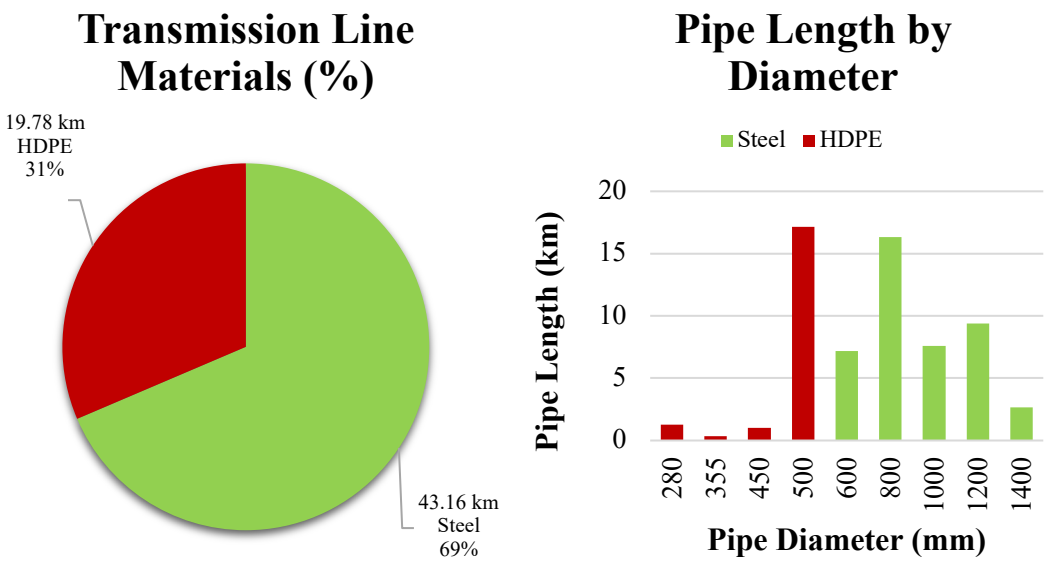


Figure 11.2: Transmission pipeline material distribution and pipe length by diameter for the Yalova Province water supply system.

In the Yalova city center and surrounding villages, the water distribution system comprises approximately 342.78 km of pipelines managed by Yalova Municipality. The network consists of 57.22 km of AC, 130.66 km of HDPE, and 154.89 km of PVC pipes. In proportional terms, AC pipes account for 16.7% of the network, HDPE pipes for 38.1%, and PVC pipes for 45.2% of the total pipeline length (**Figure 11.3**). There is very small amount of steel pipelines (2.9 km) connecting some tanks which are not included in the distribution lines. The spatial distribution of the city's distribution network and its pipe materials is shown in **Figure 11.4**.

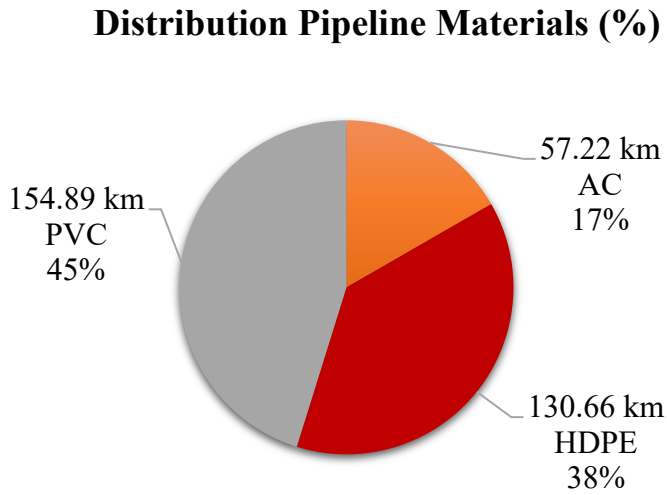


Figure 11.3: Pipeline material percentages within the water distribution network managed by Yalova Municipality.

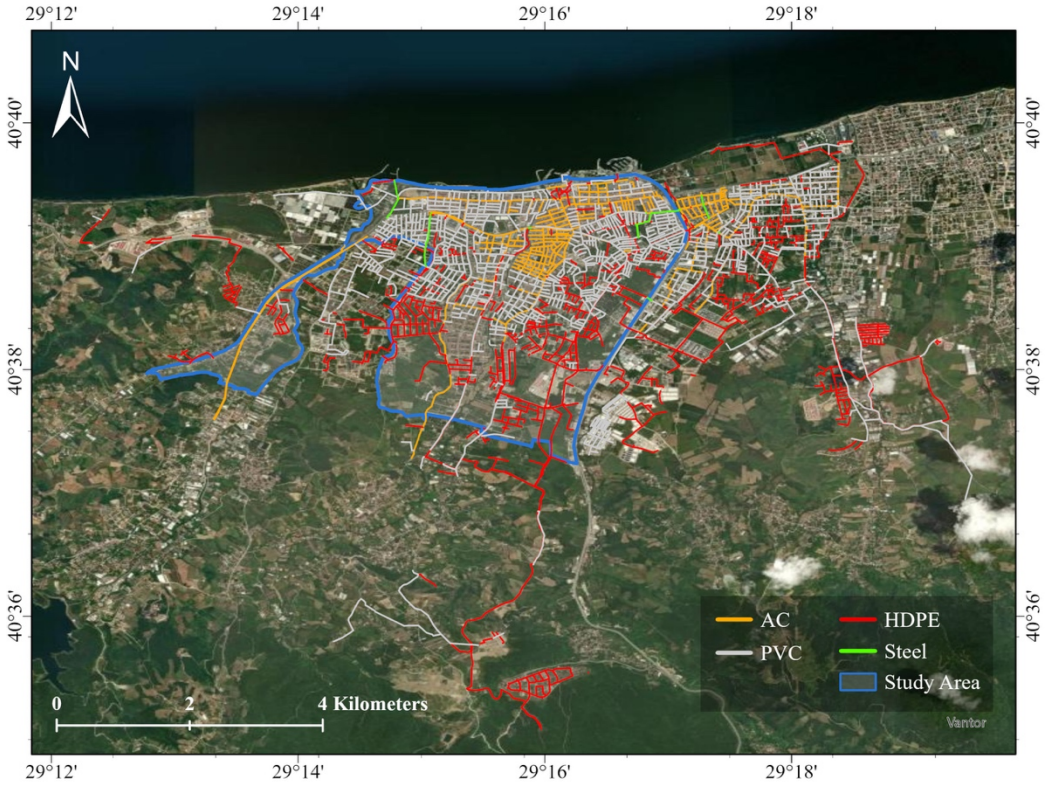


Figure 11.4: Spatial distribution of the water distribution network with respect to pipe materials within the Yalova Municipality water system.

The meetings held with the local water authorities indicate that routine maintenance and repair operations within the water distribution network are primarily on AC and PVC pipelines, The AC pipelines represent the oldest component of the network and were installed prior to the 1990s. In AC pipes, maintenance activities are mainly associated with leakage at joint connections, while localized deterioration of pipe profiles due to aging has also been observed in some sections. After the installation of AC pipelines stopped, PVC pipelines were commonly used in the system. In the last two decades, HDPE pipelines have been introduced to replace aging pipelines. The future renewal activities are planned to further upgrade the water distribution network using HDPE pipelines.

Post-earthquake observations following the 1999 Kocaeli earthquake provide additional insight into material-specific damage characteristics within the water distribution network. These observations indicate that substantial damage occurred in both AC and PVC pipelines during the 1999 event. In PVC pipelines, damage primarily occurred in the form of pipe-body buckling rather than joint-related failures. In contrast, AC pipelines, which were typically constructed in segments of

approximately 5 m, exhibited damage at pipe body and joint connections Following the 1999 Kocaeli earthquake, damaged sections of the water network were replaced with HDPE pipes.

The infrastructure risk assessment of Yalova city center was carried out under two earthquake scenarios: the Mw 7.5 design event defined in TBEC and the Mw 7.0 Prince Islands earthquake. As an initial step, the water pipeline layers were clipped to the study area using the Clip tool in ArcGIS Pro to ensure spatial consistency between the hazard and network datasets. The total network length prior to clipping was 342.78 km, whereas the portion falling within the study boundary measured 181.46 km (**Figure 11.5**).

All subsequent analyses were conducted exclusively on the water distribution lines within the study area, as the majority of transmission lines extend beyond the study boundaries. The transmission lines traverse long distances and pass through multiple geological and geotechnical hazard zones that fall outside the scope of this study; therefore, they were not evaluated within this thesis. To ensure spatial consistency and methodological coherence, the analyses were focused on the distribution network. The results corresponding to both earthquake scenarios are presented in detail in the following sections.

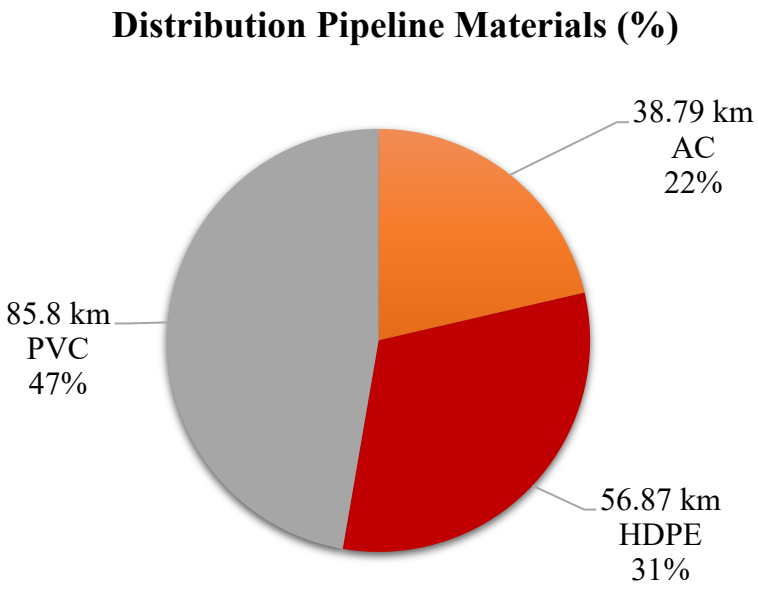


Figure 11.5: Distribution pipeline material percentages in the study area.

11.1. Scenario 1: TBEC 2018 Mw 7.5 Earthquake

As an initial step, the pipeline network was separated into liquefiable and non-liquefiable zones based on the LPI and LSN maps. The details of Scenario 1 are presented in Section 9. The spatial classification of pipelines based on LPI and LSN are presented in **Figures 11.6 and 11.7**, respectively, while the LPI and LSN maps are shown in **Figures 9.8 and 9.10**. The LPI and LSN maps were generated using the procedure of **Boulanger and Idriss [2014]** and the fines content criteria proposed by **Bray and Sancio [2006]** together with the probabilistic TBEC ground motions corresponding to a 475-year return period. The results indicate that, based on the LPI assessment, approximately 37.8% of the pipelines are located within liquefiable areas, whereas 62.2% lie in non-liquefiable zones. The distribution of these pipelines with respect to material type is illustrated in **Figure 11.8**. Similarly, the LSN-based evaluation indicates that 31.8% of the pipeline network falls within liquefiable areas, while 68.2% is located within non-liquefiable zones, with the corresponding material-based distribution shown in **Figure 11.9**.

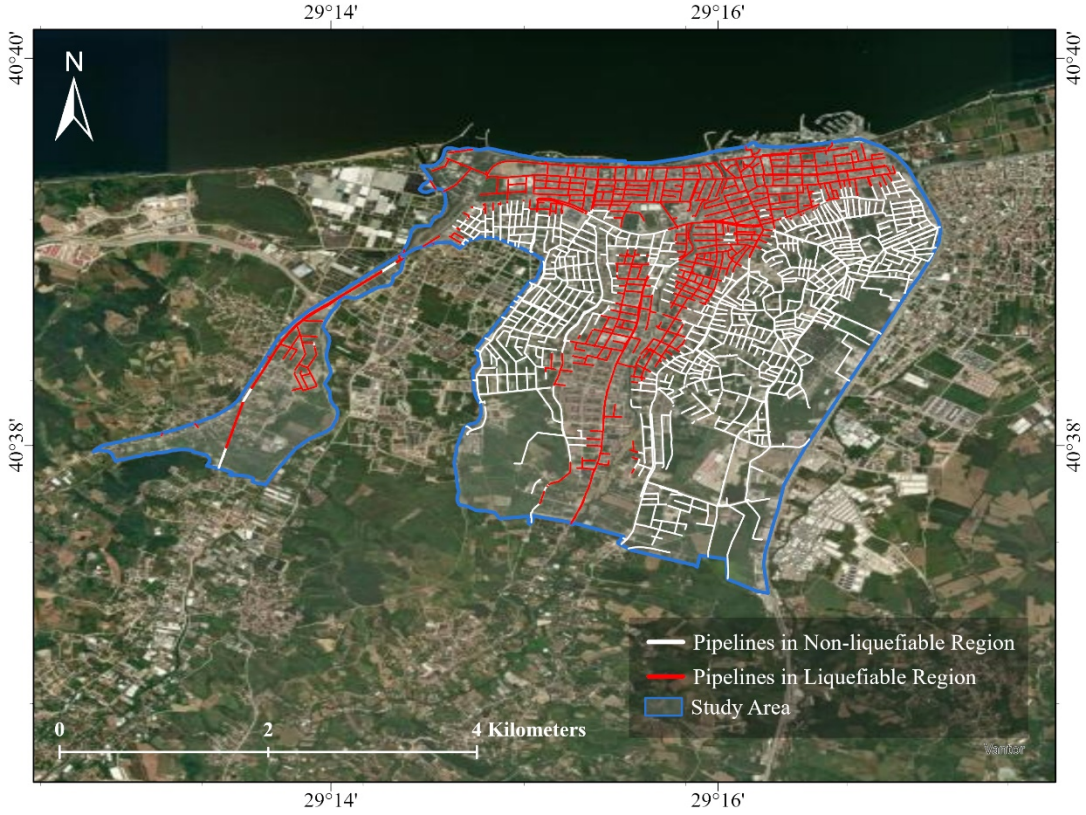


Figure 11.6: Spatial distribution of the water distribution network within liquefiable and non-liquefiable regions based on the LPI map.

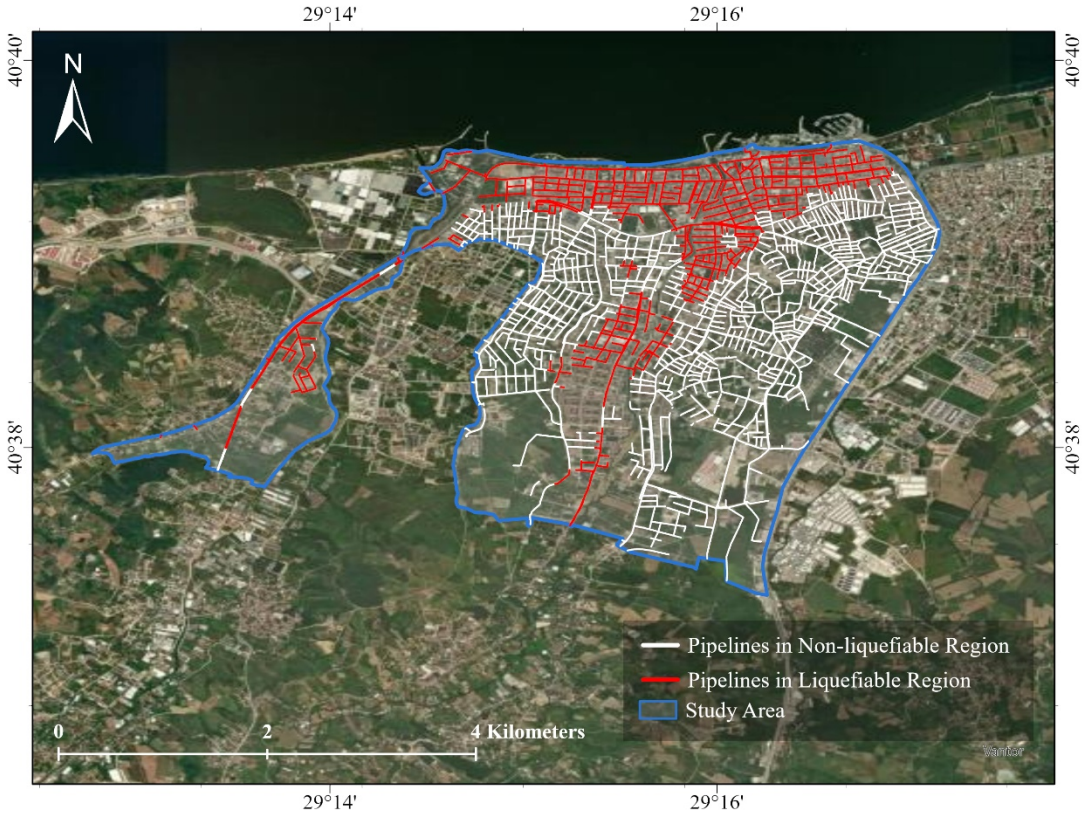


Figure 11.7: Spatial distribution of the water distribution network within liquefiable and non-liquefiable regions based on the LSN map.

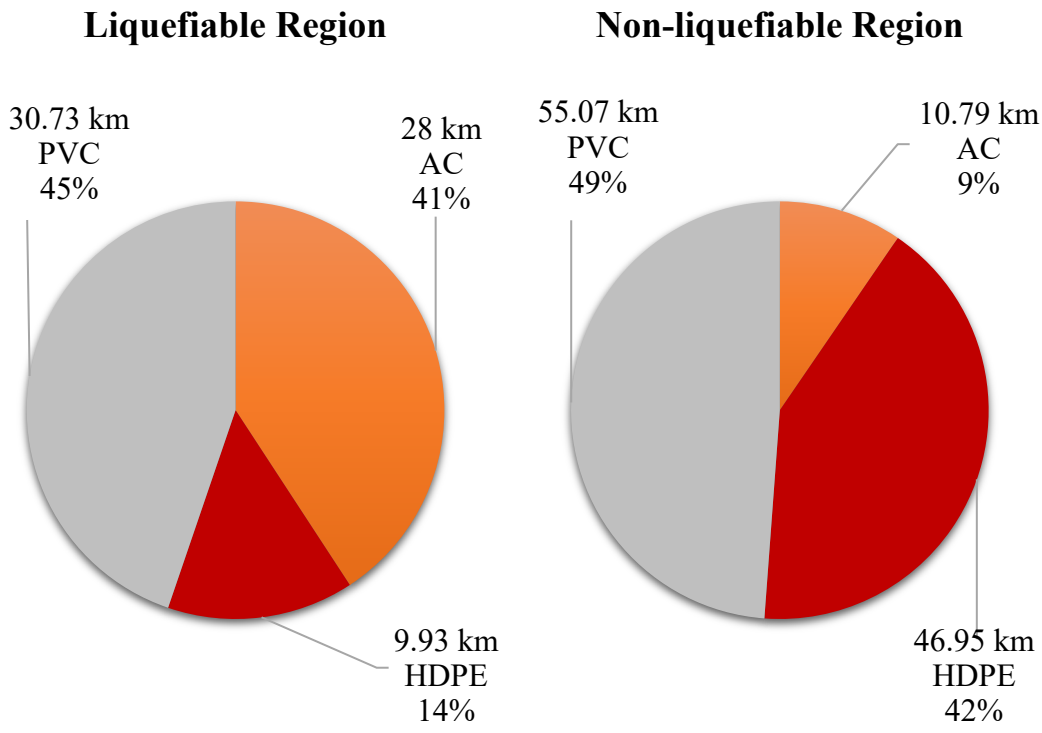


Figure 11.8: Distribution of pipeline materials and their corresponding lengths within liquefied and non-liquefied zones based on LPI in the study area.

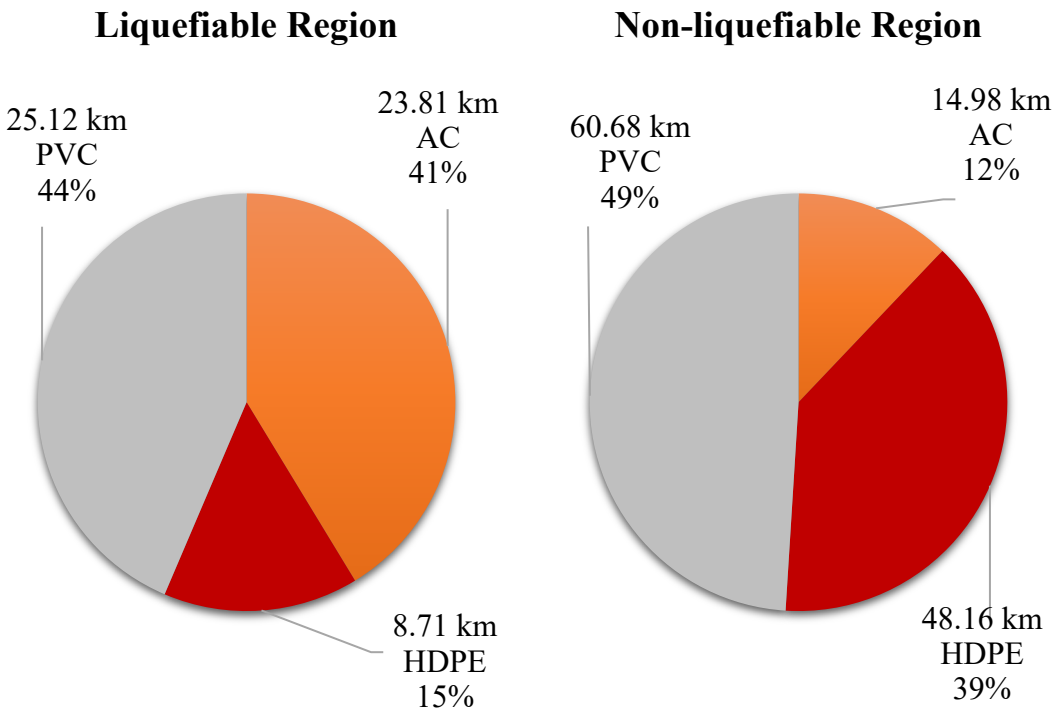


Figure 11.9: Distribution of pipeline materials and their corresponding lengths within liquefied and non-liquefied zones based on LSN in the study area.

Following the delineation of liquefiable and non-liquefiable zones based on the LSN and LPI assessments, pipeline lengths in non-liquefiable areas were classified by PGV intervals to support the prediction of TGD-induced damages. For this purpose, the PGV values for the TBEC-based Mw 7.5 scenario were obtained from the Türkiye Earthquake Hazard Map. The PGV raster was classified into integer PGV intervals and converted to polygon features to enable spatial analysis. These PGV classes were then intersected with the water pipeline network, allowing each pipeline segment to be assigned its corresponding PGV value. The length of each segment was calculated in the attribute table, and the cumulative pipeline lengths within the PGV intervals, based on the non-liquefiable zones identified using the LPI and LSN maps, were determined and summarized in **Tables 11.1 and 11.2**.

Table 11.1: Total lengths of pipelines within each PGV interval in non-liquefiable regions identified based on the LPI assessment.

PGV (cm/s)	AC	HDPE	PVC	Total (km)
35-40	0.29	6.92	1.42	8.64
40-45	10.50	40.02	53.65	10.50
Total (km)	10.79	46.95	55.07	112.81

Table 11.2: Total lengths of pipelines within each PGV interval in non-liquefiable regions identified based on the LSN assessment.

PGV (cm/s)	AC	HDPE	PVC	Total (km)
35-40	0.46	6.92	1.42	8.80
40-45	14.52	41.24	59.26	115.02
Total (km)	14.98	48.16	60.68	123.82

Furthermore, in liquefiable zones, pipeline lengths were subsequently categorized by LPI and LSN intervals to evaluate PGD-induced damages (**Tables 11.3 and 11.4**).

Table 11.3: Total lengths of pipelines within each LPI interval in liquefiable regions.

LPI	AC	HDPE	PVC	Total (km)
0-5	5.59	1.07	6.05	12.71
5-10	8.31	2.77	7.96	19.03
10-15	6.16	2.36	7.15	15.68
15-20	5.17	1.63	4.76	11.55
20-25	0.94	0.48	1.80	3.22
25-30	0.41	0.26	0.83	1.50
30-35	0.64	0.40	0.65	1.69
35-40	0.52	0.94	1.12	2.59
40-45	0.26	0.02	0.32	0.60
45-50			0.03	0.03
50-55			0.06	0.06
55-60			0.01	0.01
Total (km)	28.00	9.92	30.73	68.66

Table 11.4: Total lengths of pipelines within each LSN interval in liquefiable regions.

LSN	AC	HDPE	PVC	Total (km)
5-10	8.40	2.69	7.67	18.75
10-15	6.88	2.30	8.55	17.73
15-20	4.80	1.49	3.70	9.99
20-25	1.97	0.65	2.12	4.74
25-30	0.76	0.29	1.06	2.11
30-35	0.61	1.05	1.23	2.89
35-40	0.29	0.22	0.44	0.95
40-45	0.03	0.02	0.13	0.18
45-50	0.06		0.07	0.13
50-55	0.01		0.02	0.04
55-60			0.01	0.01
60-65			0.03	0.03
65-70			0.01	0.01
70-75			0.04	0.04
75-80			0.02	0.02
Total (km)	23.81	8.71	25.12	57.64

Following that, TGD-induced number of damages were predicted using the correlations developed in this study for Kahramanmaraş, as well as those proposed by **O'Rourke et al. [2014]**, **ALA [2001]**, **HAZUS**, and **Shih and Chang [2006]**. For PGD-induced damages, the relationships between LPI, LSN and repair rates proposed by **Toprak et al. [2019]**, together with the corresponding one-dimensional volumetric reconsolidation settlement (S_{v1D})-RR formulations were employed. The free-field settlements required for the S_{v1D} calculations were obtained using the **Ishihara and Yoshimine [1992]** procedure, as previously detailed in Chapter 10. This method was selected to maintain consistency with the original development of the S_{v1D}-RR relationships in **Toprak et al. [2019]**, while yielding settlement estimates comparable to those obtained using the **Wu et al. [2003]** approach, which provides maximum settlement values in the study area. The total lengths of pipelines within each free-field settlement interval are presented in **Table 11.5**.

Table 11.5: Total lengths of pipelines within S_{v1D} interval in liquefiable zones, calculated using the **Ishihara and Yoshimine [1992]** method.

S_{v1D} (cm)	AC	HDPE	PVC	Total (km)
1-5	4.29	0.39	2.41	7.09
5-10	9.46	2.08	10.42	21.96
10-15	4.73	1.29	5.01	11.03
15-20	1.94	1.86	2.48	6.28
20-25	1.09	1.33	1.68	4.10
25-30	0.80	0.80	1.20	2.80
30-35	0.27	0.33	0.45	1.05
35-40	0.32	0.31	0.12	0.75
40-45	0.23	0.20	0.37	0.80
45-50	0.11	0.02	0.06	0.19
50-55	0.07		0.04	0.11
Total (km)	23.31	8.61	24.24	56.16

The study provided separate repair rate equations corresponding to liquefaction probabilities of 15%, 50%, and 85%. Because liquefaction in the present study was assessed deterministically using the **Boulanger and Idriss [2014]** procedure, and since the 15% probability curve is commonly adopted for deterministic liquefaction evaluations, the equation corresponding to the 15% probability of liquefaction was used.

The damage predictions for the Yalova city center with respect to pipe materials, obtained using the available repair-rate relationships, are presented in **Tables 11.6 and 11.7**. These predictions were performed separately for liquefiable and non-liquefiable regions delineated based on the LPI- and LSN-based zonation approaches, which result in different pipeline lengths within each region and consequently affect the estimated number of damages. However, this distinction does not influence the settlement-based damage estimates, since pipeline lengths associated with settlements were determined directly based on the computed settlement magnitudes rather than the spatial extent of the liquefiable zones.

Table 11.6: Summary of the predicted number of damages for Scenario 1 based on the available repair-rate relationships in the literature, considering liquefiable and non-liquefiable regions identified using the LPI map.

	Transient Ground Deformation			**Permanent Ground Deformation**		
Pipe Materials	**Sources**	**Equations**	**Estimated Damages**	**Sources**	**Equations**	**Estimated Damages**
AC	Kahramanmaraş Case Study	$RR = 0.1535(PGV) - 2.8421$	40	Toprak et al. [2019]	$RR = 0.16LPI + 1.63$	99
	O'Rourke et al. [2014]	$log(RR) = 2.83log(PGV) - 5$	6			
	ALA [2001]	$RR = 0.0024(PGV)K_1$ $K_1 = 1.0$	3		$RR = 0.01S_{v1D} + 2.02$	78
	HAZUS	$RR = 0.0001(PGV)^{2.25}$	6			
PVC	Kahramanmaraş Case Study	$RR = 0.0744(PGV) + 0.7486$	191	Toprak et al. [2019]	$RR = 0.08LPI - 0.30$	30
	Shih and Chang [2006]	$log(RR) = 0.99log(PGV) - 2.30$	13			
	ALA [2001]	$RR = 0.0024(PGV)K_1$ $K_1 = 0.5$	4		$RR = 0.02S_{v1D} - 0.84$	45
	HAZUS	$RR = 0.0001(PGV)^{2.25}$	26			
HDPE	Kahramanmaraş Case Study	$RR = 0.0996(PGV) - 1.9848$	103			

Table 11.7: Summary of the predicted number of damages for Scenario 1 based on the available repair-rate relationships in the literature, considering liquefiable and non-liquefiable regions identified using the LSN map.

	Transient Ground Deformation			Permanent Ground Deformation		
Pipe Materials	**Sources**	**Equations**	**Estimated Damages**	**Sources**	**Equations**	**Estimated Damages**
AC	Kahramanmaraş Case Study	$RR = 0.1535(PGV) - 2.8421$	56	Toprak et al. [2019]	$RR = 0.03LSN + 2.33$	71
	O'Rourke et al. [2014]	$log(RR) = 2.83log(PGV) - 5$	7			
	ALA [2001]	$RR = 0.0024(PGV)K_1$ $K_1 = 1.0$	3		$RR = 0.01S_{v1D} + 2.02$	78
	HAZUS	$RR = 0.0001(PGV)^{2.25}$	8			
PVC	Kahramanmaraş Case Study	$RR = 0.0744(PGV) + 0.7486$	211	Toprak et al. [2019]	$RR = 0.08LSN - 0.79$	22
	Shih and Chang [2006]	$log(RR) = 0.99log(PGV) - 2.30$	14			
	ALA [2001]	$RR = 0.0024(PGV)K_1$ $K_1 = 0.5$	5		$RR = 0.02S_{v1D} - 0.84$	45
	HAZUS	$RR = 0.0001(PGV)^{2.25}$	29			
HDPE	Kahramanmaraş Case Study	$RR = 0.0996(PGV) - 1.9848$	106			

11.2. Scenario 2: Prince Islands Mw 7.0 Earthquake

Similarly, the same procedure was applied for Scenario 2, in which the pipeline network was classified using both the LPI and LSN maps derived from the stochastic ground-motion simulations of the MARTEST–SATREPS project for the Mw 7.0 Prince Islands earthquake scenario. These maps allowed the identification of liquefiable and non-liquefiable regions under the corresponding ground-motion conditions. The spatial distribution of pipelines within liquefiable and non-liquefiable regions for Scenario 2 is shown in **Figures 11.10 and 11.11**. The results indicate that, based on the LPI assessment, approximately 36.7% of the pipelines are located within liquefiable areas, while the remaining 63.3% fall within non-liquefiable zones. The distribution of these pipelines with respect to material type is illustrated in **Figure 11.12**. In comparison, the LSN-based evaluation indicates that 31.3% of the pipeline network lies within liquefiable regions, whereas 68.7% is located in non-liquefiable zones, with the corresponding material-based distribution shown in **Figure 11.13**.

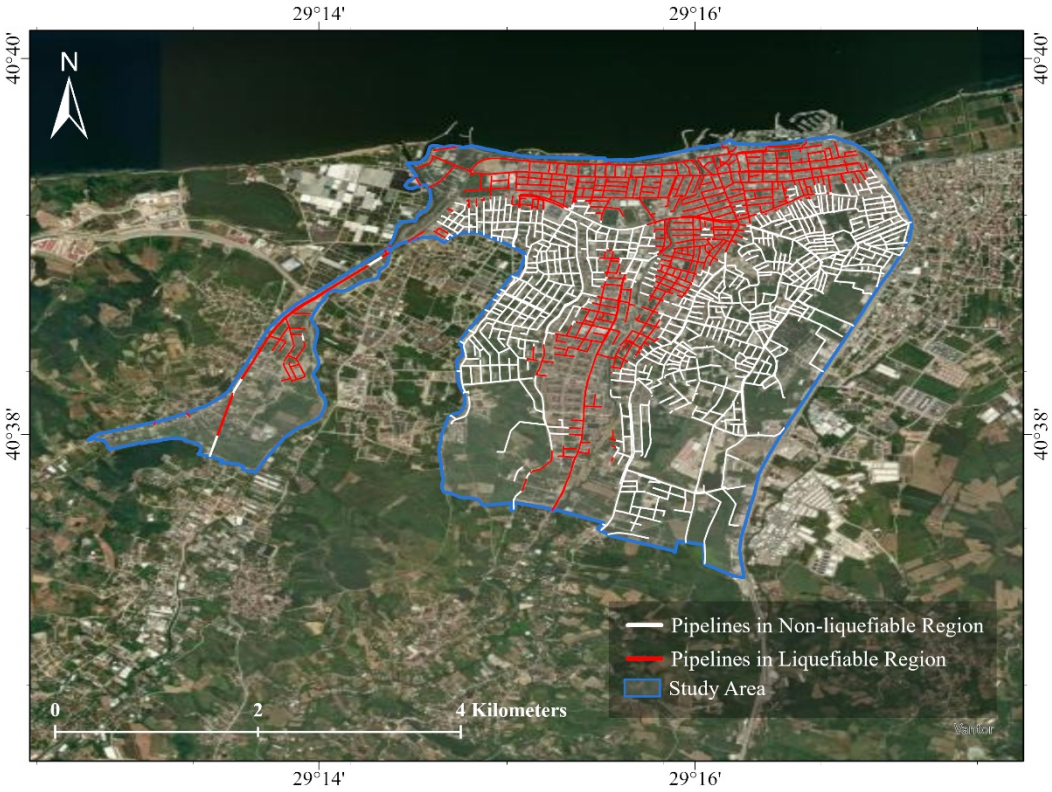


Figure 11.10: Spatial distribution of the water distribution network within liquefiable and non-liquefiable regions based on the LPI map.

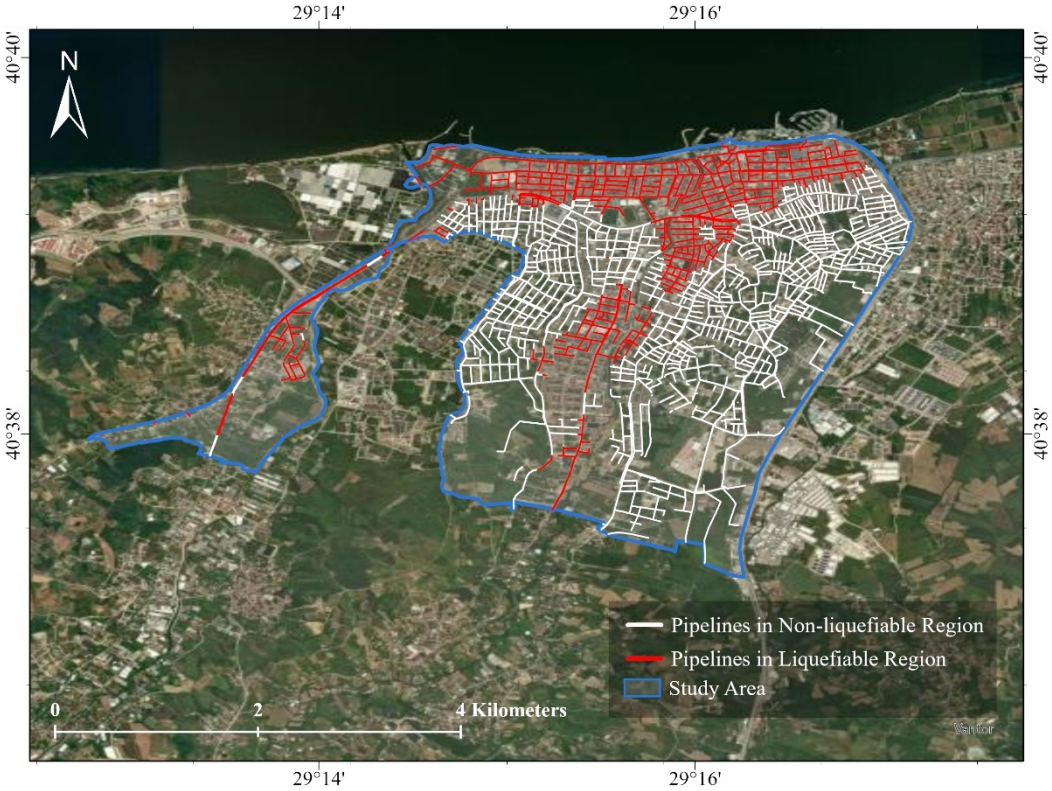


Figure 11.11: Spatial distribution of the water distribution network within liquefiable and non-liquefiable regions based on the LSN map.

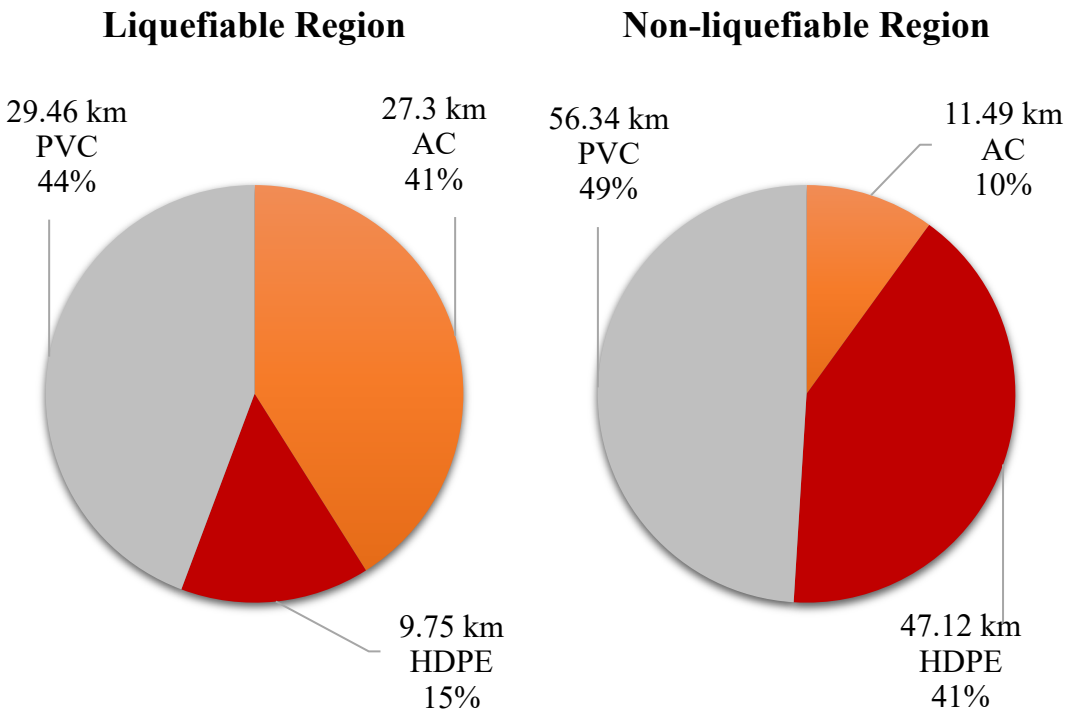


Figure 11.12: Distribution of pipeline materials and their corresponding lengths within liquefied and non-liquefied zones based on LPI in the study area.

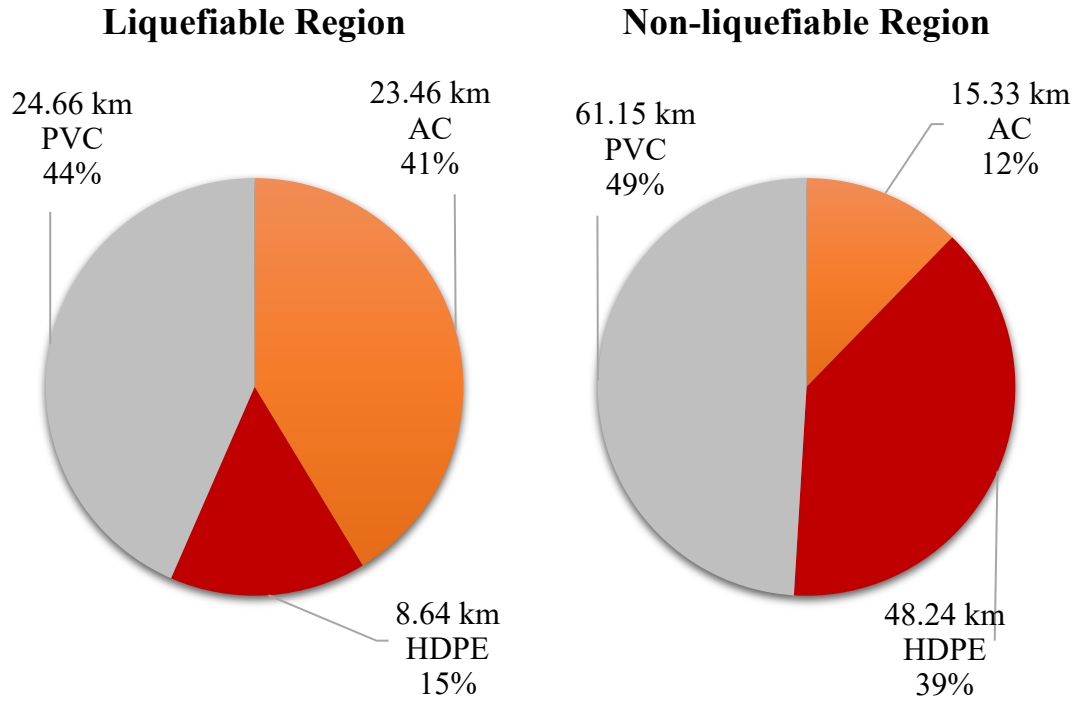


Figure 11.13: Distribution of pipeline materials and their corresponding lengths within liquefied and non-liquefied zones based on LSN in the study area.

Following the identification of non-liquefiable areas based on the LPI- and LSN-based classifications, pipeline lengths within these regions were classified by PGV intervals for use in estimating TGD-induced damages. The PGV values were derived from the Mw 7.0 Prince Islands ground-motion outputs of the MARTEST–SATREPS project and converted into a continuous PGV surface using IDW interpolation. The resulting raster was processed to create integer PGV classes, which were subsequently converted to polygon features for spatial analysis. These classes were intersected with the pipeline network, enabling each segment to be assigned its corresponding PGV value. Segment lengths were then computed, and the cumulative pipeline lengths within each PGV interval were determined separately for the non-liquefiable zones identified using the LPI and LSN maps, and summarized in **Tables 11.8 and 11.9**, respectively.

Table 11.8: Total lengths of pipelines within each PGV interval in non-liquefiable regions identified based on the LPI assessment.

PGV (cm/s)	AC	HDPE	PVC	Total (km)
50-55	1.97	32.88	13.00	47.85
55-60	9.51	14.24	43.34	67.09
Total (km)	11.48	47.12	56.34	114.94

Table 11.9: Total lengths of pipelines within each PGV interval in non-liquefiable regions identified based on the LSN assessment.

PGV (cm/s)	AC	HDPE	PVC	Total (km)
50-55	2.23	33.64	13.46	49.33
55-60	13.10	14.60	47.69	75.38
Total (km)	15.33	48.24	61.15	124.71

In addition, within liquefiable areas, pipeline lengths were classified by LPI and LSN intervals to evaluate PGD-induced damages (**Tables 11.10 and 11.11**).

Table 11.10: Total lengths of pipelines within each LPI interval in liquefiable regions.

LPI	AC	HDPE	PVC	Total (km)
0-5	5.81	1.40	6.10	13.39
5-10	7.89	3.03	8.81	19.89
10-15	6.63	2.29	6.83	15.83
15-20	4.17	1.12	3.17	8.62
20-25	1.03	0.26	1.62	3.04
25-30	0.40	0.40	0.88	1.83
30-35	0.67	0.43	0.84	1.94
35-40	0.50	0.82	0.84	2.16
40-45	0.20		0.29	0.48
45-50			0.02	0.02
50-55			0.07	0.07
Total (km)	27.30	9.75	29.46	67.26

Table 11.11: Total lengths of pipelines within each LSN interval in liquefiable regions.

LSN	AC	HDPE	PVC	Total (km)
5-10	8.17	2.71	7.91	18.79
10-15	6.97	2.21	8.34	17.52
15-20	4.66	1.48	3.44	9.59
20-25	1.91	0.65	2.00	4.56
25-30	0.82	0.32	1.02	2.17
30-35	0.56	1.06	1.22	2.83
35-40	0.25	0.18	0.41	0.85
40-45	0.03	0.02	0.11	0.15
45-50	0.06		0.07	0.14
50-55	0.01		0.02	0.04
55-60			0.03	0.03
60-65			0.01	0.01
65-70			0.01	0.01
70-75			0.04	0.04
75-80			0.02	0.02
Total (km)	23.46	8.64	24.66	56.75

For Scenario 2, estimation of TGD-induced damages followed the same analytical framework, employing the correlations developed in this study together with those of **O'Rourke et al. [2014]**, **ALA [2001]**, **HAZUS**, and **Shih and Chang [2006]**. PGD-induced damages were likewise evaluated using the LPI, LSN and S_{v1D}–repair-rate relationships of **Toprak et al. [2019]**, with the 15% liquefaction-probability curve adopted for consistency with the deterministic liquefaction assessment based on the **Boulanger and Idriss [2014]** procedure. The total lengths of pipelines within each free-field settlement interval are presented in **Table 11.12**.

Table 11.12: Total lengths of pipelines within S_{v1D} interval in liquefiable zones, calculated using the **Ishihara and Yoshimine [1992]** method.

S_{v1D} (cm)	AC	HDPE	PVC	Total (km)
1-5	4.38	0.34	2.71	7.43
5-10	9.40	2.10	10.64	22.14
10-15	4.68	1.28	4.48	10.44
15-20	1.89	1.84	2.52	6.25
20-25	1.14	1.42	1.59	4.15
25-30	0.75	0.74	1.16	2.65
30-35	0.27	0.31	0.42	1.00
35-40	0.32	0.33	0.12	0.77
40-45	0.23	0.16	0.37	0.76
45-50	0.11	0.02	0.06	0.19
50-55	0.07		0.04	0.11
Total	23.24	8.54	24.11	55.89

The corresponding damage predictions with respect to pipe materials are summarized in **Tables 11.13 and 11.14**, with liquefiable and non-liquefiable regions defined based on the LPI and LSN classifications, respectively.

Table 11.13: Summary of the predicted number of damages for Scenario 2 based on the available repair-rate relationships in the literature, considering liquefiable and non-liquefiable regions identified using the LPI map.

	Transient Ground Deformation			Permanent Ground Deformation		
Pipe Materials	**Sources**	**Equations**	**Estimated Damages**	**Sources**	**Equations**	**Estimated Damages**
AC	Kahramanmaraş Case Study	$RR = 0.1535(PGV) - 2.8421$	68	Toprak et al. [2019]	$RR = 0.16LPI + 1.63$	95
	O'Rourke et al. [2014]	$log(RR) = 2.83log(PGV) - 5$	12			
	ALA [2001]	$RR = 0.0024(PGV)K_1$ $K_1 = 1.0$	3		$RR = 0.01S_{v1D} + 2.02$	78
	HAZUS	$RR = 0.0001(PGV)^{2.25}$	11			
PVC	Kahramanmaraş Case Study	$RR = 0.0744(PGV) + 0.7486$	273	Toprak et al. [2019]	$RR = 0.08LPI - 0.30$	25
	Shih and Chang [2006]	$log(RR) = 0.99log(PGV) - 2.30$	16			
	ALA [2001]	$RR = 0.0024(PGV)K_1$ $K_1 = 0.5$	5		$RR = 0.02S_{v1D} - 0.84$	44
	HAZUS	$RR = 0.0001(PGV)^{2.25}$	50			
HDPE	Kahramanmaraş Case Study	$RR = 0.0996(PGV) - 1.9848$	161			

Table 11.14: Summary of the predicted number of damages for Scenario 2 based on the available repair-rate relationships in the literature, considering liquefiable and non-liquefiable regions identified using the LSN map.

	Transient Ground Deformation			Permanent Ground Deformation		
Pipe Materials	**Sources**	**Equations**	**Estimated Damages**	**Sources**	**Equations**	**Estimated Damages**
AC	Kahramanmaraş Case Study	$RR = 0.1535(PGV) - 2.8421$	91	Toprak et al. [2019]	$RR = 0.03LSN + 2.33$	69
	O'Rourke et al. [2014]	$log(RR) = 2.83log(PGV) - 5$	15			
	ALA [2001]	$RR = 0.0024(PGV)K_1$ $K_1 = 1.0$	3		$RR = 0.01S_{v1D} + 2.02$	78
	HAZUS	$RR = 0.0001(PGV)^{2.25}$	14			
PVC	Kahramanmaraş Case Study	$RR = 0.0744(PGV) + 0.7486$	296	Toprak et al. [2019]	$RR = 0.08LSN - 0.79$	22
	Shih and Chang [2006]	$log(RR) = 0.99log(PGV) - 2.30$	18			
	ALA [2001]	$RR = 0.0024(PGV)K_1$ $K_1 = 0.5$	5		$RR = 0.02S_{v1D} - 0.84$	44
	HAZUS	$RR = 0.0001(PGV)^{2.25}$	54			
HDPE	Kahramanmaraş Case Study	$RR = 0.0996(PGV) - 1.9848$	165			

Comparison of the two scenarios shows that TGD-induced predicted damages are higher in Scenario 2. This difference reflects the PGV levels considered in the analyses: Scenario 1 exhibits PGV values of approximately 38–45 cm/s, whereas Scenario 2 is characterized by stronger shaking with PGV values between 50 and 60 cm/s. Since all repair-rate relationships increase with PGV, the elevated PGV levels in Scenario 2 result in larger damage estimates for AC, PVC, and HDPE pipelines.

For PGD-induced damages, the estimates show a modest decrease from Scenario 1 to Scenario 2. For instance, based on the LSN-based liquefiable and non-liquefiable zonation, the PGD-induced predicted damages for Scenario 1 are 71 for AC pipelines and 22 for PVC pipelines, whereas Scenario 2 results in 69 damages for AC pipelines and 22 damages for PVC pipelines using LSN-RR relationship. Similarly, using the LPI-based liquefiable and non-liquefiable classification together with the LPI-RR relationships, the predicted PGD-induced damages increase to 99 for AC pipelines and 30 for PVC pipelines in Scenario 1, while the corresponding values for Scenario 2 are 95 for AC pipelines and 25 for PVC pipelines. This slight change in PGD-induced

damage estimations is attributed to the lower moment magnitude of 7.0 in Scenario 2 compared with 7.5 in Scenario 1, resulting in marginally smaller LPI and LSN values across the study area. Moreover, the liquefiable and non-liquefiable regions delineated using the LPI-based approach were generally more extensive than those identified using the LSN-based classification. As a result, the LPI-based analyses yielded a larger proportion of pipelines exposed to liquefaction-related effects, leading to higher estimates of PGD-induced damages compared to LSN-based analyses. In contrast, the LSN-based classification yielded a greater extent of non-liquefiable areas, which resulted in higher TGD-induced damage estimates compared to those obtained from the LPI-based analyses.

Moreover, the adopted relationships show notable differences in predicted damage levels. The relationships derived from the Kahramanmaraş case study consistently yield the highest damage estimates, representing an extreme or upper-bound damage condition. In contrast, the repair-rate models proposed in the literature provide a range of damage estimates. For AC pipelines, the relationships proposed by **O'Rourke et al. [2014]** and those implemented in **HAZUS** show comparable results, whereas for PVC pipelines, **HAZUS** generally predicts higher damage levels than **Shih and Chang [2006]**, followed by the **ALA [2001]** relationships. The relationships proposed by **Toprak et al. [2019]** were used to predict PGD-induced damages in liquefiable regions, as they provide material-specific repair-rate relationships for AC and PVC pipelines based on LPI, LSN, and S_{v1D}. However, PGD-induced damage estimation for HDPE pipelines could not be performed due to the lack of available repair-rate relationships for this pipe material.

It should be noted that the damage estimations presented herein are based on empirical repair-rate relationships developed from post-earthquake observations and records under different regional and infrastructural conditions. For instance, the LSN-, LPI-, and S_{v1D}-based repair-rate relationships proposed by **Toprak et al. [2019]**, were derived from damage data collected from the water distribution network in Christchurch, New Zealand. In contrast, the relationships developed by **Shih and Chang [2006]** reflect the characteristics of pipeline systems in Taiwan. Likewise, the repair-rate relationships derived in this study for Kahramanmaraş are representative of the local infrastructure conditions of the Kahramanmaraş water distribution system. Therefore, the damage estimates calculated for the Yalova city center should be

interpreted in the context of the characteristics of the Yalova water distribution system, including pipe materials, construction year, and overall network condition. Such differences indicate notable variations in overall system condition and maintenance levels between two cities. Nevertheless, a common characteristic shared by both infrastructure systems is the presence of aged and deteriorated AC pipelines, which were installed prior to the 1990s in Yalova and are known to exhibit brittle behavior under seismic loading. In addition, the PVC pipelines were constructed following the AC pipelines in Yalova, while in Kahramanmaraş they are known to have service ages of approximately 30 to 40 years. Post-earthquake assessments following the 1999 Kocaeli earthquake reported that a large portion of pipeline damage occurred in both AC and PVC segments. Similarly, following the 2023 Kahramanmaraş earthquakes, AC and PVC pipelines in Kahramanmaraş were also observed to experience severe damage.

While service age provides an initial indicator of pipeline condition, differences in manufacturing quality and material specifications may also influence seismic performance and damage response. For example, post-earthquake observations in Kahramanmaraş indicated that PE pipelines, which are generally expected to exhibit ductile behavior, also experienced significant damage. Thus, the applicability of these damage estimates to Yalova should be assessed in light of the local characteristics of its water distribution network.

12. CONCLUSION

This study combines field observations, municipal data, geotechnical analyses, and empirical modeling to evaluate earthquake-induced damage to water distribution systems. The first part focuses on the 2023 Kahramanmaraş earthquakes, while the second applies a parallel analytical framework to Yalova under two alternative ground-motion scenarios: a probabilistic Mw 7.5 event based on TBEC-2018, and a Mw 7.0 stochastic scenario developed within the MARTEST–SATREPS project for the Prince Islands region.

Field investigations were conducted in Kahramanmaraş Province following the 2023 Kahramanmaraş earthquakes. Collaboration with the municipality and water authorities provided access to operational data and damage reports, forming the basis of the detailed analysis presented in this study. Site visits and photographic documentation indicate that earthquake-related impacts were predominantly concentrated within the distribution network. In contrast, the transmission mains and the reservoir system did not exhibit any notable earthquake-induced problems or service interruptions.

The liquefaction assessment was performed for Kahramanmaraş city center using SPT data and established triggering procedures. The results showed that the investigated sites were not susceptible to liquefaction under the recorded ground motions. Since liquefaction was not expected, the observed pipeline damage was attributed primarily to TGD-induced mechanisms. Following that, the call records maintained by the Kahramanmaraş Water and Sewage Administration were examined. These records consist of notifications submitted by residents through the call center to report water service disruptions during the post-earthquake period. The dataset was filtered in a systematic way to remove subscriber-related entries and duplicate records, and the remaining earthquake-related failures were used in the analysis.

Based on these filtered records, empirical repair-rate correlations were developed as a function of PGV for PVC, AC, and PE pipelines. These correlations were compared with existing PGV–RR relationships reported in the literature. The repair rates obtained for Kahramanmaraş are considerably higher, which reflects the age and deteriorated condition of the system prior to the earthquake as indicated by very high

water losses. For this reason, the city's water infrastructure system is planned to be replaced completely.

The second part of the thesis focuses on Yalova, a city located in a region of high seismic risk. Liquefaction assessments were carried out using the procedures of **Boulanger and Idriss [2014]** and **Youd et al. [2001]**. Liquefaction severity was evaluated across the city center using metrics such as LPI, LSI, and LSN. The results indicate that the highest liquefaction susceptibility occurs along the shore, in the area near Safran Creek, and across the western portion of the city. These areas correspond to young alluvial and coastal-fill deposits with low penetration resistance. Furthermore, the free-field liquefaction settlements were estimated using several published frameworks for both ground-motion scenarios. These settlement distributions were mapped to illustrate the spatial variation of potential ground deformation across Yalova. After identifying the liquefaction-susceptible zones and mapping the corresponding free-field settlements, the analysis then focused on the water infrastructure. The earthquake-induced damage was predicted for both ground-motion scenarios using the repair-rate relationships developed for Kahramanmaraş together with relevant PGV–RR and LSN, LPI and S_{v1D}–RR models from the literature. Both TGD-induced and PGD-induced repair-rate predictions were assessed for each scenario.

The comparison of the two ground-motion scenarios indicates that both transient and permanent ground deformations contribute to repair demands in the distribution network, although their relative effect differs between adopted scenarios. When TGD-induced damages are compared, Scenario 2 (Mw 7.0, stochastic) produces higher TGD-related repair demands than Scenario 1 (Mw 7.5, TBEC-based). This difference is primarily attributed to the higher PGV values associated with Scenario 2, which lead to increased transient ground deformation effects. In contrast, a comparison of PGD-induced damages shows that Scenario 1 yields slightly higher PGD-related repair demands than Scenario 2. The reduced PGD-induced damage estimates obtained for Scenario 2 are related to the marginally smaller extent of liquefiable areas resulting from the lower moment magnitude of Mw 7.0 compared to Mw 7.5 in Scenario 1.

The results indicate that several parts of the Yalova city center are located in areas with high liquefaction susceptibility, where the infrastructure damage assessments show considerable levels of PGD-induced damage. In these zones, repair demands are

controlled by permanent ground deformation, reflecting the sensitivity of the existing pipeline system to liquefaction-related effects. In addition, PGV-based damage estimates for both ground-motion scenarios indicate that transient ground deformation is also expected to result in substantial pipeline damage, particularly under the higher PGV levels associated with the stochastic scenario (Scenario 2). The concentration of predicted damages in these areas highlights the importance of maintaining pipeline condition and selecting materials capable of accommodating ground deformations in liquefaction-prone zones. Moreover, the functionality of urban infrastructure systems is critical for post-earthquake response and recovery, underscoring the need to enhance the seismic preparedness of the water distribution network in Yalova.

This study also highlights the value of systematic post-earthquake documentation and consistent data sharing between municipal agencies and researchers. Such information is essential for understanding network performance and for improving the seismic preparedness of urban lifeline systems. In addition, the lessons learnt from the pipeline performance in the Kahramanmaraş provide a practical basis for future earthquake-related damage predictions and can support planning and renewal efforts in similarly vulnerable cities.

REFERENCES

ALA, (2001), "Seismic Fragility Formulations for Water Systems - Part 1 Guideline", Technical Report, American Society of Civil Engineers (ASCE), USA. https://www.americanlifelinesalliance.com/pdf/Part_1_Guideline.pdf

Ambraseys N. N., (1989). Temporary seismic quiescence: SE Turkey. *Geophysical Journal International*, 96 (2), 311–331. https://doi.org/10.1111/j.1365-246X.1989.tb04453.x

Arpat E., Şaroğlu F., (1972). The East Anatolian Fault System; thoughts on its development. *Bulletin of the Mineral Research and Exploration*, 78, 33–39. https://dergi.mta.gov.tr/files/articles/729/eng/20151007160423_729_22758073.pdf

Barenberg M. E., (1988). Correlation of pipeline damage with ground motions. Journal of Geotechnical Engineering, 114 (6), 706–711. https://doi.org/10.1061/(ASCE)0733-9410(1988)114:6(706)

Bassal P., Moug D. M., Bray J. D., Kendir S. B., Cetin K., Şahin A., (2024). Lateral spreading and flooding along the Iskenderun coast in the 2023 Kahramanmaras earthquake sequence. *Japanese Geotechnical Society Special Publication*, 10 (44), 1653–1658. https://doi.org/10.3208/jgssp.v10.OS-33-04

BELGEP, (2022), "Kahramanmaraş Merkez İçme Suyu, Kanalizasyon ve Yağmur Suyu Projesi", Technical Report.

Boulanger R. W., Idriss I. M., Mejia L. H., (1995), "Investigation and Evaluation of Liquefaction Related Ground Displacement at Moss Landing During the 1989 Loma Prieta Earthquake", Technical Report No: UCD/CGM-95/02, Center for Geotechnical Modeling, Department of Civil and Environmental Engineering, University of California at Davis, USA.

Boulanger R. W., Idriss I. M., (2006). Liquefaction susceptibility criteria for silts and clays. *Journal of Geotechnical and Geoenvironmental Engineering*, 132 (11), 1413–1426. https://doi.org/10.1061/(ASCE)1090-0241(2006)132:11(1413)

Boulanger R. W., Idriss I. M., (2014), "CPT and SPT Based Liquefaction Triggering Procedures", Technical Report No: UCD/CGM-14/01, Center for Geotechnical Modeling, Department of Civil and Environmental Engineering, University of California at Davis, USA.

Bray J. D., Sancio R. B., (2006). Assessment of the liquefaction susceptibility of fine-grained soils. *Journal of Geotechnical and Geoenvironmental Engineering*, 132 (9), 1165–1177. https://doi.org/10.1061/(ASCE)1090-0241(2006)132:9(1165)

Bray J. D., Macedo J., (2017). 6th Ishihara lecture: Simplified procedure for estimating liquefaction-induced building settlement. *Soil Dynamics and Earthquake Engineering*, 102, 215–231. https://doi.org/10.1016/j.soildyn.2017.08.026

Cabalar A. F., Canbolat A., Akbulut N., Tercan S. H., Isik H., (2019). Soil liquefaction potential in Kahramanmaras, Turkey. Geomatics, *Natural Hazards and Risk*, 10 (1), 1822–1838. https://doi.org/10.1080/19475705.2019.1629106

Capadag, E, (2017), "Yalova İli ve Çevresinin Sıvılaşma Potansiyelinin Belirlenmesi", Master's Thesis, Ataturk University.

Cetin K. O., Youd T. L., Seed R. B., Bray J. D., Stewart J. P., Durgunoglu H. T., Lettis W., Yilmaz M. T., (2004a). Liquefaction-induced lateral spreading at Izmit Bay during the Kocaeli (Izmit)-Turkey earthquake. *Journal of Geotechnical and Geoenvironmental Engineering*, 130 (12), 1300–1313. https://doi.org/10.1061/(asce)1090-0241(2004)130:12(1300)

Cetin K. O., Seed R. B., Der Kiureghian A., Tokimatsu K., Harder L. F., Kayen R. E., Moss R. E. S., (2004b). Standard penetration test-based probabilistic and deterministic assessment of seismic soil liquefaction potential. *Journal of Geotechnical and Geoenvironmental Engineering*, 130 (12), 1314–1340. https://doi.org/10.1061/(asce)1090-0241(2004)130:12(1314)

Cetin K. O., Bilge H. T., Wu J., Kammerer A. M., Seed R. B., (2009). Probabilistic model for the assessment of cyclically induced reconsolidation (volumetric) settlements. *Journal of Geotechnical and Geoenvironmental Engineering*, 135 (3), 387–398. https://doi.org/10.1061/(ASCE)1090-0241(2009)135:3(387)

Cetin K. O., Soylemez B., Guzel H., Cakir E., (2025a). Soil liquefaction sites following the February 6, 2023, Kahramanmaraş-Türkiye earthquake sequence. *Bulletin of Earthquake Engineering*, 23, 921–944. https://doi.org/10.1007/s10518-024-01875-3

Cetin K. O., Ayhan B. U., Cüceoğlu F., Yildirim S., (2025b). Performance of Reyhanlı Dam during February 6, 2023 Kahramanmaraş-Türkiye earthquake sequence. *Soil Dynamics and Earthquake Engineering*, 194, 109369. https://doi.org/10.1016/j.soildyn.2025.109369

Ceylan M., (2020), "İçme Suyu Boru Hasarlarının Detaylı İncelenmesi: Christchurch Depremi Örneği", Master's Thesis, Pamukkale University.

Chaudhari V., Pasupuleti V. D. K., Ramancharla P. K., (2013). Finite element analysis of buried continuous pipeline subjected to fault motion. *International Journal of Structural Engineering*, 4 (4), 314–331. https://doi.org/10.1504/IJSTRUCTE.2013.056981

Chung R., Ballantyne D., Comeau E., Holzer T., Madrzykowski D., Schiff A., Stone W., Wilcoski J., Borcherdt R., Cooper J., Lew H., Moehle J., Sheng L., Taylor A., Bucker I., Hayes Jr. J., Leyendecker E., O'Rourke T., Singh M., Whitney M., (1996). The January 17, 1995 Hyogoken-Nanbu (Kobe) Earthquake: Performance of Structures, Lifelines, and Fire Protection Systems. *National Institute of Standards and Technology*. https://doi.org/10.6028/NIST.SP.901

Commodity Exchange of Kahramanmaras, (2017), “2018–2021 Stratejik Planı”, Technical Report.

Cubrinovski M., Robinson K., Taylor M., Hughes M., Orense R., (2012). Lateral spreading and its impacts in urban areas in the 2010-2011 Christchurch earthquakes. *New Zealand Journal of Geology and Geophysics*, 55 (3), 255–269. https://doi.org/10.1080/00288306.2012.699895

Demirtas R., (1998), “27 Haziran 1998 Ceyhan-Misis, 22 Ocak 1997 Hatay depremleri: Doğu Anadolu Fayı yakın bir deprem serisinin hazırlık evresinde mi ?”, Technical Report. https://doi.org/10.13140/RG.2.2.23160.70403

Davis C.A., O’Rourke T. D., Adams M. L., Rho M. A., (2012), “Case study: Los Angeles water services restoration following the 1994 Northridge earthquake”, 15th World Conference on Earthquake Engineering (15WCEE), Lisbon, Portugal, 24-28 September.

DSI, (2025), Gokce Baraji, https://www.dsi.gov.tr/baraj/detay.cfm?BarajID=119, (Accessed on: 13 October 2025).

Eastern Mediterranean Development Agency, (2025), Sanayi, https://www.dogaka.gov.tr/dogu-akdeniz/kahramanmaras/sanayi, (Accessed on: 11 October 2025).

Eguchi R. T., (1991). Seismic hazard input for lifeline systems. *Structural Safety*, 10 (1–3), 193–198. https://doi.org/10.1016/0167-4730(91)90014-Z

Eidinger J., Maison B., Lee D., Lau B., (1995), “East Bay Municipal District water distribution damage in 1989 Loma Prieta earthquake”, 4th US Conference on Lifeline Earthquake Engineering, San Francisco, USA, 10-12 August.

Erdik M., (2000). Report on 1999 Kocaeli and Düzce (Turkey) earthquakes. *Structural Control for Civil and Infrastructure Engineering*, 149–186. https://doi.org/10.1142/9789812811707_0018

Flora A., Bilotta E., Valtucci F., Fierro T., Perez R., Santucci de Magistris F., Modoni G., Spacagna R., Kelesoglu M. K., Sargin S., Altinok E., Oztoprak S., Bozbey I., Aysal N., (2024). Liquefaction effects in the city of Gölbaşı: from the analysis of predisposing factors to damage survey. *Engineering Geology*, 338, 107633. https://doi.org/10.1016/j.enggeo.2024.107633

GEER, (1999), Initial Geotechnical Observations of the August 17, 1999, Kocaeli Earthquake, https://geerassociation.org/components/com_geer_reports/geerfiles/Kocaeli_1999/Report3.1Kocaeli.pdf, (Accessed on: 22 July 2025).

Görüm T., Tanyas H., Karabacak F., Yılmaz A., Girgin S., Allstadt K. E., Süzen M. L., Burgi P., (2023). Preliminary documentation of coseismic ground failure triggered by the February 6, 2023 Türkiye earthquake sequence. *Engineering Geology*, 327, 107315. https://doi.org/10.1016/j.enggeo.2023.107315

Ha D., Abdoun T. H., O'Rourke M. J., Symans M. D., O'Rourke T. D., Palmer M. C., Stewart H. E., (2010). Earthquake faulting effects on buried pipelines - Case history and centrifuge study. *Journal of Earthquake Engineering*, 14 (5), 646–669. https://doi.org/10.1080/13632460903527955

Holzer T. L., Bennett M. J., Noce T. E., Padovani A. C., Tinsley J. C., (2002), "Liquefaction Hazard and Shaking Amplification Maps of Alameda, Berkeley, Emeryville, Oakland, and Piedmont, California: A Digital Database", U.S. Geological Survey Open-file Report No: 02-296, USA.

Holzer T. L., Toprak S., Bennett M. J., (2003), "Application of the liquefaction potential index to liquefaction hazard mapping", 8th U.S.–Japan Workshop on Earthquake Resistant Design of Lifeline Facilities and Countermeasures against Liquefaction, Tokyo, Japan.

Hutabarat D., Bray J. D., (2022). Estimating the Severity of Liquefaction Ejecta Using the Cone Penetration Test. *Journal of Geotechnical and Geoenvironmental Engineering*, 148 (3). https://doi.org/10.1061/(asce)gt.1943-5606.0002744

Idriss I. M., Boulanger R. W., (2003), "Estimating Ka for use in evaluating cyclic resistance of sloping ground", 8th U.S.-Japan Workshop on Earthquake Resistant Design of Lifeline Facilities and Countermeasures against Liquefactions, Tokyo, Japan.

Idriss I. M., Boulanger R. W., (2008), "Soil Liquefaction during Earthquakes", Earthquake Engineering Research Institute (EERI), Monograph No: MNO-12, Oakland, USA.

Inan S., Cetin H., Yakupoglu N., (2024). Spring water anomalies before two consecutive earthquakes (Mw 7.7 and Mw 7.6) in Kahramanmaraş (Türkiye) on 6 February 2023. *Natural Hazards and Earth System Sciences*, 24, 397–409. https://doi.org/https://doi.org/10.5194/nhess-24-397-2024

Ishihara K., Koga Y. A., (1981). Case Studies of Liquefaction in the 1964 Niigata Earthquake. *Soils and Foundations*, 21 (3), 35–52. https://doi.org/https://doi.org/10.3208/sandf1972.21.3_35

Ishihara K., (1985), "Stability of natural deposits during earthquakes", 11th International Conference on Soil Mechanics and Foundation Engineering, San Francisco, USA, 12-16 August.

Ishihara K., Yoshimine M., (1992). Evaluation of settlements in sand deposits following liquefaction during earthquakes. *Soils and Foundations*, 32 (1), 173–188. https://doi.org/https://doi.org/10.3208/sandf1972.32.173

Iwasaki T., Arakawa T., Tokida K., (1982), „Simplified procedures for assessing soil liquefaction during earthquakes", Conference on Soil Dynamics and Earthquake Engineering, 925–939.

Jinguuji M., Toprak S., (2017). A case study of liquefaction risk analysis based on the thickness and depth of the liquefaction layer using CPT and electric resistivity data in the Hinode area, Itako City, Ibaraki Prefecture, Japan. *Exploration Geophysics*, 48 (1), 28–36. https://doi.org/10.1071/EG16137

Kahramanmaras Metropolitan Municipality, (2025), Kahramanmaras Metropolitan Municipality, https://kahramanmaras.bel.tr/, (Accessed on: 19 July 2025).

KASKI, (2024), "Kahramanmaraş Su ve Kanalizyon İdaresi Genel Müdürlüğü 2023 Yılı Faaliyet Raporu", Technical Report, Kahramanmaraş, Türkiye.

Katayama T., Kubo K., Sato N., (1975), "Earthquake damage to water and gas distribution systems", U.S. National Conference on Earthquake Engineering, Michigan, USA, 18-20 June.

Kubo K., Mogami T., (1953), "The Behaviour of Soil during Vibration", 3rd International Conference on Soil Mechanics and Foundation Engineering, Switzerland. https://www.issmge.org/publications/online-library

Lange D., Kopp H., Royer J. Y., Henry P., Çakir Z., Petersen F., Sakic P., Ballu V., Bialas J., Özeren M. S., Ergintav S., Géli L., (2019). Interseismic strain build-up on the submarine North Anatolian Fault offshore Istanbul. *Nature Communications*, 10 (1). https://doi.org/10.1038/s41467-019-11016-z

Lemnitzer A., Arduino P., Dafni J., Franke K. W., Martinez A., Mayoral J., El Mohtar C., Pehlivan M., Yashinsky M., (2021). The September 19, 2017 MW 7.1 CENTRAL-Mexico earthquake: Immediate observations on selected infrastructure systems. *Soil Dynamics and Earthquake Engineering*, 141 (106430). https://doi.org/10.1016/j.soildyn.2020.106430

Maruyama Y., Kimishima K., Yamazaki F., (2011). Damage assessment of buried pipes due to the 2007 Niigata Chuetsu-Oki earthquake in Japan. *Journal of Earthquake and Tsunami*, 5 (1), 57–70. https://doi.org/10.1142/S179343111100098X

Maurer B. W., Green R. A., Cubrinovski M., Bradley B. A., (2014). Evaluation of the Liquefaction Potential Index for Assessing Liquefaction Hazard in Christchurch, New Zealand. *Journal of Geotechnical and Geoenvironmental Engineering*, 140 (7). https://doi.org/10.1061/(asce)gt.1943-5606.0001117

Milashuk S., Crane W., (2012). Pipeline damage caused by transient ground deformation: Case study of 2010 Darfield and 2011 Christchurch earthquakes. *Soil Dynamics and Earthquake Engineering*, 41, 84–88. https://doi.org/10.1016/j.soildyn.2012.05.011

Nacaroğlu, E., (2010), "Deprem Etkisiyle Oluşan Boru Hasarlarının Coğrafi Bilgi Sistemleri (CBS) ve Kümeleme Analizi ile Değerlendirilmesi", Master's Thesis, Pamukkale University.

New Zealand Water & Wastes Association (NZWWA), (2010), "2009/2010 National Performance Review Report: Water Utilities", Technical Report, New Zealand.

Ni P., Mangalathu S., Yi Y., (2018). Fragility analysis of continuous pipelines subjected to transverse permanent ground deformation. *Soils and Foundations*, 58 (6), 1400–1413. https://doi.org/10.1016/j.sandf.2018.08.002

O'Rourke M. J., Ayala G., (1993). Pipeline damage due to wave propagation. *Journal of Geotechnical Engineering*, 119 (9). https://doi.org/10.1061/(ASCE)0733-9410(1993)119:9(1490)

O'Rourke T. D., Jeon S. S., Toprak S., Cubrinovski M., Hughes M., Van Ballegooy S., Bouziou D., (2014). Earthquake response of underground pipeline networks in Christchurch, NZ. *Earthquake Spectra*, 30 (1), 183–204. https://doi.org/10.1193/030413EQS062M

Ozcep F., Zarif H. (2009). Variations of soil liquefaction safety factors depending on several design earthquakes in the city of Yalova (Turkey). *Scientific Research and Essay*, 4 (6), 594–604.

PEER, (2000a), Documenting incidents of ground failure resulting from the August 17, 1999 Kocaeli, Turkey Earthquake, https://apps.peer.berkeley.edu/publications/turkey/adapazari/index.html, (Accessed on: 11 August 2025).

PEER, (2000b), Geotechnical site investigation at selected lateral spread sites (Phase 4: Yalova), https://apps.peer.berkeley.edu/publications/turkey/adapazari/phase4/yalova/index.html, (Accessed on: 11 August 2025).

Scawthorn C., Miyajima M., Ono Y., Kiyono J., Hamada M., (2006). Lifeline aspects of the 2004 Niigata ken Chuetsu, Japan, earthquake. *Earthquake Spectra*, 22 (1), 89–110. https://doi.org/10.1193/1.2173932

Seed H. B., Idriss I. M., (1971). Simplified Procedure for Evaluating Soil Liquefaction Potential. *Journal of the Soil Mechanics and Foundations Division*, 97 (9). https://doi.org/10.1061/JSFEAQ.0001662

Seed H. B., Tokimatsu K., Harder L. F., Chung R. M., (1985). Influence of SPT Procedures in Soil Liquefaction Resistance Evaluations. *Journal of Geotechnical Engineering*, 111 (12). https://doi.org/10.1061/(ASCE)0733-9410(1985)111:12(1425)

Seed R. B., Cetin K. O., Moss R. E. S., Kammerer A., Wu J., Pestana J., Riemer M., Sancio R. B., Bray J. D., Kayen R. E., Faris A., (2003). Recent advances in soil liquefaction engineering: A unified and consistent framework. https://www.researchgate.net/publication/314359545

Şengör A. M. C., Tüysüz O., Imren C., Sakınç M., Eyidoğan H., Görür N., Le Pichon X., Rangin C., (2005). The North Anatolian Fault: A new look. *Annual Review of Earth and Planetary Sciences*, 33, 37–112. https://doi.org/10.1146/annurev.earth.32.101802.120415

Shamoto Y., Zhang J. M., Tokimatsu K., (1998). New charts for predicting large residual post-liquefaction ground deformation. *Soil Dynamics and Earthquake Engineering*, 17 (7–8), 427–438. https://doi.org/10.1016/S0267-7261(98)00011-6

Shih B. J., Chang C. H., (2006). Damage survey of water supply systems and fragility curve of PVC water pipelines in the Chi–Chi Taiwan earthquake. *Natural Hazards*, 37, 71–85. https://doi.org/10.1007/s11069-005-4657-9

Şimşek C., Akinci G., Fistikoğlu O., Canli K., Sözbilir H., Ayol A., Bilgiç E., (2024). Response of water resources to the Kahramanmaraş earthquakes (MW 7.7 and MW 7.6) that occurred on February 6, 2023, on the East Anatolian Fault Zone (Türkiye). *Turkish Journal of Earth Sciences*, 33 (1), 69–84. https://doi.org/10.55730/1300-0985.1899

Sonmez H., Gokceoglu C., (2005). A liquefaction severity index suggested for engineering practice. *Environmental Geology*, 48 (1), 81–91. https://doi.org/10.1007/s00254-005-1263-9

SBB, (2023), "2023 Kahramanmaraş Ve Hatay Depremleri Raporu", Technical Report, Türkiye Cumhuriyeti Strateji ve Bütçe Başkanlığı, Türkiye.

Taftsoglou M., Valkaniotis S., Papathanassiou G., Karantanellis E., (2023). Satellite Imagery for Rapid Detection of Liquefaction Surface Manifestations: The Case Study of Türkiye–Syria 2023 Earthquakes. *Remote Sensing*, 15 (17). https://doi.org/10.3390/rs15174190

Takada S., Tanabe K., Yamajyo K., Katagiri S., (1987). Liquefaction Analysis for Buried Pipelines. *Developments in Geotechnical Engineering*, 45, 319–333. https://doi.org/10.1016/B978-0-444-98955-0.50028-8

Tang A. K., Eng P., Eng C., Asce F., (2011). Lifelines performance of the Mw 8.8 off shore Biobío, Chile earthquake. *Procedia Engineering*, 14, 922–930. https://doi.org/10.1016/j.proeng.2011.07.116

TBEC, (2018), Turkish Building Earthquake Code, https://resmigazete.gov.tr/eskiler/2018/03/20180318M1-2-1.pdf, (Accessed on: 19 August 2025).

Tokimatsu K., Seed H. B., (1984), "Simplified Procedures for The Evaluation of Settlements in Clean Sands", Technical Report No: UCB/EERC-84/16, Earthquake Engineering Research Center, College of Engineering, University of California at Berkeley, USA.

Tonkin and Taylor, (2013), "Liquefaction Vulnerability Study", Technical Report No: 52020.0200/v.10.

Toprak S., (1998), "Earthquake Effects on Buried Lifeline Systems", PhD Dissertation, Cornell University.

Toprak S., Holzer T. L., (2003). Liquefaction Potential Index: Field Assessment. *Journal of Geotechnical and Geoenvironmental Engineering*, 129 (4), 315–322. https://doi.org/10.1061/(ASCE)1090-0241(2003)129:4(315)

Toprak S., Taskin F., Cem Koc A. (2009). Prediction of earthquake damage to urban water distribution systems: A case study for Denizli, Turkey. *Bulletin of Engineering Geology and the Environment*, 68 (4), 499–510. https://doi.org/10.1007/s10064-009-0230-1

Toprak S., Nacaroğlu E., Koç A. C., (2015), "Seismic Response of Underground Lifeline Systems". In: A. Ansal, Editor, Perspectives on European Earthquake Engineering and Seismology, Geotechnical, Geological and Earthquake Engineering, vol 39. Springer, Cham. https://doi.org/10.1007/978-3-319-16964-4_10

Toprak S., Nacaroglu E., Koc A. C., O'Rourke T. D., Hamada M., Cubrinovski M., Van Ballegooy S., (2018). Comparison of horizontal ground displacements in Avonside area, Christchurch from air photo, LiDAR and satellite measurements regarding pipeline damage assessment. *Bulletin of Earthquake Engineering*, 16 (10), 4497–4514. https://doi.org/10.1007/s10518-018-0317-9

Toprak S., Nacaroglu E., van Ballegooy S., Koc A. C., Jacka M., Manav Y., Torvelainen E., O'Rourke T. D., (2019). Segmented pipeline damage predictions using liquefaction vulnerability parameters. *Soil Dynamics and Earthquake Engineering*, 125 (105758). https://doi.org/10.1016/j.soildyn.2019.105758

Toprak S., Wham B. P., Nacaroglu E., Ceylan M., Dal O., Senturk A. E., (2024a). Impact of Seismic Geohazards on water supply systems and pipeline performance: Insights from the 2023 Kahramanmaras Earthquakes. *Engineering Geology*, 340 (107681). https://doi.org/10.1016/j.enggeo.2024.107681

Toprak S., Nacaroğlu E., Ceylan M., Dal O., Tunç Ş. C., Şentürk A. E., İnce M. B., (2024b), "2023 Kahramanmaraş Depremlerinde Su ve Kanalizasyon Sistemlerinde Gözlemler", 19th National Soil Mechanics and Geotechnical Engineering, Ankara, Türkiye, 16-18 October. https://zmgm19.com/index.php/bildiriler/

Toprak S., Nacaroglu E., Wham B., Sakamoto M., Uckan E., Guldur Erkal B., Dal O., Ceylan M., Kaya E. S., Bayraktar M., Senturk A. E., Cappa R., (2024c), "Impacts and lessons from the February 2023 earthquakes on urban infrastructure systems", Symposium on the February 2023 Earthquakes from the Perspective of Civil/Earthquake Engineering, 239–254, Adana, Türkiye, 18-20 January.

Toprak S., Wham B., Nacaroglu E., Ceylan M., Dal O., Senturk A. E., Tunc S. C., Ince, M. B., (2024d). Field Observations on Water Systems after the February 2023 Kahramanmaras Earthquakes (Mw 7.7, Mw 7.6), in Field Observations and Data on Strong Motion, Geotechnical, and Infrastructure Impacts of the February 2023 Kahramanmaras Earthquakes (Mw 7.7, Mw 7.6). DesignSafe-CI. https://doi.org/10.17603/ds2-3zdf-0b28

Toprak S., Zulfikar A. C., Mutlu A., Tugsal U. M., Nacaroglu E., Karabulut S., Ceylan M., Ozdemir K., Parlak S., Dal O., Karimzadeh S., (2025a). The aftermath of 2023 Kahramanmaras earthquakes: evaluation of strong motion data, geotechnical, building, and infrastructure issues. *Natural Hazards*, 121, 2155–2192. https://doi.org/10.1007/s11069-024-06890-w

Toprak S., Nacaroğlu E., Dal O., Şentürk A. E., Ceylan M., Tunç Ş. C., İnce, M. B., (2025b). Post-earthquake condition of lifeline systems following the Kahramanmaraş. *Natural Disaster Research Report*, (61), 1–8. https://doi.org/10.24732/NIED.00007004

Toprak S., Wham B. P., Nacaroglu E., Ceylan M., Dal O. (2025c). Performance of water systems during the February 6th Kahramanmaras earthquakes. *Earthquake Spectra*, 41 (1), 322 –353. https://doi.org/10.1177/87552930241293571

Toprak S., Nacaroğlu E., Dal O., Ceylan M., Şentürk A. E., Tunç Ş. C., İnce M. B., (2025d), "2023 Kahramanmaraş depremleri sonrası su sistemi hasarları ve iyileştirme çalışmaları", 10th Turkish Conference on Earthquake, Istanbul, Türkiye, 8-10 October. http://hdl.handle.net/11527/27769

Toprak S., Çiçek F., Tunç Ş. C., Övünç E. E., Bingöl M., Karakoç F. B., (2025e), "Sıvılaşma tehlike analizi ve potansiyel haritalarının oluşturulması: Yalova il merkezi.", 10th Turkish Conference on Earthquake Engineering, Istanbul, Türkiye, 8-10 October. http://hdl.handle.net/11527/27769

Toprak S., Wham B. P., Nacaroglu E., Sakamoto M., Tunc S. C., Davis C. A., Uckan E., Dal O., Ceylan M., Senturk A. E., Kaya E. S., Ince M.B., (2026a). Assessment of Infrastructure Failures in the 2023 Kahramanmaras Earthquakes. *ASCE OPEN: Multidisciplinary Journal of Civil Engineering*, 4 (1). https://doi.org/10.1061/AOMJAH.AOENG-0103

Toprak S., Tunc S. C., Ovunc E. E., Yagci A. L., Dal, O., (2026b). Post-seismic Turbidity Response in the Goksu Stream After the 2023 Kahramanmaras Earthquakes. *Natural Hazards*. https://doi.org/10.1007/s11069-025-07885-x

Turkish Statistical Institute, (2025), Population statistics portal, https://nip.tuik.gov.tr/, (Accessed on: 17 November 2025).

Uckan E., Aksel M., Atas O., Toprak S., Kaya E. S., (2024). The performance of transmission pipelines on february 6th, 2023 Kahramanmaras earthquake: a series of case studies. *Bulletin of Earthquake Engineering*, 23, 1203–1222. https://doi.org/10.1007/s10518-024-01957-2

Ulusay R., Aydan Ö, Kumsar H., (2024). Ground liquefaction caused by 6 February 2023 Kahramanmaraş earthquakes of Türkiye and some assessments on its extent and impacts on built environment. *Bulletin of Engineering Geology and the Environment*, 83 (447). https://doi.org/10.1007/s10064-024-03946-w

Unal E. O., Kocaman S., Gokceoglu C., (2024). Impact assessment of geohazards triggered by 6 February 2023 Kahramanmaras Earthquakes (Mw 7.7 and Mw 7.6) on the natural gas pipelines. *Engineering Geology*, 334 (107508). https://doi.org/10.1016/j.enggeo.2024.107508

Vazouras P., Dakoulas P., Karamanos S. A., (2015). Pipe-soil interaction and pipeline performance under strike-slip fault movements. *Soil Dynamics and Earthquake Engineering*, 72, 48–65. https://doi.org/10.1016/j.soildyn.2015.01.014

Wang X., Han J., Kang A., Naggar M. H. E., Miao H., Xu C., (2024). Seismic fragility analysis of buried pipelines under Kahramanmaraş ground motions. *Engineering Geology*, 337 (107596). https://doi.org/10.1016/j.enggeo.2024.107596

Wham B. P., Dashti S., Franke K., Kayen R., Oettle N. K., (2017). Water supply damage caused by the 2016 Kumamoto earthquake. *International Association of Lowland Technology*, 19 (3), 165–174. https://www.researchgate.net/publication/324441842

Wu J., Seed R. B., Pestana J. M., (2003), "Liquefaction Triggering and Post-Liquefaction Deformation of Monterey 0/30 Sand Under Uni-directional Cyclic Simple Shear Loading", Geotechnical Engineering Research Report No: UCB/GE-2003/01, University of California, Berkeley, USA.

Yalova Chamber of Commerce and Industry, (2021), "Yalova Sanayi Durum Raporu", Technical Report, Yalova, Türkiye.

Yalova Municipality, (2016), "Mikrobölgeleme Etüt Raporu", Technical Report, Yalova, Türkiye.

Yalova Municipality, (2025), İklim ve Coğrafya, https://Www.Yalova.Bel.Tr/Public/Sayfa/Iklim-ve-Cografya, (Accessed on: 21 November 2025).

Governor of Yalova, (2019), 17 Ağustos 1999 Marmara Depremi'nin 20. Yıldönümünün Anma Etkinlikleri Düzenlendi, https://www.yalova.gov.tr/17-agustos-1999-marmara-depreminin-20-yildonumunun-anma-etkinlikleri-duzelendi, (Accessed on: 13 December 2025).

Yeleser L., (2006), "Kahramanmaraş ve Yakın Kuzeyinin Mühendislik Jeolojisi Özellikleri", Master's Thesis, Kahramanmaras Sutcu Imam University.

Yilmaz I., Yavuzer D., (2005). Liquefaction potential and susceptibility mapping in the city of Yalova, Turkey. *Environmental Geology*, 47 (2), 175–184. https://doi.org/10.1007/s00254-004-1141-x

Yoshimine M., Nishizaki H., Amano K., Hosono Y., (2006). Flow deformation of liquefied sand under constant shear load and its application to analysis of flow slide of infinite slope. *Soil Dynamics and Earthquake Engineering*, 26 (2-4), 253–264. https://doi.org/10.1016/j.soildyn.2005.02.016

Youd T. L., (2014), “Ground failure investigations following the 1964 Alaska earthquake”, 10th U.S. National Conference on Earthquake Engineering, Alaska, USA, 21-25 July. https://doi.org/10.4231/D3DN3ZW6P

Youd T. L., Idriss, I. M., Andrus R. D., Arango I., Castro G., Christian J. T., Dobry R., Finn W. D. L., Harder L. F., Hynes M. E., Ishihara K., Koester J. P., Liao S. S. C., Marcuson W. F., Martin G. R., Mitchell J. K., Moriwaki Y., Power M. S., Robertson P. K., Seed R. B., Stokoe K. H., (2001). Liquefaction Resistance of Soils: Summary Report from the 1996 NCEER and 1998 NCEER/NSF Workshops on Evaluation of Liquefaction Resistance of Soils. *Journal of Geotechnical and Geoenvironmental Engineering*, 127 (10). https://doi.org/10.1061/(ASCE)1090-0241(2001)127:10(817)

Zhang G., Robertson P. K., Brachman R. W. I., (2002). Estimating liquefaction-induced ground settlements from CPT for level ground. *Canadian Geotechnical Journal*, 39 (5), 1168–1180. https://doi.org/10.1139/t02-047

Zhang G., Robertson P. K., Brachman R. W. I., (2004). Estimating Liquefaction-Induced Lateral Displacements Using the Standard Penetration Test or Cone Penetration Test. *Journal of Geotechnical and Geoenvironmental Engineering*, 130 (8). https://doi.org/10.1061/ASCE1090-02412004130:8861

BIOGRAPHY

Seyhmus Can TUNC successfully completed his B.Sc. Civil Engineering at Gebze Technical University in 2023. During his undergraduate studies, he devoted himself to improve his vision by actively participating in the conferences and seminars. As part of the TÜBİTAK STAR 2247-C Trainee Researcher Scholarship Program, he worked as a research intern for six months. He not only paid attention to improve his technical aspects but also focused on communication and personal skills. To enhance his global experience, he participated in the Summer Work and Travel Exchange Program, visiting the United States in both 2022 and 2023. Upon graduating as the top student of the department, he began his M.Sc. studies in Civil Engineering at Gebze Technical University, under the supervision of Prof. Dr. Selçuk TOPRAK. Between June 2024 and August 2025, he worked as a research assistant in the Department of Civil Engineering at Istanbul Gelişim University.

PUBLICATIONS AND PRESENTATIONS FROM THE THESIS

Toprak S., Wham B. P., Nacaroglu E., Sakamoto M., Tunc S. C., Davis C. A., Uckan E., Dal O., Ceylan M., Senturk A. E., Kaya E. S., Ince M.B., (2026). Assessment of Infrastructure Failures in the 2023 Kahramanmaras Earthquakes. *ASCE OPEN: Multidisciplinary Journal of Civil Engineering*, 4 (1). https://doi.org/10.1061/AOMJAH.AOENG-0103

Toprak S., Çiçek F., Tunç Ş. C., Övünç E. E., Bingöl M., Karakoç F. B., (2025), "Sıvılaşma tehlike analizi ve potansiyel haritalarının oluşturulması: Yalova il merkezi.", 10th Turkish Conference on Earthquake Engineering, Istanbul, Türkiye, 8-10 October. http://hdl.handle.net/11527/27769

Toprak S., Nacaroğlu E., Dal O., Ceylan M., Şentürk A. E., Tunç Ş. C., İnce M. B., (2025), "2023 Kahramanmaraş depremleri sonrası su sistemi hasarları ve iyileştirme çalışmaları", 10th Turkish Conference on Earthquake, Istanbul, Türkiye, 8-10 October. http://hdl.handle.net/11527/27769

Toprak S., Nacaroğlu E., Dal O., Şentürk A. E., Ceylan M., Tunç Ş. C., İnce, M. B., (2025). Post-earthquake condition of lifeline systems following the Kahramanmaraş. *Natural Disaster Research Report*, (61), 1–8. https://doi.org/10.24732/NIED.00007004

Toprak S., Nacaroğlu E., Ceylan M., Dal O., Tunç Ş. C., Şentürk A. E., İnce M. B., (2024), "2023 Kahramanmaraş Depremlerinde Su ve Kanalizasyon Sistemlerinde Gözlemler", 19th National Soil Mechanics and Geotechnical Engineering, Ankara, Türkiye, 16-18 October. https://zmgm19.com/index.php/bildiriler/

Toprak S., Wham B., Nacaroglu E., Ceylan M., Dal O., Senturk A. E., Tunc S. C., Ince, M. B., (2024). Field Observations on Water Systems after the February 2023 Kahramanmaras Earthquakes (Mw 7.7, Mw 7.6), in Field Observations and Data on Strong Motion, Geotechnical, and Infrastructure Impacts of the February 2023 Kahramanmaras Earthquakes (Mw 7.7, Mw 7.6). DesignSafe-CI. https://doi.org/10.17603/ds2-3zdf-0b28